Understanding the neural baroreflex: Pulsatility, baroreflex sensitivity and system identification - experimentation and analysis

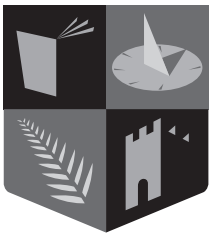

Ollscoil
Mhá Nuad
Ollscoil na hÉireann
Má Nuad

Hasana Bagnall Hare

A thesis submitted for the degree of
Doctor of Philosophy

Maynooth University

Faculty of Science and Engineering, Electronic Engineering Department

October 2023

Head of the department: Prof. Gerard Lacey
Supervisor: **Prof. John V. Ringwood**

Contents

Abstract v

Declaration of authorship vii

Acknowledgements ix

List of Figures xi

List of Tables xvii

List of abbreviations xix

1 Introduction 1

1.1 Motivation . . . 2
1.2 Objectives and contributions . . . 4
1.3 List of publications . . . 7
1.4 Thesis layout . . . 8

2 Blood pressure and the baroreflex: A comprehensive background 11

2.1 Blood pressure . . . 12
2.2 The neural baroreflex model . . . 14
2.2.1 Baroreceptors . . . 14
2.2.2 Central nervous system . . . 15
2.2.3 Cardiac branches . . . 17
2.2.4 Peripheral resistance branches . . . 17
2.3 Low frequency oscillations . . . 18
2.4 Hypertension and antihypertensive treatments . . . 19
2.4.1 Baroreceptor activation therapy . . . 19
2.4.2 Characteristics of the neural baroreflex . . . 21
2.5 Baroreflex sensitivity estimation methods . . . 23
2.5.1 Oxford method . . . 24
2.5.2 Existing non-invasive BRS estimation methods . . . 24
2.5.3 Sequence methods . . . 27

3 Protocol for the identification of the neural baroreflex characteristic in sheep 31
3.1 Introduction . . . 31
3.2 Details of the experiment . . . 32
3.2.1 Experimental setup . . . 33
3.2.2 Data acquisition and analysis equipment . . . 33
3.2.3 Selection of excitation signal . . . 34
3.3 Modelling preliminaries . . . 36
3.3.1 Considerations from physical system . . . 36
3.3.2 Data preprocessing . . . 38
3.4 Model identification . . . 38
3.4.1 Frequency domain . . . 39
3.4.2 Time domain . . . 42
3.5 Model validation . . . 47
3.5.1 Frequency domain validation . . . 47
3.5.2 Time domain validation . . . 48
3.6 Conclusion . . . 49

4 Investigating the accuracy of sequence methods as a reliable non-invasive baroreflex sensitivity estimation method 51
4.1 Introduction . . . 52
4.2 Analytic overview of sequence methods . . . 53
4.2.1 Sequences within a system identification framework . . . 53
4.2.2 Generic analysis of sequence methods . . . 54
4.3 Numerical example . . . 57
4.3.1 Problem setup . . . 58
4.3.2 Sequence selection . . . 61
4.3.3 Gain estimation methods . . . 63
4.4 Experimental analysis . . . 63
4.4.1 EuroBaVar data set . . . 63
4.4.2 BRS estimation methods employed . . . 64
4.5 Results . . . 66
4.5.1 Numerical example results . . . 66
4.5.2 EuroBaVar data set results . . . 67
4.6 Discussion . . . 67
4.6.1 Numerical example . . . 67
4.6.2 Experimental example . . . 70
4.6.3 Observations . . . 71
4.7 Conclusion . . . 71

5 Understanding the interplay between baroreflex gain, low frequency oscillations, and pulsatility in the neural baroreflex 73
5.1 Introduction . . . 74
5.2 Testing the model . . . 75
5.2.1 Cardiac branches . . . 75
5.2.2 Homeostatic analysis . . . 76
5.3 Arterial compliance . . . 79
5.4 Including pulsatility . . . 81
5.5 Model simplification . . . 83
5.5.1 Arterial compliance simplification . . . 83
5.5.2 Pulsatility representation . . . 84
5.5.3 Describing function approximation . . . 89
5.6 Mathematical model . . . 89
5.7 Determining the conditions for LF oscillation . . . 93
5.7.1 Analytical solution . . . 94
5.7.2 Simulation results . . . 94
5.8 Effect of an absence of pulsatility . . . 97
5.9 Predominance of the cardiac or peripheral branches . . . 98
5.10 Conclusion . . . 100

6 Investigating the relationship between pulsatility and Mayer waves 105
6.1 Introduction . . . 106
6.1.1 Mechanical circulatory support . . . 107
6.2 Animal study . . . 110
6.3 Human trial - Details of the trial . . . 111
6.3.1 Experimental set up . . . 112
6.3.2 Data acquisition and analysis equipment . . . 113
6.3.3 Acquisition challenges . . . 115
6.4 Assessing Mayer wave identifiability in irregularly sampled, sparse data 116
6.4.1 The impact of sparse date on the MAP frequency spectrum through a test case . . . 116
6.5 Results . . . 119
6.5.1 Animal study . . . 119
6.5.2 Human study . . . 127
6.6 Observations and limitations . . . 129
6.7 Conclusions . . . 130

7 Conclusion and future work 133
7.1 Summary and conclusions . . . 133
7.2 Future work . . . 135

Appendices

A Clinical trial documentation **139**
A.1 Consent forms and information leaflets 141
A.1.1 Patient 141
A.1.2 Participant 145
A.2 Datasheet 148

B Clinical trial recordings **149**
B.1 Human study results 150
B.1.1 Control 1 150
B.1.2 Control 2 152
B.1.3 Control 3 154
B.1.4 Control 4 156
B.1.5 Control 5 158
B.1.6 Control 6 160
B.1.7 Control 7 162
B.1.8 Control 8 163
B.1.9 Control 9 165
B.1.10 Patient 01 167
B.1.11 Patient 03 171
B.1.12 Patient 04 172
B.1.13 Patient 07 174

C EuroBaVar sparse data test case **177**

Bibliography **191**

Abstract

Blood pressure is a dynamic measurement that continuously changes based on a variety of physiological needs. Adequate blood pressure is crucial for a variety of reasons, such as organ perfusion, oxygen circulation, and the excretion of harmful toxins. Prolonged periods of blood pressure abnormalities, such as hypotension and hypertension, can lead to an array of adverse events, including myocardial infarction and stroke. Understanding blood pressure dynamics can aid the early diagnosis and slow the development of adverse cardiovascular conditions. This thesis aims to provide additional information about the neural baroreflex, the short term regulator of blood pressure.

A protocol to characterise the neural baroreflex from data recorded, where the baroreceptors remain intact, is presented. The method allows for both time- and frequency- domain model identification that accurately represent the neural baroreflex.

Mayer waves, or low-frequency oscillations, are observed in blood pressure readings, occurring at approximately 0.1Hz in humans. The origin and prognostic value of these waves are currently being explored. In this thesis, a baroreflex model is extended to include compliance and pulsatility. This model is then used to determine the conditions under which low-frequency oscillations occur, with a focus on the effect of blood pressure pulsatility on their presence. The analysis suggests that as pulsatility decreases, the incidence of Mayer waves increases. This hypothesis is then examined experimentally.

The functionality of the baroreflex is evaluated through baroreflex sensitivity estimation. A decrease in baroreflex sensitivity has been proven to be a reliable indicator of adverse cardiovascular events. The current gold standard is the Oxford method, an invasive procedure that cannot be performed in routine clinical settings. Hence, there is a need for a non-invasive alternative. This thesis examines the viability of sequence methods, a popular non-invasive alternative, as a reliable estimation method.

This thesis explores a collection of studies which, individually, have their own unique contributions. However, collectively the studies work to increase the understanding of blood pressure regulation, providing insight to aid the development of baroreflex assessment methods and potentially aid the identification of potential sources of baroreflex dysregulation.

Declaration of authorship

I, Hasana Bagnall Hare, declare that this thesis titled 'Understanding the neural baroreflex: Pulsatility, baroreflex sensitivity and system identification - experimentation and analysis' and the work presented in it are my own. I confirm that:

- This work was done wholly or mainly while in candidature for a research degree at this University.
- Where any part of this thesis has previously been submitted for a degree or any other qualification at this University or any other institution, this has been clearly stated.
- Where I have consulted the published work of others, this is always clearly attributed.
- Where I have quoted from the work of others, the source is always given. With the exception of such quotations, this thesis is entirely my own work.
- I have acknowledged all main sources of help.
- Where the thesis is based on work done by myself jointly with others, I have made clear exactly what was done by others and what I have contributed myself.

Date: _____

Signature: _____

Acknowledgements

Personal

First and foremost, I am deeply grateful to my supervisor, Professor John Ringwood, for his guidance and assistance throughout my PhD journey. From as early as my undergraduate degree, John has been a pillar of knowledge and mentorship, first introducing me to the world of blood pressure regulation. Not only has John's guidance been in regard to my research project, but also in the refining of both my presentation and writing skills.

I am extremely grateful to the Mater University Hospital for facilitating the clinical trial documented in this thesis. Namely, Professor Niall Mahon for his pivotal role in designing the study and obtaining ethical approval. Mary Ryan for coordinating the patients. Andrew Kennedy for ongoing access to measurement equipment to carry out training and practice recordings. I am extremely thankful for both the patients and medical staff that volunteered to take part in the trial.

In the same vein, I would like to thank my collaborators in the Department of Physiology and the Department of Biomedical Engineering at Auckland University. In particular, I would like to thank Professor Simon Malpas, Dr. Rohit Ramchandra, Dr. Sarah-Jane Guild and Dr. Fiona McBryde, for making my stay in New Zealand as enjoyable as possible through rain, shine and even a cyclone. Their generosity in sharing invaluable experimental data, coupled with their willingness to answer any and all of my physiology questions, has been instrumental in shaping my PhD project.

Additionally, I would like to thank the staff in the Department of Electronic Engineering. Ann Dempsey has provided tremendous moral support throughout my time at Maynooth University. John Maloco and Denise Buckley are the sole reason my PC runs. Carrie Anne Barry has provided assistance throughout my PhD journey, and her advice during the writing of this thesis was indispensable. Violeta McLoone for her guidance throughout various projects in this thesis.

My warmest thanks to both present and past members of COER. Although not officially a COER PhD student, I have spent many lunches (and evenings) having amazing

conversations and countless laughs with you all. With a special thanks to both Ahsan, Marco, Edo, Yerai and Meabh.

I reserve a special thanks to my friends and family (both human and animal) for their unwavering emotional support and understanding throughout this process. My mam, dad and sister have fostered my love of STEM from a young age, and continually supported me through the pursuit of my PhD. Celine, Shauna, Orla, and Claire, my closest friends, have consistently offered unwavering support during the most challenging moments of my PhD candidacy. I want to thank my boyfriend, Dan, for his constant encouragement, and his unwavering belief in me, even when I doubted my own capabilities.

Finally, I am lucky to have many amazing people in my life, and attempting to name everyone would inevitably lead to my thesis doubling in size.

Institutional

Gratitude is expressed to Maynooth University for supporting this work through the Women in STEM Hume (WISH) scholarship.

List of Figures

1.1 A model representing the neural baroreflex loop, containing both peripheral resistance and cardiac branches. BP_{set} refers to the resting BP value, varies between species and is dependant on the metabolism. CNS refers to the central nervous system. BP_{out} refers to the current blood pressure value. 3

2.1 Pressure natriuresis curve. Taken from [60] 13
2.2 A computational model representing the neural baroreflex loop, containing the dynamical components for the CNS (G_{CNS}), sympathetic cardiac (G_{pc}) branch, sympathetic cardiac (G_{sc}) branch and the sympathetic resistance (G_{sr}) branch, along with the baroreflex curves ($f(x)$), time delays associated with nerve conductivity ($e^{-s\tau}$)), physiological constants (stroke volume (V_h) and baseline renal sympathetic nerve activity (r^*))) 15
2.3 Generic $tan^{-1}(\ )$ function related to (2.2), used to parameterise steady state response of baroreflex to deviations in BP from set point. . . . 16
2.4 Illustration depicting the implementation of barostim therapy, taken from [116]. 20
2.5 Example of valid sequence selection. The graph highlights three instances where three, or more, matching increases/decreases in both the input ($u(t)$) and the output ($y(t)$) are observed. 29

3.1 An illustration of experimental set up, showing the location of the stimulation electrode and BP measurement catheter. Adapted from [54]. 33
3.2 Zero meaned response of mean arterial pressure (MAP) to a pseudo random binary sequence (PRBS) via the carotid sinus baroreceptor. . 35
3.3 Response of MAP to CS baroreceptor stimulation. Stimulation signals of various keying frequency and voltage amplitude were applied to one of the CS baroreceptors for various lengths of time to determine which signals elicit a strong, clear change in blood pressure. 36
3.4 Block diagram representing the neural baroreflex. Note that $d(t)$ represents uncontrolled/unmeasured effectors that influence MAP. $G(p)$ includes both the neural and peripheral baroreflex arcs, excluding the baroreceptors. The time-domain differential operator is denoted by p while $G(p)$ and $H(p)$ are, in general, rational functions of p. 38

3.5 Spectra of the measured MAP signal (—), and of the PRBS sequences with switching periods of 5s (—) and 10s (—). 39
3.6 Frequency response of the neural baroreflex estimated from (3.1) (*). With subplot a) the magnitude response, b) the phase response and c) the coherence function 40
3.7 Frequency response of the neural baroreflex estimated from (3.1) (*), the frequency response of G_{MF} in (3.3), (- - -) and the poles (vertical dashed line) and zero (vertical dotted lines) of G_{MF}. 42
3.8 Persistence of excitation in the measured PRBS signal 44
3.9 Block diagram, showing the evaluation of the model residual $e(k, \theta)$. Note that G_0 and H_0 are the true system and noise models, respectively. 46
3.10 White noise test: (—) the autocorrelation function (ACF) of $\epsilon(t)$ for G_{BJ}, (—) the autocorrelation function (ACF) of $\epsilon(t)$ for $2(G_{BJ})$, (—) the maximum correlation for a white noise signal of ϵ's length . 47
3.11 Frequency domain validation of G_{MF} annd G_{BJ} against the measured signals. Measured frequency response (*), G_{MF} (·····), G_{BJ} (-·-·),$2(G_{BJ})$ (-·-·) 48
3.12 B) Time domain validation of G_{MF} annd G_{BJ} against the measured signals. PRBS stimulation signal (—), MAP (—), G_{MF} (·····), G_{BJ} (- - -),$2(G_{BJ})$ (-·-·) 49

4.1 Numerical experiment set up. The input signal $u(t)$ is formed by passing a sequence of random numbers through a low pass filter. The system is described by a simplain gain, in this case $k = 2$. The output $y(t)$ is formed by the output of the filter and additive white noise $e(t)$. Sequence selection is determined by the valid sequence criteria (outlined in Table 4.2). Using the sequences, the system's gain is estimated using a gain estimation method (outlined in section 4.3.3) 58
4.2 Parametrisation of the relationship between average sequence length and cut-off frequency 59
4.3 Examining the effect of Ω_C and SNR, on the maximum sequence length achieved in $u(t)$ and $y(t)$. — denotes the input signal $u(t)$ with * and * marking alternate valid sequences, — denoted the output of the system before the noise signal is added ($2^*u(t)$), — denoted the noise signal $e(t)$ and — denotes the output signal $y(t)$ with * and * marking alternate valid sequences 60
4.4 The variance(σ_y^2) for various Ω_c and SNR. 62

4.5 Three estimation methods applied to the numerical example: (a) GEM 1: a linear regression fit to the entire data sets, (b) GEM 2: a linear regression fit to selected (sequence) data points, and (c) GEM 3: a linear regression fit to each individual sequence. m represents the overall gain estimate from each method, n_p represents the number of data points considered in (a) and (b), while n_{seq} represents the number of sequences considered in (c). For this illustration, a specific cut-off frequency ($\Omega_c = 0.1$), SNR ($= 0dB$), and a reduced number of data points in $u(t)$ and $y(t)$, are chosen to clearly highlight the differences between the three methods. $\hat{k}$ represents the estimated gain for each GEM method, n_p represents the number of data points used in the analysis for GEM 1 and GEM 2, with n_s representing the number of sequences used in GEM 3. 64

5.1 Steady state analysis of the cardiac section of the neural baroreflex for a range of MAP values. MAP_{set}, MAP set point; $f_{pc,sc}()$ activation characteristics for pc and sc, respectively; $G_{pc,sc}(0)$ dynamics for pc and sr respectively; $g(U_P, U_s)$, the cardiac function determining HR. . 76

5.2 HR for a range of MAP values when all baroreflex dynamics are considered to be in steady state 77

5.3 Homeostatic analysis of the neural baroreflex. Δ_{BP}, MAP error; $f_{pc,sc,sr}$ activation characterictics for pc, sc and sr, respectively; $G_{pc,sc,sr}$ dynamics for pc,sc and sr, respectively; f_h, heart rate; V_h, stroke volume; q_b, blood flow; r^*, base resistance; R_p, peripheral resistance. 78

5.4 Model output for the homeostatic analysis of the neural baroreflex . . 78

5.5 2 Element Windkessel Model 80

5.6 3 Element Windkessel Model 80

5.7 4 Element Windkessel Model 81

5.8 The inclusion of a compliance model in the relationship between CO, PR and BP. 82

5.9 The neural baroreflex, extended to include compliance, $c(q_b, R_P)$ and BP pulsatility, P, represented as a pressure signal 82

5.10 Pulsatile BP signal, P 82

5.11 The neural baroreflex simplified for analytical purposes 83

5.12 Compliance approximation for the analytical solution. q_b, blood flow; R_p, peripheral resistance; $\overline{R_p}$, mean peripheral resistance; C, arterial compliance. 84

5.13 Equivalent non-linearity concept, articulating the inclusion of a high frequency dither signal, $d(t)$, into a modified non-linear system. . . . 85

5.14 Piecewise linear approximation of one BP cycle. 86

5.15 Altered parasympathetic cardiac activation function, β_{pc} , with the inclusion of pulsatility 87
5.16 Altered sympathetic cardiac activation function, β_{sc}, with the inclusion of pulsatility 88
5.17 Altered sympathetic resistance activation function, β_{sr}, with the inclusion of pulsatility 88
5.18 Showing the break point in the baroreflex loop and the injection of a sinusoid to determine conditions for sustained LF oscillation 90
5.19 Performance surface for $J = \sum_{i=1}^{3} \gamma_i r_i^2$, showing optimal solution for $(A',\, \omega')$ 95
5.20 Investigating the threshold of K_c which gives rise to LF oscillations . 95
5.21 The frequency spectra of the BP signal under conditions where LF oscillations, demonstrating the harmonics present in the LF oscillation. 96
5.22 LF oscillations in BP for the normal (pulsatile) case, for nominal and increased K_c values. The LF oscillations is measured at a period of $3.257s$, corresponding to a frequency of $0.307Hz$. 96
5.23 Simulation results for the pulsatile (Cases 1 and 3) and non-pulsatile cases (Case 2), where pulsatility is represented both by EQNL values or the inclusion of a physical pulsatility signal P. Note that $K_c = K_c^{nom}$. The three cases illustrated are documented in Table 5.5. 98
5.24 Oscillations formed from all branches for K_C' 101
5.25 Oscillations formed from all branches for $2K_C'$ 101
5.26 Oscillations formed from all branches for $3K_C'$ 102
5.27 Oscillations formed from all branches for $4K_C'$ 102
5.28 Oscillations formed from all branches for $5K_C'$ 103

6.1 Normal ECG. Taken from [6] 107
6.2 Representation of normal ECG (a) and CHF ECG signal (b). Taken from [71] 108
6.3 Arterial blood pressure waveforms. Taken from [20] 109
6.4 Shows the position of the CNAP modules finger cuff. Taken from [114] 113
6.5 Example of an irregularly sampled, sparse, MAP signal from a VAD patient 116
6.6 Frequency spectrum for the complete MAP dataset 118
6.7 Eurobavar Subject B003 - investigating the effect of interpolation on the FFT in the case of sparse data with 50% of the original complete dataset 120
6.8 Eurobavar Subject B003 - investigating the effect of interpolation on the FFT in the case of sparse data with 30% of the original complete dataset 121

6.9 Eurobavar Subject B003 - investigating the effect of interpolation on the FFT in the case of sparse data with 10% of the original complete dataset . . . 122
6.10 Control subjects 1 through 3 . . . 123
6.11 Control subjects 4 through 6 . . . 124
6.12 Control subjects 1 through 3 . . . 125
6.13 Control subjects 4 through 6 . . . 126
6.14 Patient 2 - Recording 1 . . . 127
6.15 Control 4 - Recording 1 . . . 128

A.1 Study Datasheet . . . 148

B.1 Control 1 - Recording 1 . . . 150
B.2 Control 1 - Recording2 . . . 151
B.3 Control 2 - Recording 1 . . . 152
B.4 Control 2 - Recording 2 . . . 153
B.5 Control 3 - Recording 1 . . . 154
B.6 Control 3 - Recording 2 . . . 155
B.7 Control 4 - Recording 1 . . . 156
B.8 Control 4 - Recording 2 . . . 157
B.9 Control 5 - Recording 1 . . . 158
B.10 Control 5 - Recording 2 . . . 159
B.11 Control 6 - Recording 1 . . . 160
B.12 Control 6 - Recording 2 . . . 161
B.13 Control 7 - Recording 1 . . . 162
B.14 Control 8 - Recording 1 . . . 163
B.15 Control 8 - Recording 2 . . . 164
B.16 Control 9 - Recording 1 . . . 165
B.17 Control 9 - Recording 2 . . . 166
B.18 Patient 01 - Recording 1 . . . 167
B.19 Patient 01 - Recording 2 . . . 168
B.20 Patient 01 - Recording 3 . . . 169
B.21 Patient 01 - Recording 4 . . . 170
B.22 Patient 03 - Recording 1 . . . 171
B.23 Patient 04 - Recording 1 . . . 172
B.24 Patient 04 - Recording 2 . . . 173
B.25 Patient 07 - Recording 1 . . . 174
B.26 Patient 07 - Recording 2 . . . 175

C.1 Eurobavar Subject A004 - investigating the effect of interpolation on the FFT in the case of sparse data with 50% of the original complete dataset . . . 178

C.2 Eurobavar Subject A004 - investigating the effect of interpolation on the FFT in the case of sparse data with 30% of the original complete dataset . . . 179
C.3 Eurobavar Subject A004 - investigating the effect of interpolation on the FFT in the case of sparse data with 10% of the original complete dataset . . . 180
C.4 Eurobavar Subject A005 - investigating the effect of interpolation on the FFT in the case of sparse data with 50% of the original complete dataset . . . 181
C.5 Eurobavar Subject A005 - investigating the effect of interpolation on the FFT in the case of sparse data with 30% of the original complete dataset . . . 182
C.6 Eurobavar Subject A005 - investigating the effect of interpolation on the FFT in the case of sparse data with 10% of the original complete dataset . . . 183
C.7 Eurobavar Subject B003 - investigating the effect of interpolation on the FFT in the case of sparse data with 50% of the original complete dataset . . . 184
C.8 Eurobavar Subject B003 - investigating the effect of interpolation on the FFT in the case of sparse data with 30% of the original complete dataset . . . 185
C.9 Eurobavar Subject B003 - investigating the effect of interpolation on the FFT in the case of sparse data with 10% of the original complete dataset . . . 186
C.10 Eurobavar Subject B004 - investigating the effect of interpolation on the FFT in the case of sparse data with 50% of the original complete dataset . . . 187
C.11 Eurobavar Subject B004 - investigating the effect of interpolation on the FFT in the case of sparse data with 30% of the original complete dataset . . . 188
C.12 Eurobavar Subject B004 - investigating the effect of interpolation on the FFT in the case of sparse data with 10% of the original complete dataset . . . 189

List of Tables

2.1 Time Delays for Baroreflex Model shown in Figure 2.2 [148] 15

2.2 Parameters for nonlinear static baroreflex characteristics arctan functions [148] 17

2.3 Baroreflex sensitivity estimation methods using non invasive blood pressure signals and their characteristics. BPV refers to BP variations and RRV refers to R-R interval variations 28

4.1 The average sequence length for various combinations of Ω_c and SNR. 61

4.2 Sequence selection criteria used for the numerical example 61

4.3 Valid sequence criteria used with the experimental data. 66

4.4 Gain estimation using three methods, (i) GEM 1: linear regression applied to entire data set, (ii) GEM 2: linear regression applied to data points selected through the sequence method and (iii) GEM 3: average slope of the regression coefficient of each sequence. The criteria column corresponds to the valid sequence criteria outlined in Table 4.2, Ω_c represents the normalised cut-off frequency of the LPF and SNR represents the SNR of the $e(t)$.It should be noted that the true gain of the system is 2. 68

4.5 BRS estimates from 6 sequence methods applied to the 21 participants of the EuroBaVar study[99]. (1a)Sequence method: 3, or more, consecutive paralleled increases/decreases in both BP and RR, a minimum r of 0.7, a minimum BP threshold of 1mmHg and a minimum R-R interval threshold of 4ms, (1b)Sequence method: 3, or more, consecutive paralleled increases/decreases in both BP and R-R and a minimum r of 0.7, (1c)Sequence method: 4, or more, consecutive paralleled increases/decreases in both BP and RR, a minimum BP threshold of 1mmHg and a minimum R-R threshold of 5ms, (2a) LF estimation from McLoone's method, (2b) HF estimation from McLoone's method, and (2c) average of the LF and HF estimations from McLoone's method. The green highlighted rows indicate the two patients with impaired baroreflexes, with the blue highlighted rows indicate patients with underlying conditions that may have a lowered BRS estiamtion than the healthy volunteers. The yellow highlighted cells indicate the cases where sequence method estimates were not higher than SI based estimates. NaN indicates an inability to obtain a BRS estimate. 69

5.1 Parameters for the steady state analysis of the cardiac section of the neural baroreflex. The values for all parameters are derived from experimental studies, each of which are referenced in Section 2.2. . . 77
5.2 Segmentation of Clinical Data 86
5.3 Modification of β values due to the inclusion of pulsatility 88
5.4 Comparative LF oscillation amplitude for analytical and simulation results 97
5.5 Test Conditions 98
5.6 Sensitivity values for propagation through various cardiac and resistance branches, using a dc gain approximation, along with LF oscillations BP amplitudes (OA, in mmHg) for corresponding branches from simulation. 100

6.1 The American College of Cardiology (ACC) and the American Heart Association (AHA) classification for chronic heart failure (CHF). . . . 107
6.2 Datasheet information for subject group. A sample datasheet can be found in Appendix A. A green highlighted row denotes the patients where recordings were successful. Date of implantation represents the date the VAD was inserted. For the diagnosis column, 1= Ischaemic cardiomyopathy and 2= Non-ischaemic cardiomyopathy. PI is the pulsatility index obtained from the LVAD's external display. The subject group had a mix of HeartMate 2 and 3's inserted, the HeartMate column reflects which model the patient has. 114
6.3 Datasheet information for control group. 114
6.4 Which sheep have Mayer waves? 123
6.5 Contingency table corresponding to the results shown in Table 6.4 . . 124
6.6 Which subjects have Mayer waves? 129
6.7 Contingency table corresponding to the results shown in Table 6.6 . . 129

List of abbreviations

ACC . . . . . American College of Cardiology

ACF . . . . . Autocorrelation function

AHA . . . . . American Heart Association

ARX . . . . . AutoRegressive with an eXogenous input

ARMAX . . . . AutoRegressive Moving average with an eXogenous input

BA . . . . . Baroreflex Activation

BJ . . . . . Box-Jenkins

BP . . . . . Blood pressure

BRS . . . . . Baroreflex sensitivity

BPV . . . . . Blood pressure variability

cBA . . . . . Conventional baroreflex activation

CDC . . . . . Centre for disease control and prevention

CHF . . . . . Chronic heart failure

CL . . . . . Closed loop

CNS . . . . . Central nervous system

CO . . . . . Cardiac output

CS . . . . . Carotid Sinus

CSNA . . . . . Cardiac sympathetic nerve activity

CSP . . . . . Carotid sinus pressure

DC . . . . . Direct current

DF . . . . . Describing function

ECG . . . . . Electrocardiogram

EQNL . . . . . Equivalent nonlinearity

FDA . . . . . US Food and Drug Authority

FFT . . . . . Fast Fourier transform

GAFD . . . . . Gaussian average filtering decomposition

GEM . . . . . Gain estimation method

HHT . . . . . Hilbert-Huang transform

HP . . . . . High pass

HR . . . . . Heart rate

HSE . . . . . Health service executive

InterMACS . . Interagency Registry for Mechanically Assisted Circulatory Support

LF . . . . . Low frequency

LFOs . . . . . Low frequency oscillations

LP . . . . . Low pass

LPV . . . . . linear parameter-varying

LTI . . . . . Linear time-invariant

MAP . . . . . Mean arterial pressure

MCS . . . . . Mechanical circulatory support

MF . . . . . Manual fit

NUFFT . . . . Non-uniform fast Fourier transform

OA . . . . . Oscillation amplitude

OR . . . . . Odds ratio

Pa . . . . . Arterial pressure

pc . . . . . Parasympathetic cardiac

PN . . . . . Pressure natriuresis

PR . . . . . Peripheral resistance

PRA . . . . . Right atrial pressure

PRBS . . . . . Pseudo random binary sequence

RBF . . . . . Renal blood flow

RHT . . . . . Resistant hypertension

rpm . . . . . Revolutions per minute

RR . . . . . R-R interval

RSNA . . . . . Renal sympathetic nerve activity

sBA . . . . . Smart baroreflex activation

SBP . . . . . Systolic blood pressure

sc . . . . . Sympathetic cardiac

SHAM . . . . . No intervention

SI . . . . . System identification

sr . . . . . Sympathetic peripheral resistance

SNA . . . . . Sympathetic nerve activity

SNR . . . . . Signal-to-noise ratio

SV . . . . . Stroke volume

TPR . . . . . Total peripheral resistance

TRS . . . . . Trigonometric regressive

VAD . . . . . Ventricular assist device

WHO . . . . . World health organisation

1 Introduction

Contents

1.1 Motivation 2
1.2 Objectives and contributions 4
1.3 List of publications 7
1.4 Thesis layout 8

The baroreflex is the homeostatic mechanism that maintains blood pressure (BP), ensuring adequate perfusion. The baroreflex is a fast negative feedback loop, i.e. a system that feeds some function of the output back in a manner that reduces fluctuations in the output, caused by changes in the input or external disturbances. The baroreflex detects changes in blood pressure(BP; the output) through mechano-sensitive receptors called baroreceptors. The receptors inform the central nervous system (CNS) of fluctuations in BP through frequency modulated signals carried along afferent nerves. The CNS in turn, responds to the changes and attempts to counteract them by altering cardiac output (CO) and peripheral resistance (PR) though signals carried along efferent nerves to the heart and smooth muscle surrounding arteries. The simplified relationship for BP being [59]:

$$BP = CO.PR \tag{1.1}$$

- BP represents mean arterial pressure, measured in $mmHg$.
- CO represents cardiac output, calculated by multiplying heart rate (HR) with stroke volume (SV), measured in ml/s.

- PR is the resistance of the arteries to blood flow, measured as $mmHg\ s/l$.

The subsystems responsible for altering CO and PR, in the regulation of BP, are well articulated through a number of baroreflex models, as shown in Figure 1.1. Other than CO and PR, known as short term regulators of BP, there are a number of other factors that can influence BP [150]. Hormones, such as Cortisol, Epinephrine and Renin-Angiotensin, circulate through blood and can cause vasodilation (the expansion of blood vessels) or vasoconstriction (narrowing of blood vessels) [170]. Paracrines, such as Nitric Oxide, excreted by human cells can cause local vasodilation in the areas into which they are released [122]. Metabolic factors can also cause changes in blood pressure in response to an increase in local metabolic demands, such as changes in oxygenation levels, similar to those observed during exercise [138].

The baroreflex is one of the many systems within the human body that function in tandem to maintain homeostasis; these systems can operate from cell level, to organ level, and at various timescales in between. It should be noted that these systems are not mutually exclusive but are interlinked, as demonstrated in Guyton's integrative physiology model [58], meaning that altering one variable in one system may have a ripple effect in surrounding systems, or on systems that respond to the same hormones.

Control theory has an array of methods that can be applied to not only closed-loop (CL) systems, but to systems with unknown parameters, lending itself well to the examination of physiological systems. Further investigation into the control of BP, namely using control systems methods, would help to progress understanding of the regulation of BP.

1.1 Motivation

Hypertension is the sustained elevation of blood pressure and puts individuals at a higher risk of cardiac events, stroke, renal disease, dementia and a host of other serious illnesses [117]. In 2017, the Centre for Disease Control and Prevention conducted a survey on the adult population of America and concluded that nearly 50% of the population had hypertension (sustained, elevated BP)[147]. In 2021, the World Health Organisation estimates that only 1 in 5 adults with hypertension have their condition under control [127]. Despite the number of anti-hypertensive drugs available, there is still a large percentage of the hypertensive population with resistant hypertension (RHT, involving the concurrent use of > 3 different classes of anti-hypertensive drugs at maximum doses, including a diuretic [18]). The majority of antihypertensive medication

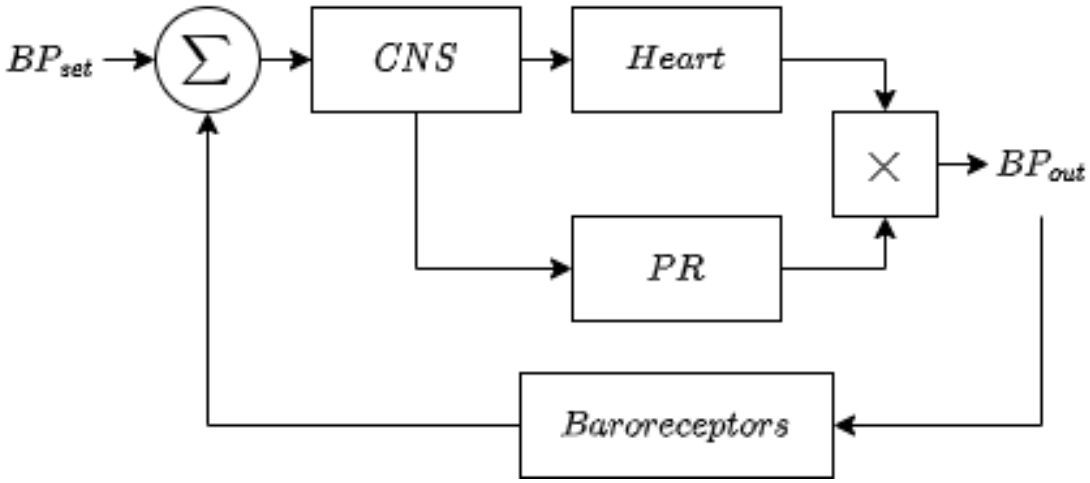

Figure 1.1: A model representing the neural baroreflex loop, containing both peripheral resistance and cardiac branches. BP_{set} refers to the resting BP value, varies between species and is dependant on the metabolism. CNS refers to the central nervous system. BP_{out} refers to the current blood pressure value.

can be categorised in one of four ways: (a) minimising the constriction of arterial walls, by reducing the production or absorption of Angiotensin II (a vasoconstrictor), (b) encouraging the dilation of arterial walls, by blocking calcium from entering the blood vessels, or directly supplementing the production of vasodilators, (c) reducing the responsiveness of the baroreflex to changes in BP caused by stress, through the inhibition of the adrenergic receptor response to adrenaline, and (d) diuretics, which encourage the kidneys to move and excrete additional fluid and salt in urine [84].The large array of antihypertensive medication available target the PR branch of the baroreflex. Antihypertensive medication attempts to correct hypertension by reducing PR in the baroreflex; however the low percentage of patients with controlled hypertension suggests that there are other portions of the baroreflex that may be the cause of hypertension in the majority of cases.

This idea that hypertension is caused by something other than the dysregulation of PR is mirrored in the classification of hypertension patients. Hypertension is classified as: (a) primary (also known as essential [173]), characterised by high BP where the cause is unknown, and (b) secondary, caused by known medical condition, such as renal disease, endocrine disease or vascular disease. 90% of hypertensive patients are categorised as primary, with only 10% classified as secondary [62]. The high percentage of individuals with primary hypertension indicates a gap in knowledge when it comes to the control of BP and, in turn, the causes of hypertension.

Hypertension is not only extremely prominent in the general population but is also associated with the survival rate of myocardial infarction, "with hypertensive patients having almost three times the mortality of normotensive patients" [76]. A better understanding of the baroreflex and its mechanisms may help to increase the variety of antihypertensive treatments developed in the future, addressing the underlying cause of hypertension in a larger percentage of the population.

The studies carried out in this thesis aim to provide additional information about the baroreflex in an attempt to better understand it's functionality. A popular simplified baroreflex model is extended to include cardiac pulsatility and arterial compliance. The model is then used to examine the role of cardiac pulsatility in moderating the neural baroreflex. In addition, a potential protocol is presented that may be utilised to determine the characteristics of the neural baroreflex, which could be used to refine hypertension treatment methods. Moreover, it evaluates the theoretical framework of a popular non invasive baroreflex assessment method.

1.2 Objectives and contributions

The work presented in this thesis is a collection of studies connected by their ability to provide information about the baroreflex or to help evaluate its functionality. The objectives and contributions of each study is summarised as follows:

Objective 1: To develop a protocol to characterise the neural baroreflex in closed loop, with the baroreceptors intact.
Contribution 1: Chapter 3 shows the development of a protocol for the determination of the dynamics of the neural baroreflex in sheep. The protocol includes a measurement procedure, followed by a data post-processing stage that utilises techniques from the control sciences. In particular, the excitation signal used to stimulate the carotid sinus is refined, following an initial test, to provide suitable coverage of the effective bandwidth of the neural baroreflex, while special consideration is given to the fact that the data is obtained in CL, where the animal's neural baroreflex is intact. Both time- and frequency-domain identification techniques are applied to the recordings to determine both parametric time-domain models, and non-parametric frequency response data that accurately represent the neural baroreflex.
The experimental data used in this study was from sheep studies recorded by researchers in the Department of Physiology in Auckland University. The stimulation signal was created and refined by me, based on priori knowledge shared by the researchers in Auckland and a number of publications. The stimulation signal was applied at

the end of a number of baroreflex stimulation experiments being carried out in Auckland University.

Objective 2: Under certain circumstances, including haemorrhage and other states of physiological distress, the gain of the neural baroreflex can increase, causing low frequency (LF) oscillations (sometimes termed Mayer waves) in BP. Though their purpose is unclear, the origins of these LF oscillations has previously been explained via a nonlinear feedback model, focusing on the peripheral resistance as a MAP actuator only [151]. The objective is to present analytical and simulation results explaining the incidence of LF oscillation under varying degrees of pulsatility for the full neural baroreflex, containing both PR and cardiac branches, along with a compliance model characterised as a Windkessel model. In the context of this thesis, pulsatility refers to the continuous contraction and subsequent relaxation of the cardiac muscles, resulting in cyclical blood pressure and flow.

Contribution 2: Chapter 5 presents both analytical and simulation results that explain the LF oscillation phenomenon for the full neural baroreflex, containing both PR and cardiac branches. A popular simplified baroreflex model that was derived using experimental data, representing the baroreflex as a negative feedback loop, mediating both cardiac output and peripheral resistance through the central nervous system, is extended to include cardiac pulsatility and compliance through the use of additional experimental data. The extended model is then used to examine the effect of blood pressure pulsatility, or a lack thereof, on the neural baroreflex and how it contributes to the presence of LF oscillations.

The analysis carried out in Chapter 5 hypothesises that, as pulsatility decreases, the incidence of Mayer waves increases. Chapter 6 examines this hypothesis experimentally.

The experimental data used in the study detailed in Chapter 5 came from rabbit experiments from both published studies and recorded signals, shared by researchers in the Department of Physiology in Auckland University.

The experimental data used in Chapter 6 is a mix of both experimental data from sheep and clinical data in humans. The sheep data was from existing studies shared by the Department of Physiology in Auckland University. The clinical trial (human study) was carried out in collaboration with the Professor Niall Mahon and the cardiology Department in the The Mater Misericordiae University Hospital. I oversaw the application for ethical approval, initiated the collaboration with LiDCo to use one

of the BP measurement devices for the trial, personally contacted the participants and recorded all measurements taken as part of the trial.

Objective 3: The sequence methods are popular non-invasive baroreflex sensitivity (BRS) estimation methods known to introduce significant bias in the BRS estimate, even when great care is taken in sequence selection. The objective of this project is to investigate the validity of the sequence method as a baroreflex sensitivity estimation method from theoretical and numerical stand points.
Contribution 3: Chapter 4 depicts a critical examination of the theoretical foundation behind the use of sequence method for baroreflex sensitivity estimation using both data generated from a known mathematical model and spontaneous baroreflex data. The analysis aims to explain the persistent positive bias seen in BRS estimates obtained using sequence methods[23]. The sequence selection criteria associated with sequence methods have been refined over the years in an attempt to minimise the noise present in the sequences; an analysis of the effect of these refinements on the baroreflex gain estimate is also presented.

The experimental data came from the open access dataset known as the EuroBaVar dataset [99].

1.3 List of publications

Published

- J. V. Ringwood, **H.Bagnall-Hare**, *"Understanding the interplay between baroreflex gain, low frequency oscillations, and pulsatility in the neural baroreflex"*, Biocybernetics and Biomedical Engineering, Elsevier 40(3), 1291–1303, 2020.

Under review

- **Hasana Bagnall-Hare**, Rohit Ramchandra, Sarah-Jane Guild, Fiona McBryde, Julia Shanks and John V. Ringwood *"Protocol for the identification of the neural baroreflex characteristics in sheep"*
- **Hasana Bagnall-Hare**, Violeta I. McLoone, John V. Ringwood *"On the accuracy of sequence methods for baroreflex sensitivity estimation"*
- **Hasana Bagnall-Hare**, Violeta I. McLoone and John V. Ringwood *"Reliable estimation of baroreflex sensitivity using closed-loop identification from spontaneous data"*

1.4 Thesis layout

This thesis details 3 studies, all are linked by their analysis of blood pressure signals and the insights they provide into the baroreflex.

Chapter 2 provides a general outline to blood pressure, the baroreflex and the models that characterise the baroreflex and some background on the control science theories implemented in the projects. Each subsequent chapter details the work carried out in a different project and will have a background subsection, containing the background information relevant to that project.

Chapter 3 details the development of a protocol to excite the neural baroreflex through baroreceptor stimulation, with the baroreceptors intact, recording the subsequent changes in BP. Followed by the application of system identification methods to identify both time- and frequency- domain models that characterise the neural baroreflex.

Chapter 4 shows the investigation of sequencing data on gain estimation from a mathematical perspective, followed by the development of a controlled numerical example where sequence methods can be further tested on a system with known gain. Finally, it examines the prevalence of positive bias in baroreflex sensitivity gain estimates obtained using sequence method in comparison to methods derived from the control sciences.

Chapter 5 extends the work of previous publications to examine the conditions under which LF oscillations take place using a model that considers PR branch, cardiac branch, compliance, and the presence, or absence, of pulsatility. The work contains an analytical solution for the presence of LF oscillations, which is shown to have a solution consistent with results from computer simulation of the model, and also those determined experimentally. Furthermore, an analysis is included which examines the relative importance of individual cardiac (sympathetic and parasympathetic) branches and peripheral resistance branches in mediating LF oscillations. This is performed both through an analytical sensitivity analysis and simulation.

The analytical study carried out in Chapter 5 proposes the hypothesis that there is an increase in the incidence of Mayer waves as pulsatility decreases. Chapter 6 articulates the experimental set up and results for experiments testing the hypothesis proposed in Chapter 5. This hypothesis is investigated in both sheep and humans, where blood pressure readings are taken from a group with little, to no pulsatility, heart failure

subjects (sheep, n=6) or ventricular assist device (VAD) outpatients (humans, n = 10). The results are compared to a control group of sheep (n=6) and age matched humans(n=10).

Finally, Chapter 7 provides concluding remarks of this thesis and a discussion of possible future work.

2

Blood pressure and the baroreflex: A comprehensive background

Contents

2.1 Blood pressure 12
2.2 The neural baroreflex model 14
2.2.1 Baroreceptors 14
2.2.2 Central nervous system 15
2.2.3 Cardiac branches 17
2.2.4 Peripheral resistance branches 17
2.3 Low frequency oscillations 18
2.4 Hypertension and antihypertensive treatments 19
2.4.1 Baroreceptor activation therapy 19
2.4.2 Characteristics of the neural baroreflex 21
2.5 Baroreflex sensitivity estimation methods 23
2.5.1 Oxford method 24
2.5.2 Existing non-invasive BRS estimation methods 24
2.5.3 Sequence methods 27

The manifestation of hypertension, as well as other blood pressure-related conditions, is caused by the failure of one or more blood pressure control mechanisms. To identify the source of dysregulation, it is necessary to first understand the 'normal' case. Only then can impairments be properly corrected.

Section 2.1 introduces blood pressure and its effectors. Section 2.2 details the neural

baroreflex model and the components used to articulate its dynamical behaviour. Section 2.3 introduces the concept of low frequency oscillations, a feature observed in blood pressure signals. Section 2.4 covers the state of the art on antihypertensive treatments, namely the development of device based therapies. Section 2.5 provides an overview of BRS estimation methods.

2.1 Blood pressure

The human body circulates approximately five litres of blood continually. This is done through an intricate vascular system, that maintains adequate pressure to ensure constant blood flow. Sufficient BP guarantees that blood circulates throughout the entire body, carrying oxygenated and nutrient rich blood to tissue and organs, while transporting waste products to the liver and kidneys to be excreted from the body.

A number of mechanisms rely heavily on the nutrients and oxygen carried in blood, with hypotension (continuous, low BP) compromising cellular and organ function [19, 145]. In addition, hypertension (sustained, high BP) can cause end organ damage. If left untreated, hypertension can lead to an array of adverse events such as heart attacks, stroke and kidney failure [37].

The short term regulation of blood pressure is driven by changes in CO and PR as articulated in Section 1, influenced by parasympathetic nerve activity, sympathetic nerve activity, stroke volume, and arterial elasticity. These mechanisms respond to short term metabolic needs such as stress, postural changes and exercise. Other negative-feedback mechanisms influencing BP include the renin-angiotensin-aldosterone system and the renal pressure natriuresis, albeit with a slower reaction time than the arterial baroreceptor reflexes [145].

The Renin Angiotensin system is initiated by the kidneys when Renin is released into the blood stream. Renin causes the protein produced by the liver, Angiotensin, to seperate into individual components, one of which is Angiotensin I. Angiotensin I does not have any effect on BP, but when converted by Angiotensin-converting enzymes into Angiotensin II, becomes a vasoconstrictor. The localised vasoconstriction, caused by Angiotensin II, causes an increase in BP. This mechanism is modelled in [150]. An increase in Angiotensin II can also initiate a response from the endocrine system.

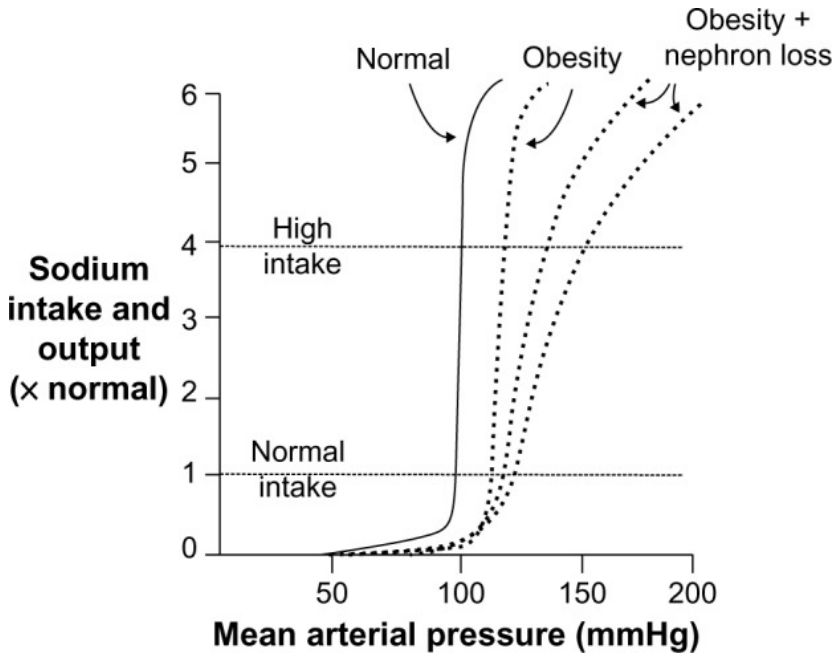

Figure 2.1: Pressure natriuresis curve. Taken from [60]

The endocrine system is a series of glands that excrete hormones, one of which is the adrenal gland, responsible for the production of Aldosterone, Cortisol and other Adrenaline-like hormones [65]. An excess of aldosterone can cause the retention of salt and water, and the loss of potassium, causing an increase in BP.

The pressure natriuresis (PN) curve is the relationship between sodium intake or output and blood pressure (BP). A change in the quantity of sodium consumed, or the rate sodium is excreted, can cause BP to increase or decrease. An increase in excretion of sodium causes BP to reduce, and the inverse occurs for a decrease [70]. Conditions such as hypertension or obesity can cause the PN curve to shift to the right (shown in Figure 2.1), causing a change in the slope of the curve, impairing the kidney's ability to respond to changes in BP. An impaired kidney, typically the cause of secondary hypertension, will maintain a balance between the intake/excretion of sodium but does so to the detriment of BP [60].

Another thing worth noting is that all of the above effectors of BP vary in their contributions to the changes in BP depending on age, sex, and situation of the individual.

The studies carried out as part of this thesis focus predominately on the baroreflex with the remaining BP effectors being considered as unmeasurable disturbances, or assumed to not be active over the relatively short time scales associate with the neural baroreflex.

2.2 The neural baroreflex model

The neural baroreflex is a short term regulator of BP, ensuring adequate organ perfusion. The baroreflex monitors changes in BP and attempts to counteract them by altering PR and/or CO. In essence, the neural baroreflex activates smooth muscle in the peripheral resistance, and also modulates heart rate, in response to disturbances in BP, or metabolic needs. BP is measured in the aortic arch and the carotid sinus, with the CNS using these measurements to provide an appropriate control signal to the BP 'actuators' i.e. the PR and heart, via sympathetic and parasympathetic pathways.

Several mathematical models of the neural baroreflex, combining both the resistance and cardiac branches have been proposed. While all are developed using a combination of experimental data and physiological knowledge, they employ different analytical tools, and pursue different objectives. For example, [69], a mathematical model developed using human data, employs cross-recurrence analysis to examine the coupling between heart-rate and vascular sympathetic tone, while [77, 162], both human mathematical models, examine heart-rate variability for chaotic behaviour. The computational model in [89] is used to examine the effect of disease on cardiovascular autonomic regulation, and [14] examines the haemodynamic response to blood volume perturbations.

The mathematical model proposed in this thesis extends the work reported in a number of previous publications notably [151], which examines the conditions under which LF oscillations take place, but only consider the PR baroreflex. [148] considers both PR and cardiac branches, but ignores both BP pulsatility and arterial compliance. [152] articulates the effect of pulsatility on the baroreflex gain, but uses a simplified model of the baroreflex, containing only the PR loop, and also ignores arterial compliance. Finally, [8] includes both cardiac and PR branches, along with pulsatility, but omits arterial compliance. The results in [8] are exclusively simulation based. The remainder of this section details the neural baroreflex model (with the parameters of a rabbit) that will be extended in Chapter 5, illustrated in Figure 2.2.

2.2.1 Baroreceptors

The baroreflex monitors changes in BP via baroreceptors, mechanosensitive receptors that detect changes in the arterial wall strain, and are located in both the aortic arch and the carotid sinus (CS) [5]. When baroreceptors detect a change in arterial wall tension they inform the CNS via frequency modulated signals that travel along the nerves. The increase in the nerve firing frequency, initiated by an increase in arterial

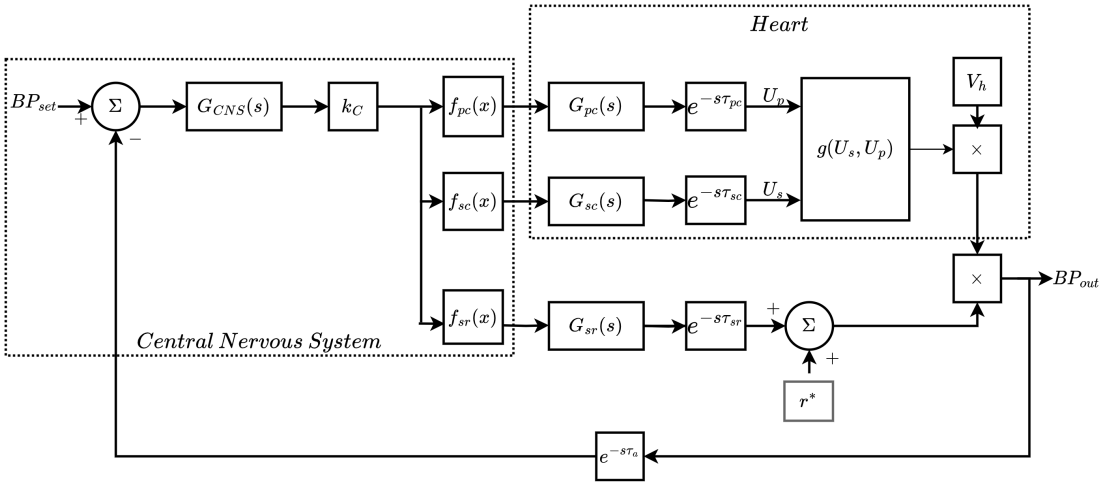

Figure 2.2: A computational model representing the neural baroreflex loop, containing the dynamical components for the CNS (G_{CNS}), sympathetic cardiac (G_{pc}) branch, sympathetic cardiac (G_{sc}) branch and the sympathetic resistance (G_{sr}) branch, along with the baroreflex curves ($f(x)$), time delays associated with nerve conductivity ($e^{-s\tau}$)), physiological constants (stroke volume (V_h) and baseline renal sympathetic nerve activity (r^*)))

wall strain, indicates an increase in BP (and vice versa for a decrease in BP). The CNS, in turn, responds to a change in BP by altering cardiac output and peripheral resistance in order to maintain homeostasis.

In the neural baroreflex model, the baroreceptors are simply modelled as a nerve conduction delay of τ_a s, which also includes the afferent nerve delay. Some researchers [82] have suggested that the baroreceptors may have high-pass frequency characteristics, although it is not entirely clear whether such characteristics are due to the baroreceptors themselves, or the CNS, since typical experiments measure the response in sympathetic nerve activity (SNA) to baroreceptor activation.

Table 2.1: Time Delays for Baroreflex Model shown in Figure 2.2 [148]

τ_{pc}	τ_{sc}	τ_{sr}	τ_a
0.3	0.8	0.85	0.5

2.2.2 Central nervous system

The CNS, composed of the brain and the spinal cord, is responsible for taking in information from a variety of sensors around the body, processing the information

recorded by the sensors, and sending motor signals as appropriate [16]. In the case of the baroreflex, the CNS uses measurements from the baroreceptors and provides an appropriate control signal to the BP 'actuators' i.e. PR and heart, via sympathetic and parasympathetic pathways. In this study, a notional mean arterial pressure (MAP) set-point is present in the CNS [129], which may be varied, depending on metabolic needs, etc. The difference between the set-point and the true BP value is the driver of the system response. The CNS dynamics are articulated by the transfer function [68]:

$$G_{CNS(s)} = e^{-s\tau_b}\frac{1.33s+1}{s+1} \tag{2.1}$$

The CNS also contains the activation characteristics, f_{pc}, f_{sc}, and f_{sr} which articulate the nonlinear steady-state response of parasympathetic cardiac (pc), sympathetic cardiac (sc) and sympathetic peripheral resistance (sr) nerve signals, respectively, to deviations in MAP away from the set point, BP_{set}. These non-linearities are more commonly referred to as baroreflex curves and articulate the relationship between BP and nerve activity [110]. f_{pc}, f_{sc}, and f_{sr} are all sigmoidal in form (see Fig.2.3), each parametrised with a $tan^{-1}(\ )$ function [31]:

$$f(x) = h\ tan^{-1}(\beta(x-x^*)) + y^*\ , \tag{2.2}$$

with parameters as shown in Table 2.2. Note that, in Table 2.2, no x^* value is given. Given that we utilise a set point, the base (homeostatic) condition will be that the BP error will be zero (i.e. $x^* = 0$), with the y^* values therefore setting the baseline tone of sympathetic and parasympathetic activity.

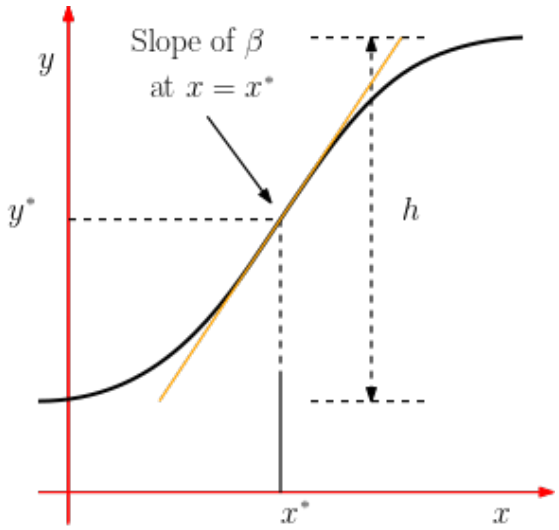

Figure 2.3: Generic $tan^{-1}(\ )$ function related to (2.2), used to parameterise steady state response of baroreflex to deviations in BP from set point.

Table 2.2: Parameters for nonlinear static baroreflex characteristics arctan functions [148]

Baroreflex Branch	β	h	y^*
Parasympathetic Cardiac (pc)	-0.1342	42.5	65.5
Sympathetic Cardiac (sc)	0.035	30	42.5
Sympathetic Resistance (sr)	0.04	29	185

2.2.3 Cardiac branches

The cardiac branch of the baroreflex alters cardiac output through changes in HR and SV. The inputs to the heart block are the sympathetic and parasympathetic cardiac signals from the CNS, with the output being blood flow rate. Separate dynamics operate on the sympathetic (G_{sc}) and parasympathetic (G_{pc}) channels [148], via:

$$G_{pc}(s) = k_{pc}\frac{1}{1.22s+1}\ , \tag{2.3}$$

$$G_{sc}(s) = k_{sc}\frac{1}{1.29s^2+1.29s+1}\ , \tag{2.4}$$

where $k_{pc} = 0.148$ and $k_{sc} = 0.181$, while there are also nerve conduction delays of τ_{sc} and τ_{pc} in the sympathetic and parasympathetic channels, respectively (see Table 2.1). The heart rate is determined as a function of both sympathetic and parasympathetic signals as:

$$g(U_p, U_s) = f_h = k_p U_p + k_s U_s + f_o \tag{2.5}$$

where $k_s = 0.88$, $k_p = -1.2$ [148], and $f_o = 220$ [10] denotes the base heart rate, with value $f_o = 215\ beats/min$ for a rabbit. Finally, blood flow, q_b, is determined from

$$q_b = f_h V_h \tag{2.6}$$

where V_h is the heart stroke volume, given as 0.51 cc per kg of body weight, m_r [1], where $m_r = 2.9kg$ [56].

2.2.4 Peripheral resistance branches

PR is the resistance in the circulatory system to the flow of blood. The modelled PR subsystem focuses exclusively on the neural control of PR, altering PR by contracting or relaxing the smooth muscle surrounding the arteries, above a base resistance of r^* [148]. Hormonal, metabolic, myogenic and paracrinal effects are ignored, given the short timescale of PR effectors considered in this study, and a single branch is used to represent the aggregated effects of innervated resistance in the kidney, muscles, gut,

and skin. A sympathetic nerve conduction delay of τ_{sr} (see Table 2.1) is included in the PR branch, as well as a dynamic block, $G_{sr}(s)$ [148] relating the response in PR to SNA:

$$G_{sr}(s) = k_r \frac{11s^2 + 6.64s + 1}{4.27s^4 + 21s^3 + 36s^2 + 22s + 1} \tag{2.7}$$

where $k_r = 0.0005$.

2.3 Low frequency oscillations

Low-frequency oscillations (LFOs), often called Mayer waves [73] occur at frequencies below respiration and heart rate, typically at around 0.1 Hz in humans and 0.3 HZ in rabbits. The LF oscillation frequency is dependent on species size with the length of the nerve conduction paths (i.e. conduction delay), being responsible for the frequency variation. There is a lot of debate around the origin of LFOs [73, 74], the two theories being: (a) The pacemaker theory, the idea that the oscillations are thought to be pace-maker like activity originating in an autonomous oscillator located within the CNS [26], or (b) the baroreflex theory, the idea that a limit cycle exists around the baroreflex as a sign of dysregulation [88].

There are a number of physiological conditions and interventions which have been shown to affect the presence/absence of LF BP oscillations. These include hypoxia [31], haemorrhage [111], and modulation of nitric oxide synthesis [21]. Invariably, these interventions involve modulation of the overall baroreflex gain, which is consistent with (b) the baroreflex theory for LF oscillations in [151]. Given the array of physiological conditions that affect the manifestation of Mayer waves, the diagnostic potential of Mayer waves is called into question. There is some discussion surrounding whether, or not, the strength of the Mayer waves could be used to diagnose certain conditions. However, the limited knowledge surrounding origin of Mayer waves, means that additional research needs to be carried out to determine their origin, and in turn potentially provide information surrounding their prognostic capabilities.

One phenomenon which has the potential to alter baroreflex gain, and consequently affect the presence/absence of LF oscillations, but has received relatively little exposure in the literature, is BP pulsatility. BP pulsatility is diminished in patients with heart failure; as the heart deteriorates the ejection fraction decreases, reducing pulsatility. BP pulsatility is also reduced in cases where cardiac flow assist devices, such as VADs or turbine-based artificial hearts, are used. Some evidence exists [26] showing that a reduction in pulsatility is accompanied by an increase in the incidence of LF

oscillations. [194] compared the presence of Mayer waves in dogs with total heart failure, before and after the insertion of pulsatile VADs, noting a decrease in the presence of Mayer waves after insertion. [193] and [196] noted a similar occurrence in goats. [195] noted an increase in Mayer waves during counterpulsation ventricular assist mode, in comparison to copulsation ventricular assist mode. The specific focus of the current research is to establish the link between pulsatility, baroreflex gain and the presence/absence of LF oscillations as a surrogate measure of baroreflex gain.

2.4 Hypertension and antihypertensive treatments

Not only does hypertension effect a large percentage of the global population, it also increases the risk of premature death [121]. Persistent, prolonged periods of hypertension increase the risk of serious and potentially life-threatening conditions, such as heart disease, stroke and kidney damage [107]. While the ideal solution is to prevent the development of hypertension through lifestyle choices, the prevalence of hypertension in the general population demonstrates a need for effective antihypertensive medication. While the efficacy of antihypertensive medication has improved significantly in recent years, there is still a need for alternative therapies. Device-based approaches, including renal denervation [27] and baroreceptor activation therapies [64], are currently being developed but are in the initial clinical trial stage and require further testing to validate their validity [136].

2.4.1 Baroreceptor activation therapy

The majority of patients with RHT also have high levels of sympathetic activity, suggesting a need for sympathetic activity based therapies [39] [104]. Sympathetic based therapies involve placing electrodes on one, or both, branches of the CS and applying a stimulation signal to activate the baroreceptors [54], illustrated in Figure 2.4. Research investigating the viability of regulating BP via baroreceptor stimulation dates back to the 1960s; however, the therapy was not refined enough, and the treatment was considered too undeveloped to be used consistently for sustained results. The unreliability of baroreceptor activation (BA), combined with major advances in anti-hypertensive medication at the time, put a halt to BA research, until the early 2000s, when CVRx Inc., a US start up, introduced the first generation CS stimulator (RHEOS) [104] [54]. RHEOS is capable of providing sustained reductions in BP for 6 years but the invasiveness, short battery life, along with the surgical complications

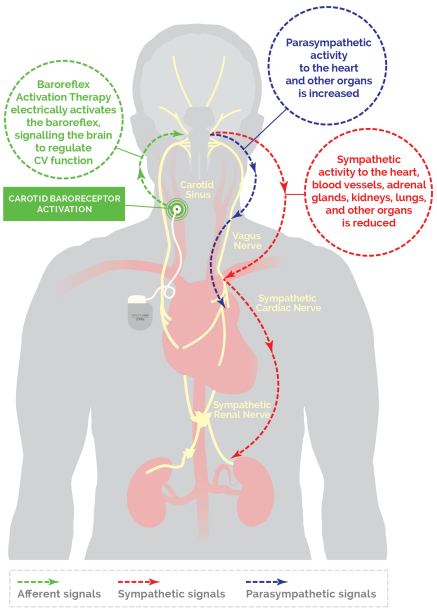

Figure 2.4: Illustration depicting the implementation of barostim therapy, taken from [116].

and nerve injury associated with the device meant that it was not approved by the US Food and Drug Authority (FDA).

A second generation device, the Barostim Neo, a unilateral CS baroreflex amplification device, which is clinically applied in Europe, has a less invasive implantation procedure and an increased battery life [54]. The Barostim Neo has been proven to show sustained reductions in BP for at least 24 months in patients with RHT, along with proven efficacy and safe to use in patients with renal failure, heart failure and reduced ejection fraction, conditions often seen in patients with RHT [54]. While the device shows promising results for the reduction in BP long term, trials using control participants are needed to demonstrate that the treatment is not a placebo, along with further investigations into the long term effects and side-effects associated with the therapy.

While BA appears to be an effective treatment for hypertension, it is well known that prolonged blood pressure increases cause the baroreceptors to 'reset' to the new blood pressure levels in an attempt to minimise blood pressure variability (BPV, a risk factor of cardiovascular events in those with RHT [44]) [181]. In an attempt to prolong the efficacy of BA therapies, an alternative protocol for BA therapy, smart BA, is being researched currently, where the applied stimulation signal adapts to the real time BP signal. [183] demonstrates the effect conventional BA (cBA) and smart BA (sBA), in comparison to no intervention (SHAM), has on both BP and BPV in rats over the course of 2 hours. While both cBA and sBA lowered BP, the subjects with cBA displayed increased episodes of hypotension (compared to SHAM), where sBA

appeared to prevent the episodes of hypotension. sBA simultaneously diminished the BPV, with no notable change observed in subjects with cBA [183]. While there is a case to be made for sBA, further investigation is needed into the optimal BP level and whether the optimal BP level needs to be adjusted throughout the day. An adaptive BP will account for the fluctuations that accompany metabolic needs, such as a drop in BP at night or the increase in BP observed during exercise.

In addition to the idea of smart BA, the use of intermittent stimulation of the baroreceptors compared to constant stimulation is also being tested [157]. [157] demonstrates that intermittent stimulation provides sufficient excitation to lower MAP, while reducing the incidences of excessive decreases in MAP. While barostim therapies are showing promising results, further understanding on the frequency characteristics of the baroreflex and the baroreceptors will help to refine BA protocols.

2.4.2 Characteristics of the neural baroreflex

Previous authors [81] randomly perturbed CS pressure (CSP, using a binary white noise signal) in anaesthetised, vagotomised, and aortic denervated rabbits, while simultaneously measuring renal sympathetic nerve activity (RSNA) and cardiac sympathetic nerve activity (CSNA). The transfer functions representing CSP-CSNA and CSP-RSNA reveal different responses in the cardiac and renal branches of the baroreflex to dynamic baroreflex activation. [56] characterised the dynamic relationship between sympathetic nerve acivity (SNA) and renal blood flow (RBF) in anaesthetised rabbits by applying a pseudo-random binary sequence (PRBS) signal directly to the renal nerves, while [80] investigates the relationship between the left and right CS baroreceptors in rabbits. [80] use white noise to stimulate the receptors, they demonstrate that the summation of the gain values of the neural arc responses to unilateral stimulation, is equal to that of bilateral stimulation.

While providing key information about the baroreflex, or portions of it, the experiments carried out in [56], [80] and [81] were carried out in open loop, i.e. with baroreceptor denervation, eliminating the feedback mechanism. While it is difficult (but possible) to isolate and change CS pressure in animals, it is not permitted in humans [156]. Combined with the fact that barostim therapies are applied to the baroreflex in closed loop, there is a need to develop reliable methods and protocols to estimate open loop baroreflex dynamics from closed loop experimental data. Closed loop pressure perturbations applied to the CS can be divided into two categories: (a) disturbances

introduced directly into the receptor, external pressure to the neck or changing the hydrostatic level of the head, or (b) disturbances introduced through the cardiovascular system, through hemorrhage or lower-body negative pressure.

The authors of [125] stimulated the carotid sinuses using neck pressure and suction, investigating the contributions of cardiac output and vascular conductance to carotid mediated changes in mean arterial pressure during exercise. While external pressure stimuli are preferred due to their noninvasive nature, methods such as externally applied neck pressure can be an unreliable input, as it can be difficult to determine what portion of the pressure signal was transferred onto the CS. [106] demonstrated that the application of positive and negative pressure to the neck does not transmit through the neck chamber perfectly or identically, with an 86% transmission of positive pressure and only a 64% transmission in negative pressure.

[161] investigates the cardiovascular response to various pulsatile pressures in the CS, in anaesthetised dogs considering both intact and severed vagal nerves. The carotid sinuses were functionally isolated and the CS was clamped. The reflex responses of MAP, CO and total peripheral resistance (TPR) to an array of excitation signals, with various pressures, frequencies and peak to peak amplitudes, were observed to examine the carotid sinus reflex. CS pressure was manipulated by a function generator connected to the carotid arteries via a four-way glass junction. Cardiovascular system altering processes, such as haemorrhaging and pressure pulse injections, provide a more definitive excitation signal but can be difficult to execute. Determining open loop dynamics from closed loop data is highly dependant on a linear-gain assumption; to uphold this assumption the haemorrhage needs to be mild (10%) and rapid (within 30s), so the reflex compensation can fully develop before humoral controls and vascular autoregulatory mechanism are activated [156]. Pressure pulse injection tests take advantage of the latency of the baroreflex, carrying out tests where the input signals have a pulse duration of 1-2s. The latency allows the input to be considered uncorrelated with the output, creating a pseudo open loop. However, the assumptions render the use of the model to be relatively limited [156].

[79] characterises the very low-frequency range (0.001 - 0.01Hz) response to carotid sinus stimulation using Gaussian white noise as a stimulant. [3] proposes a closed loop cardiovascular system identification method, introduced as two separate model structures, articulating the closed loop contributions of cardiac output (CO) and right atrial pressure (PRA) to arterial pressure (Pa) fluctuations, while characterising the contributions of Pa and PRA to short-term TPR fluctuations. [4] presents clinical

validation for the cardiovascular system identification method proposed in [3].

Clearly, the study of the baroreflex characteristics is crucial in understanding both long-term (potentially hypertensive) and short-term blood pressure control, while measurement of baroreflex sensitivity [99] has also been shown to be a useful measure of baroreflex health.

2.5 Baroreflex sensitivity estimation methods

When analysing physiological systems, the interconnected nature of the human body typically confounds the analysis problem. However, in some cases the interactions between systems can be beneficial, namely the baroreflex sensitivity (BRS) index. The BRS is a well established metric that can assess the autonomic control of the cardiovascular system, by utilising the relationship between the baroreflex and the cardiovascular system [90]. The BRS index quantifies the relationship between blood pressure and R-R interval (the time elapsed between two successive R-waves of the QRS signal on the electrocardiogram), where R-R interval variations are considered a response to changes in blood pressure (BP). A high BRS index is indicative of a strong relationship between BP and R-R interval, therefore demonstrating a robust baroreflex, with the opposite suggesting the baroreflex is impaired.

After further investigation, which increased the understanding of the baroreceptor-heart rate reflex first observed in 1936 [46, 137], has facilitated the use of BRS as an indicator of cardiovascular decline.The baroreceptor reflex is known to alter patients' responses to certain drugs; therefore, it can be useful to estimate the BRS in clinical settings to achieve optimal treatment plans. The analysis of BRS has been shown to provide insight into a number of medical conditions and their progression [174, 185]. Various studies demonstrate that BRS shows potential as a diagnostic tool in patients with a number of conditions. Lanfranchi *et al* [97] demonstrate that high levels of sympathetic activity, when sustained, often seen in patients with an impaired baroreflex, could lead to end organ damage. Decreases in BRS estimates is shown to be linked to higher mortality in patients with heart failure [**?**], indicating the potential of BRS as a prognostic factor in cardiology, e.g. an indicator of cardiac mortality in patients following adverse cardiac events such as myocardial infarction. A number of studies have looked at the link between BRS, changes in BRS, and its ability to determine future cardiac events [92, 93**?** , 91, 99, 130, 184]. In addition to potential BRS use in cardiology, a number of studies investigate its use as an overall prognosis risk marker in

patients with hypertension [128], by investigating the relationship between baroreflex sensitivity and hypertension [133, 181].

2.5.1 Oxford method

The Oxford method [169] is the current gold standard for BRS estimation, using a vasodilator or constrictor to elicit a strong change in BP, and the subsequent RR-interval change recorded. The relationship between BP and RR-interval is plotted, a linear regression line [118] is fit to the data, and the regression coefficient (slope) identified as the BRS gain. The invasive nature of the test makes it impossible to carry out in a routine clinical setting, is expensive, and can be unsafe to perform on patients with a number of underlying conditions [189]. Since the ability to accurately, and safely, assess BRS is most beneficial for patients with a history of cardiac events or cardiac related underlying conditions, the majority of which cannot safely undergo the Oxford procedure, the need for a simple, non-invasive alternative is paramount. To date, no gold standard for non-invasive BRS estimation exists, though a number of methods have been proposed, ranging from spectral analysis methods [153] to regression methods [36],and everything in between [192, 12, 167, 99].

2.5.2 Existing non-invasive BRS estimation methods

In an attempt to find a reliable non-invasive BRS estimation method, a number of time and frequency domain approaches are investigated. All methods, irrespective of mathematical approach, work off of CL data and make the assumption that there is a linear relationship between SBP and RR interval. In addition, some techniques employ pre-processing techniques or data selection.

2.5.2.1 Time-domain Methods

Most BRS estimation methods take time domain recordings of RR interval and (usually) systolic blood pressure (SBP) and simply perform a linear regression of RR interval against SBP. In most cases, the RR interval and SBP data is pre-processed into 'sequences', which are sequences of 3, or more, concurrently increasing (or decreasing) transitions in SBP and RR interval [24, 29, 78, 52]. One difficulty with sequences is identification of the correct 'lag' between the transition in RR interval and the change in SBP that produced it [24]. This difficulty is compounded,

given that that data is considered on a 'per beat' basis, i.e. without a consistent time interval between measurements. In most cases, contiguous sequences are used to produce individual BRS estimates, which are then used to obtain a global average. In contrast, Gouveia *et al* [52] fit a global regression line through all selected sequences, a method that was further developed in [51] and [50]. Patients with cardiac disease generally have a low number of valid sequences in their recordings, which can reduce the accuracy of the BRS estimate obtained. An insufficient number of sequences can also be an issue with patients with autonomic dysfunction, the low variability in their blood pressure signals generally reducing the number of sequences extracted [126].

The 'Z-coefficient' method [36] obtains a statistical coefficient of dependency between SBP and RR interval. (SBP, RR) pairs that have a high coefficient value are selected and a linear regression line is fit to the selected data; in turn, the regression coefficient is considered as the BRS estimate [22]. A disadvantage of the Z-coefficient method is that it requires long portions of data for the probability functions to be reliable.

Some researchers have developed more complex time series representations of the baroreflex. These models vary greatly in complexity from models that consider RR interval to be solely a function of SBP [142], to RR interval dependant on SBP, coloured noise and respiration, obtained from specific breathing protocols [135], and everything in between [67, 40, 124, 30].

Wu *et al* [192] develop a nonlinear model based on the Volterra-Weiner framework, using spontaneous data from both normotensive and hypertensive patients. The spontaneous nature of the recordings generally mean that there is little excitation of the system, in turn questioning the need for the added complexity of the non-linearity (normally associated with larger amplitude variations).

A number of researchers have considered the CL nature of the baroreflex. Baselli *et al* [12, 11] propose a CL model portraying the relationship between RR interval, SBP and respiration. [40, 124, 139] utilise bivariate autoregressive modelling to calculate the transfer function between RR interval and SBP. While the models themselves are evaluated in the time domain, the BRS gain is obtained from the frequency response of the identified models.

2.5.2.2 Frequency-domain Methods

The frequency range for the baroreflex is generally divided into two bands: the low frequency (LF) component, associated with parasympathetic and sympathetic activity, in the range of 0.04Hz-0.15Hz, and the high frequency (HF) component, associated predominantly with the vagal parasympathetic modulation related to respiration [109], in the range 0.15Hz - 0.4Hz. Robbe *et al* [153] also define a very low frequency range associated with vasomotor activity caused by changes in temperature and task adaptation, in the range 0.02Hz - 0.06Hz.

A transfer function method was first proposed by Robbe at al [153] and involves the calculation of the magnitude of the transfer function between SBP and RR interval in the LF and HF bands using spectral techniques. The Fourier transfer function, and coherence function, are defined as:

$$H_{RS}(f) = \frac{G_{RS}(f)}{G_S(f)} \tag{2.8}$$

and

$$C_{RS}(f) = \frac{|G_{RS}(f)|^2}{|G_R(f)||G_S(f)|} \tag{2.9}$$

respectively, where G_{RS} is the cross-spectral density of SBP and RR interval, with G_S and G_R representing the spectral densities of RR interval and SBP, respectively. Finding the frequency response of an autoregressive or input/output time domain model also provides a means to determine the spectral densities [178]; however, such a calculation route strictly places associated BRS methods within the time domain class of BRS estimation techniques. The coherence function, $C_{RS}(f)$ can be used as a measure of the significance of the coupling between SBP and RR interval at a frequency f. The frequency-dependent gain quantity $\alpha(f)$, defined in equation (2.10), has also been used [131] as an estimate of BRS:

$$\alpha(f) = \sqrt{\frac{G_R(f)}{G_S(f)}} \tag{2.10}$$

Use of spectral methods for BRS estimation is popular among a number of research groups. Choi *et al* [24] study the effect of postural changes using both the transfer function method and the α-index for BRS estimation. Davies *et al* [29] examine the reproducibility of BRS estimates in control subjects, and in patients with chronic heart failure (CHF), adopting an α-index method, using AR modelling for spectral estimation. Pagani *et al* [131] assess BRS by the α-index method, employing a two-way autoregressive bivariate model for spectral estimation. Maestri *et al* [108] perform a

study to compare different methods for estimating BRS, including the transfer function method in [153] and the α-index method in [131]. Pitzalis *et al* [139] investigate the effect of controlling breathing rates on BRS estimates, using an estimation method similar to that in [131]. Glos *et al* [48] examine the positive effect of ventilation on BRS, using the α-index method.

Lin *et al* [101] estimate BRS via the Gaussian average filtering decomposition (GAFD). Rudiger *et al* [155] propose an alternative approach to the autoregressive and DFT methods for spectral estimation. The trigonometric regressive (TRS) approach provides estimates of the required power spectra, with a transfer function subsequently calculated. Li *et al* [100] further refine the multiple TRS approach by investigating the impact of the data segment settings by applying the TRS technique to the EuroBaVar dataset.

Finally, Singh *et al* [167] propose the use of an improved Hilbert-Huang transform (HHT). The HHT was developed to analyse nonlinear and non-stationary data, similar to blood pressure measurements. The main drawbacks of the HHT, mode mixing and end effect, are overcome in the improved HHT by multiplying the signals by cosine windows and enhancing the empirical mode decomposition (EMD). The improved HHT approach shows an increased number of cases where BRS estimates can be calculated.

Table 2.3 contains a short description for all non invasive BRS estimation methods, both time- and frequency-domain, discussed in this subsection.

2.5.3 Sequence methods

Over the past three decades, sequence methods have become a popular method for non-invasive measurement of BRS [24, 29, 78, 52, 179, 42]. A sequence method, first introduced by Di Rienzo in 1985 [33], analyses BP and ECG signals, recorded without any external stimulus, for correlated increases or decreases in both the input (BP) and output (RR-interval). Under the sequence method philosophy, a set of data points is considered a valid sequence if it has three, or more, consecutive increasing or decreasing points in input and output data. Examples of positive-going and negative-going sequences are shown in Fig. 2.5. Following sequence selection, a regression line is fit to each individual input/output sequence. The 'gain' for the sequence is the regression coefficient and the BRS for the data set is determined as the average of all the regression coefficients.

Table 2.3: Baroreflex sensitivity estimation methods using non invasive blood pressure signals and their characteristics. BPV refers to BP variations and RRV refers to R-R interval variations

Method type	Description	Ref
TF methods	BRS is considered the gain of the transfer function between BPV and RRV in the frequency band (0.07-0.14Hz)	[153]
α methods	BRS is considered the gain of the relationship between BPV and RRV at a specific frequency range, typically the frequency range 0.04-0.15Hz.	[131]
GAFD methods	BRS is obtained by applying a Gaussian averaging filter to BPV and RRV in the frequency range of interest.	[101]
TRS methods	BRS is considered the gain of the power spectra between BPV and RRV	[155, 100]
HHT methods	BRS is calculated by applying combining the HHT and EMD to account for the non-linear interactions between RRV and BPV when calculating the gain.	[167]
Seq methods	BRS is calculated as the average gain of the linear regressions applied each sequence. A sequence is 3, or more, concurrently increasing (or decreasing) transitions in BP and RR interval.	[24, 29, 78, 52]
Z-coefficient	BRS is calculated as the gain of a linear regression applied to selected BP/RR pairs with a high coefficient value.	[36, 22]

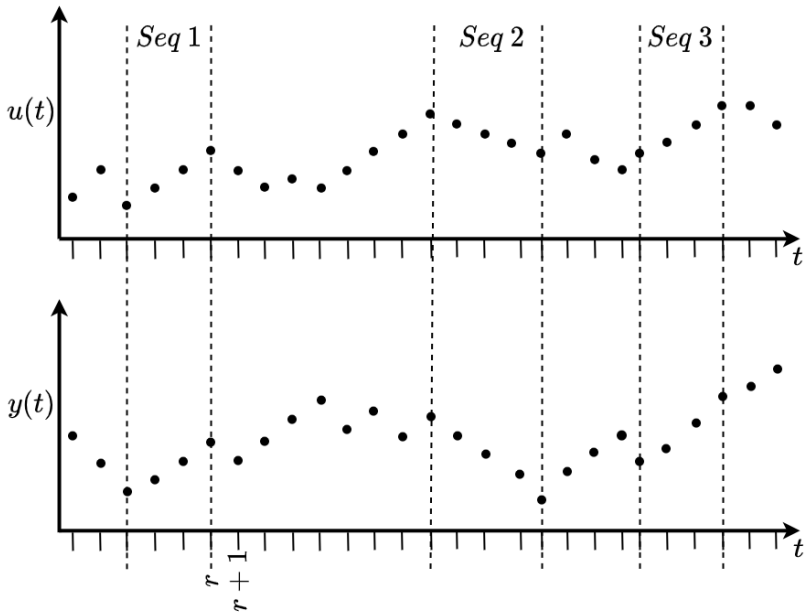

Figure 2.5: Example of valid sequence selection. The graph highlights three instances where three, or more, matching increases/decreases in both the input ($u(t)$) and the output ($y(t)$) are observed.

In contrast, Gouveia *et al* [52] fit a global regression line through all selected sequences, a method that was further developed in [51] and [50]. In 1988, Bertinieri *et al* [13] further refined the sequence selection criteria to include a minimum changes of at least $\geq 1mmHg$ in blood pressure, $\geq 4ms$ in RR-interval, and a delay of one beat is assumed [13]. Since then, various researchers have chosen to use a variety of minimum thresholds, delays and some include a minimum correlation coefficient (r) in an attempt to make the gain estimates more robust to noise. In 2009, Laude *et al* [98] investigated the optimal combination of minimum sequence lengths, variable thresholds, delays and r values, in an attempt to standardise the sequence selection criteria. The authors carried out their experiment on mice data sets, investigating BRS estimation using sequences of various lengths, using various BP/R-R interval thresholds and different delays between the input and output. It also investigates whether a minimum r is required. The study concluded that the sequence method, when applied to data from mice, should consider sequences of three beats, or more, with a delay of zero or three beats. Thresholds for the r, SBP, or R-R interval were deemed unnecessary.

3

Protocol for the identification of the neural baroreflex characteristic in sheep

Contents

3.1 Introduction 31
3.2 Details of the experiment 32
3.2.1 Experimental setup 33
3.2.2 Data acquisition and analysis equipment 33
3.2.3 Selection of excitation signal 34
3.3 Modelling preliminaries 36
3.3.1 Considerations from physical system 36
3.3.2 Data preprocessing 38
3.4 Model identification 38
3.4.1 Frequency domain 39
3.4.2 Time domain 42
3.5 Model validation 47
3.5.1 Frequency domain validation 47
3.5.2 Time domain validation 48
3.6 Conclusion 49

3.1 Introduction

As discussed in Section 2.4, hypertension is a global issue with an increasing need for alternative, effective, antihypertensive treatments such as BA therapies. To further

develop sBA protocols, increased understanding of the neural baroreflex characteristics is vital.

This chapter articulates the process of developing a protocol used to determine the dynamics of the neural baroreflex. The protocol includes a measurement procedure, followed by a data post-processing stage, which draws on techniques from the control sciences. The excitation signal used, a PRBS signal, is known to provide sufficiently stimulate nerves while minimising the likelihood of subject fatigue when attempting to identify the frequency characteristics of portions of the baroreflex. In particular, the excitation signal used to stimulate the carotid sinus is refined, following an initial test, to ensure the frequency range associated with the neural baroreflex is excited. Another factor, that impacts the identification techniques used, was the fact that the data is obtained in closed loop (CL), where the animal's nerves were not denervated, in other words, the neural baroreflex is intact. Both time- and frequency-domain identification techniques are employed, which results in parametric time-domain models and non-parametric frequency response data.

The remainder of the chapter is laid out as follows. Section 3.2 contains the details of the experimental setup. Section 3.3 explains physical considerations that may influence identification techniques, and the data pre-processing techniques used. Section 3.4 discusses both the frequency and time domain identification methods used. Section 3.5 investigates the validity of the identified models, in both the time and frequency domain, and the extent in which the models can be cross validated, while Section 3.6 draws conclusions from the study.

3.2 Details of the experiment

Experiments were conducted on one anesthetized, adult female Romney sheep weighing 55 kg. The animal was housed in an individual crate in the proximity of other sheep and acclimatised to laboratory conditions (18 °C, 50% relative humidity, 12:12 hour light/dark cycle) and human contact prior to experimental protocols. Sheep were fed daily (2 kg/day), water ad libitum, and supplemental hay and chaff as needed. All experiments and surgical procedures were approved by the Animal Ethics Committee of the University of Auckland. Anaesthesia was induced with intravenous propofol (5 mg/kg; AstraZeneca, U.K.) and, following intubation, was maintained with 1.5-2.0% isoflurane/O2 (Lunan Better Pharmaceutical, China).

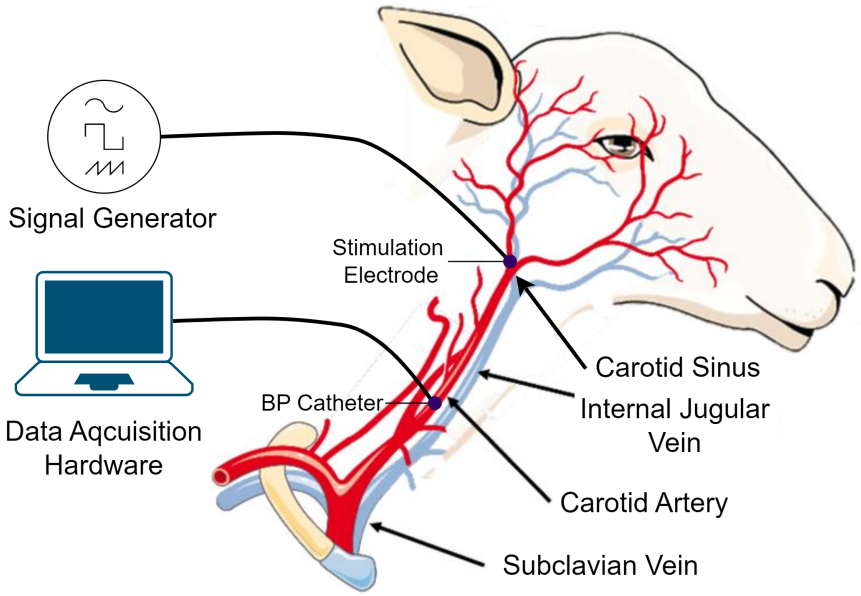

Figure 3.1: An illustration of experimental set up, showing the location of the stimulation electrode and BP measurement catheter. Adapted from [54].

3.2.1 Experimental setup

Once the animal was anaesthetised, the animal was placed on its back. A solid state BP catheter was inserted into the carotid artery to allow measurement of BP in the animal. Following this, the carotid artery bifurcation on the contralateral side was exposed and the carotid artery gently cleared of surrounding connective tissue. A custom made electrode was placed around the carotid artery, and the artery was stimulated at 5V and 10 Hz. The voltage and frequency was selected based on priori knowledge from stimulation studies carried out by the Department of Physiology in the University of Auckland. If no response in BP was observed, the electrode site was moved until a reproducible BP decrease was observed. Once this site was found, the electrodes were maintained in place around the artery and the PRBS sequence commenced. The experimental setup can be observed in Figure 3.1

3.2.2 Data acquisition and analysis equipment

Blood pressure (BP; mmHg) was recorded on a computer using a data acquisition unit (Micro1401-3, Cambridge Electronic Design, U.K.) and data acquisition software (Spike2, Cambridge Electronic Design, U.K.). The PRBS and BP signals were sampled at $100Hz$, then exported from the acquisition software as a .txt file. The data was then analysed using MATLAB.

3.2.3 Selection of excitation signal

To identify the frequency response of biological systems, researchers have traditionally applied a number of sine waves at various different frequencies sequentially. While sine waves are effective at replicating the natural signals present in nerve fibers, there are some limitations to their use. Applying individual sinusoids in succession, leads to long experiment times, and can frequently result in subject fatigue, particularly when attempting to identify frequency responses for systems that mainly operate in a low frequency range. In regard to stimulation of the neural baroreflex, an array of alternative stimulation signals have been used, as discussed in Section 2.4.2

A number of input signals were considered when identifying the input signal for this study, ultimately a pseudo random binary sequence (PRBS) was chosen. A PRBS signal is made up of a series of highs and lows that occur randomly (illustrated by the blue like in Figure 3.2). At a fixed interval (known as the switching period) the sequence either maintains its current value (low -> low or high -> high), or toggles (low -> high or high -> low) creating a signal that exhibits behaviour similar to that of a truly random signal. The nature of PRBS sequences mean that a large frequency range can be tested over a shorter period of time than serial sinusoidal tests, while simultaneously reducing the likelihood of subject fatigue. The randomness associated with PRBS signals results in a flat frequency spectrum of PRBS signals, lending to balanced frequency response analysis. While both white noise and PRBS both over come the fatigue issue that arises from a series of sine waves, the selection of a minimum switching speed for PRBS signals allow for a flat spectrum within a given frequency range. In this instance, the range of interest being 0Hz to 0.1Hz.

PRBS signals have been shown to effectively excite the baroreceptors in a number of studies. [141] investigates the viability of using PRBS signals to obtain the frequency response of carotid sinus receptors. [140] demonstrated that the use of PRBS signals obtain similar frequency responses to those obtained through sine testing, with a significantly shorter test length. [56] demonstrates that a PRBS provides sufficient excitation in renal nerves to produce a measurable change in renal blood flow, while providing adequate frequency resolution. [47] demonstrates the use of PRBS to excite the closed loop baroreflex via the carotid sinus in rabbits.

A preliminary test, shown in Figure 3.3, was carried out to determine an appropriate keying frequency (tonal signal), voltage amplitude and switching period for the PRBS stimulation. Specifically, an excitation signal at 5V amplitude and 10Hz tone elicited a

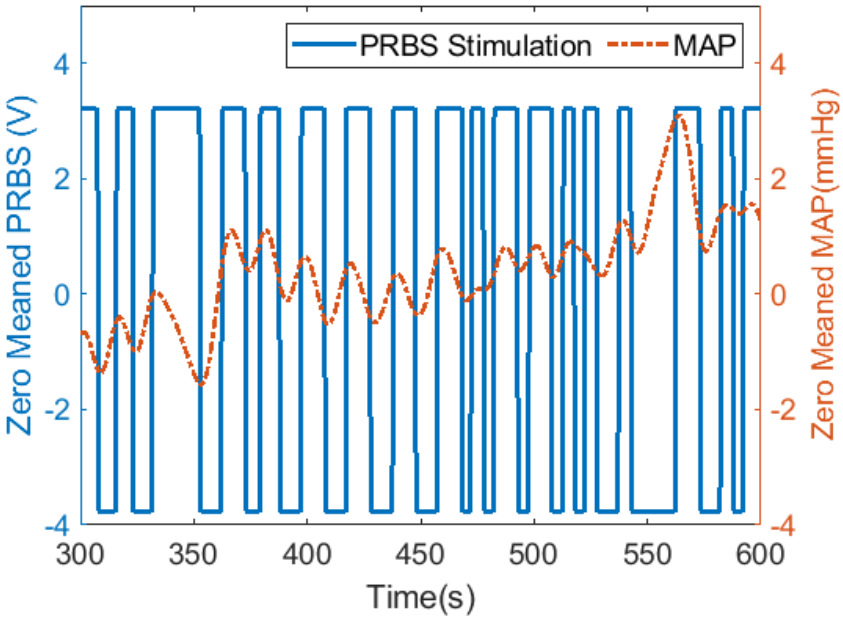

Figure 3.2: Zero meaned response of mean arterial pressure (MAP) to a pseudo random binary sequence (PRBS) via the carotid sinus baroreceptor.

clear, strong decrease in BP. After stimulating the baroreceptors, a transient decrease in BP was observed for between 5 and 10s before steady-state, suggesting that a PRBS with a minimum switching period of 5-10s would provide a suitable balance between amplitude resolution (giving an acceptable S/N ratio) and frequency range (shorter minimum switching interval gives extended signal bandwidth). Two PRBS signals with a switching period of 5s and 10s were generated; their frequency spectrum (shown in Figure 3.5) was obtained using the fast Fourier transform (FFT). From Figure 3.5, it can be seen that 5s minimum switching period (red line) provides a flatter frequency spectrum than the 10s minimum switch period (blue line) between $0Hz$ and $0.1Hz$, ie. a consistent frequency spectrum across the frequency range associated with the baroreflex.

3.2.3.1 Experimental method

The PRBS, with a minimum switching period of 5s, was applied by manually switching the 5V and 10Hz signal on and off over the course of 20 minutes. While manual switching may produce different characteristics to an exact computer-generated PRBS, this variability can help to further flatten the frequency spectrum of the 'measured' PRBS'. The actual applied PRBS signal was measured during the experiment, and will be referred to as the measured PRBS.

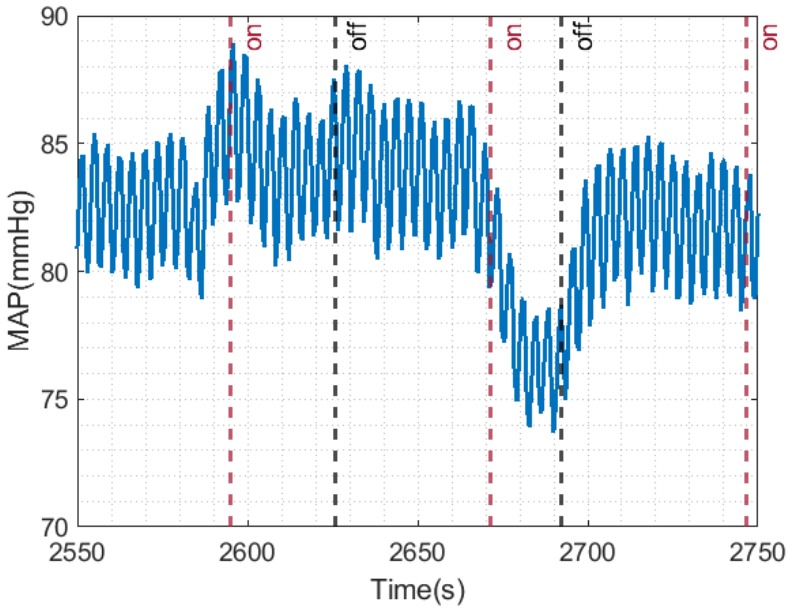

Figure 3.3: Response of MAP to CS baroreceptor stimulation. Stimulation signals of various keying frequency and voltage amplitude were applied to one of the CS baroreceptors for various lengths of time to determine which signals elicit a strong, clear change in blood pressure.

It should be noted that the resting BP of the sheep under anaesthesia was lower than conscious conditions at the commencement of the trial. To ensure decreases in BP were observable, the animal was placed on an infusion of phenylephrine solution (a vasoconstrictor; 2mg in 30ml), at a rate of 20ml/hour, to ensure that BP was sufficiently high, and that a significant drop in blood pressure could be observed.

Figure 3.2 shows the zero-meaned measured PRBS signal and MAP response. When the PRBS signal is "high" there was a clear reduction in MAP, and when the PRBS was "low" MAP began to increase again.

3.3 Modelling preliminaries

3.3.1 Considerations from physical system

The interconnected nature of human physiology generates significant challenges in isolating subsystems and their response to an individual causal variable. In addition, due to the plethora of feedback control systems that maintain homeostasis, true open-loop data can only be obtained by surgical or pharmaceutical intervention, which may produce their own unwanted side effects. These issues must be considered

when attempting to measure open-loop characteristics from measured closed-loop data.

Blood pressure variables BP is regulated by physiological needs via hormonal, neural and intrinsic factors. Both cardiac output and peripheral resistance are major influences of BP and are neurally controlled via the central nervous system. In addition, both CO and TPR can be altered by a number of intrinsic factors depending on metabolic needs [123]. A variety of hormones circulate throughout the body such as prostaglandins, renin, angiotension, and aldrosterone, all of which can cause localised vasodilation or vasoconstriction [146]. As noted in Section 3.2, the subject was on a constant infusion of phenylepherine, a vasoconstrictor used to increase BP [120].

Closed loop system The aortic and carotid receptors were retained intact for the experiment, with the baroreflex operating in (normal) closed loop, as shown in Figure 3.4. While identification of the open-loop dynamics, $G(p)$, is achievable with closed loop data, there are a number of limitations which should be considered. Since, in general, the purpose of a feedback loop is to make the closed-loop system less sensitive to changes than the open loop system, the closed loop data can be less informative than pure open loop data [103].

Identification methods, used to elicit open-loop dynamics from closed loop data, can be divided into three categories: (a) direct methods, where the measured input-output signals are used and the feedback loop is ignored, (b) indirect methods, where some information about the feedback is available and an effective open-loop input signal can be formed, and (c) joint input-output methods, where both input and output signals are treated as outputs driven by noise and the feedback system [103]. The appropriate method to use is dependant on the prior system knowledge available, and the ability to accurately measure certain variables. In the current study, the feedback loop is assumed to be unknown, leading to the choice of a direct method. The direct method treats the system as if it was open loop; however, appropriate choice of a time domain identification method can ameliorate the effect of correlated feedback (see Section 3.4.2) and the facility to inject an external input, which is uncorrelated with the noise/disturbance, also helps to resolve the open-loop dynamics from the measured closed-loop data [45]. However, one drawback of using the direct method, is that a poor noise model can lead to a biased representation of the system [177]. The presence of a very strong, or dynamically complex noise signal, can cause certain identification techniques to fail, such as such as spectral analysis, correlation analysis, output error and subspace methods [103].

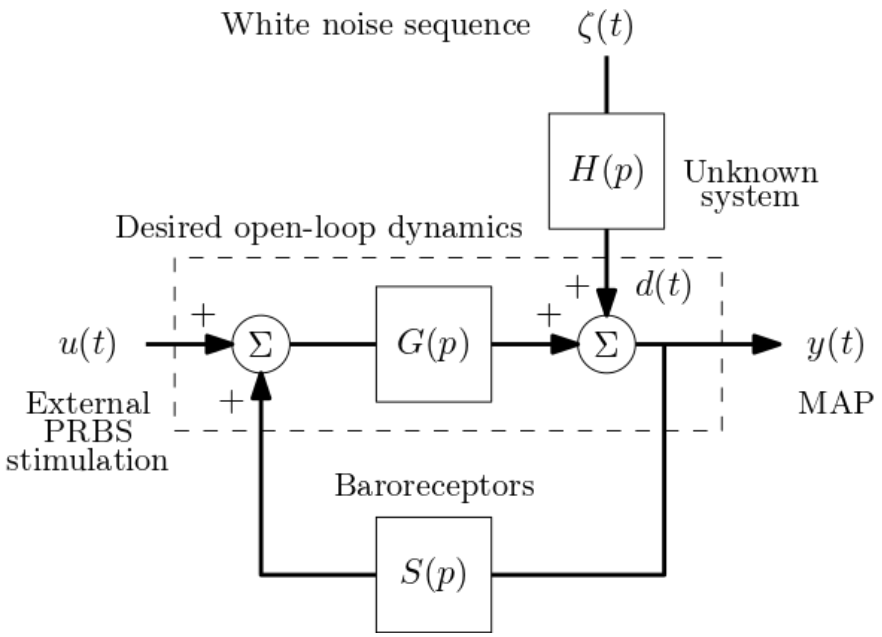

Figure 3.4: Block diagram representing the neural baroreflex. Note that $d(t)$ represents uncontrolled/unmeasured effectors that influence MAP. $G(p)$ includes both the neural and peripheral baroreflex arcs, excluding the baroreceptors. The time-domain differential operator is denoted by p while $G(p)$ and $H(p)$ are, in general, rational functions of p.

3.3.2 Data preprocessing

The measured output signal is BP, containing oscillatory components due to the cardiac ($1 - 1.3Hz$ in sheep) and respiratory ($0.26 - 0.56Hz$ in sheep) cycles, as evident in Figure 3.5. The neural baroreflex characteristics associated with the baroreceptors lie in the frequency range $0 - 0.1Hz$. In order to isolate MAP, cardiac and respiratory signals were removed by passing the measured BP signal through an 8^{th} order Butterworth low-pass filter with a cut-off frequency of $0.1Hz$. The input and output signals were resampled to $2Hz$ using a FIR low pass filter to ensure anti-aliasing and the phase delay introduced by the filter was compensated for by using forward/backward filtering.

3.4 Model identification

Model identification approaches can be classified into two broad categories, time- and frequency-domain identification, depending on the nature of the system data used to determine the model parameters. Frequency domain analysis can be particularly useful for determining the general dynamic behaviour of a system, and getting a clear understanding how the system will respond to a broad range of stimuli, while time domain identification focuses on the production of a model which can reproduce the

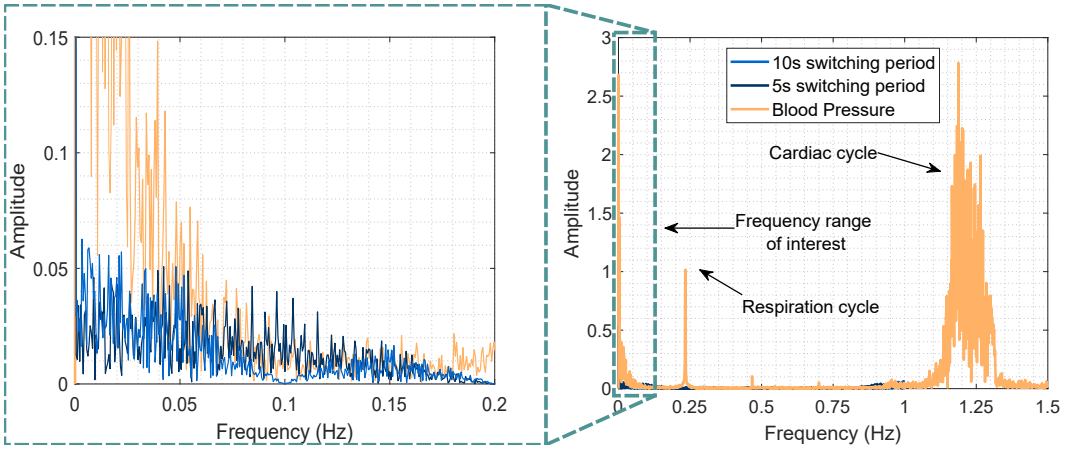

Figure 3.5: Spectra of the measured MAP signal (—), and of the PRBS sequences with switching periods of 5s (—) and 10s (—).

output signal, for a given data set, to a high degree of fidelity. This can be useful to try to predict how the system will respond to specific stimuli, or predict trends that may occur over time, Typically, time-domain models are useful in examining the transient behaviour of the system.

In both time- and frequency-domain approaches, it is of crucial importance that the test signal excites the complete range of system dynamics over their active frequency range. This issue explains the level of consideration involved in the development of the experimental protocol in Section 3.2.

3.4.1 Frequency domain

The frequency response of the neural baroreflex (from $u(t)$ to $y(t)$ in Figure 3.4), shown in Figure 3.6, was estimated [103] using:

$$\hat{G}_N(e^{i\omega}) = \frac{\hat{\Phi}^N_{yu}(\omega_0)}{\hat{\Phi}^N_u(\omega_0)}, \tag{3.1}$$

where, $\hat{\Phi}^N_{yu}(\omega_0)$ denotes the cross spectrum of the input and output signals, and $\hat{\Phi}^N_u(\omega_0)$ denotes the auto spectrum of the input.
To identify how well the two signals are coupled, the coherence C_{xy} between the measured PRBS and MAP, shown in Figure 3.6, was calculated using:

$$C_{xy} = \frac{|P_{cy}(f)|^2}{P_{xx}(f)P_{yy}(f)} \tag{3.2}$$

where, Pxy is the cross spectrum and P_{xx} and P_{yy} are the power spectra of signals input and output signals x and y, respectively. Non-overlapping sections of 256 data points were used in the coherence calculations.

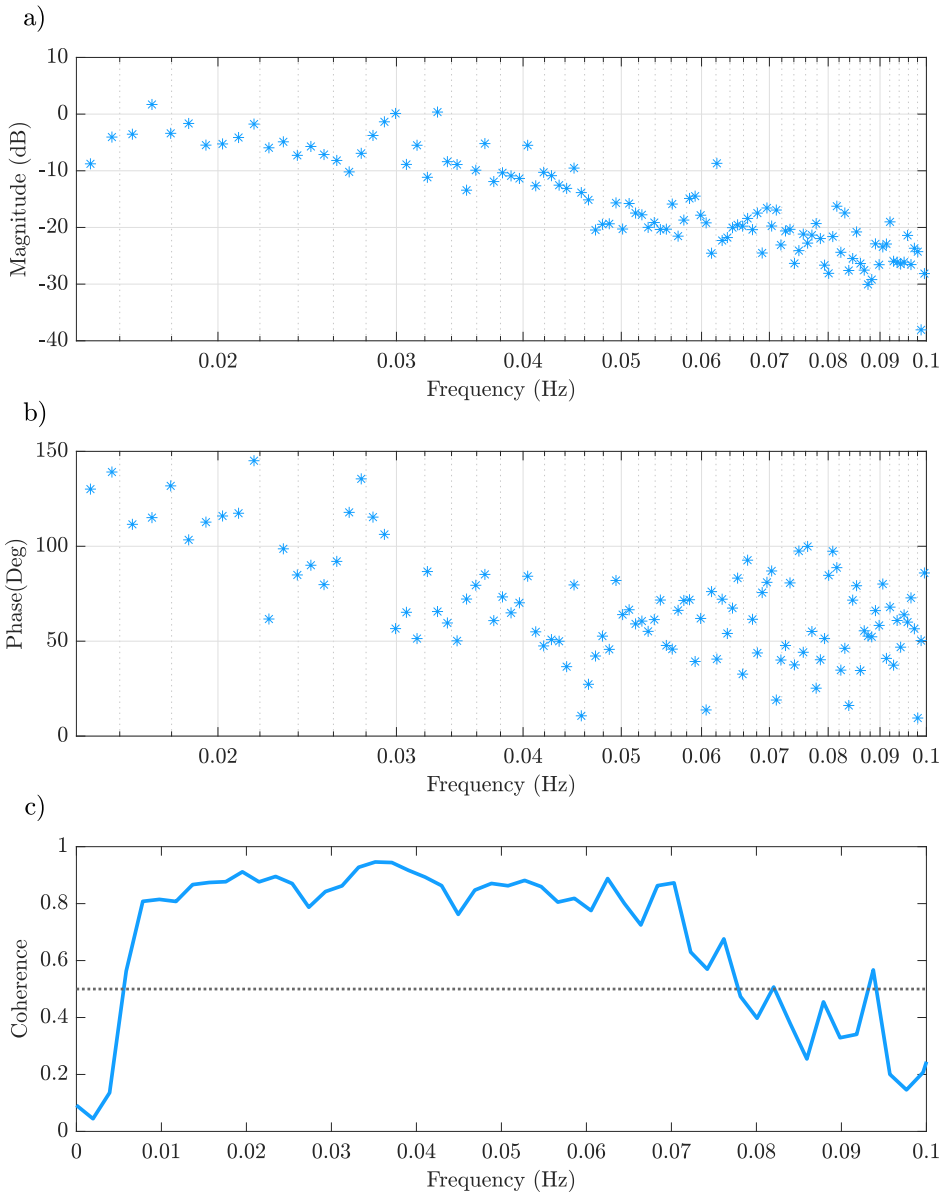

Figure 3.6: Frequency response of the neural baroreflex estimated from (3.1) (*). With subplot a) the magnitude response, b) the phase response and c) the coherence function

The coherence between the PRBS and MAP signals was > 0.5 from $0.005\,Hz$ to $0.07\,Hz$. Given that the longest pseudo half-period of the PRBS is $34.48s$, corresponding to a frequency of $0.0145\,Hz$, data below $0.0145\,Hz$ are not considered, as they are not excited directly by the input signal. A transfer function, with a frequency response similar to Figure 3.7, was determined by manually examining the magnitude plot for breakpoints corresponding to $\pm 20dB/$decade changes in slope, indicating the presence of a pole ($-20\ dB/$decade) or zero ($+20\ dB/$decade). The transfer function in (3.3) was identified, characterised by three poles and one zero (the locations of which are shown in Figure 3.7):

$$\begin{aligned} G_{MF}(s) &= \frac{-0.015488(s+0.5655)}{(s+0.1571)(s+0.2199)(s+0.2702)} \\ &= \frac{-0.01556s - 0.0088}{s^3 + 0.6472s^2 + 0.1364s + 0.0093} \end{aligned} \tag{3.3}$$

with the MF subscript denoting a manual fit, noting that s denotes the frequency-domain differential Laplace operator (p is the equivalent time-domain operator), with the frequency response determined by the substitution $s \to j\omega$.
With the subsequent development of a time-domain model, which has an exclusively discrete-time representation, the model of (3.3) can be transformed into discrete time, for comparative (and other) purposes. The discrete time equivalent was obtained by pole zero matching, with individual poles and zeroes of (3.3) converted using:

$$z_i = e^{s_i T_s} \tag{3.4}$$

where
T_s is the sampling interval ($T_s = 0.5s$),
s_i is the pole/zero location in continuous time, and
z_i is the pole/zero location in discrete time,
with the gain of the matched discrete-time equivalent usually normalised to match the d.c. (zero frequency) gain of the original continuous-time system. Note that z is the frequency-domain forward shift operator, equivalent to q in the time domain. The discrete time equivalent of (3.3), using pole-zero matching, is:

$$\begin{aligned} G_{MF}(z) &= \frac{-0.0018935(z-0.7537)(z+1)}{(z-0.9245)(z-0.8959)(z-0.8736)} \\ &= \frac{-0.001893z^{-1} + 0.0004663^{-2} - 0.001427^{-3}}{1 - 2.6940z^{-1} + 2.4186z^{-2} - 0.7236z^{-3}} \end{aligned} \tag{3.5}$$

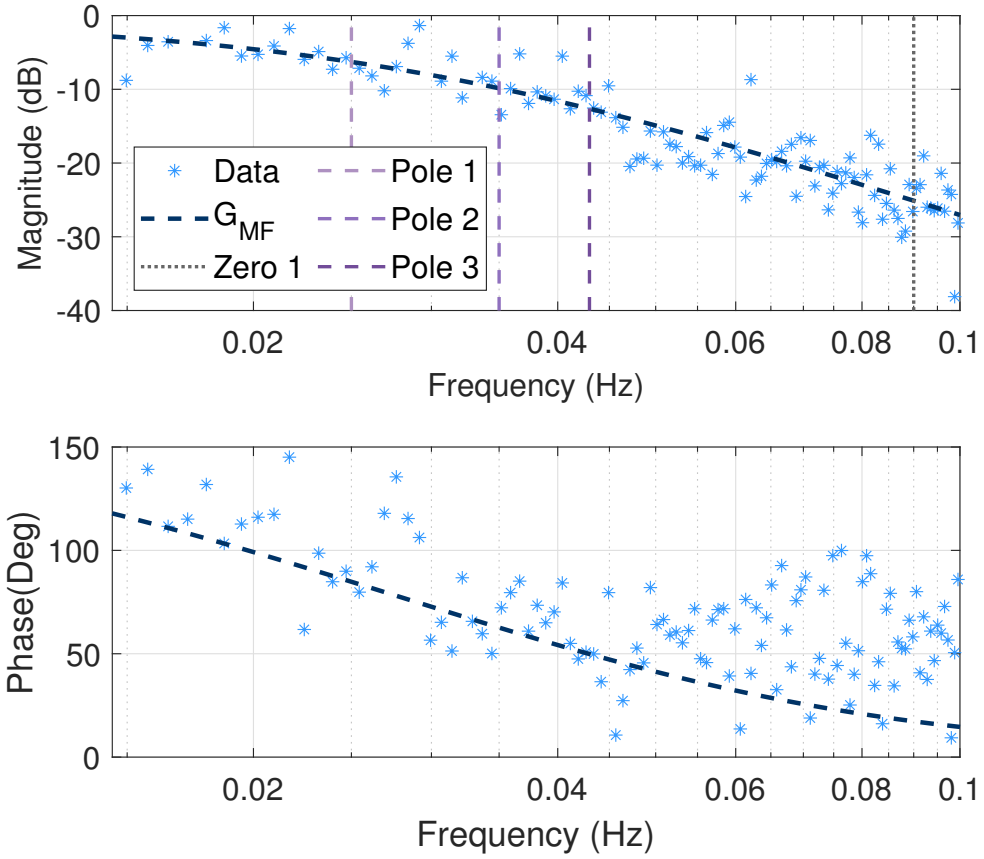

Figure 3.7: Frequency response of the neural baroreflex estimated from (3.1) (*), the frequency response of G_{MF} in (3.3), (- - -) and the poles (vertical dashed line) and zero (vertical dotted lines) of G_{MF}.

3.4.2 Time domain

A high level of noise in output data from closed loop systems can render frequency domain identification methods ineffective, potentially resulting in an inaccurate model [103]. This is due to the inability to identify a separate noise model in the frequency domain, while time-domain approaches, in contrast, allow the identification of a separate noise model. However, even with the separate dynamic noise model available in the time domain, not all closed-loop systems are identifiable. [57] concludes that the use of direct identification, with a prediction error method applied to general linear models, is a good approach “as if it fails, then no other method will succeed, using the data".

3.4.2.1 Model structure

In the time-domain identification step, given that sampled data is used, a discrete time system representation is used, via a general time-domain model structure of:

$$y_k = \underbrace{\frac{B(q)}{F(q)}}_{G_d(q)} u_k + \underbrace{\frac{C(q)}{D(q)}}_{H_d(q)} \zeta_k \tag{3.6}$$

where y_k is the output signal, u_k is the input signal, ζ_k is an unknown white noise sequence, with a mean value of zero and is assumed to be uncorrelated with past or future values of u_k. k is the discrete-time index, where $t = kT_s$. $G_d(q)$ is the open-loop system of interest, made up of polynomials $B(q)$ and $F(q)$, with $H_d(q)$ the noise model, inversely stable, monic and independent of the input signal, made up of polynomials $C(q)$ and $D(q)$, as shown in Figure 3.4, in (3.6), where q denotes the forward difference operator i.e. $q(f(k)) = f(k+1)$, and

$$B(q) = q^{n_\delta}(b_1 + b_2 q^{-1} + ... + b_{n_b} q^{-n_b}), \tag{3.7}$$

$$C(q) = c_1 q^{-1} + ... + c_{n_c} q{-}n_c, \tag{3.8}$$

$$D(q) = 1 + d_1 q^{-1} + ... + d_{n_d} q^{-n_d}, \tag{3.9}$$

$$F(q) = 1 + f_1 q^{-1} + ... + f_{n_f} q^{-n_f}, \tag{3.10}$$

where n_δ is the number of steps of pure delay between u_k and y_k. (3.6) describes the general form of a Box-Jenkins model, offering considerable dynamic freedom in the form of both the system ($u_k \rightarrow y_k$) and the noise ($\zeta_k \rightarrow y_k$) model [15].

With $D(z) = F(z)$, resulting in an ARMAX (AutoRegressive Moving average with an eXogenous input) model, the denominator polynomial is common to both the model and the noise model, limiting the dynamics of the noise model. Retaining a unique $C(z)$ polynomial allows for a moving average term on the noise model, allowing greater freedom in the noise model [177]. Forcing $D(z) = F(z)$ and $C(z) = 1$, resulting in an ARX (AutoRegressive with an eXogenous input) model, where the noise passes through the denominator dynamics of the model [103].

It should be noted that, while the time domain identification procedure (Section 3.4.2) explicitly identifies the noise model polynomials $C(q)$ and $D(q)$, these have little value in themselves, other than to avoid corruption of the $B(q)$ and $F(q)$ model polynomials due to noise colouring effects. However, they do have utility in a post-hoc analysis of the model residual, which gives a measure of the model fidelity.

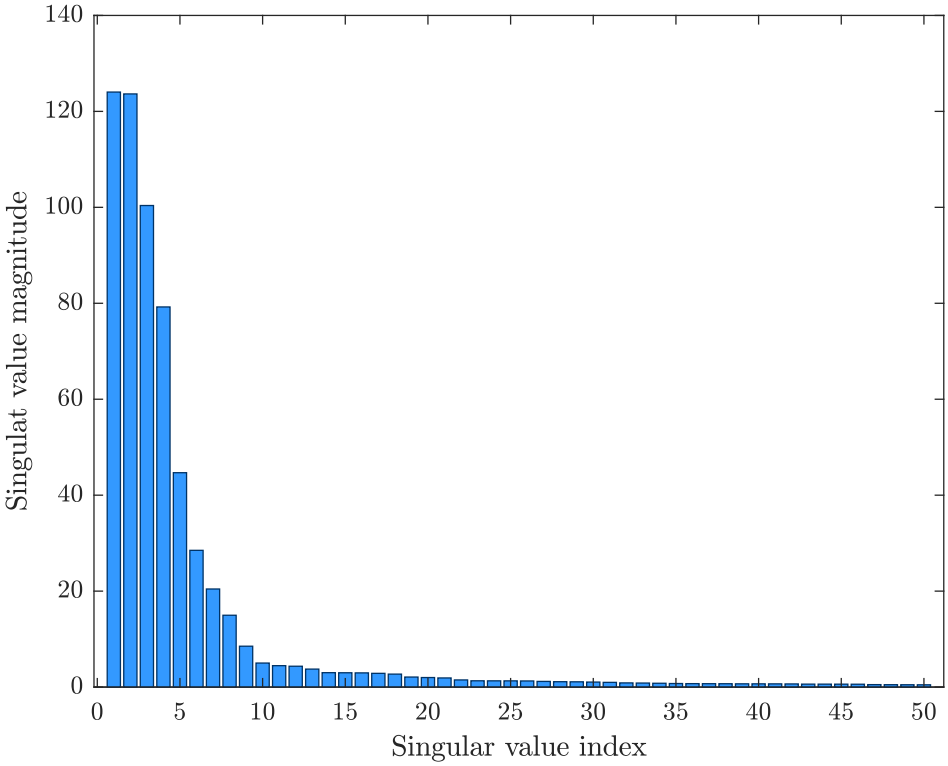

Figure 3.8: Persistence of excitation in the measured PRBS signal

3.4.2.2 Model order determination and parameter estimation

The persistence of excitation determines to what extent the input signal, u_k, excites the system, in turn determining the order to which the system can be accurately modelled. In general, if the spectrum $\Phi_u(\omega)$, of u_k, is nonzero at at least n points, a model of order n can be uniquely identified. A convenient mathematical formulation, involving the *covariance matrix*, $\bar{R}$, of u_k can be made, via:

$$\bar{R} = \begin{pmatrix} R_{u_0} & R_{u_1} & \dots & R_{u_{n-1}} \\ R_{u_1} & R_{u_0} & \dots & R_{u_{n-2}} \\ \vdots & \vdots & \ddots & \vdots \\ R_{u_{n-1}} & R_{u_{n-2}} & \dots & R_{u_0} \end{pmatrix}, \tag{3.11}$$

where:

$$R_{u_\tau} = E[u_k u_{k-\tau}] \tag{3.12}$$

is defined as the *covariance* of u_k, where τ is an integer, while $E[\,]$ is the expectation (averaging) operator. If $\bar{R}$ is non-singular, then u_k is persistently exciting of order n and a model of order n can be uniquely identified. If $\bar{R}$ is singular, the number of non-zero singular values (i.e. the *rank* of $\bar{R}$) determines the order of the model that can be identified. A useful relation is that, for each separate sinusoidal frequency in

u_k, $\bar{R}$ contains two non-zero singular values.

The matrix $\bar{R}$ was obtained up to a potential order of 50, i.e. the singular values of a 50x50 covariance matrix were evaluated with the PRBS signal, as shown in Figure 3.8. Considering the number of significant (non-zero) singular values, a model of order up to 20 can be identified using this input signal.

To determine the model order of the system, u_k and y_k were divided into evaluation and validation data with a 2:1 ratio. The order of the $B(q)$ and $F(q)$ polynomials, n_b, n_δ, and n_f, were selected based on (3.5), giving $n_b = 3$, $n_f = 3$ and $n_\delta = 1$. n_c and n_d, associated with polynomials $C(q)$ and $D(q)$, were obtained using loss function analysis, minimising the mean-square prediction error (in the spirit of prediction error methods [103])

$$MSE = \frac{1}{n}\sum_{i=0}^{n}(y_i - \hat{y}_i)^2 \tag{3.13}$$

between the measured output, y_k, and the output predicted by the identified model, $\hat{y}_k$, with:

$$\theta = [b_1...b_{nb}\ c_1...c_{nc}\ d_1...d_{nd}\ f_1...f_{nf}], \tag{3.14}$$

$$\hat{y}(k|\theta) = \frac{D(q)B(q)}{C(q)F(q)}u_k + \frac{C(q) - D(q)}{C(q)}y_k, \tag{3.15}$$

for combinations of $C(q)$ and $D(q)$, with polynomials of order $n_c = 0:3$ and $n_d = 1:3$. The validation data was passed through the identified model $G_d(q)$, to assess the utility of the model on unseen data. Note that while evaluation (training) data is used to determine the individual model parameters (θ), for model order determination, each candidate model was passed through a separate *validation* data set in order to assess the generalisation capability of each model structure, to avoid overfitting. A similar loss function analysis was used to identify n_c and n_d as 0 and 1, respectively, resulting in the final parameterised (discrete) time-domain model:

$$G_{BJ}(q) = \frac{-0.003879q^{-1} + 0.006462q^{-2} - 0.002618q^{-3}}{1 - 2.924q^{-1} + 2.856q^{-2} - 0.931q^{-3}}, \tag{3.16}$$

$$H_{BJ}(q) = \frac{1}{1 - 0.9992q^{-1}}, \tag{3.17}$$

with the BJ subscript denoting the Box-Jenkins form of the model.

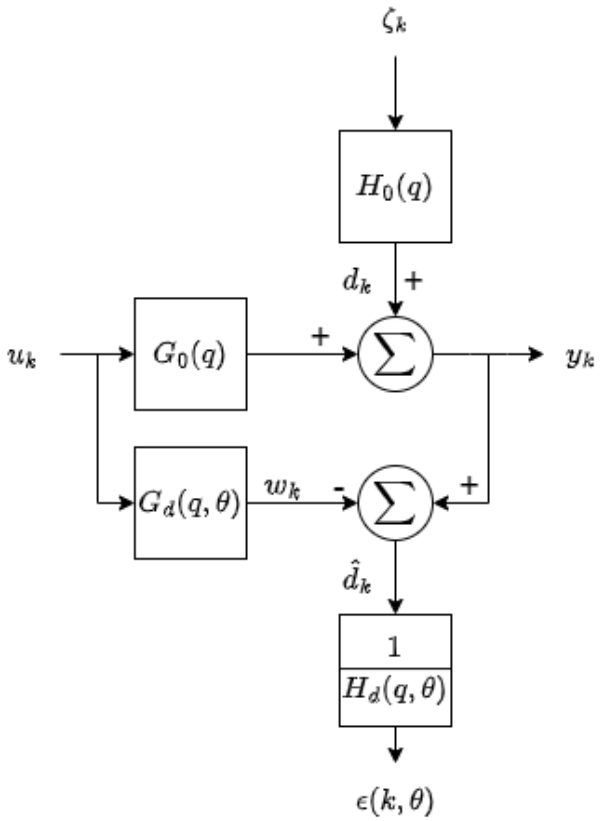

Figure 3.9: Block diagram, showing the evaluation of the model residual $e(k,\theta)$. Note that G_0 and H_0 are the true system and noise models, respectively.

3.4.2.3 Residual analysis

With the assumption that the model of (3.6) is driven by a white noise sequence ζ_k, a test for whiteness of the model residual can now be performed, as an indicator of model fidelity, as shown in Figure 3.9. The estimated ζ_k signal, ϵ_k, is obtained using:

$$\epsilon_k = \frac{1}{H_{BJ}(q,\theta)}(y_k - w_k), \tag{3.18}$$

where

$$w_k = G_{BJ}(q,\theta)u_k \tag{3.19}$$

The degree to which ϵ_k is uncoloured (white), can be revealed by examination of the autocorrelation function (ACF) of $\epsilon(t)$, shown in Figure 3.10. Since the ACF remains within bounds determined by white noise signals of similar length, the identified model is considered a good estimate of the true system.

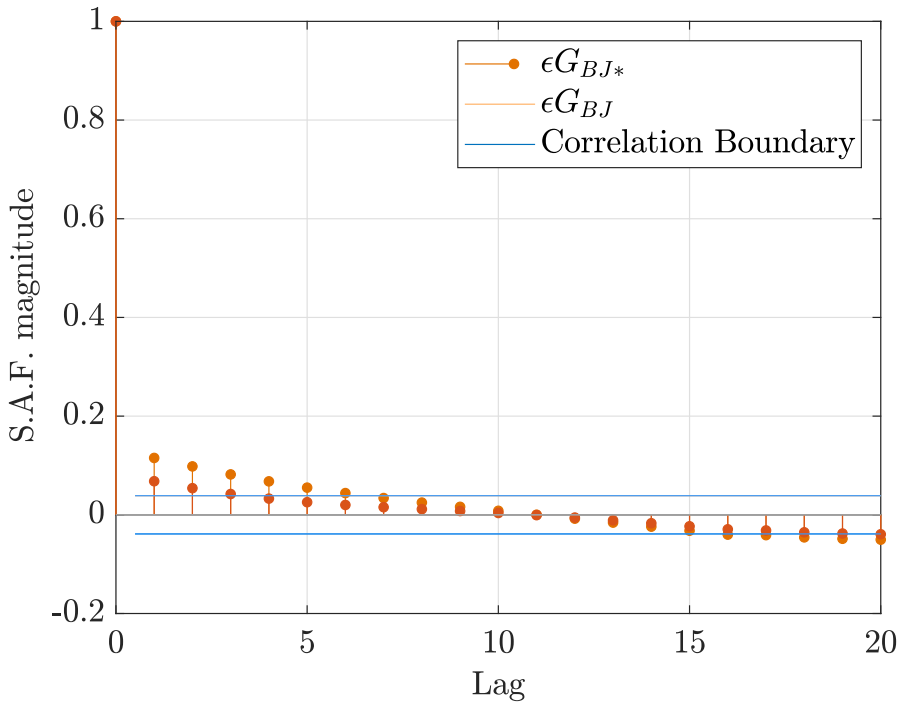

Figure 3.10: White noise test: (—) the autocorrelation function (ACF) of $\epsilon(t)$ for G_{BJ}, (—) the autocorrelation function (ACF) of $\epsilon(t)$ for $2(G_{BJ})$, (—) the maximum correlation for a white noise signal of ϵ's length

3.5 Model validation

A simple cross-validation test is now performed on the time-domain ($G_{BJ}(q)$) and frequency-domain (G_{MF}) models to examine their validity in the frequency and time domains, respectively.

3.5.1 Frequency domain validation

Figure 3.12 shows the measured (from (3.1)) frequency response, and the frequency response of G_{MF} and G_{BJ}. It is seen that G_{MF} provides a relatively good fit for the magnitude plot, while G_{MF} predicts a phase response that is slightly lower than the measured frequency response. Note that the slope of the model response does not level out around 0.5Hz in line with the frequency response associated with the data, but this is a compromise, given a comparatively good fit to the magnitude data. G_{BJ} follows the general shape of the magnitude plot but with a gain offset of -6 dB. However, G_{BJ} aligns better with the phase response than G_{MF}. If a better frequency-domain fit for $G_{BJ}(q)$ is desired, a gain factor of 2 (corresponding to 6dB) can be incorporated into the model via $B^*(q) = 2B(q)$, improving the magnitude fit of $G^*_{BJ}(q)$ (incorporating

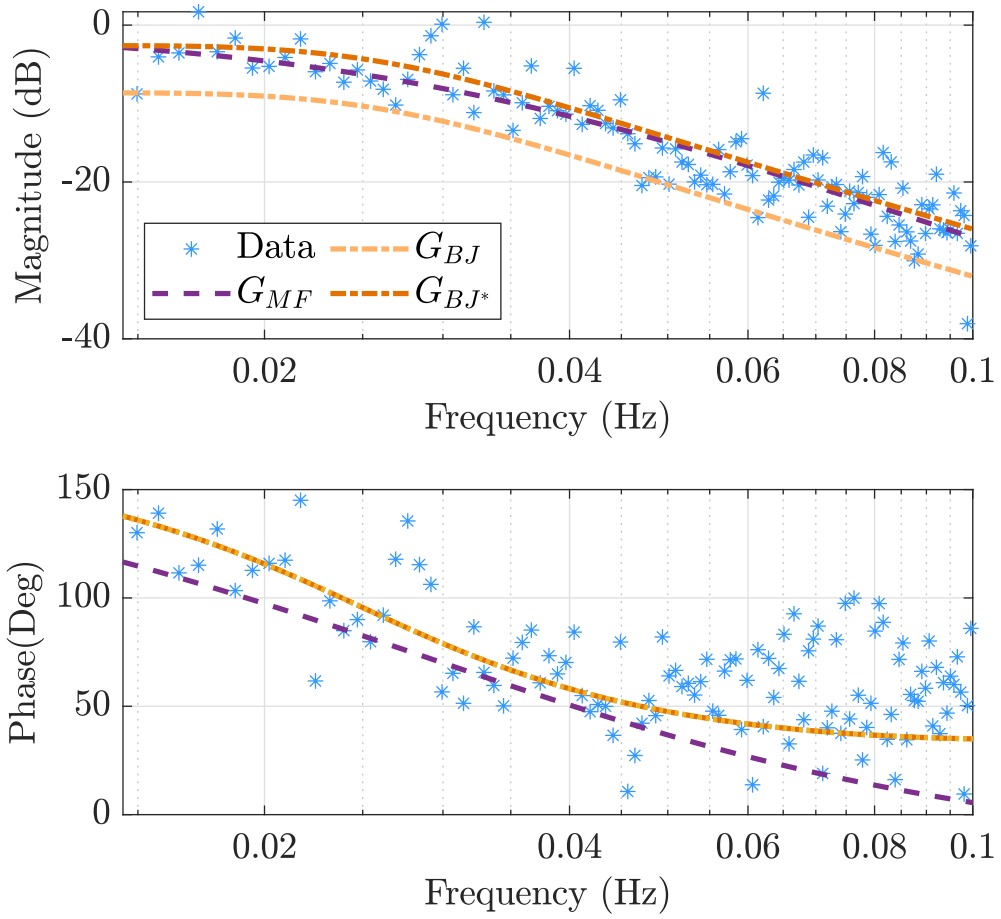

Figure 3.11: Frequency domain validation of G_{MF} annd G_{BJ} against the measured signals. Measured frequency response (*), G_{MF} (·····), G_{BJ} (-·-·-),2(G_{BJ}) (-·-·-)

$B^*(q)$) with the frequency-domain data, as shown in Figure 3.12. However, note that $G^*_{BJ}(q)$ is still valid, in terms of residual analysis, as confirmed by Figure 3.9.

3.5.2 Time domain validation

While, $G_{MF}(s)$ provides a relatively good fit to the frequency-domain data, this is not the case in the time domain. This is perhaps unsurprising, since $G_{MF}(s)$ was determined with a frequency-domain performance objective. Figure 3.11 shows that, while $G_{MF}(q)$ (derived from $G_{MF}(z)$ in (3.5)) is capable of replicating the high frequency components of the time domain signals, it fails to recreate the low frequency components. $G_{BJ}(q)$ provides a significantly better fit for the time domain data, unlike the refined $G^*_{BJ}(q)$.

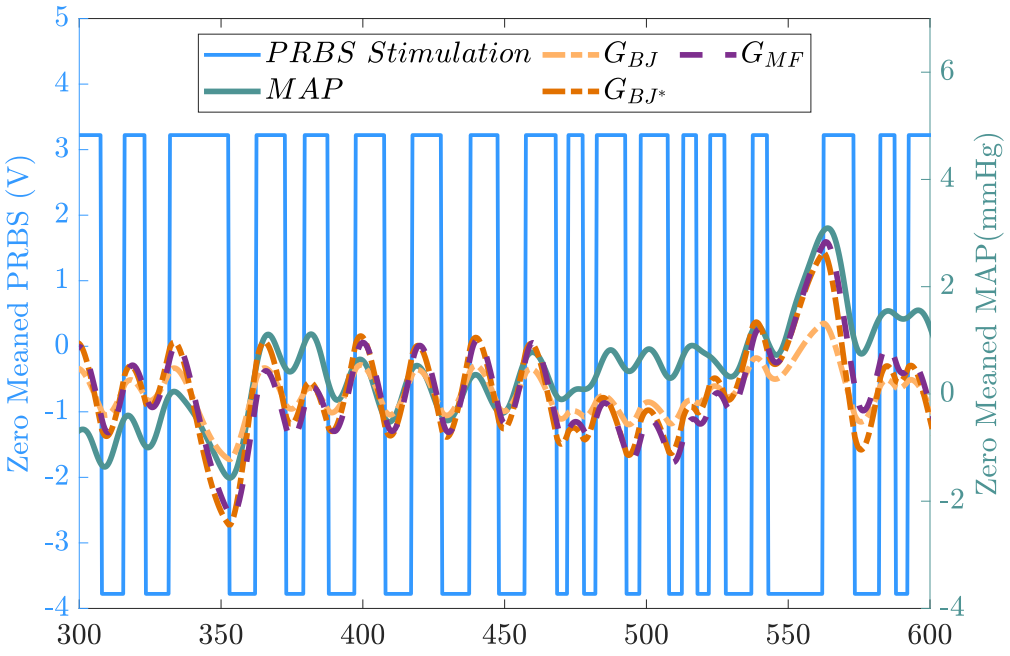

Figure 3.12: B) Time domain validation of G_{MF} annd G_{BJ} against the measured signals. PRBS stimulation signal (—), MAP (—), G_{MF} (····), G_{BJ} (- - -),$2(G_{BJ})$ (-·-·)

3.6 Conclusion

This chapter outlines the development of a protocol to estimate the dynamics of the neural baroreflex in sheep. A refined PRBS baroreceptor excitation was used, with procedures for the determination of both time- and frequency-domain models described. In particular, the time-domain methods are rooted in techniques established within the control-systems community, with methods selected based on the nature of the data obtained in closed loop.

From the results presented, it is clear that neither time- nor frequency-domain approaches applied individually can provide models with high fidelity in both domains, though some model tuning can subsequently be carried out to improve fidelity in one, or other, domains (example shown where the steady-state gain of $G_{BJ}(q)$ was adjusted via $B^*(q)$). Ultimately, the choice of model, determined using time- or frequency-domain techniques, along with appropriate tuning, will depend on the specific application need. In general, frequency domain approaches are typically utilised when the aim of the investigation is to identify the overall characteristics, as it provides a clear, complete picture of the systems dynamics, as is the aim for this study. However, time-domain models provide a far better fit for specific stimulation studies, as they

allow for investigation into the systems response in specific situations.

The study of baroreflex characteristics is crucial in understanding both long-term and short-term BP control. The inability to acquire open loop readings of the neural baroreflex in humans calls for the need to estimate open loop dynamics from closed loop readings. The protocol proposed is one stepping stone on the path to obtaining and understanding the neural baroreflex characteristics. This study is limited to the extent that, while the protocol is proven, the models developed cannot be considered to be representative of a statistical sample of animals and a more comprehensive study, but using the developed protocol, is the subject of future research.

The main contribution of this work is the development of a protocol to identify both time- and frequency- domain models of the neural baroreflex with the baroreceptors intact (ie. using closed loop experimental data). In the present study, BP is recorded, while an excitation signal (PRBS) is applied directly to non-denervated baroreceptors in a sheep. The choice of a PRBS signal was driven by its ability to sufficiently stimulate nerve signals, while also applying signals containing frequency components across the frequency range of interest, without over exerting the subject. The relationship between the carotid sinus baroreceptors and mean arterial pressure is examined. The study does not purport to offer a statistical treatment over a set of animals, but rather to establish a viable protocol for measurement of open-loop baroreflex characteristics from CS stimulation.

4

Investigating the accuracy of sequence methods as a reliable non-invasive baroreflex sensitivity estimation method

Contents

4.1 Introduction 52
4.2 Analytic overview of sequence methods 53
4.2.1 Sequences within a system identification framework . . . 53
4.2.2 Generic analysis of sequence methods 54
4.3 Numerical example 57
4.3.1 Problem setup 58
4.3.2 Sequence selection 61
4.3.3 Gain estimation methods 63
4.4 Experimental analysis 63
4.4.1 EuroBaVar data set 63
4.4.2 BRS estimation methods employed 64
4.5 Results 66
4.5.1 Numerical example results 66
4.5.2 EuroBaVar data set results 67
4.6 Discussion 67
4.6.1 Numerical example 67
4.6.2 Experimental example 70
4.6.3 Observations 71
4.7 Conclusion 71

4.1 Introduction

Chapter 3 details a potential protocol to identify characteristics of the neural baroreflex, which can aid in understanding the functionality of the baroreflex. However, understanding the baroreflex only gets us so far. Once we understand how the baroreflex works, its important to assess it and identify metrics that indicate when its dysregulated. One metric being BRS, this chapter examines a popular non-invasive BRS estimate and aims to determine its validity as a BRS method.
Assessing and monitoring the functionality of the baroreflex has been shown to provide valuable insights into the management of patients with cardiac diseases [94, 95]. The current gold standard for baroreflex sensitivity estimation, the Oxford method [169], as explained in Section 2.5.1 is incapable of being carried out in a routine clinical setting, resulting in the need for a non-invasive alternative. As outlined in Section 2.5.2, a number of non-invasive alternatives have been proposed, and have the capability to distinguish between impaired and non impaired subjects. While there is not currently a gold standard for non-invasive BRS estimation, sequence methods are rapidly emerging as a popular method. Results obtained from recent non-invasive BRS methods are being compared to those obtained using the sequence methods [83, 23, 132], identifying the sequence methods as the *de facto* gold standard for non-invasive BRS estimation. As sequence methods become more prevalent, their reliability as accurate BRS estimators is called into question.

In 2019, *Silvia et al* [165] investigated the BRS estimates obtained using sequence methods applied to the complete BP and R-R interval series, in comparison to those obtained from a low-pass (LP) and high-pass (HP) filtered series. The results show correlation between estimates obtained from the original series and the HP series, with little to no association with the LP estimates. This suggests that sequence methods only quantify short term fluctuations in the baroreflex, failing to accurately capture long term effects. In 2020, *Wessel et al* [188] concluded that the sequence selection criteria are incapable of distinguishing between the random and baroreflex controlled sequences, their results suggesting that sequence methods have "a potentially large methodological bias as an estimate for the baroreflex sensitivity". In 2020, *Chen et al* [23] calculated BRS in rats using the traditional, invasive, Oxford method, and compared them to estimates obtained using sequence methods (applied to spontaneous readings). Their results show a positive bias in the mean gain estimates, and a high standard deviation, for the BRS estimates obtained using sequence methods, compared to those obtained using the Oxford method.

In the absence of a definitive BRS range for impaired and non impaired subjects, the family of sequence methods can only be validated from a theoretical standpoint. While several studies, note a positive bias in BRS estimates obtained using the sequence methods, this study provides a critical examination of the theoretical foundation behind the use of sequence methods for baroreflex sensitivity estimation. The work presented in this chapter is motivated by not only the need to find an effective non invasive BRS estimation method, but to also ensure the validity of the possible methods in the absence of a definitive range of BRS values obtained from non invasive recordings. The aim of this study is to investigate the source of the positive bias apparent in BRS estimates, and determine whether the refinements to the sequence selection criteria are sufficient to overcome the bias.

This chapter is organised as follows: Section 4.2 analyses the effect sequencing data has on gain estimation; Section 4.3 details the development of a controlled numerical example where sequence methods can be tested on a system with a known gain; Section 4.4 demonstrates the prevalence of positive gain bias in BRS estimates using sequence methods, in comparison to methods from the control systems sciences; Section 4.5 presents the results of the study; Section 4.6 discusses the results of the study, and Section 4.7 draws conclusions on the study.

4.2 Analytic overview of sequence methods

The recent increase in popularity of sequence methods calls for a rigorous analysis of the sequence methods to verify their validity as a reliable identification method. In this section, the effects sequencing data has on any associated noise contamination and, in turn, its effects on gain estimation, are considered.

4.2.1 Sequences within a system identification framework

Spontaneous BP and ECG readings, such as the EuroBaVar dataset [99], are continuous BP and ECG readings taken from individuals without any external interventions/stimulus imposed for the purpose of the recordings, i.e. the closed-loop baroreflex is intact. Spontaneous recordings are used to obtain non-invasive BRS estimates. When dealing with closed-loop data, a number of fundamental properties must be considered when modelling the system's behaviour.

Identification methods, used to elicit open-loop dynamics from closed loop data, can be divided into three categories[103]: (a) direct methods, where the measured

input-output signals are used and the feedback loop is ignored, (b) indirect methods, where some information about the feedback is available and an effective open-loop input signal can be formed, and (c) joint input-output methods, where both input and output signals are treated as outputs driven by noise and the feedback system. Spontaneous BP and ECG readings do not provide any information about the feedback loop or noise present in the system, meaning that direct methods are appropriate when dealing with the development of BRS estimation methods from spontaneous BP and ECG readings. However,it should be noted that direct methods, applied as if the feedback does not exist, only work well if the true system can be described within the chosen model structure (both the dynamic model and the noise model). In time-domain identification, given that sampled data is used, a discrete time system representation is used, via a general time-domain model structure of:

$$y(t) = G(q)u(t) + H(q)e(t) \tag{4.1}$$

where $y(t)$ is the output signal (RR-interval), $u(t)$ is the input signal (BP), and $e(t)$ is an unknown white noise sequence, with a mean value of zero and assumed to be uncorrelated with past or future values of $u(t)$. t is the discrete-time index. $G(q)$ is the open-loop system of interest, with $H(q)$ representing the noise model.

With this approach, if an inadequate noise model ($H(q)$) is used, deviations from the true noise characteristics will introduce bias in the estimate of system $G(q)$. Sequence methods consider $G(q) = k$, where k is a positive rational number, and $H(q) = 0$. Since sequence methods, in essence, consider the system to be a simple gain and do not account for any dynamics, in either the main system or the noise model, a bias in the BRS estimate is highly likely.

4.2.2 Generic analysis of sequence methods

The interconnected nature of the human body means that no one mechanism operates in isolation. Even under resting conditions, a number of subsystems work in unison to maintain homeostasis. In the case of BRS estimation, we are solely interested in the interactions between changes in BP and changes in R-R interval, all other effectors of R-R interval are considered noise. Unlike during the Oxford method, where it can be assumed that there is no other mechanism that alters R-R interval, non-invasive BP recordings are taken passively from patients, meaning that the output signals analysed contain an unmeasurable amount of noise, like the effect of respiration and the sinus node on R-R interval. In this section, we explore the effect sequencing data with noise

has on the sequences identified.

Suppose that the input signal (such as BP) for a system (such as the baroreflex) is described by a ramp (representing a continuous increase in BP) of the form:

$$u(t) = p\ t \tag{4.2}$$

where t is the discrete-time index and p can take on the values $+1, -1$. This input is passed through the system described by a simple gain (such as BRS gain), with the output corrupted by measurement noise $e(t) = [-n, n]$, as:

$$y(t) = s\ k\ u(t) + e(t) \tag{4.3}$$

where $k < n$. We assume that the gain, k, is +ve, though s can take on the values $+1, -1$. In the case of baroreflex sensitivity, s is always $+1$ (i.e. a +ve change in blood pressure causes a +ve change in R-R interval), but we will retain the flexibility in order to determine general conclusions. Now, a sequence is selected where the output is going in a consistent direction, in a similar manner to 'Seq 1' shown in Fig. 2.5,

$$Y(r, i) = [y(r - i)\ y(r - i + 1)\ \ldots\ y(r - 1)\ y(r)] \tag{4.4}$$

and we assume that the next point, $y(r + 1)$, is inflected, compared to the points in $Y(r, i)$. Four cases, corresponding to all possible combinations of p and s will now be considered.

Case 1: $p = +1\ ,\ s = +1$ The input to the system is a +ve going ramp:

$$u(t) = t. \tag{4.5}$$

The system is described by:

$$y(t) = k\ u(t)\ +\ e(t). \tag{4.6}$$

For an inflection:

$$y(r + 1) + e(r + 1) < y(r) + e(r), \tag{4.7}$$

but

$$y(r + 1) = y(r) + k, \tag{4.8}$$

giving, from (4.7), that

$$e(r + 1) < e(r) - k. \tag{4.9}$$

and $e(r)$ is positively biased with respect to $e(r + 1)$, with the result that the estimate for k from the sequence $Y(r, i)$ is positively biased.

Case 2: $p = +1\ ,\ s = -1$ The input to the system is a +ve going ramp:

$$u(t) = t. \tag{4.10}$$

The system is described by:

$$y(t) = -k\ u(t)\ +\ e(t). \tag{4.11}$$

For an inflection:

$$y(r+1) + e(r+1) > y(r) + e(r), \tag{4.12}$$

But

$$y(r+1) = y(r) - k, \tag{4.13}$$

giving, from (4.12), that

$$e(r+1) > e(r) + k. \tag{4.14}$$

and $e(r)$ is negatively biased with respect to $e(r+1)$, with the result that the estimate for k from the sequence $Y(r,i)$ is negatively biased.

Case 3: $p = -1\ ,\ s = +1$ The input to the system is a -ve going ramp:

$$u(t) = -t. \tag{4.15}$$

The system is described by:

$$y(t) = k\ u(t)\ +\ e(t), \tag{4.16}$$

For an inflection:

$$y(r+1) + e(r+1) > y(r) + e(r), \tag{4.17}$$

But

$$y(r+1) = y(r) - k, \tag{4.18}$$

giving, from (4.17), that

$$e(r+1) > e(r) + k. \tag{4.19}$$

and $e(r)$ is negatively biased with respect to $e(r+1)$, with the result that the estimate for k from the sequence $Y(r,i)$ is negatively biased.

Case 4: $p = -1\ ,\ s = -1$ The input to the system is a -ve going ramp:

$$u(t) = -t. \tag{4.20}$$

The system is described by:

$$y(t) = -k\ u(t)\ +\ e(t). \tag{4.21}$$

For an inflection:

$$y(r+1) + e(r+1) < y(r) + e(r), \tag{4.22}$$

But

$$y(r+1) = y(r) + k, \tag{4.23}$$

giving, from (4.7), that

$$e(r+1) < e(r) - k. \tag{4.24}$$

and $e(r)$ is positively biased with respect to $e(r+1)$, with the result that the estimate for k from the sequence $Y(r,i)$ is positively biased.

4.3 Numerical example

Section 4.2.2 provides a generic analysis on sequencing data with a noise component, highlighting the bias introduced into gain estimates from said sequences. In this section, we introduce a controlled numerical example, where we investigate these points to build on the above analysis. In the context of BRS estimation, the system is the baroreflex, a system interconnected with a number of other subsystems operating continually. Due to the unmeasurable nature of the noise components, such as respiration and the influence of the sinus node, and the lack of definitive BRS estimates associated with a healthy and impaired baroreflex, we introduce an ideal system. The ideal system is used to investigate, numerically, the effect of the sequence methods under known, controlled, conditions. Specifically, Cases 1 and 3, detailed in Section 4.2.2, where the system is a simple positive gain, with additive noise, with both positive- and negative-going input sequences, depicted in Fig. 4.1, are examined within a numerical framework.

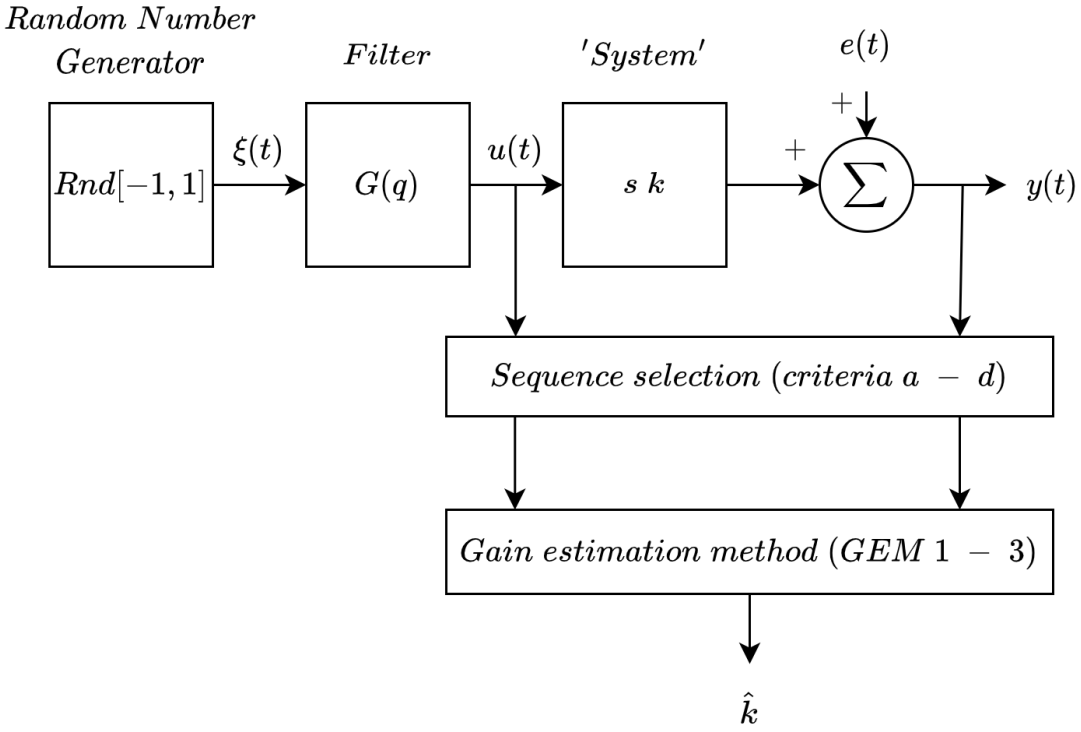

Figure 4.1: Numerical experiment set up. The input signal $u(t)$ is formed by passing a sequence of random numbers through a low pass filter. The system is described by a simplain gain, in this case $k = 2$. The output $y(t)$ is formed by the output of the filter and additive white noise $e(t)$. Sequence selection is determined by the valid sequence criteria (outlined in Table 4.2). Using the sequences, the system's gain is estimated using a gain estimation method (outlined in section 4.3.3)

4.3.1 Problem setup

Input signal: The input signal, a surrogate for BP, is generated using a zero mean, random number generator, which is passed through a discrete time 7^{th} order Butterworth filter with transfer function:

$$F(q) = \frac{b_o + b_1 q + ... + b_n q^n}{1 + a_1 q + ... + a_n q^n} \tag{4.25}$$

where n is the order of the model, q is the backward shift operator, and the a_i and b_i are chosen to achieve unity dc gain. The signal was filtered both forward and backwards, giving zero phase distortion, and an effective filter order of 14. Note that there is a strong relationship between Ω_c, the normalised filter cut-off frequency, and the maximum sequence length L_{max} that can be achieved in $u(t)$, given by the approximate relation:

$$L_{max} \approx 3.26 + 7e^{-8\Omega_c} \tag{4.26}$$

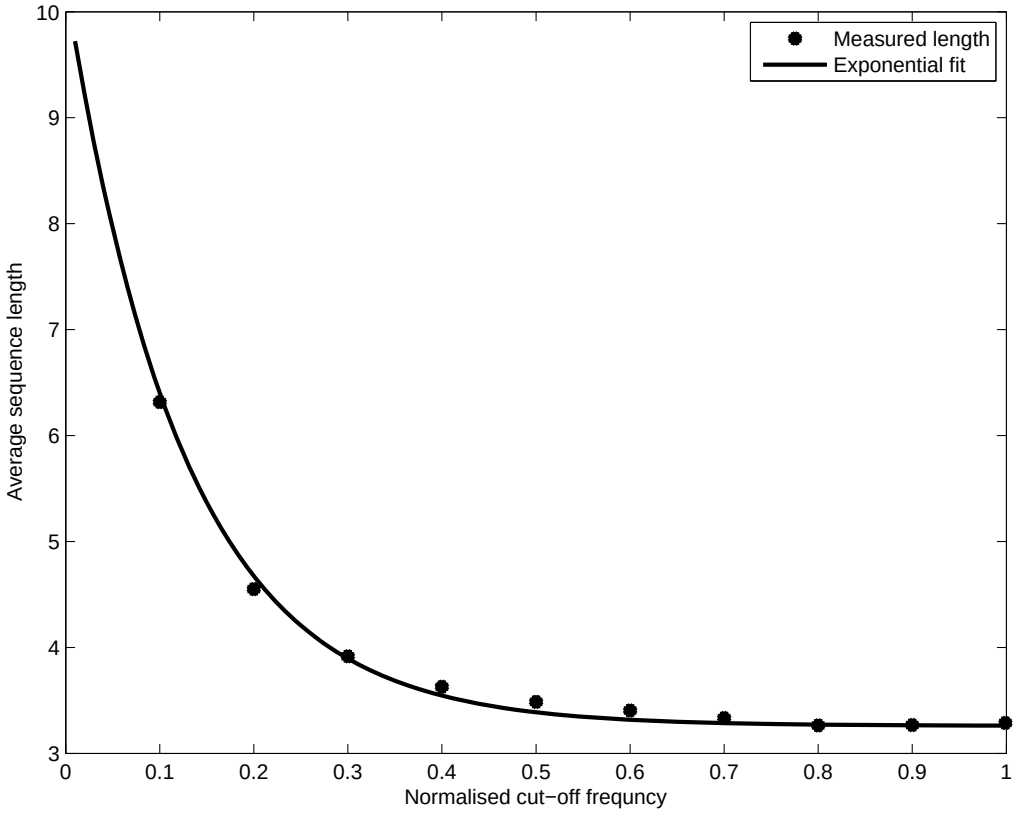

Figure 4.2: Parametrisation of the relationship between average sequence length and cut-off frequency

The fit of the exponential approximation in equation (4.26) is shown in Fig.4.2. However, the maximum sequence length, determined by the simultaneous minimum in both $u(t)$ and $y(t)$, is also dependent on the signal-to-noise ratio (SNR) in $y(t)$, which is determined by the amplitude, m, of the measurement noise, $e(t)$. The relationship between Ω_c and the maximum sequence length that can be achieved in $u(t)$, and SNR and the maximum sequence length that can be achieved in $y(t)$, is illustrated in Figure 4.3. The average sequence length for various combinations of Ω_c and SNR are shown in Table 4.1.

System: The system, a surrogate for baroreflex sensitivity, is a simple gain of 2, with additive zero mean white noise. The noise signal is a surrogate for unquantified factors that influence the R-R interval.

Output signal: The output of the simulated system, a surrogate for R-R interval, is:

$$y(t) = 2u(t) + e(t) \tag{4.27}$$

where $u(t)$ is the input, $e(t)$ is zero mean white noise, and $y(t)$ is the output.

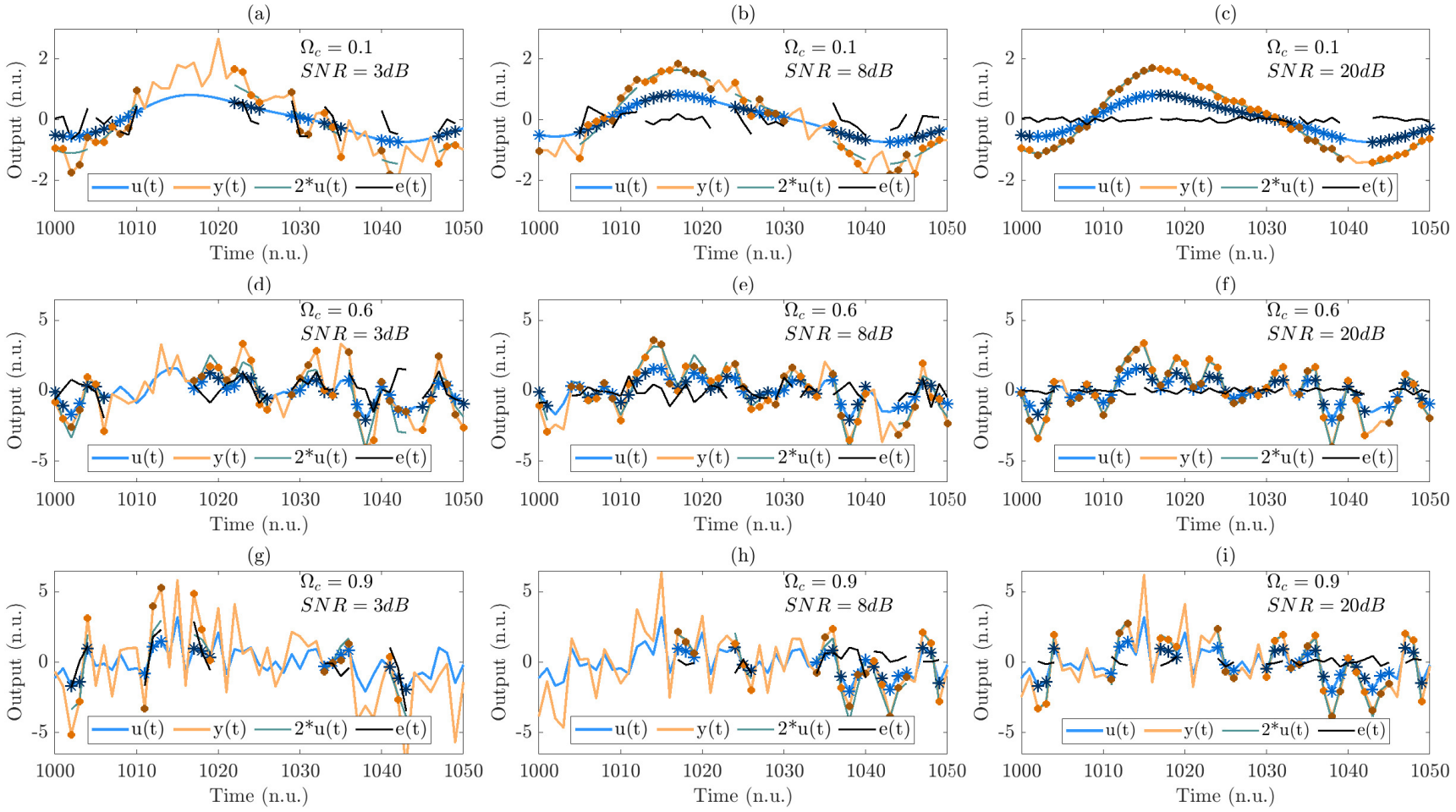

Figure 4.3: Examining the effect of Ω_C and SNR, on the maximum sequence length achieved in $u(t)$ and $y(t)$. — denotes the input signal $u(t)$ with * and * marking alternate valid sequences, — denoted the output of the system before the noise signal is added ($2^*u(t)$), — denoted the noise signal $e(t)$ and — denotes the output signal $y(t)$ with * and * marking alternate valid sequences

Table 4.1: The average sequence length for various combinations of Ω_c and SNR.

Ω_c \ SNR	3dB	8dB	20dB
0.1	3.538	3.759	6.049
0.2	3.734	4.195	6.321
0.3	3.739	4.164	5.166
0.4	3.641	3.849	4.280
0.5	3.534	3.496	3.722
0.6	3.360	3.351	3.439
0.7	3.262	3.262	3.304
0.8	3.211	3.232	3.286
0.9	3.219	3.236	3.278
0.99	3.233	3.250	3.306

Table 4.2: Sequence selection criteria used for the numerical example

Criteria	Sequence length	r	Input threshold	Output threshold
a	3+	0	No	No
b	3+	0.85	No	No
c	3+	0.7	Yes	Yes
d	4+	0	Yes	Yes

4.3.2 Sequence selection

After generating both $u(t)$ and $y(t)$, valid sequences are extracted. In the literature, a number of variations on the criteria for a valid sequence are presented, as detailed in Section 2.5.3. This study considers four sets of selection criteria, as documented in Table 4.2.

The input and output thresholds used for criteria c and d in Table 4.2 are calculated using:

$$Input\ threshold = \frac{BP\ threshold}{\sigma^2_{BP}} \times \sigma^2_u, \tag{4.28}$$

where σ^2_{BP} denotes the variance in BP, σ^2_u denoted the variance on the input signal, and

$$Output\ threshold = \frac{RR\ threshold}{\sigma^2_{RR}} \times \sigma^2_y, \tag{4.29}$$

where σ^2_{RR} denotes the variance in RR-interval, and σ^2_y denotes the variance on the output signal. The relationship between σ^2_u and f_c is characterised as:

$$\sigma^2_u = f_c \sigma^2_{rnd} \tag{4.30}$$

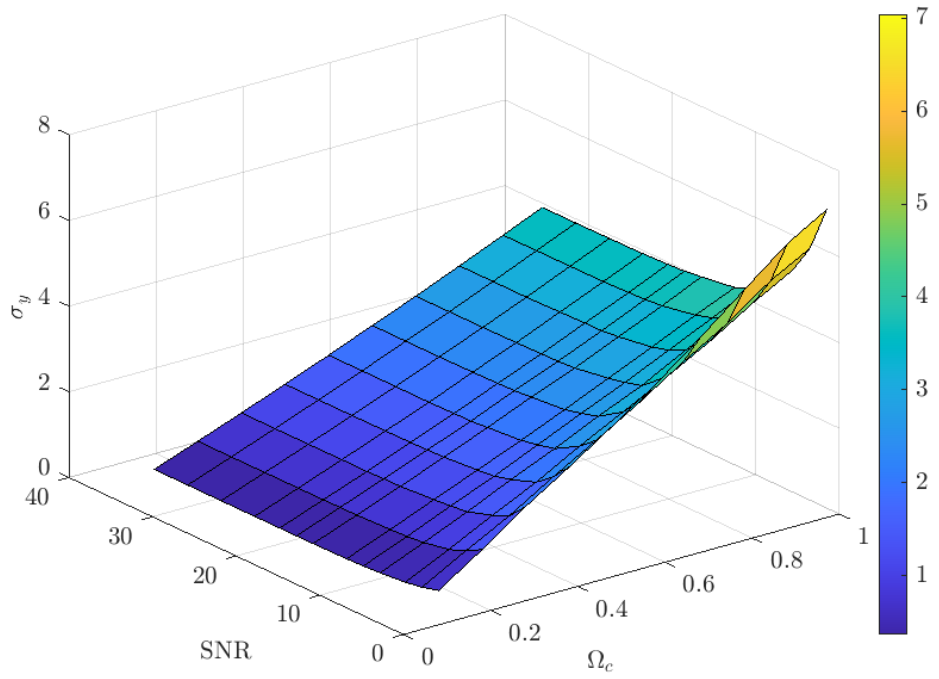

Figure 4.4: The variance(σ_y^2) for various Ω_c and SNR.

where σ_{rnd}^2 is the variance on the signal generated by the random number generator. The relationship between σ_y^2, f_c, and SNR is illustrated in Figure 4.4 and characterised as:

$$\sigma_y^2 = k_1 f_c e^{-k_2 SNR} + k_3 f_c \tag{4.31}$$

The input and output variances change with Ω_c and SNR, in turn varying the input and output thresholds in each case. σ_x^2 decreases as Ω_c decreases, while σ_y^2 decreases as Ω_c decreases and increases as SNR decreases, as illustrated in Figure 4.4.

These four criteria were chosen to examine the effects of sequence selection refinements and to what extent, if any, they improve the accuracy of the gain estimates, in comparison to the original sequence method [33]. Criteria set (a) represents the original sequence method [33]; criteria set (b), a sequence method with an additional threshold on r; criteria set (c), a method with both r and minimum signal thresholds; and, criteria set (d), a method with a longer minimum sequence length and minimum signal thresholds. It should also be noted that while, in the literature, some methods account for a delay between the input and output, a lag is not considered in the current numerical case, as there is no delay in the system generating $y(t)$ from $u(t)$.

4.3.3 Gain estimation methods

To examine the accuracy of sequence methods GEM 2 and GEM 3 as baroreflex gain estimation methods, their performance is compared to a non-sequence-based gain estimation method GEM 1. GEM 1 through 3 are defined as follows :

Gain estimation method 1 (GEM 1): Linear regression applied to the complete data set, where the gain is the regression coefficient [118].

Gain estimation method 2 (GEM 2): Linear regression applied to all data points identified as valid sequences, where the gain is the regression coefficient [52].

Gain estimation method 3 (GEM 3): Linear regression applied to individual (valid) sequences, where the gain is the average of all the individual regression coefficients [34].

Methods 2 and 3 are applied four times, using the four sequence selection criteria detailed in Table 4.2. Fig. 4.5 provides an illustration of the three gain estimation methods in action, highlighting the differences in their use of the data, and showing that GEM 2 results in a smaller number of data points compared to GEM 1, with multiple (individual) regression lines for GEM 3.

4.4 Experimental analysis

The efficacy of sequence methods, as a BRS estimation method, is now examined, via the EuroBaVar experimental data set [99]. BRS estimates, obtained from the spontaneous blood pressure signals, are examined for trends that align with those seen in the numerical example, i.e. positive bias in BRS estimates calculated using the sequence methods, compared to alternative, system identification (SI) based methods.

4.4.1 EuroBaVar data set

The EuroBaVar dataset [99] is an open source dataset consisting of 42 files corresponding to spontaneous, non-invasive BP and HR readings, from 21 subjects in both supine and standing positions for approximately 10 minutes. The data is recorded on a beat by beat basis, using a Finapres® system, for BP, and an ECG system, for RR-interval. Subjects 13 and 18 are considered to have an impaired baroreflex, while a

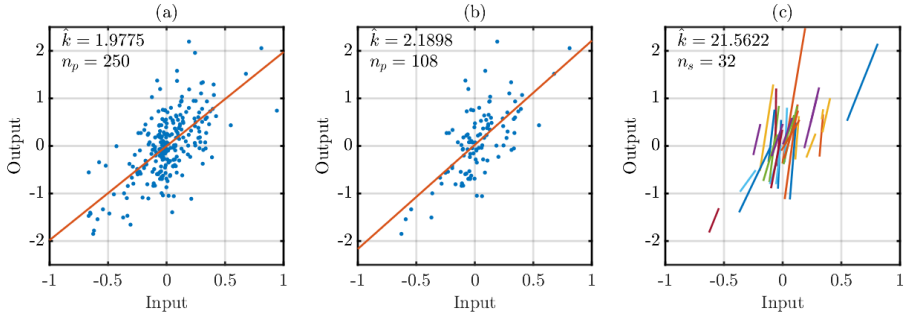

Figure 4.5: Three estimation methods applied to the numerical example: (a) GEM 1: a linear regression fit to the entire data sets, (b) GEM 2: a linear regression fit to selected (sequence) data points, and (c) GEM 3: a linear regression fit to each individual sequence. m represents the overall gain estimate from each method, n_p represents the number of data points considered in (a) and (b), while n_{seq} represents the number of sequences considered in (c). For this illustration, a specific cut-off frequency ($\Omega_c = 0.1$), SNR ($= 0dB$), and a reduced number of data points in $u(t)$ and $y(t)$, are chosen to clearly highlight the differences between the three methods. $\hat{k}$ represents the estimated gain for each GEM method, n_p represents the number of data points used in the analysis for GEM 1 and GEM 2, with n_s representing the number of sequences used in GEM 3.

number of subjects are considered to be at risk of impaired baroreflex due to underlying conditions. Valid, non-invasive, BRS estimation methods must be capable of clearly distinguishing subjects 13 and 18 as impaired, while also (ideally) highlighting the subjects at risk of an impaired baroreflex with a lower BRS estimate than the healthy volunteers.

4.4.2 BRS estimation methods employed

To examine the accuracy of sequence methods for BRS estimation, BRS estimates calculated using 7 estimation methods applied to the EuroBaVar dataset are compared. Methods 1a through 1d, outlined in Table 4.3, represent 4 sequence methods with equivalence to the sequence selection criteria used in the numerical case, outlined in Table 4.2.

Methods 2a through 2c represent BRS estimation methods based on a rigorous SI approach developed by *McLoone et al* [115]. As a definitive BRS range for impaired and non-impaired subjects has not been established, the accuracy of all methods can only be analysed theoretically. The McLoone method was selected for comparison because it was developed using principles from the control sciences. A summary of the data preprocessing and the initial steps, are the same for each of methods 2a $\rightarrow$ 2c, as follows:

- Resample signals $u(t)$ and $y(t)$ at a regular sampling period of $T = 2/3s(1.5Hz)$, approximately the average RR interval across all the patients.
- Pass $u(t)$ and $y(t)$ through Butterworth filters with high pass $\Omega_c = 0.05$ and low pass $\Omega_c = 0.5Hz$ cut-off frequencies. The frequency range used is that specifically associated with the human baroreflex [109].
- An autoregressive moving average (ARMAX) model is fit to the data using a prediction error method:

$$y_k = \underbrace{\frac{B(q)}{A(q)}}_{G_{yu}(q)} u_k + \underbrace{\frac{C(q)}{A(q)}}_{H_{ye}(q)} \zeta_k, \tag{4.32}$$

- A Gaussian-based non-uniform weighting function, $W(f)$, is applied to the frequency response of the identified model ($G_{yu}(f)$), where

$$W(f) = e^{-\frac{(f-f_0)^2}{2\sigma^2}}, \tag{4.33}$$

  with σ a constant, which determines the width of the Gaussian weighting function.
- In general, a representative average value on a continuous frequency variable f, over a range $[f_{min}, f_{max}]$, can be obtained as:

$$BRS(f_{min}, f_{max}) = \frac{1}{N_w} \int_{f_{min}}^{f_{max}} W(f).|G_{yu}(f)|df, \tag{4.34}$$

  where $W(f)$ defines the 'weighting' applied at each frequency over the interval $[f_{min}, f_{max}]$, f_0 is the centre frequency of each band, and N_w is a normalisation factor, where

$$N_w = \int_{f_{min}}^{f_{max}} W(f)df. \tag{4.35}$$

  If G_{yu} is only available at N_f discrete frequency points $f_i = f_{min} + i\,\Delta f \;\;,\;\; i = 0, 1, \ldots, N_f - 1$, where Δf is the frequency interval between points, then equation (4.34) becomes:

$$BRS = 1/N_w \sum_{i=0}^{N_f - 1} W(i).|G_{yu}(i)|, \tag{4.36}$$

  with $N_w = \sum_{i=1}^{N_f} W(i)$.

There are three BRS estimates calculated using methods 2a -2c, all with varying frequency ranges $[f_{min}, f_{max}]$:

Method 2a:

- BRS $_{\text{LF}}$ gain is calculated using equation (4.36) with a frequency range $f_{min} = 0.05$ to $f_{max} = 0.15Hz$

Method 2b:

- BRS $_{HF}$ gain is calculated using equation (4.36) with a frequency range $f_{min} = 0.15$ to $f_{max} = 0.4Hz$

Method 2c:

- BRS gain is the average of the gain estimates obtained from methods 2a and 2b.

Table 4.3: Valid sequence criteria used with the experimental data.

Criteria	Sequence length	r	BP threshold (mmHg)	RR threshold(ms)
a	3+	0	0	0
b	3+	0.85	0	0
c	3+	0.7	4	1
d	4+	0	4	1

4.5 Results

4.5.1 Numerical example results

The analysis carried out in Section 4.2.2 demonstrates the effect of sequencing data sets on the noise properties of the system, demonstrating that the gain obtained from the sequenced data is positively biased, ie. the baroreflex gain is overestimated. The numerical example investigates these findings through a dedicated numerical example, where the notional baroreflex gain is equal to 2. Table 4.4 shows the gain estimates obtained using the gain estimation methods outlined in Section 4.3 (GEM 1, 2 & 3). Over the years, a number of refinements to the sequence selection criteria have been proposed (Section 2.5.3), to improve the fidelity of the sequence methods, and reduce the effect of noise on the gain estimates. To investigate the effects of the refinements on the gain estimates, four different sequence criteria (outlined in table 4.2) were applied to the generated data($u(t)$ and $y(t)$).

Considering the original sequence method (GEM 3 using criteria a in Table 4.3), it is apparent that this sequence method returns higher gain estimates than those obtained using linear regression analysis (GEM 1), with the accuracy of the estimates decreasing as the amount of noise added to the system increases. While GEM 2 does provide

a significantly better estimate compared to GEM 3, using all the data (via GEM 1) proves to be the most resilient to noise.

The effect of the refinements on the gain estimate were investigated through the addition of threshold and correlation coefficients limits to the sequence selection process (criteria (b) and (c)). The refinements do improve the accuracy of the gain estimates, but only marginally. However, the increase in minimum sequence length from 3 to 4 (criteria (d)) provides a significant improvement in the accuracy of GEM 3 across a number of cases, though fidelity still suffers for cases with significant additive noise.

4.5.2 EuroBaVar data set results

Considering the analytical examination (Section 4.2.2), and the increased gain estimates observed when using the sequence methods in the numerical example, the results suggest that consistently higher BRS gains are obtained using the sequence methods examined. From Table 4.5, which contains the BRS estimates obtained using the methods outlined in Section 4.4, the results show that, in the majority of cases, the BRS estimates obtained using sequence methods are consistently higher than those obtained using a SI-based approach that accounts for the closed-loop nature of the baroreflex, with the exceptions highlighted by a yellow cell colour.

Table 4.5 also identifies those subjects deemed to have an impaired baroreflex, i.e. Subjects 13 and 18, highlighted by a green row colour, *and* the patients with underlying conditions at risk of an impaired baroreflex, highlighted by a blue row colour. For these special cases, it should be noted that, not only do the sequence methods overestimate the gain, but there are also a number of cases where a BRS estimate cannot be obtained from the data using sequence methods, the majority of which are subjects deemed to have an impaired baroreflex. This means that sequence methods frequently fail in cases where accurate BRS estimation is vital.

4.6 Discussion

4.6.1 Numerical example

Sequencing data for the purpose of BRS estimation is considered to help reduce the effects of unmeasurable external stimuli on the R-R and BP signals, by choosing 'baroreceptor-like' events, with the objective of increasing the accuracy of the gain estimates obtained [33]. From Table 4.4, in the case of the numerical example where

Table 4.4: Gain estimation using three methods, (i) GEM 1: linear regression applied to entire data set, (ii) GEM 2: linear regression applied to data points selected through the sequence method and (iii) GEM 3: average slope of the regression coefficient of each sequence. The criteria column corresponds to the valid sequence criteria outlined in Table 4.2, Ω_c represents the normalised cut-off frequency of the LPF and SNR represents the SNR of the $e(t)$.It should be noted that the true gain of the system is 2.

Criteria	Linear Regression Analysis							Sequence Methods		
	SNR / Ω_c	GEM 1			GEM 2			GEM 3		
		3dB	8dB	20dB	3dB	8dB	20dB	3dB	8dB	20dB
a	0.1	2.02	2.00	2.00	2.14	2.09	2.03	15.92	10.13	4.72
	0.2	1.98	2.00	2.00	2.15	2.12	2.01	7.25	4.58	2.46
	0.3	1.99	2.00	2.00	2.17	2.10	2.00	4.92	3.36	2.18
	0.4	1.99	2.01	2.00	2.14	2.07	2.00	3.64	2.67	2.08
	0.5	2.01	2.00	2.00	2.13	2.04	2.00	2.99	2.41	2.04
	0.6	2.02	1.99	2.00	2.10	2.03	2.00	2.69	2.28	2.03
	0.7	2.00	1.99	2.00	2.07	2.02	2.00	2.42	2.17	2.01
	0.8	1.99	2.00	2.00	2.10	2.05	2.00	2.39	2.15	2.02
	0.9	2.00	2.00	2.00	2.10	2.04	2.01	2.32	2.12	2.01
	0.99	2.01	2.00	2.00	2.07	2.03	2.01	2.32	2.10	2.02
b	0.1				2.14	2.09	2.03	15.54	10.15	4.74
	0.2				2.15	2.12	2.01	6.85	4.55	2.45
	0.3				2.17	2.10	2.00	4.69	3.36	2.17
	0.4				2.14	2.07	2.00	3.54	2.68	2.08
	0.5				2.13	2.04	2.00	2.91	2.43	2.05
	0.6				2.10	2.03	2.00	2.66	2.29	2.03
	0.7				2.07	2.02	2.00	2.41	2.19	2.01
	0.8				2.10	2.05	2.00	2.39	2.17	2.02
	0.9				2.10	2.04	2.01	2.30	2.14	2.01
	0.99				2.07	2.03	2.01	2.30	2.11	2.02
c	0.1				2.15	2.10	2.03	14.59	8.72	4.29
	0.2				2.15	2.12	2.01	6.77	4.44	2.41
	0.3				2.18	2.10	2.00	4.51	3.18	2.11
	0.4				2.14	2.07	2.00	3.56	2.64	2.07
	0.5				2.13	2.04	2.00	2.92	2.40	2.04
	0.6				2.10	2.03	2.01	2.58	2.26	2.02
	0.7				2.08	2.02	2.00	2.41	2.17	2.01
	0.8				2.10	2.04	2.00	2.34	2.15	2.02
	0.9				2.10	2.04	2.01	2.31	2.12	2.01
	0.99				2.07	2.03	2.01	2.30	2.10	2.02
d	0.1				2.25	2.16	2.04	8.54	5.76	2.70
	0.2				2.18	2.15	2.01	4.09	3.14	2.13
	0.3				2.15	2.11	2.01	2.78	2.48	2.05
	0.4				2.09	2.06	2.01	2.40	2.20	2.03
	0.5				2.07	2.05	2.01	2.19	2.10	2.01
	0.6				2.07	2.05	2.02	2.13	2.07	2.02
	0.7				2.05	2.03	2.01	2.07	2.05	2.01
	0.8				2.04	2.04	2.01	2.05	2.04	2.02
	0.9				2.05	2.04	2.01	2.06	2.04	2.02
	0.99				2.04	2.04	2.01	2.07	2.04	2.02

Table 4.5: BRS estimates from 6 sequence methods applied to the 21 participants of the EuroBaVar study[99]. (1a)Sequence method: 3, or more, consecutive paralleled increases/decreases in both BP and RR, a minimum r of 0.7, a minimum BP threshold of 1mmHg and a minimum R-R interval threshold of 4ms, (1b)Sequence method: 3, or more, consecutive paralleled increases/decreases in both BP and R-R and a minimum r of 0.7, (1c)Sequence method: 4, or more, consecutive paralleled increases/decreases in both BP and RR, a minimum BP threshold of 1mmHg and a minimum R-R threshold of 5ms, (2a) LF estimation from McLoone's method, (2b) HF estimation from McLoone's method, and (2c) average of the LF and HF estimations from McLoone's method. The green highlighted rows indicate the two patients with impaired baroreflexes, with the blue highlighted rows indicate patients with underlying conditions that may have a lowered BRS estiamtion than the healthy volunteers. The yellow highlighted cells indicate the cases where sequence method estimates were not higher than SI based estimates. NaN indicates an inability to obtain a BRS estimate.

Data set:	Supine							Standing						
Method / Subject	Sequence Method				McLoone Method			Sequence Method				McLoone Method		
	1a	1b	1c	1d	2a	2b	2c	1a	1b	1c	1d	2a	2b	2c
1	9.74	9.85	6.26	8.35	2.36	4.72	3.54	5.65	5.52	4.71	6.58	1.98	2.25	2.12
2	12.78	14.44	4.96	5.46	1.62	4.82	3.22	4.57	4.76	4.08	6.75	3.84	1.85	2.85
3	8.64	11.16	10.77	NaN	3.16	5.71	4.44	6.66	5.89	2.82	4.09	2.28	2.10	2.19
4	18.85	19.61	14.35	15.72	10.00	11.66	10.83	3.71	3.69	3.63	5.73	5.59	2.90	4.25
5	5.51	5.49	4.4	6.6	3.10	1.92	2.51	1.65	1.66	1.68	2.85	1.06	0.66	0.86
6	22.52	22.45	17.05	22.05	7.51	11.08	9.30	4.75	4.76	4.55	6.17	3.77	2.66	3.21
7	21.86	25.4	14.06	11.51	4.98	11.98	8.48	16.13	19.03	6.42	8.62	2.89	4.50	3.69
8	49.84	64.57	17.23	30.63	4.02	16.36	10.19	24.72	26.59	12.77	13.25	7.24	9.01	8.13
9	10.40	10.4	8.39	9.75	3.02	5.97	4.49	8.42	8.52	5.75	7.9	2.32	2.32	2.32
10	13.80	14.89	10.47	9.21	5.46	9.99	7.73	7.63	7.81	5.13	8.63	3.18	5.92	4.55
11	12.90	12.44	9.01	12.62	2.63	2.58	2.60	6.75	6.8	4.99	5.79	1.45	2.07	1.76
12	8.00	9	5.83	NaN	3.84	7.37	5.61	16.16	11.24	7.61	9.34	2.13	6.97	4.55
13	4.61	4.64	2.33	NaN	0.48	1.45	0.96	1.35	1.35	NaN	NaN	0.25	0.33	0.29
14	9.58	10.07	6.13	6.82	3.86	2.29	3.08	6.63	6.75	4.87	6.72	1.98	1.02	1.50
15	13.47	13.78	8.53	10.01	1.95	3.04	2.49	5.60	5.68	3.93	5.49	2.14	1.93	2.03
16	26.51	25.8	14.83	17.23	9.59	13.31	11.45	6.85	6.91	6.4	8.11	6.67	5.77	6.22
17	17.08	16.82	13.11	16.94	14.09	9.16	11.63	5.98	6.17	5.25	7.31	7.25	2.89	5.07
18	3.12	3.11	NaN	NaN	0.23	0.79	0.51	2.44	2.28	NaN	NaN	0.11	0.60	0.35
19	30.82	32.81	15.39	19.95	7.30	6.06	6.68	11.52	11.81	7.7	11.28	4.89	1.77	3.33
20	13.73	14.25	8.81	11.99	3.55	4.08	3.82	7.99	7.6	5.71	13.52	3.75	3.09	3.42
21	44.62	48.04	38.86	NaN	27.85	39.74	33.80	19.55	16.74	10.67	14.11	10.82	9.89	10.36

the noise introduced into the system is exactly known and specifiable, it is apparent that the sequence methods examined overestimate the gain of the system, with particular sensitivity to measurement noise. In comparison, the two linear regression methods both perform better where significant noise is present; however, it should be noted that, in the case where only sequenced data points (GEM 2) are used, the gain estimated is still biased. This indicates that the data points not selected contain important information about the system, and are useful for improvement in gain estimate fidelity.

While more recent sequence methods contain refinements to the sequence selection criteria, involving the use of correlation coefficient limits and input/output thresholds, the results in Table 4.4 show that they provide little improvement in the majority of cases. In the cases that there is improvement, the difference, unfortunately, is marginal.

4.6.2 Experimental example

Following on from Section 4.6.1, BRS estimates obtained using sequence methods (see 4.4.2 Method 1a-d), are compared with those obtained using a rigorous SI protocol (see 4.4.2 Method 2a-c) for instances of gain overestimation, similar to that seen in the numerical example. From Table 4.5, it is apparent that the BRS estimates obtained using the sequence methods have consistently higher values than those obtained with the SI based identificaton method.

However, one main cause for concern with sequence methods, is the inability to detect sufficient valid sequences to make a realistic BRS estimate in patients with an impaired baroreflex. This is compounded further by the addition of refinements, where the correlation co-efficient and BP and RR interval thresholds may not be met, as a dysfunctional baroreflex will result in poor responses in RR interval, caused by changes in BP. Sequence methods require concurrent increases/decreases in BP and RR-interval, which are not always present in subjects with impaired baroreflex, as seen in Subjects 13 and 18, in Table 4.5.

4.6.3 Observations

This study investigates the apparent overestimation of BRS gain observed when using sequence methods in a number of studies [99, 23, 188], by analysing the effect that sequencing data has on gain estimation (Section 4.2.2). The analysis suggests that sequence methods are limited by the fact that sequenced R-R interval data contains a significant amount of noise (ie. non-baroreflex related effects). The events excluded by the sequence method appear to contain key information about the gain of the system, with the exclusion of the corresponding data points leading to persistent overestimation of the gain of the system.

The spontaneous nature of the R-R interval and BP readings could play a role in the inability of sequence methods to distinguish between 'baroreflex like' and 'un-baroreflex' events. The Oxford method applies linear regression analysis to a dataset, where the observed change in R-R interval is primarily driven by a sudden strong change in BP, minimising the effect of non-baroreflex effectors on R-R interval. The inclusion of planned movements, that are known to stimulate the baroreflex [**?**] during the recordings, could potentially improve the accuracy of sequence methods, by ensuring the sequences selected are 'baroreflex like'. Known baroreflex stimulating movements include the Valsalva maneuver [49], timed sit-to-stand maneuver [66], and the neck chamber technique [38], all of which would continue to allow for BRS estimation in a routine, clinical setting. The recording and analysis of experimental data, where patients carry out the above movements, would allow researchers to investigate if the addition of dedicated baroreflex stimulating movements improve the accuracy of the sequence method.

4.7 Conclusion

The work presented in this study, provides a detailed analysis of sequence methods and their efficacy as BRS estimation methods, from a SI perspective. An initial analytical approach outlines how sequencing data sets can lead to biased gain estimates. This is then confirmed through a numerical example, demonstrating that, in the case of a system represented by a single gain (as in the case with most BRS estimation methods), the sequencing of data leads to gain overestimation, especially in cases where there is significant noise present. Recent refinements made to sequence methods, *viz.* the addition of a correlation metric and a minimum threshold, improve the situation to some extent, but are insufficient in completely rectifying the bias in the gain estimates.

The limitations of sequence methods outlined from the analytical study, and the numerical example, are borne out in the analysis of the experimental data. This can be seen in the consistently higher BRS estimates obtained using sequence methods, in comparison to those obtained using a rigorous SI method. The analysis carried out, especially in the experimental analysis, shows potential cause for concern with using the sequence method as a BRS estimation method, and subsequently the estimates being used as a diagnostic tool for subjects with an impaired baroreflex.

5

Understanding the interplay between baroreflex gain, low frequency oscillations, and pulsatility in the neural baroreflex

Contents

5.1 Introduction 74
5.2 Testing the model 75
5.2.1 Cardiac branches 75
5.2.2 Homeostatic analysis 76
5.3 Arterial compliance 79
5.4 Including pulsatility 81
5.5 Model simplification 83
5.5.1 Arterial compliance simplification 83
5.5.2 Pulsatility representation 84
5.5.3 Describing function approximation 89
5.6 Mathematical model 89
5.7 Determining the conditions for LF oscillation 93
5.7.1 Analytical solution 94
5.7.2 Simulation results 94
5.8 Effect of an absence of pulsatility 97
5.9 Predominance of the cardiac or peripheral branches 98
5.10 Conclusion 100

5.1 Introduction

The human body displays a variety of oscillatory phenomena, many related to the necessary natural means by which flow (of both air and fluids) can be generated. The oscillatory patterns observed in respiration and blood flow are considered to be reasonably well understood; however, the origins of some rhythms are still being debated, such as LFOs in BP, often termed Mayer waves when observed in humans [73], occurring at roughly 0.1Hz. Since we use the same inlet and outlet for breath, it stands to reason that a reciprocating (oscillating) flow is employed. However, in the case of the closed-cycle circulatory system, there is a choice (especially considering artificial hearts) between a turbine-type pump and a pulsatile pump. Pulsatility in blood flow is something that we take for granted in healthy humans and animals, and is an inevitable consequence of nature's relative difficulty in synthesising a turbine-type heart. Thus, we may imagine that blood flow (and pressure) pulsatility is an unavoidable 'side effect' of an inability to synthesise a constant-flow pump. However, some evidence now suggests that pulsatility may have an important function in maintaining perfusion, to ensure that there is an adequate supply of oxygen and nutrients to vital organs. For example, [187] demonstrated that when a subject was dependant on a non-pulsatile heart, the perfusion to a number of capillaries was reduced significantly, but not restored to some capillaries when pulsatility was recovered. While the reason for this isn't fully known, [175] noted that "Pulsatile flow generates higher circuit pressures and shear forces than nonpulsatile flow at comparable pump flow and patient mean arterial pressure". This suggests that non pulsatile flow may not produce sufficient pressure for the blood to reach capillaries, with the loss in pressure causing them to collapse, and when restored the pressure from pulsatile flow is not sufficient to re-establish flow to the now collapsed capillaries. However, further investigation into the role pulsatility plays in maintaining perfusion is required before any definitive conclusions can be drawn.

Heart failure results in an inability to deliver enough oxygen throughout the body. Heart failure is caused by a weakening of the heart muscles, or an increase in muscle stiffness, in turn causing a decrease in the pumping potential. One avenue of treatment for heart failure patients is the insertion of an artificial heart, or ventricular assist device (VAD). There are two categories of insertable device, pulsatile- or continuous-flow devices. The larger size of pulsatile devices, coupled with their shorter lifespan, generally leads to a preference for turbine based models [182]. While the benefits of continuous-flow devices are also demonstrated by improvements in patient outcomes [168], there is still some concern regarding the long term physiological effects of

diminished pulsatile blood flow [112, 159, 171].

This chapter, through the development of a mathematical baroreflex model, combined with analysis techniques from the control sciences, examines the role of pulsatility in moderating the neural baroreflex and, among other things, shows a relationship between BP pulsatility and LF (Mayer) waves. In particular, the analysis shows that, if a significant *increase* to the baroreflex gain occurs in an individual with reduced or absent pulsatility, there are potential consequences for long-term healthy BP dynamics. Other models for the neural baroreflex, combining both resistance and cardiac branches, have been proposed, but employ different analytical tools, and pursue different objectives. For example, [69] employs cross-recurrence analysis to examine the coupling between heart-rate and vascular sympathetic tone, while [77, 162] examine heart-rate variability for potential chaotic behaviour. The model of [89] is used to examine the effect of disease on cardiovascular autonomic regulation, and [14] examines the haemodynamic response to blood volume perturbations.

5.2 Testing the model

Two tests were carried out on the neural baroreflex model shown in Figure 2.2. The first was to ensure that both cardiac branches (parasympathetic and sympathetic) worked in tandem to achieve adequate HR changes to various BP signals. Subsequently, a steady state analysis was carried out on the complete model to ensure that homeostasis is consistent and as expected.

5.2.1 Cardiac branches

The cardiac branches of the neural baroreflex in Figure 2.2 were isolated, as shown in Figure 5.1. In [9], [85] and [110], clinical tests were carried out to show the response of HR in relation to a change in MAP in rabbits. The HR response to changes in MAP plotted in all three studies were representations of the average HR for 8, 2 and 7 rabbits, respectively. All three studies yielded a HR response curve in the shape of a reversed sigmoid with a horizontal range (representing HR) of approximately 200. The rabbits' resting conditions gave a HR value of approximately $220\ beats/min$, and a MAP value of $80mmHg$. These values served as the test parameters for a 'resting' state. To ensure the physiological accuracy of the model, a range of MAP values were input into the cardiac branches (Figure 2.2) and HR was recorded, if the model is

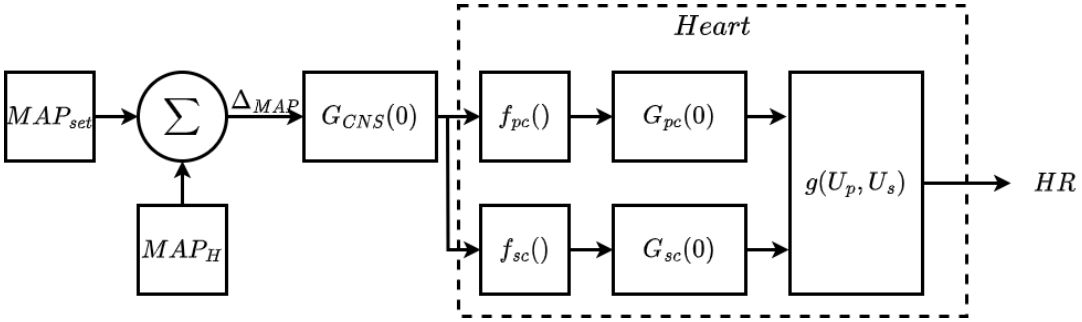

Figure 5.1: Steady state analysis of the cardiac section of the neural baroreflex for a range of MAP values. MAP_{set}, MAP set point; $f_{pc,sc}()$ activation characteristics for pc and sc, respectively; $G_{pc,sc}(0)$ dynamics for pc and sr respectively; $g(U_P, U_s)$, the cardiac function determining HR.

physiologically accurate, the test should produce results similar to those observed in the three experiments.

For the test, all dynamic components (G_{CNS}, G_{pc} and G_{sc}) were set to their steady-state equivalent ($s = 0$), resulting in a DC gain of 1 for all three dynamic components. All other variables in the model were defined as specified in Table 5.1. A range of MAP values, MAP_H = [1:1:200], were passed through the model, producing the resultant HR signal illustrated in Figure 5.2. The observed HR response matches the sigmoidal shape observed matches those recorded experimentally in [9] and [110], where major changes in HR occur between a MAP value of 40 and 100mmHg. Notably, at a MAP value of $80mmHg$, the HR is $220\ beats/min$, consistent with the resting MAP and HR values observed in rabbits, validating the cardiac branches as physiologically accurate.

5.2.2 Homeostatic analysis

In order to prove that the system, from a static balance point of view (homeostasis), is consistent, a steady-state analysis is performed. This is similar to the steady-state analysis carried out on the cardiac branch, where all dynamic blocks reduce to their DC gain, as shown in Figure 5.3. Under such conditions, the MAP_H error should be zero. Since $\Delta_{MAP} = 0$, the outputs of f_{pc}, f_{sc}, and f_{sr} are y^*_{pc}, y^*_{sc}, and y^*_{sr}, respectively, as given in Table 2.2. Under these conditions, MAP is expected to be equal to MAP_{set}, which should be a MAP of $80mmHg$, as shown in Figure 5.4. An output of $80mmHg$ was observed, confirming homeostasis.

Table 5.1: Parameters for the steady state analysis of the cardiac section of the neural baroreflex. The values for all parameters are derived from experimental studies, each of which are referenced in Section 2.2.

Parameter	Assigned Value
MAP_{set}	80
m^*	0
n^*	0
C_{pc}	-0.1342
C_{sc}	0.02
V_{pc}	33
V_{sc}	42.5
K_p	-1.2
K_s	0.88
MAP_H	1:1:200

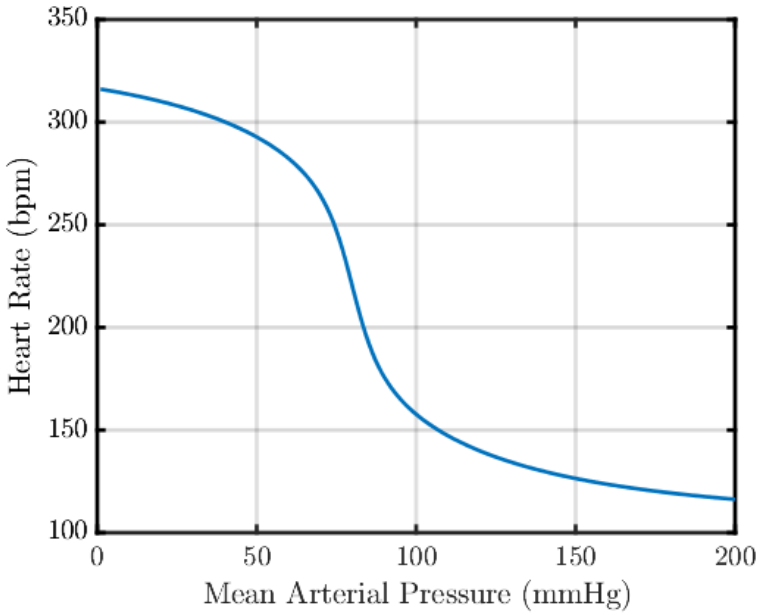

Figure 5.2: HR for a range of MAP values when all baroreflex dynamics are considered to be in steady state

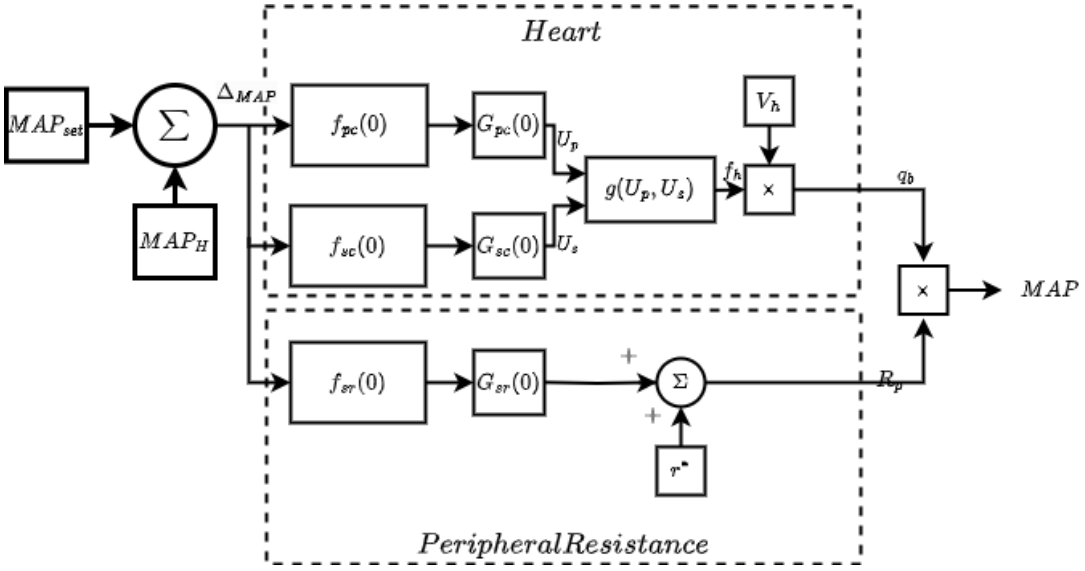

Figure 5.3: Homeostatic analysis of the neural baroreflex. Δ_{BP}, MAP error; $f_{pc,sc,sr}$ activation characterictics for pc, sc and sr, respectively; $G_{pc,sc,sr}$ dynamics for pc,sc and sr, respectively; f_h, heart rate; V_h, stroke volume; q_b, blood flow; r^*, base resistance; R_p, peripheral resistance.

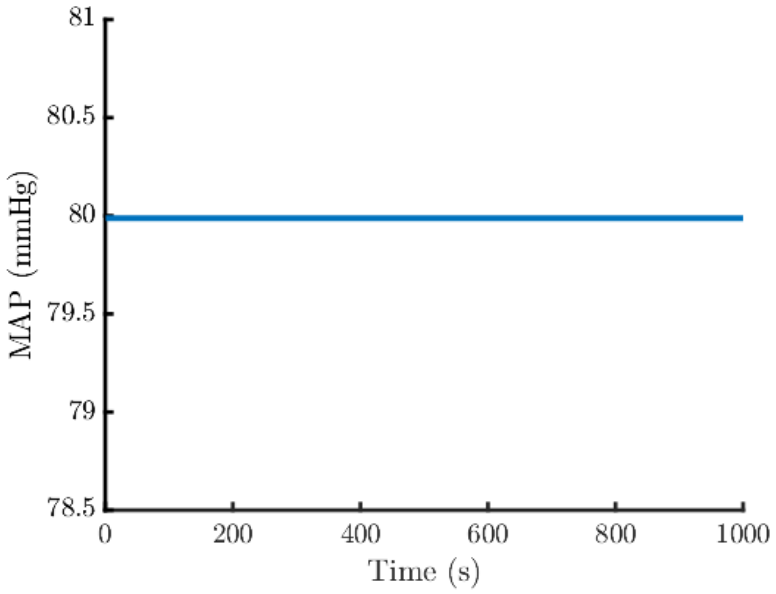

Figure 5.4: Model output for the homeostatic analysis of the neural baroreflex

5.3 Arterial compliance

The model used to articulate the baroreflex is detailed in Section 2.2 [148]. This model is extended by the inclusion of a compliance model in place of the simplified Ohm's law-like relationship in Equation (1.1), used in previous models [148]. Arterial compliance is the ability of the arterial wall to distend as the volume of blood increases. The classic definition of compliance is the Spencer and Denison relationship shown in equation 5.1 [172].

$$C = \frac{\Delta V}{\Delta P} \tag{5.1}$$

Compliance can be altered by many factors such as age, menopause and lifestyle. A low arterial compliance has been associated with various diseases such as diabetes. As you age, arterial compliance decreases, leading to a higher risk of hypertension. Windkessel models are used to model arterial compliance, the elasticity of arteries that dampens the pulsatile nature of blood flow. This is derived from the belief that the relationship between BP and cardiac output is that of Ohm's Law [150]. Thus, arterial compliance can be modelled as a low pass filter, through linking various phenomena to electronic components [149]:

- Resistors model the resistance presence as blood flows through arteries and veins of diminishing diameter. While this resistance is typically considered non-linear in the case of laminar blood flow, it can be modelled by a linear relationship [28]:
$$Z = \frac{P}{F} \tag{5.2}$$
- Capacitors represent arterial compliance, as flow represents current, and the rate of change of the pressure corresponds to voltage, giving [28]:
$$Z = C\frac{dP}{dt} \tag{5.3}$$
- Inductors represent the inertia of blood. Blood flows due to the difference in pressure between two ends of the artery or vein. Making the assumption that the rate of blood flow changes linearly we get [28]:
$$Z = L\frac{dF}{dt} \tag{5.4}$$

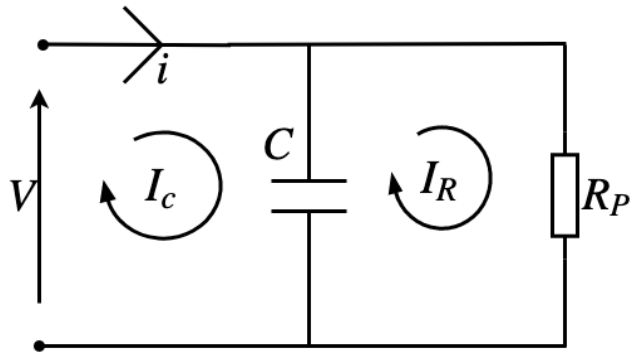

Figure 5.5: 2 Element Windkessel Model

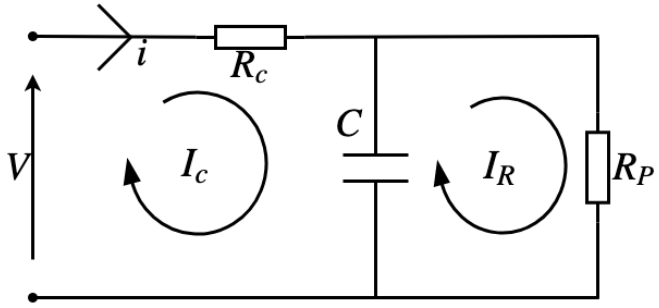

Figure 5.6: 3 Element Windkessel Model

Similar to low pass filters, Windkessel models can be of varying complexity. A wide range of Windkessel models can be derived from various combinations of Equations 5.2 through 5.4 [149]. The most basic being the 2-element model as shown in figure 5.5. The 2-element model accounts for compliance, C and peripheral resistance, R_p. To determine the BP output of the system, a state space representation is derived [61]:

$$\begin{aligned} \dot{x} &= \left[-\frac{1}{R_p C} \right] x + \left[\frac{1}{C} \right] u \\ y &= [1]x + [0]u \end{aligned} \tag{5.5}$$

where $x = P$, blood pressure and $u = f$, blood flow. This is true for all subsequent state space representations.

A 3-element model, shown in Figure 5.6, accounts for compliance, C, peripheral resistance, R_p, and impedance associated with the aorta, R_c [61]:

$$\begin{aligned} \dot{x} &= \left[-\frac{1}{R_p C} \right] x + \left[\frac{1}{C} \right] u \\ y &= [1]x + [R_c]u \end{aligned} \tag{5.6}$$

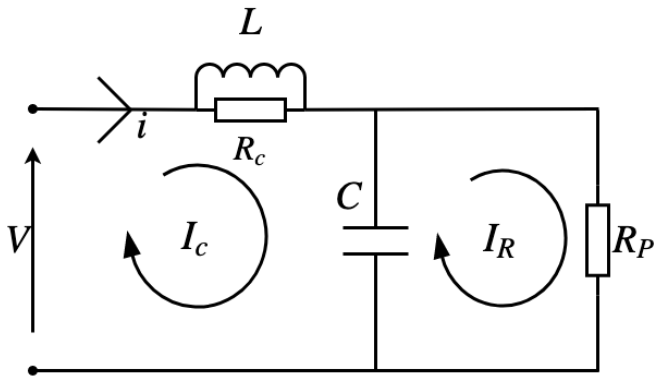

Figure 5.7: 4 Element Windkessel Model

A variety of four element models are available due to the interchangeability of the inductor, L and the impedance, R_c. A 4-element model, shown in Figure 5.7, represents a classic second order low pass filter and accounts for compliance, C, peripheral resistance, R_p, impedance associated with the aorta, R_c, and inertia of blood, L [149] [61]:

$$\dot{x} = \begin{bmatrix} -\frac{1}{R_p C} & 0 \\ 0 & -\frac{R_c}{L} \end{bmatrix} x + \begin{bmatrix} \frac{1}{C} \\ \frac{R_c}{L} \end{bmatrix} u \qquad (5.7)$$
$$y = [1 - R_c]x + [R_c]u$$

For this study, arterial compliance is modelled using a first-order Windkessel model [17] containing resistive (R_p denoting total PR) and capacitive effects, as shown in Figure 5.5 , and effectively dampening the pulsatile effects of blood flow, due to its low-pass frequency characteristics. The inclusion of the compliance model changes the relationship between CO and PR, as shown in Figure 5.8, changing the baroreflex model in Figure 2.2 to that shown in Figure 5.9. Considering that R_p is a variable, but appears as a parameter of the Windkessel model, it is potentially problematic from an analytical viewpoint, so an approximation will be employed in Section 5.5.1.

5.4 Including pulsatility

Pulsatility is introduced into the model, shown in Figure 5.9, through the addition of a pulsatile BP signal, P, illustrated in Figure 5.10. The pulsatile signal represents one complete period of a clinical measurement of BP in the abdominal aorta of a rabbit [55], the signal is then zeroed at the $80mmHg$ point.

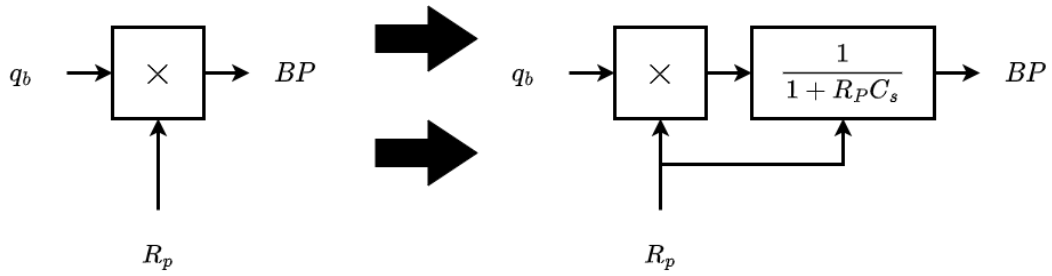

Figure 5.8: The inclusion of a compliance model in the relationship between CO, PR and BP.

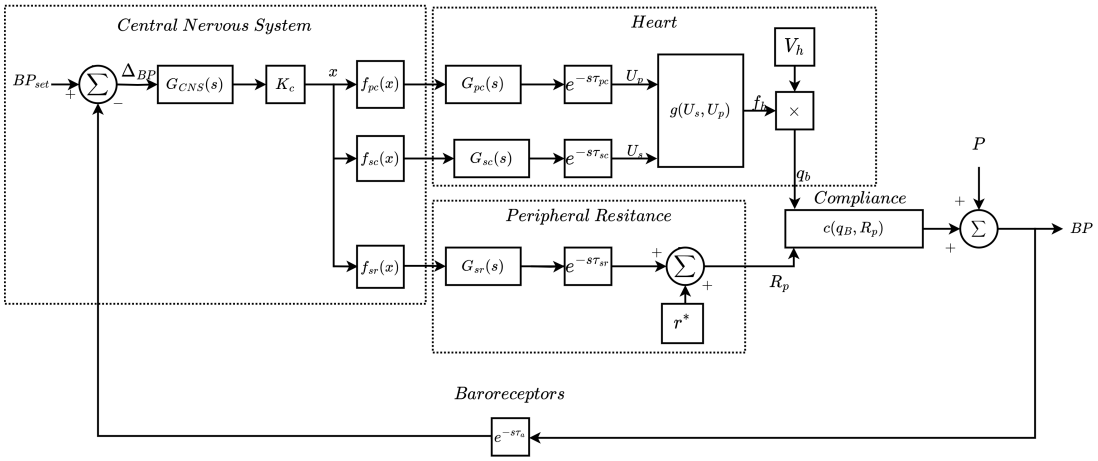

Figure 5.9: The neural baroreflex, extended to include compliance, $c(q_b, R_P)$ and BP pulsatility, P, represented as a pressure signal

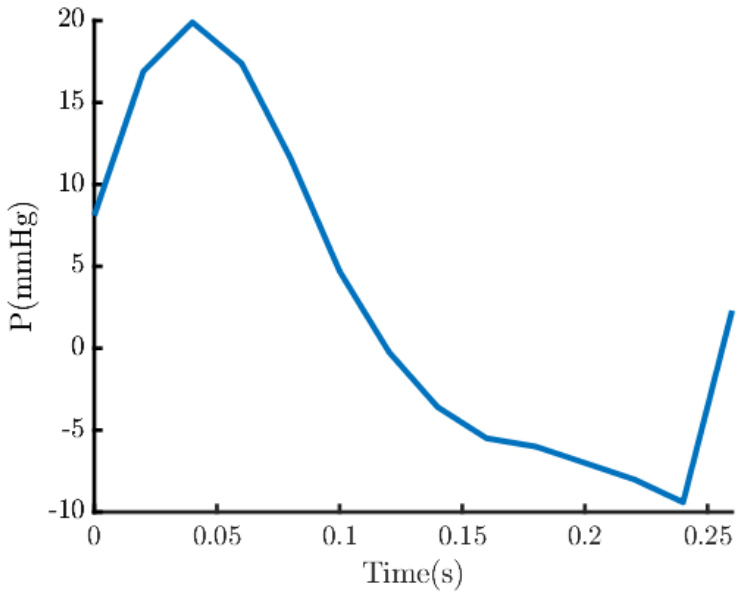

Figure 5.10: Pulsatile BP signal, P

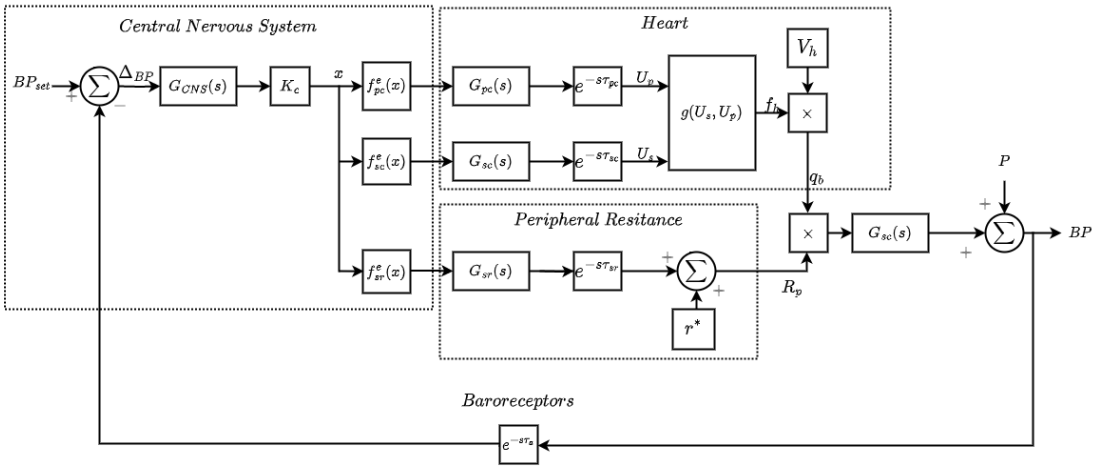

Figure 5.11: The neural baroreflex simplified for analytical purposes

5.5 Model simplification

Developing a set of analytical conditions for LF oscillations in the baroreflex is one of the primary goals of this study. To achieve this, it is important that there is a compact and system-orientated description of the system, and importantly, one which places the system description firmly within the framework of linear time-invariant (LTI) analysis. To attain this: (a) the compliance model must be simplified to reduce the parametric variation to aid analysis, (b) the external pulsatile signal must be absorbed into a system-type description, and finally, (c) the non-linear characteristics, f_{pc}, f_{sc}, and f_{sr}, must be articulated as a linearised but effective, amplitude dependant (describing) function. The addition of the three simplifications alters the baroreflex model from that shown in Figure 5.9 to that shown in Figure 5.11. The remainder of this chapter will detail how each simplification was carried out.

5.5.1 Arterial compliance simplification

A significant difficulty with the arterial compliance model, from an analysis perspective, is that the subsystem currently belongs to the class of linear parameter-varying (LPV) systems. In particular, the relationship between q_b and BP is:

$$\frac{BP(s)}{q_b(s)} = G_c(s) = \frac{R_p(t)}{1 + R_p(t)Cs} \tag{5.8}$$

where $R_p(t)$ is a time varying parameter of the system. It is possible to retain the essence of the effect of a varying R_p by using the true value of R_p in the numerator of (5.8), while using a constant (mean) value, $\overline{R_p}$ in the denominator of (5.8):

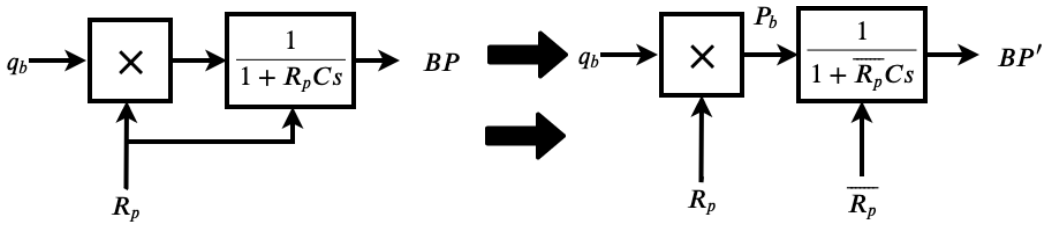

Figure 5.12: Compliance approximation for the analytical solution. q_b, blood flow; R_p, peripheral resistance; $\overline{R_p}$, mean peripheral resistance; C, arterial compliance.

$$\frac{BP'(s)}{p_b(s)} = G_c'(s) = \frac{1}{1+\overline{R_p(t)}Cs} \ , \tag{5.9}$$

where p_b is the MAP signal derived from the classic Ohm's law relationship, excluding compliance, as:

$$p_b = q_b R_p \ , \tag{5.10}$$

as demonstrated in Figure 5.12. This is justified by the fact that the main effect is a *gain* change, due to the numerator instance of R_p (note that the dc gain of (5.8) is $R_p(t)$), while a variation in the dynamic response around the mean value of R_p in the denominator ($\overline{R_p}$) will be minimal. Though the system on the right-hand side of Figure 5.12 is still parameter varying, it is significantly easier to analyse. A steady-state analysis yields:

$$\overline{R_p} = r^* + G_{sr}(0)y_{sr}^* \tag{5.11}$$

5.5.2 Pulsatility representation

In Figure 5.9, pulsatility is included as a second input, P, into the model. However, for the purpose of mathematical analysis, P, is absorbed into the static non-linear characteristics, f_{pc}, f_{sc}, and f_{sr} to produce *equivalent non-linearities* f_{pc}^e, f_{sc}^e, and f_{sr}^e. This provides a significant simplification by observing the frequency separation between the variations in MAP (which include LF oscillations) and pulsatility. In the 'equivalent non-linearity'(EQNL) procedure, a system with an input $x(t)$, containing a relatively LF input $r(t)$ and a high frequency 'dither' signal $d(t)$, can be represented as a modified non-linear system [166], as shown in Figure 5.13. In this instance, $r(t)$ is the low frequency oscillations at 0.1Hz and $d(t)$ is the pulsatile blood pressure signal at approximately 3.7Hz.

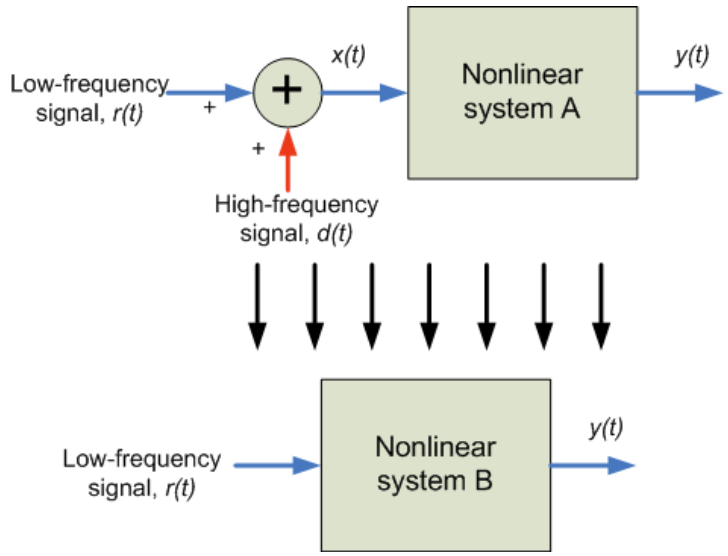

Figure 5.13: Equivalent non-linearity concept, articulating the inclusion of a high frequency dither signal, $d(t)$, into a modified non-linear system.

To develop a new non-linearity (non-linear system B ($f^e(x)$), subject only to a LF signal $r(t)$, from an original non-linear system A ($f(x)$) which is subject to LF ($r(t)$) and HF ($d(t)$) signals, an EQNL must first be determined from the high frequency signal. Additional details on this procedure can be found in [152] and [166]. The EQNL is highly specific to the nature of the dither signal $d(t)$, in this case the pulsatile signal P,

With an original non-linear system $y = f(x)$, where $x = r(t) + d(t)$, gives:

$$y = f(r(t) + d(t)) \tag{5.12}$$

The output of the EQNL corresponding to the non-linear system is:

$$\overline{y} = \int_{-\infty}^{\infty} f(r(t) + q)p(q)\ dq \tag{5.13}$$

where $p(q)dq$ is the probability that, for any time t, the dither signal $d(t)$ lies in the range q to $q + dq$, and $d(q)$ is the probability density function for the dither signal. The probability density function for the dither signal is:

$$p(q) = -\frac{dF(p)}{dp} = \frac{1}{2A} \tag{5.14}$$

The parameters for the dither signal were obtained from a piecewise linear approximation of the signal P, a clinical measurement of BP in the abdominal aorta of a rabbit. One cycle of the data was divided into 4 segments, three triangles and one flat line, as shown in Figure 5.14. The specific parameters for each segment can be found in Table 5.2.

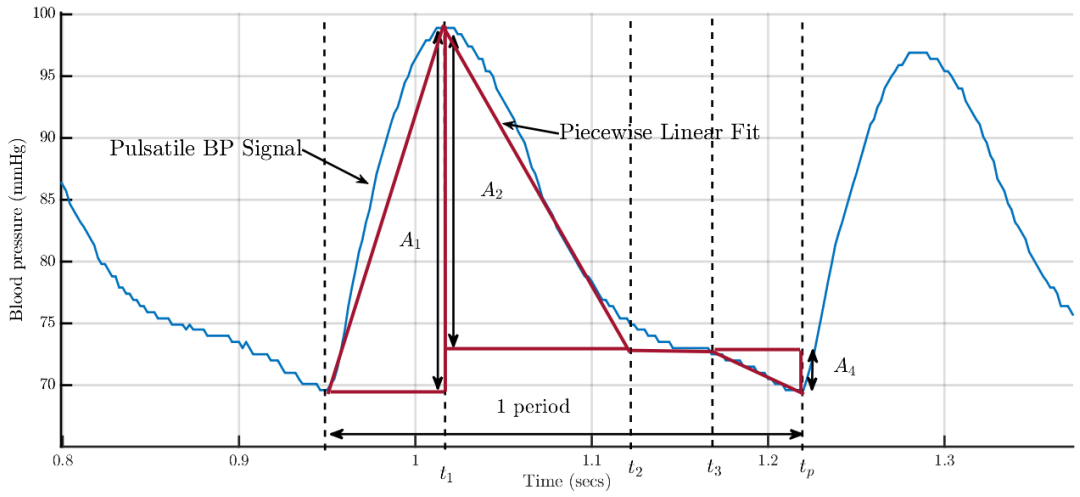

Figure 5.14: Piecewise linear approximation of one BP cycle.

Table 5.2: Segmentation of Clinical Data

Segment	1	2	3	4
Parameter	$t_o - t_1$	$t_1 - t_2$	$t_2 - t_3$	$t_3 - t_p$
A (height)	29.18	26.02	0	3.37
τ (length)	0.068	0.104	0.0452	0.053

Segments 1, 2 and 4 are represented by triangles with varying heights, A_i, and their respective EQNL outputs can be obtained by inserting the appropriate A_i into Equation (5.15):

$$\overline{y_{i=1,2,4}} = \int_{b-A_i}^{b+A_i} \frac{1}{2A_i}[h\ tan^{-1}(\beta(r+q)) + y^*]\ dq \tag{5.15}$$

$$\begin{aligned}\overline{y_{i=1,2,4}} = \frac{h}{2A_i}((r+q)tan^{-1}(\beta(r+q))) \\ -\frac{h}{4A_i\beta}ln|\beta^2(r+q)^2+1| + y^*(r+q))\Big|_{b-A_i}^{b+A_i}\end{aligned} \tag{5.16}$$

Segment 3 is approximated by a flat line, resulting in a constant probability function for the time interval $t_2 - t_3$, giving an EQNL output of:

$$\overline{y_3} = h\ tan^{-1}(\beta(r+q)) + y^* \tag{5.17}$$

The total EQNL output is the sum of all four segment components, weighted by factors α_i, corresponding to the relative portions of the total period $t_p - t_o$, from Figure 5.14:

$$\overline{y} = \alpha_1\overline{y_1} + \alpha_2\overline{y_2} + \alpha_3\overline{y_3} + \alpha_4\overline{y_4} \tag{5.18}$$

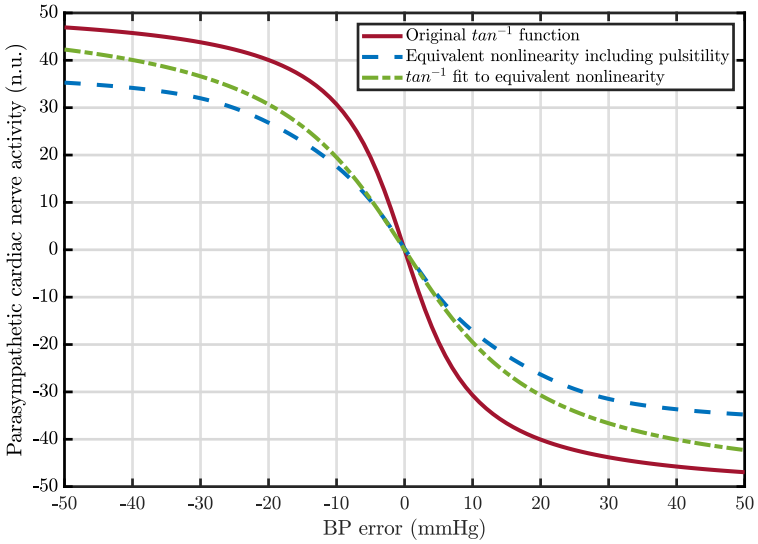

Figure 5.15: Altered parasympathetic cardiac activation function, β_{pc} , with the inclusion of pulsatility

where $\alpha_1 = 0.252$, $\alpha_2 = 0.385$, $\alpha_3 = 0.167$, $\alpha_4 = 0.196$. Note that $\Sigma\alpha_i = 1$. In order to get the $f \rightarrow f^e$ for each of f_{pc}, f_{sc}, and f_{sr}, Eq. (5.18) is used in conjunction with (5.16) and (5.17), with the appropriate β and y^* values for $\overline{y_1}$, $\overline{y_2}$, $\overline{y_3}$, and $\overline{y_4}$ taken from Table 2.2, as appropriate.

Note that, since the EQNL depends only on the relative areas of the piecewise approximations to the pulsatile signal segments, and the proportions of the period occupied by those segments, but *not* on the period of the dither signal itself (so long as $d(t)$ is significantly HF, relative to $r(t)$), a fixed frequency for $d(t)$ (effectively the heart rate) can be used in subsequent analysis and simulation.

The *equivalent non-linearities* f^e_{pc}, f^e_{sc}, and f^e_{sr} are now determined for the non-linear characteristics f_{pc}, f_{sc}, and f_{sr}, shown in Figures 5.15, 5.16 and 5.17, respectively. Note that a $tan^{-1}(\ )$ fit has been generated to the EQNL in each case, so that a specific change in the linearised 'gain' at (x^*, y^*), due to the presence of pulsatility, may be calculated for each case. The results are shown in Table 5.3. It may be noted, from Figures 5.15, 5.16 and 5.17 that, while the fit of the $tan^{-1}(\ )$ function to the EQNL is generally good in the region of the function origin, it is less good at the extremities. This is somewhat deliberate, within the limits of approximation of the fitted $tan^{-1}(\ )$ functions. Specifically, the EQNL is precisely matched at the origin, so that a representative β value can be determined for the EQNL. If desired, a more precise parametric approximation can be determined using a combination of parametric functions, including an $tan^{-1}(\ )$ and a saturation characteristic [152].

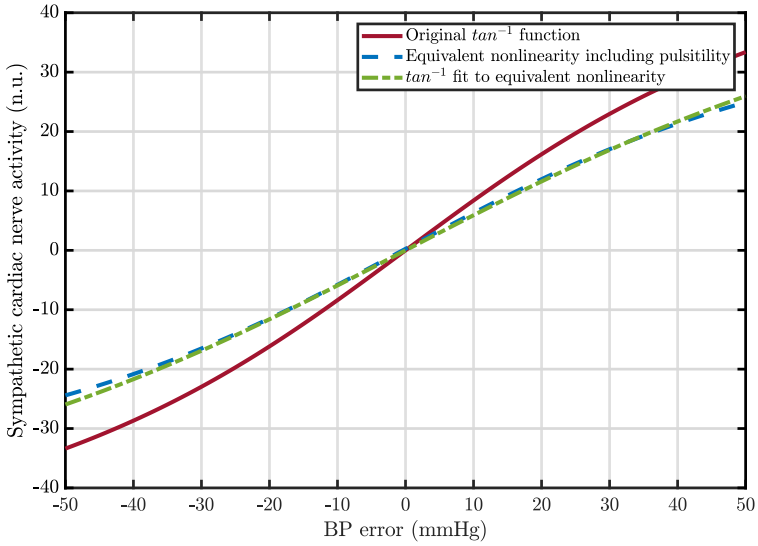

Figure 5.16: Altered sympathetic cardiac activation function, β_{sc}, with the inclusion of pulsatility

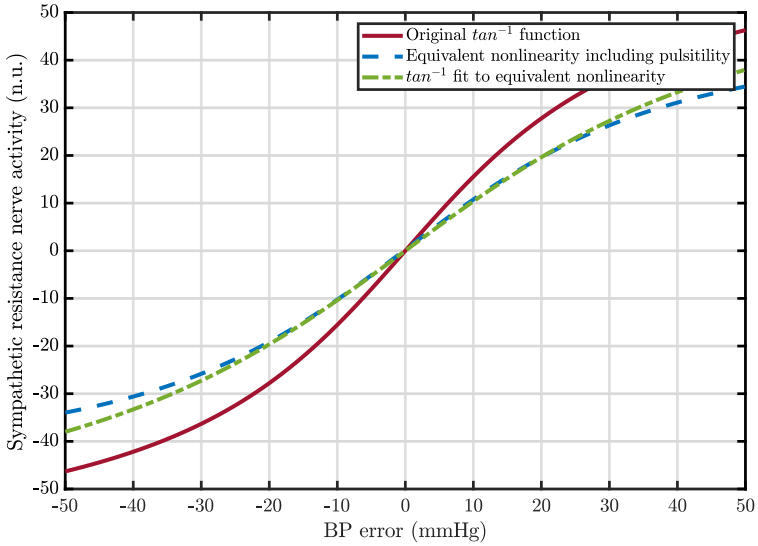

Figure 5.17: Altered sympathetic resistance activation function, β_{sr}, with the inclusion of pulsatility

Table 5.3: Modification of β values due to the inclusion of pulsatility

Arctan Function	β_{pc}	β_{sc}	β_{sr}
Original Arctan (Case 1&2)	-0.1342	0.035	0.04
EQNL Arctan (Case 3)	-0.1342*0.55	0.035*0.875	0.04*0.82

5.5.3 Describing function approximation

The static non-linear characteristics, f^e_{pc}, f^e_{sc}, and f^e_{sr}, are represented by their *describing functions*, simplifying the analytical manipulation of the functions f^e_{pc}, f^e_{sc}, and f^e_{sr}. The describing function (DF) approximation essentially assumes a sinusoidal input to a non-linearity (useful for the analysis of LF oscillations), and calculates the effective 'gain' of the system (which is dependent on amplitude of the input), with respect to the fundamental component of the output [7]. For the $tan^{-1}(\ )$ function of Equation (2.2) and Figure 2.3, the DF has been calculated [31] as:

$$DF(X) = \frac{2h}{\beta X^2}\left(\sqrt{1+\beta^2X^2}-1\right) \tag{5.19}$$

where the input to the non-linearity is $x(t) = Xsin(\omega t)$. The expression in (5.19) may be further simplified [31], for asymptotic values of X, to:

$$DF(X) \rightarrow \frac{2\ h}{X} \quad , \quad X \rightarrow \infty \tag{5.20}$$

for large X and,

$$DF(X) = \ \ h\beta(1-\beta^2X^2) \quad , \quad X \rightarrow 0\ . \tag{5.21}$$

for small X. The use of the DF in this application is justified, since the major assumption that the DF relies on, i.e. that output harmonics are significantly attenuated, is satisfied through G_{pc}, G_{sc} and G_{sr}, all having low-pass frequency response characteristics. Furthermore, we are primarily interested in the propagation of LF (fundamental) oscillations, rather than the existence of harmonic components. In any case, the dominance of the fundamental will be demonstrated in Section 5.7.2.

5.6 Mathematical model

Consider the baroreflex model in Figure 5.11. LF oscillations can be analysed in 2 ways. The first, and most direct, approach is to simulate the model and examine for conditions under which oscillations in BP occur. While such simulation studies are useful, they provide little indication of the bigger picture, outside the set of specific tests performed. It would therefore be beneficial if an alternative analytical route could be pursued, employing the simplifications of Section 5.5.

In [151], it was possible to employ a DF approximation, in combination with classical (linear) Nyquist stability analysis, to determine conditions under which LF oscillations would occur. In that analysis, the gain of the CNS, K_{CNS}, was seen to be instrumental

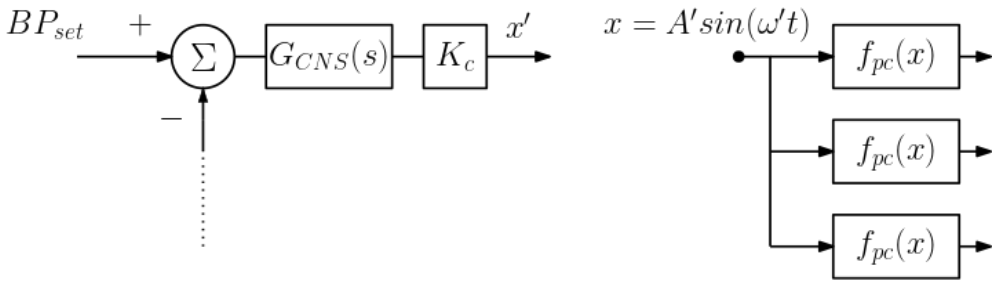

Figure 5.18: Showing the break point in the baroreflex loop and the injection of a sinusoid to determine conditions for sustained LF oscillation

in the modulation of LF oscillations, as will be shown in the current case. However, for the model of Figure 5.11, an equivalent approach is not possible, given the multiple branches and diverse dynamics in each path. Rather, an approach, inspired by [148], is employed, where a notional LF (sinusoidal) oscillatory signal is injected at x, and propagated around the baroreflex, to determine a set of conditions under which the original signal might arrive back at x' i.e. the conditions for sustained oscillations, as shown in Figure 5.18.

If sustained oscillations occur, assuming the fundamental component of x' to be $x'' = A''sin(\omega'' t + \phi'') + \overline{X''}$, then the following must hold:

$$\omega'' = \omega' \,, \tag{5.22}$$

$$A'' = A' \,, \tag{5.23}$$

$$\phi'' = 0 \,, \tag{5.24}$$

$$\overline{X''} = 0 \,, \tag{5.25}$$

corresponding to conditions on frequency, amplitude, phase and offset, respectively. We assume that $x(t)$ has no dc component, since the system of Figure 5.11 is assumed to be in homeostasis (see more on this in Section 5.2.2).

Using the configuration in Figure 5.18, the signal $x(t)$ first passes through the three non-linearities, f_{pc}, f_{sc} and f_{sr}, resulting in the DF outputs:

$$z_{pc} = DF_{pc} A' sin(\omega' t) + y^*_{pc} \tag{5.26}$$

with

$$DF_{pc} = \frac{2h_{pc}}{\beta_{pc} A'^2}(\sqrt{1 + \beta^2_{pc} A'^2} - 1), \tag{5.27}$$

$$z_{sc} = DF_{sc} A' sin(\omega' t) + y^*_{sc} \tag{5.28}$$

with

$$DF_{sc} = \frac{2h_{sc}}{\beta_{sc}A'^2}(\sqrt{1+\beta_{sc}^2A'^2}-1), \tag{5.29}$$

and

$$z_{sr} = DF_{sr}A'sin(\omega' t) + y_{sr}^* \tag{5.30}$$

with

$$DF_{sr} = \frac{2h_{sr}}{\beta_{sr}A'^2}(\sqrt{1+\beta_{sr}^2A'^2}-1). \tag{5.31}$$

The heart output flowrate, f_h', is now:

$$f_h' = N_{pc}sin(\omega' t + \phi_{pc}) + N_{sc}sin(\omega' t + \phi_{sc}) + \overline{f_h} \tag{5.32}$$

where,

$$N_{pc} = k_p k_{pc}|G_{pc}(\omega')|DF_{pc}A', \tag{5.33}$$

$$\phi_{pc} = \angle G_{pc}(\omega') - \omega'\tau_{pc}, \tag{5.34}$$

$$N_{sc} = k_s k_{sc}|G_{sc}(\omega')|DF_{sc}A', \tag{5.35}$$

$$\phi_{sc} = \angle G_{sc}(\omega') - \omega'\tau_{sc}, \tag{5.36}$$

$$\overline{f_h} = k_p k_{pc} y_{pc}^* + k_s k_{sc} y_{sc}^* + f_o. \tag{5.37}$$

or

$$N_c sin(\omega' t + \phi_c) + \overline{f_h} \tag{5.38}$$

where

$$\phi_c = tan^{-1}\frac{N_{pc}sin(\phi_{pc}) + N_{sc}sin(\phi_{sc})}{N_{pc}cos(\phi_{pc}) + N_{sc}cos(\phi_{sc})}, \tag{5.39}$$

$$N_c = \sqrt{i^2+j^2}, \tag{5.40}$$

with

$$i = N_{pc}cos(\phi_{pc}) + N_{sc}cos(\phi_{sc}), \tag{5.41}$$

$$j = N_{pc}sin(\phi_{pc}) + N_{sc}sin(\phi_{sc}). \tag{5.42}$$

From (2.6),

$$q_b' = V_h N_c sin(\omega' t + \phi_c) + \overline{q_b'} \tag{5.43}$$

where

$$\overline{q_b'} = V_h \overline{f_h}, \tag{5.44}$$

Now propagating $z_{sr}(t)$ through the peripheral resistance branch, get

$$R_p' = N_{sr}sin(wt + \phi_{sr}) + \overline{r} \tag{5.45}$$

where,

$$N_{sr} = k_r|G_{sr}(\omega')|DF_{sr}A' \tag{5.46}$$

$$\phi_s r = \angle G_{sr}(\omega') - \omega'\tau_{sr} \tag{5.47}$$

$$\overline{r} = k_r y^*_{sr} + r^* \tag{5.48}$$

The cardiac (5.43) and resistance (5.45) branches are combined via the simplified arterial compliance model as shown in Figure 5.12:

$$BP' = |G_c(\omega')|N_p sin(\omega' t + \phi_p) + k(\omega') + \angle G_c(\omega') + \overline{r}\overline{q'_b} \tag{5.49}$$

where

$$\phi_c = tan^{-1}\frac{N^*_c sin(\phi_c) + N^*_{sr} sin(\phi_{sr})}{N^*_c cos(\phi_c) + N^*_{sr} cos(\phi_{sr})} \tag{5.50}$$

$$N^*_c = \overline{r}V_h N_c \tag{5.51}$$

$$N^*_{sr} = \overline{q'_b}N_{sr} \tag{5.52}$$

$$k(\omega) = \frac{V_h N_c N_{sr}}{2} cos(\phi_c - \phi_{sr}) \tag{5.53}$$

$$N_p = \sqrt{m^2 + n^2} \tag{5.54}$$

with

$$m = N^*_c cos(\phi_c) + N^*_{sr} cos(\phi_{sr}) \tag{5.55}$$

$$n = N^*_c sin(\phi_c) + N^*_{sr} sin(\phi_{sr}) \tag{5.56}$$

Note that, in (5.53), the amplitude of the harmonics of ω' are assumed to be negligible compared with the fundamental, so just the fundamental component is retained. This is justified, as in Section 5.5.3, by the fact that the dynamics of G_{pc}, G_{sc}, and G_{sr} are low-pass, and therefore attenuate relatively high frequency harmonics, with further validation in Section 5.7.2.

The BP' signal is now fed back through the baroreceptor delay to the CNS dynamics:

$$\begin{aligned} x''(t) = K_c|G_{CNS}(\omega')|\{PB_{set} - \overline{r}\overline{q'_b} - k(\omega') \\ -N_p sin(\omega' t + \phi_p - \omega'(\tau_a) + \angle G_{CNS}(\omega') + \pi)\} \end{aligned} \tag{5.57}$$

Since we have assumed, in (5.53), that the harmonics of BP' are negligible, x'' in (5.57) clearly contains only the fundamental component of ω' and the condition of (5.22) becomes redundant. The amplitude condition of (5.23), in residual form, from (5.57), becomes:

$$K_c|G_{CNS}(\omega')||G_c(\omega')|(\omega')K_P - A' = 0 \tag{5.58}$$

while the phase and offset conditions of (5.24) and (5.25) become, respectively:

$$\phi_p - \omega'(\tau_a) + \angle G_{CNS}(\omega') + \angle G_c(\omega') + \pi = 0 \tag{5.59}$$

and

$$K_c|G_{CNS}(\omega')|\{PB_{set} - \overline{r}\overline{q_b'} - k(\omega')\} = 0\ . \tag{5.60}$$

Equations (5.58) to (5.60) describe the set of conditions for sustained oscillations with a fundamental frequency ω'.

5.7 Determining the conditions for LF oscillation

K_c is primarily responsible for mediating LF oscillations in the baroreflex, investigating the relationship between K_c, and the presence or absence of LF oscillations will help to establish a set of conditions for which LF oscillations occur. The value for K_c is somewhat arbitrary, since any experimental evaluation would require that all nerve fibres at the outputs of f_{pc}, f_{sc}, and f_{sr} are fully recruited, which is impossible to achieve in experimental practice. However, K_c can be estimated by recognising that K_c is primarily responsible for mediating LF oscillations [151], and it therefore seems likely that the brain modulates K_c in response to different adverse physiological conditions e.g. hypoxia [110], haemorrhage [111], etc. In particular, given that LF oscillations are instigated/accentuated during adverse physiological conditions, one possibility is to establish a value of K_c in the 'normal' physiological state (including pulsatility), which is just below that required to initiate LF oscillations. This value is set at $K_c^{nom} = 7$ for the (normal) pulsatile case, where a 10% increase results in the onset of LF oscillations.

LF oscillations are now initiated by an increase in K_c by 25%, consistent with the data in [31], showing a 25% increase in β in the change from normoxia to hypoxia (10% O_2 + 3%CO_2). In our simulation, this will be effected by an increase in K_c from its nominal value of $K_c = 7$ to $K_c' = 1.25K_c^{nom} = 8.75$. The remainder of this section investigates the presence of LF oscillations through both the analytical solution from Equations (5.58) to (5.60), and computer simulation of the model in Figure 5.9, using the Matlab/Simulink platform.

5.7.1 Analytical solution

From Equations (5.58), (5.59), and (5.60), we can identify the cost function to minimise as:

$$J = \sum_{i=1}^{3} \gamma_i r_i^2 \tag{5.61}$$

where

$$\begin{aligned} r_1 &= K_c|G_{CNS}(\omega')||G_c(\omega')|(\omega')K_P - A' \ , \\ r_2 &= \phi_p - \omega'(\tau_a) + \angle G_{CNS}(\omega') + \angle G_c(\omega') + \pi \ , \\ r_3 &= K_c|G_{CNS}(\omega')|\{PB_{set} - \overline{r}\overline{q_b'} - k(\omega')\} \end{aligned}$$

where the weighting factors γ_i reflect the relative magnitude units of the r_i.
The Levenberg-Marquardt algorithm [119] was used to solve the non-linear least squares problem represented by minimising (5.61). In order to investigate the sensitivity of the solution to the optimisation algorithm used, trust-region [25] and simplex [96] algorithms were also tested, giving consistent results. For a value of K_c', the performance surface for (5.61) is shown in Figure 5.19, showing a broadly convex surface. The algorithm found a local minimum at $\omega = 0.3187Hz$ and $A' = 16.4504$, for an initial value range of $0.25Hz < \omega < 0.45Hz$ and $10 < A < 50$, which also defines the maximum domain of attraction within which this solution can be found. For a uniform residual weighting ($\gamma_i = 1 \ , \ 1 \leq i \leq 3$), a residual vector of $[r_1 \ r_2 \ r_3] = [-1.0656 \ \ -0.1244 \ \ 0.0439]$ is obtained.

The most useful solution parameters from the minimisation of (5.61) are ω' and A', which give the frequency and amplitude of the LF oscillations, respectively. The examination of A' may be used as binary indication of oscillations, where a value of $A' = 0$ indicates no oscillations. Figure 5.20 shows the change in oscillation amplitude (A') with variation in K_c. Note the expected threshold at $K_c = 7.7$ for the normal (pulsatile) case.

5.7.2 Simulation results

Figure 5.21 shows the relative magnitude of the LF oscillation fundamental, and validating that harmonic amplitudes for LF oscillations are small (<10%), compared to the fundamental amplitude, providing strong evidence for ignoring the harmonics of the fundamental frequency ω' in the analytical solution presented in Section 5.6.

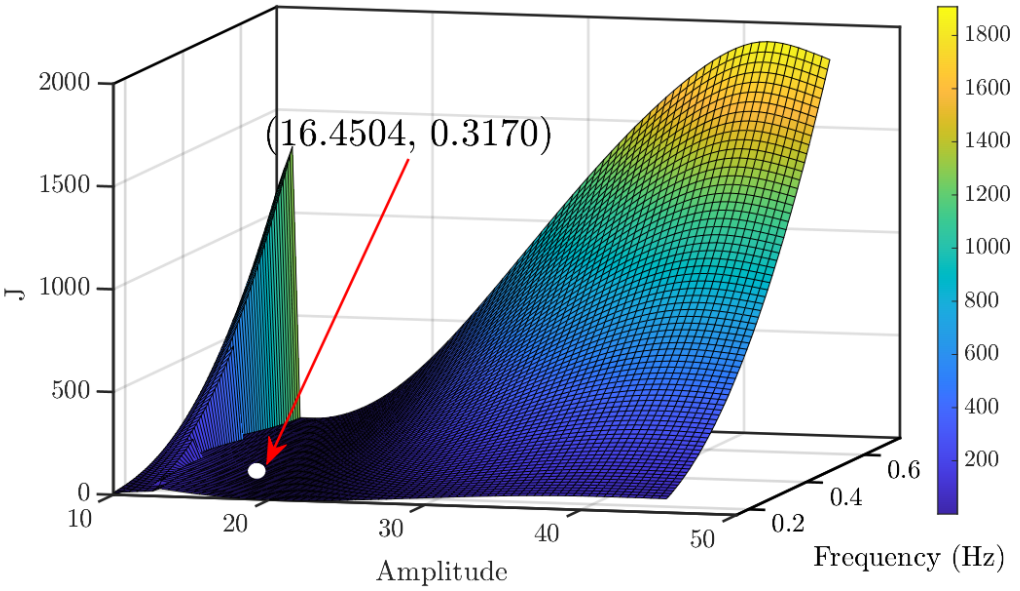

Figure 5.19: Performance surface for $J = \sum_{i=1}^{3} \gamma_i r_i^2$, showing optimal solution for $(A',\ \omega')$

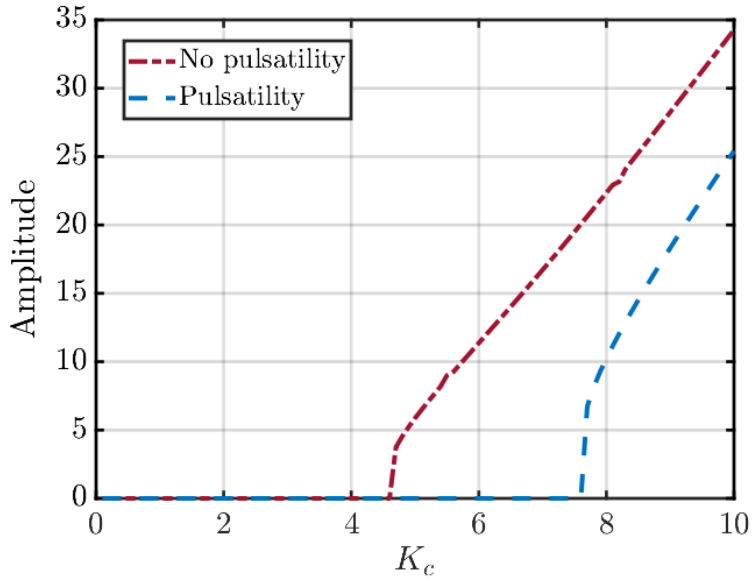

Figure 5.20: Investigating the threshold of K_c which gives rise to LF oscillations

However, while a fundamental-based analysis for the solution of LF oscillations may be appropriate, the presence of harmonics means that the LF oscillations are not perfectly sinusoidal.

While the simulation demonstrates that no LF oscillations occur for the nominal choice of $K_c^{nom} = 7$, Figure 5.22 also shows that the situation for $K_c = 7(1 + 0.25) = 8.75$,

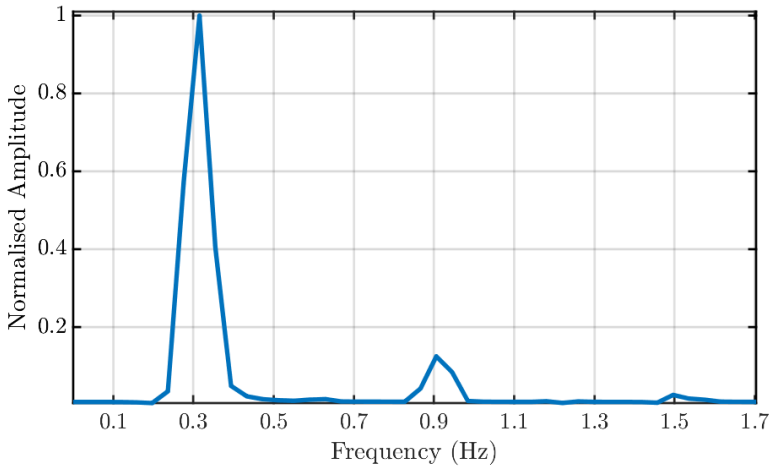

Figure 5.21: The frequency spectra of the BP signal under conditions where LF oscillations, demonstrating the harmonics present in the LF oscillation.

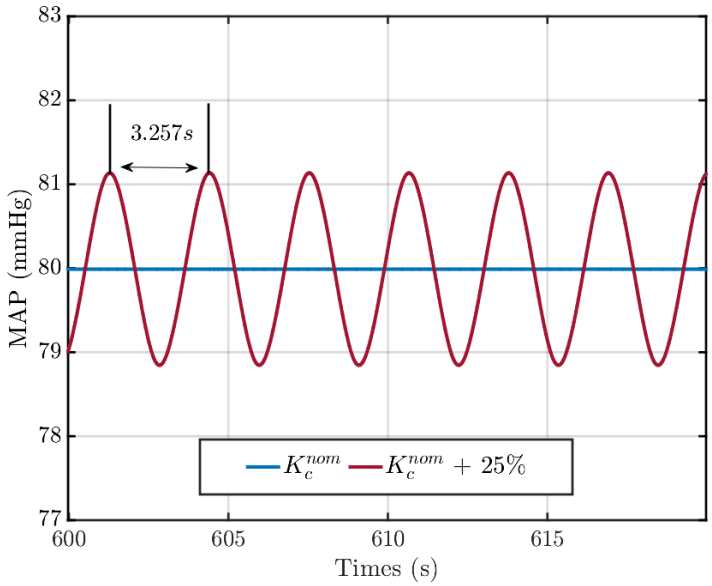

Figure 5.22: LF oscillations in BP for the normal (pulsatile) case, for nominal and increased K_c values. The LF oscillations is measured at a period of $3.257s$, corresponding to a frequency of $0.307Hz$.

Table 5.4: Comparative LF oscillation amplitude for analytical and simulation results

Case	A'	BP osc. ampl. (mmHg)	Osc. freq. (Hz)
Analytical soln.	16.4504	~ 1.38	0.317
Simulation	15.1	~ 1.34	0.307

where a LF BP oscillation of 1.34 mmHg occurs, consistent with the analytical solution of Section 5.7.1. The comparative results for A', LF oscillation amplitude and frequency, for both the analytical and simulation cases are detailed in Table 5.4. The results shown are in good agreement with the experimental LF BP oscillation frequency of 0.3 Hz observed in [72].

5.8 Effect of an absence of pulsatility

Under certain medical interventions, blood pulsatility may be reduced or eliminated, for example, by insertion of an artificial (turbine-type) heart, or the inclusion of a LVAD. The effect of pulsatility on the neural baroreflex both via manipulation of the baroreflex functions f_{pc}, f_{sc}, and f_{sr}, or by inclusion/exclusion of the signal P in the simulation.

Examining the EQNLs shown in Figures 5.15, 5.16, and 5.17, with reference to Table 5.3, provides some insight on the changes in baroreflex gain caused by the addition of pulsatility. In particular, it is evident that the *addition* of pulsatility causes a significant *reduction* in overall baroreflex gain, apparent in the decrease in the β_{xx} from their 'original' values to their EQNL values, with a gain reduction of up to 55% (for β_{pc}).

The hypothesis was tested using the simulation, where pulsatility was represented either by the addition of a physical pulsatile signal P (Case 1), as shown in Figure 5.11, or by omitting P but using the EQNL values for the β_{xx} (Case 3), outlined in Table 5.3. If both P is omitted and the original β_{xx} values are used, pulsatility is considered absent (Case 2). Table 5.5 shows the details of the 3 cases examined. The change in baroreflex gain, caused by an absence in pulsatility, is mirrored in the simulation, shown in Figure 5.23. In Figure 5.23, the trace for Case 1 (see Table 5.5) contains the BP pulsatility (green line) which is not completely dampened by arterial compliance, but confirms agreement with the trace for Case 3. Figure 5.20 shows the variation in oscillation amplitude (A') with variations in K_c for the non-pulsatile case (red trace). Note the significant reduction in the threshold value of K_c in the

Table 5.5: Test Conditions

Case	Baroreflex function parameters	Pulse signal P present
1	f_{xx}	Yes
2	f_{xx}	No
3	f^e_{xx}	No

non-pulsatile case.

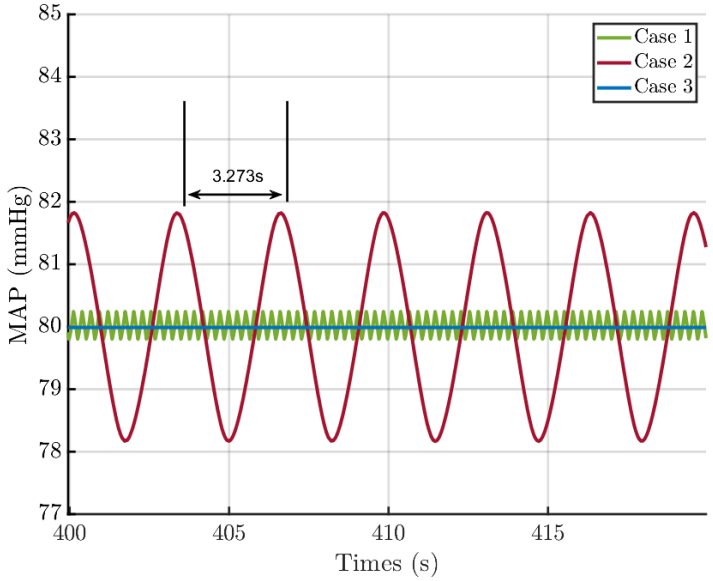

Figure 5.23: Simulation results for the pulsatile (Cases 1 and 3) and non-pulsatile cases (Case 2), where pulsatility is represented both by EQNL values or the inclusion of a physical pulsatility signal P. Note that $K_c = K_c^{nom}$. The three cases illustrated are documented in Table 5.5.

5.9 Predominance of the cardiac or peripheral branches

Given that the neural control of BP is mediated through a number of pathways, as illustrated in Figure 5.11, and LF oscillations may propagate, its reasonable to be curious about the predominance of these branches, if predominence of a branch exists. Liu et al [102] conclude that the cardiac branch is relatively unimportant in the dynamic regulation of BP and the mediation of LF oscillations in MAP. To examine the relative strength/gain of each of the branches of the model in Figure 5.11, we perform a simple sensitivity study, which examines the raw (dc) gain from Δ_{BP} to

BP, from the simplified model of Figure 5.3. While a dc analysis does not include the dynamic effects of G_{pc}, G_{sc} and G_{sr}, their effects will be relatively consistent between paths, and their low-pass cut-off frequency is relatively high, compared to the LF oscillation frequency of 0.33 Hz, as are the arterial compliance dynamics.

From Figure 5.3, the following sensitivity functions are introduced and may be easily calculated:

$$S_{sr}^{BP} = \left.\frac{dBP}{d\Delta_{BP}}\right|_{\substack{f_{pc}=y_{pc}^* \\ f_{sc}=y_{sc}^*}} = \overline{q_b} k_{sr} \beta_{sr} \tag{5.62}$$

which articulates the sensitivity of BP to Δ_{BP} along the peripheral resistance path, and

$$S_c^{BP} \left.\frac{dBP}{d\Delta_{BP}}\right|_{f_{sr}=y_{sr}^*} = \overline{R_p} V_h (k_p k_{pc} \beta_{pc} + k_s k_{sc} \beta_{sc}) \tag{5.63}$$

which articulates the sensitivity of BP to Δ_{BP} along the complete cardiac path (pc & sc), where $\overline{R_p}$ is given from Equation (5.11) and

$$\overline{q_b} = V_h (k_p k_{pc} y_{pc}^* + k_s k_{sc} y_{sc}^* + f_o) \tag{5.64}$$

The individual sensitivities along the parasympathetic and sympathetic cardiac branches can also be evaluated, respectively, as:

$$S_{pc}^{BP} = \left.\frac{dBP}{d\Delta_{BP}}\right|_{\substack{f_{sr}=y_{sr}^* \\ f_{sc}=y_{sc}^*}} = \overline{R_p} V_h k_p k_{pc} \beta_{pc} \tag{5.65}$$

and

$$S_{sc}^{BP} = \left.\frac{dBP}{d\Delta_{BP}}\right|_{\substack{f_{sr}=y_{sr}^* \\ f_{pc}=y_{pc}^*}} = \overline{R_p} V_h k_s k_{sc} \beta_{sc} \tag{5.66}$$

The gain calculated for each branch, calculated using the sensitivity functions in (5.62) to (5.66), is shown in Table 5.6. The sensitivity values suggest a predominance of the cardiac branch over the resistance branch, while the parasympathetic cardiac is favoured over the sympathetic cardiac.

Simulation studies were also used to investigate the relative importance of various branches in mediating LF oscillations. Figures 5.24, 5.25, 5.26, 5.27 , 5.28 and Table 5.6 show the achieved oscillation amplitude (OA) in BP and the associated oscillation frequency, for removal of various branches (for example, in the pc column, only the pc branch is active). The simulation results provide additional insight to the sensitivity functions. For a value of $K_c = K_c'$ (with pulsatility included), no single branch is capable of supporting LF oscillations. As K_c is increased (upto $5K_c'$), individual

Table 5.6: Sensitivity values for propagation through various cardiac and resistance branches, using a dc gain approximation, along with LF oscillations BP amplitudes (OA, in mmHg) for corresponding branches from simulation.

Branch	K_c	All	sr	sc	pc	sc
Sensitivity fn.	-	-	S_{sr}^{BP}	S_{c}^{BP}	S_{pc}^{BP}	S_{sc}^{BP}
Sensitivity (x10^{-4})	-	-	53	67	50	17
BP OA	K_c'	1.05	0	0	0	0
Frequency		0.3	0	0	0	0
BP OA	$2K_c'$	3.55	0.68	0.79	0.99	0
Frequency		0.286	0.256	0.384	0.400	0
BP OA	$3K_c'$	4.08	1.96	1.10	1.32	0.19
Frequency		0.278	0.256	0.384	0.400	0.169
BP OA	$4K_c'$	4.295	2.29	1.25	1.48	1.47
Frequency		0.277	0.263	0.37	0.4	0.169
BP OA	$5K_c'$	4.455	2.46	1.34	1.59	1.72
Frequency		0.27	0.256	0.37	0.385	0.169

branches become capable of sustaining LF oscillations but, crucially, none of the achieved LF oscillations frequency values correspond with experimental evidence [72]. This is primarily due to the variety of conduction and phase delays in each individual branch, while the full model contains a mixture of these dynamical components that appears to correctly articulate the oscillations observed experimentally. Overall, there is a strong suggestion that both cardiac and resistance branches are crucial in the support of LF BP oscillations.

5.10 Conclusion

The analysis carried out in this chapter compliments experimental findings [143, 194], where an increase in baroreflex gain is generally accompanied by an increase in incidence of LF oscillations, suggesting that LF oscillations have the potential to be used as a surrogate diagnostic tool for changes in baroreflex gain.

In this chapter, a model for the neural baroreflex is presented that accounts for arterial compliance and the inclusion of arterial pulsatility, with particular focus on the components that mediate LF oscillations. The model is first simplified using an array of analytical tools to allow for an algebraic solution for LF oscillatory conditions, providing information about the role of the baroreflex in mediating LF oscillations.

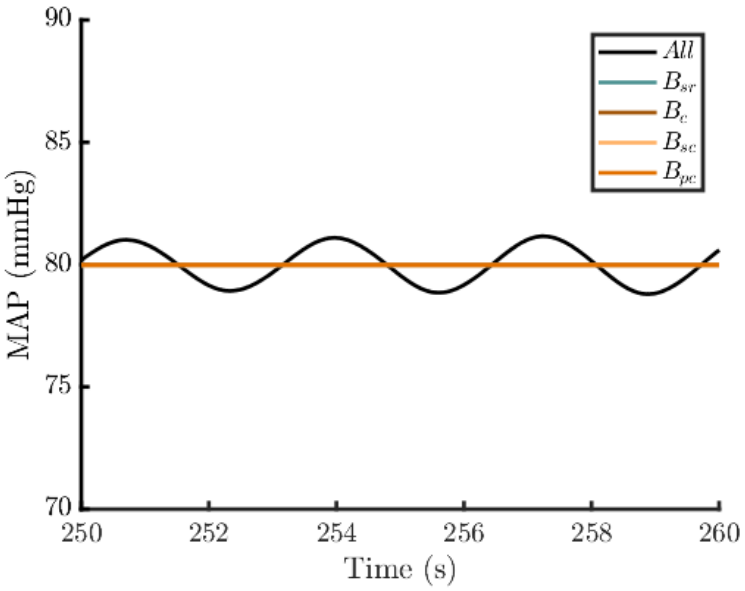

Figure 5.24: Oscillations formed from all branches for K'_C

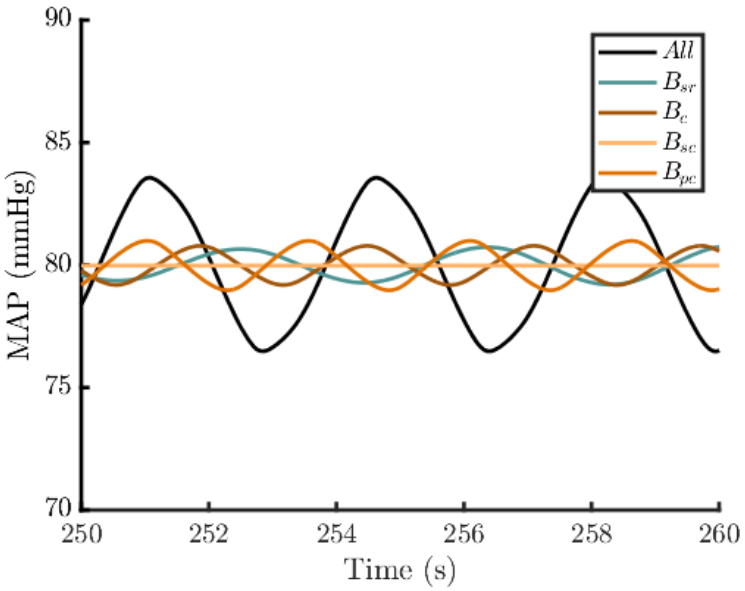

Figure 5.25: Oscillations formed from all branches for $2K'_C$

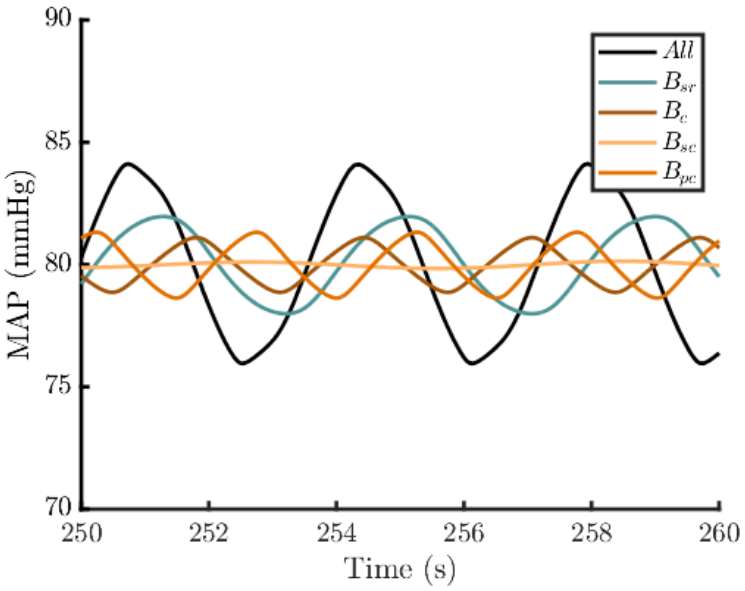

Figure 5.26: Oscillations formed from all branches for $3K'_C$

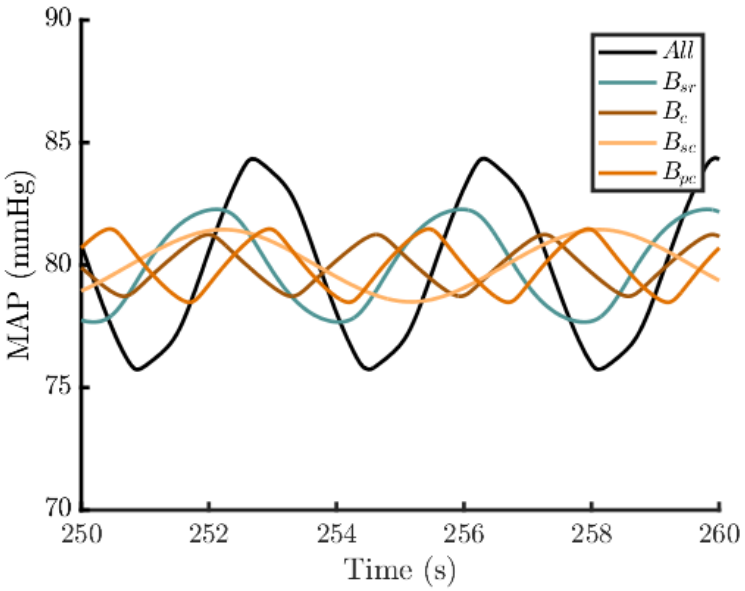

Figure 5.27: Oscillations formed from all branches for $4K'_C$

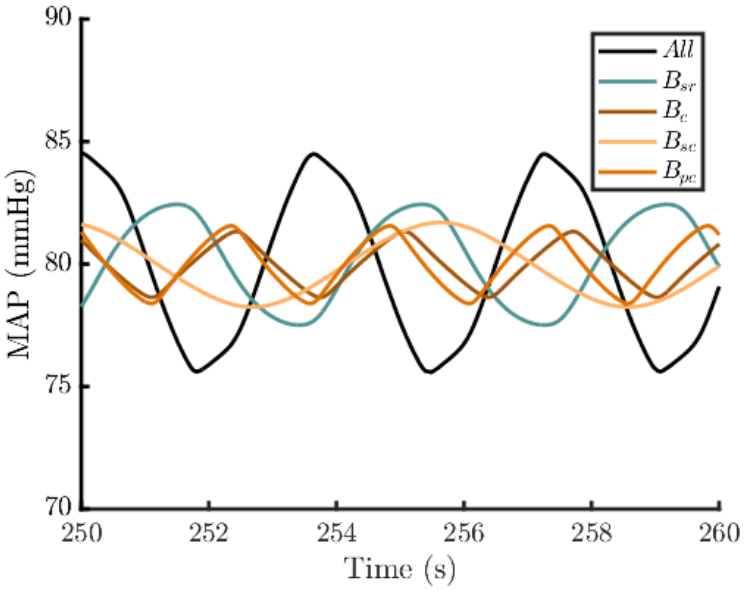

Figure 5.28: Oscillations formed from all branches for $5K'_C$

In particular, Section 5.7 demonstrates the key role changes in the CNS 'gain' plays, which can result from an array of external stimuli or internal physiological stress (e.g. haemorrhage, hypoxia, etc). Specifically, the use of the 'equivalent non-linearity', in representing pulsatility, reveals a significant increase in overall baroreflex gain as a result of a *loss of pulsatility*, which may have important implications for patients in receipt of artificial (turbine-based) hearts, or VADs. Such a change in CNS gain is shown to give rise to Lf oscillations, demonstrated experimentally [143, 194].

Overall, the model, and the analysis contained in this chapter, provides a toolbox for the analysis of the interplay between baroreflex gain, LF oscillations and blood pulsatility. One of the important conclusions is that LF oscillations are mediated by a combination of cardiac and peripheral resistance branches, while establishing the key role of baroreflex gain as the mechanism by which LF oscillations are modulated. In turn, the baroreflex gain is seen to be substantially influenced by pulsatility and physiological stress.

6

Investigating the relationship between pulsatility and Mayer waves

Contents

6.1 Introduction 106
6.1.1 Mechanical circulatory support 107
6.2 Animal study 110
6.3 Human trial - Details of the trial 111
6.3.1 Experimental set up 112
6.3.2 Data acquisition and analysis equipment 113
6.3.3 Acquisition challenges 115
6.4 Assessing Mayer wave identifiability in irregularly sampled, sparse data 116
6.4.1 The impact of sparse date on the MAP frequency spectrum through a test case 116
6.5 Results 119
6.5.1 Animal study 119
6.5.2 Human study 127
6.6 Observations and limitations 129
6.7 Conclusions 130

There is much discussion surrounding the prognostic potential of Mayer waves, but before we can determine its prognostic capabilities we must first understand why and when it occurs. A number of studies carried out on subject with little, to no pulsatility, have noted the presence of Mayer waves [143, 194]. However, the studies themselves do not investigate the incidence of Mayer waves relative to pulsatility,

including whether they occur at a lower, equal or higher rate in the case of low pulsatility compared to normal pulsatility.
The mathematical analysis carried out in Chapter 5 suggests that, as pulsatility decreases, there is an increased occurrence of Mayer waves, using a detailed baroreflex model. This current chapter aims to examine this hypothesis experimentally in both sheep with artificially induced CHF and human VAD patients. Sections 6.2 and 6.3 details the experimental set up and experimental protocol. Section 6.4 details the post-processing techniques applied to the recorded data. Section 6.5 articulates the results of the study. Finally, Section 6.7 discusses the conclusions that can be drawn from the experimental results, along with the limitations of the analysis.

6.1 Introduction

The heart is a fist-sized organ, responsible for driving blood around the body, via the circulatory system. The heart drives blood by consistent, rhythmic contractions that are initiated by electrical signals, controlling the heart's alternating contraction and relaxation. These electrical signals are detectable through an electrocardiogram (ECG), a sample of which is shown in Figure 6.1.

Chronic heart failure (CHF) occurs when the heart fails to pump sufficient blood, resulting in inadequate tissue perfusion. CHF is often attributed to an underlying myocardial disease [176]. According to the Irish Health Service Executive (HSE), CHF ranks as one of the most common causes of hospitalisation in patients over the age of 65. Approximately 7% of those between 75 and 85 are considered to have CHF, a number which increases to 15% for those over the age of 85.

The American College of Cardiology (ACC) and the American Heart Association (AHA) have established a classification system for CHF patients (shown in Table 6.1). This classification system starts at Stage A, encompassing patients with risk factors for heart failure, but no structural damage, through to stage D, characterised as the stage at which even maximal supportive therapy cannot account for the deficiency on heart function. When a patient reaches stage D, major intervention becomes necessary, either through a heart transplant or mechanical circulatory support (MCS). As CHF progresses, there is a resultant decrease in pulsatility, as illustrated in Figure 6.2.

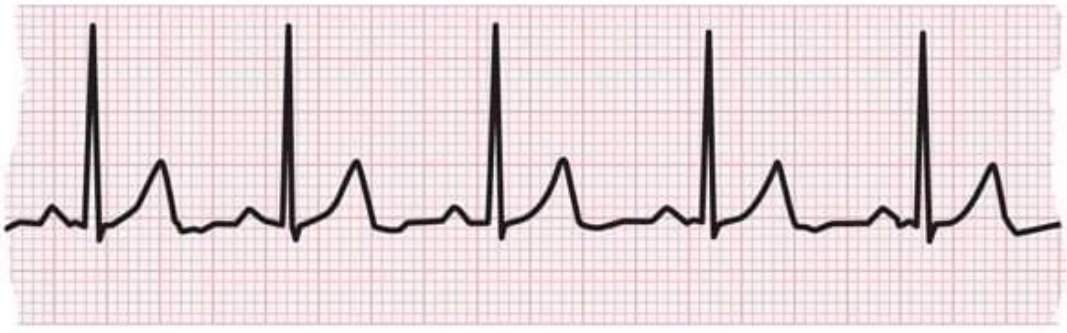

Figure 6.1: Normal ECG. Taken from [6]

Table 6.1: The American College of Cardiology (ACC) and the American Heart Association (AHA) classification for chronic heart failure (CHF).

Stage	Description
A	High risk for heart failure No structural heart disease
B	Structural heart disease No symptoms of heart failure
C	Structural heart disease Symptoms of heart failure
D	Severe structural heart disease Refractory heart failure

6.1.1 Mechanical circulatory support

In 1966, De Bakey performed a landmark procedure, the first successful VAD implantation in a patient with advanced CHF. This patient relied on the VAD for ten days, until they underwent a heart transplant [32]. In recent years, there has been a major surge in the use of MCS devices, namely VADs. Not only are VADs being considered as a bridge to transplant, but also as a destination therapy for patients with advanced CHF. The classification of MCS devices was initially divided into two categories [182]:

- **Pulsatile flow devices** where the device uses displacement pumps to replicate the natural pulsating action achieved by the heart. Pulsatile flow devices achieve the pulse-like effect though the use of pneumatically or electrically actuated sacs,

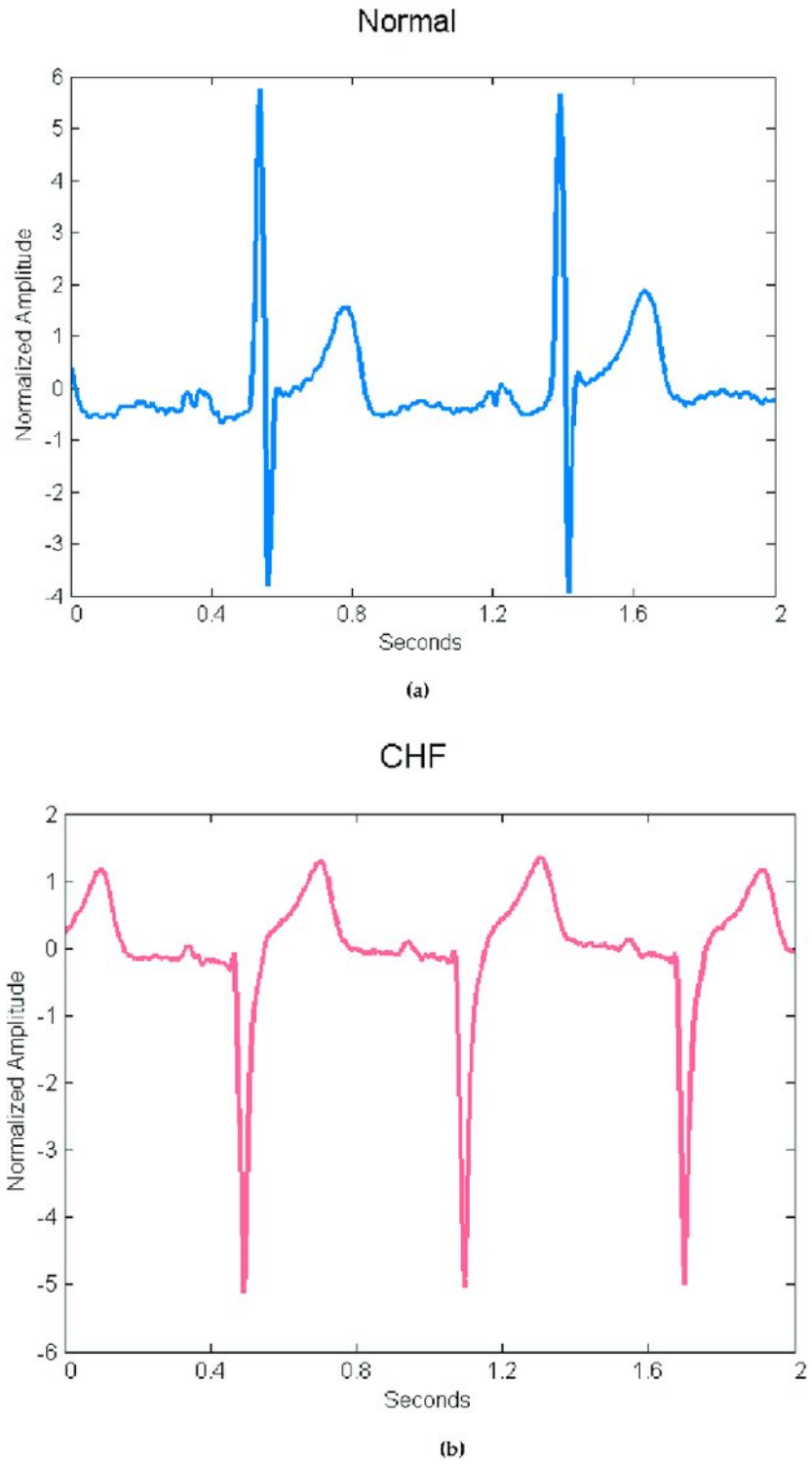

Figure 6.2: Representation of normal ECG (a) and CHF ECG signal (b). Taken from [71]

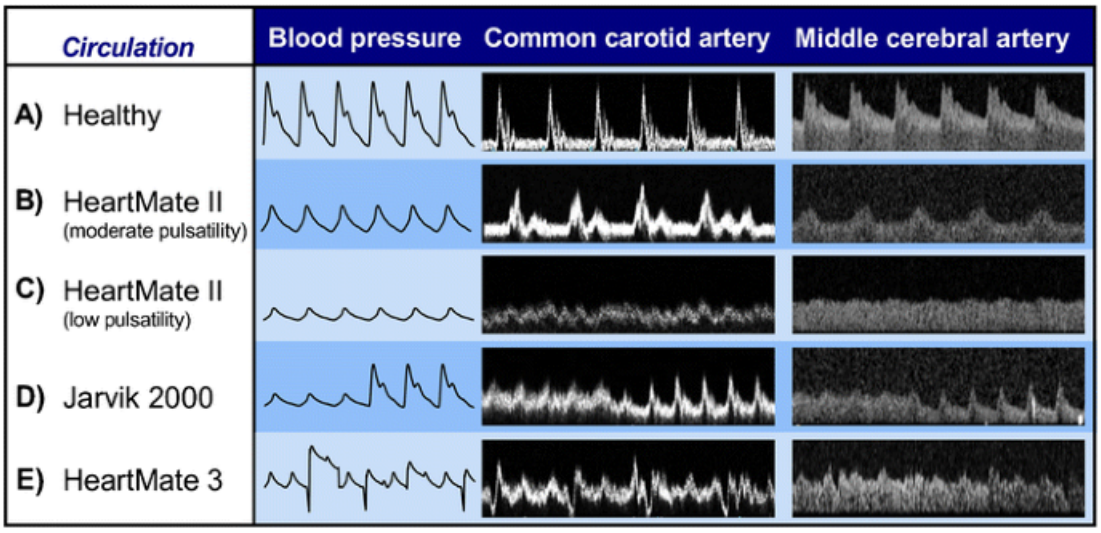

Figure 6.3: Arterial blood pressure waveforms. Taken from [20]

diaphragms or pusher plates [182]. The mechanical components used to achieve the pulsatile flow are typically the cause of a number of adverse events and high incidence of mechanical malfunction. Consequently, a low device lifespan is observed in patients with such devices.
Examples of pulsatile devices include: Novacor LVAD [154], Thoratec PVAD [41] and Abiomed BVS5000 [35].

- **Continuous flow devices,** in contrast, circulate blood through a continuous flow turbine, creating a constant stream of blood from the heart. In theory, continuous flow devices are void of any cyclic pressure gradient; however, this is not the typical case. The native ventricle frequently has some residual cardiac activity, leading to some pulsatility observed in patients with continuous flow VADs [75]. This residual pulsatility is observed in Figure 6.3, where case (b) and (c) depict varying degrees of residual pulsatility after turbine-based VAD implantation, in contrast with case (a) which shows the blood pressure signal for a healthy individual. It should also be noted, that although continuous flow devices address the longevity issue with pulsatile devices, they are still accompanied by their own set of adverse events [20].
  Examples of continuous flow devices include: Heartmate II [53], Jarvik 2000 [190] and InCor [160].

The Interagency Registry for Mechanically Assisted Circulatory Support (InterMACS) reported in 2006 of the 98 implantable devices, 68 were pulsatile, intracorporeal devices [86, 164]. By 2013, this trend shifted in the opposite direction with 2420 of 2506 implantable devices recorded by InterMACS being continuous flow, intracorporeal

devices [87]. This transition in research and development focus was largely driven by the increased longevity of turbine-based devices. Nevertheless, with the prevalence of continuous flow devices, accompanied by an array of adverse events, the question now turns to whether the lack of pulsatility plays a role in the development of certain adverse events, such as ischemic and hemorrhagic stroke, vascular dysfunction, arterial stiffness, etc. [20].

Recent studies exploring the relationship between pulsatility and VAD patients has prompted the development of a third classification of VADs:

- **Continuous flow device with a pseudo pulse:** Among the newest generation of VADs lies the Heartmate III, a continuous flow device that introduces an artificial pulse, "beating" 30 times per minute, achieved by modulating the rotor speed [2].

The technological evolution of MCS devices allows for a more comprehensive and critical study of the pathophysiology of CHF, and the long term effects of MCS usage [134]. One avenue of investigation pertains to the relationship between the occurence of Mayer waves in relation to decreases in pulsatility.

6.2 Animal study

Twelve sheep were studied, six with CHF and six healthy controls. Ramchandra et al [144] shared pre-clinical data recorded from two experiments, carried out in the Department of Physiology in Auckland University. Note, the animal study utilised experimental data previously recorded by the Department of Physiology in the University of Auckland. I was not way involved in the study design or execution. The animal study considers 12 subjects, 6 CHF sheep with an ejection fraction of 45% [163], and 6 control sheep[186].

The CHF group were adult (3–5 year old) female Romney sheep. The sheep were housed in individual crates, and acclimatized to laboratory conditions (18 °C, 50% relative humidity, 12 h light–dark cycle) and human contact for 1 week before any experiments. Sheep were fed 2–2.5 kg/day (Country harvest pellets) and had access to water ad libitum. All animal experiments and surgical procedures followed relevant guidelines and were approved by the Animal Ethics Committee of the University of Auckland (#2082).

CHF was induced through weekly (1-3 weeks) embolizations. 3 days post embolization, ECGs were analysed to determine the ejection fraction, embolizations ceased when the ejection fraction reached 45%. The BP recordings used were recorded 3 months after the final embolization. BP measurements were recorded using a probe located in the ascending aorta (the first section of the aorta). Recording were taken from conscious sheep in heart failure on a desktop computer with a CED micro 1401 interface and a data acquisition program (Spike2 v8, Cambridge Electronic Design, UK). Further information about the CHF group can be found in [163].

The control group were dry ewes (50-70 kg; 3–4 years old). The sheep were acclimated to a standard pellet diet and the laboratory for at least 1 week prior to undergoing surgery. All sheep were housed in individual metabolic home crates with multiple sheep in the same room, and constant visual contact with one another, at a constant temperature (18 °C) and humidity during an automated 12–12 h dark–light cycle (lights on from 0600 to 1800). Food and water were supplied ad libitum, except for the short duration during the experiments.

To allow measurement of arterial pressure, a 3.5 Fr solid state pressure catheter (SPR-524, Millar, Houston, TX) was implanted into the carotid artery. On the day of each experiment, the arterial pressure pressure catheter was connected to a dual channel pressure control unit (PCU-2000, Millar Inc, Houston TX). BP signals were recorded using PowerLab and LabChart (ADInstruments, v8.15, Sydney, Australia). Further information can be found in [186]. The BP signals used in this study is the baseline signals recorded from the normotensive group in Vari *et al*'s study.

6.3 Human trial - Details of the trial

The human trial was carried out in collaboration with the Department of Cardiology at the Mater Hospital. I was heavily involved in the creation of the application for ethical approval (Institutional Review Board Reference: 1/378/1759). I created the agreement with Masimo (formerly LiDCo) for the use of their non invasive blood pressure device for the period of the trial. I recruited subjects with the help of the VAD clinic staff, and took all BP measurements during their outpatient appointments. Finally, I anonymised and analysed all data from the trial.

6.3.1 Experimental set up

For the study in human subjects, significant care was taken when selecting a patient group. Three patient groups were considered:

- CHF patients pre-op: They are typically on an array of medication to treat their condition, a number of such medications can affect the incidence of Mayer waves.
- Post-op VAD in-patients: They are typically on a myriad of medication to assist with the recover from surgery, minimise the likelihood of adverse events and to reduce pain and discomfort. Any combination of such medications can affect the incidence of Mayer waves. The severity of VAD insertion surgery means recovery time varies greatly, making it difficult to identify windows where post-op patients could be considered medically stable and recordings could be taken.
- VAD surveillance clinic out-patients: They are typically a few months post op and on the least medication of all the groups considered. They are also seen in a scheduled clinical on a regular basis, making it easy to identify windows to schedule recordings.

Following careful consideration, the VAD outpatients were selected as the patient group. This was motivated by an attempt to reduce the number of external factors influencing the attenuation of Mayer waves, along with the ability to take measurements in the hospital during their regularly scheduled clinic visits. The inclusion criteria for the test group was, patients with a VAD that were considered medically stable. Patients who fit this criteria were contacted prior to their outpatient appointment, the study was explained to them and then they were asked if they would participate in the trial.

The study recruited 20 subjects, 10 stable VAD patients (1 woman, 9 men) and 9 healthy well-matched participants (not patients; 1 woman, 8 men). Following enrolment into the study, two ten-minute non-invasive BP recordings were taken, in the hospital, using LiDCOrapid monitor and CNAP (continuous noninvasive arterial pressure) module [105] with finger cuffs. A subject data form, in Appendix A.2 was completed during enrolment, the form includes information on patient demographics and medical history. It is also worth noting that this is a pilot study to gather preliminary data on the method of measurement. A sample size calculation is thus not carried out. This study provides data for future study sample size calculations. Previous studies have been carried out in animals using invasive procedures [143, 194]. In this study BP measurements were taken non-invasively.

Figure 6.4: Shows the position of the CNAP modules finger cuff. Taken from [114]

Subjects were seated in a consultation room, and acclimated to the investigator and the room. The investigator described the objectives of the study, the consent form, and each subject was given a patient (subject group) or participant (control group) information leaflet, as appropriate, as shown in Appendix A.1.1 and A.1.2, respectively.

Following the signing of the consent form, the investigator described how the BP measurement device operates and how the finger cuff is positioned. The subjects were connected to the CNAP module, as shown in Figure 6.4, and asked to sit for 10 minutes. The subjects were asked if they would like to take a break before the second ten-minute recording was taken in the same position.

On the day of the trial, the signals for each subject were isolated, and each file was anonymised through the use of a unique subject identifier. At the end of the clinic, the investigator sat down with the VAD clinic nurse to complete the study datasheet for each patient. The datasheet information is summarised in Tables 6.2 and 6.3 for the VAD and control group, respectively.

It should be noted that one subject in the VAD group (V01) asked for the finger cuff to switch fingers after 5 mins, leading to 4 five-minute recordings. In addition, the control group recordings were taken from hospital staff during clinics. Towards the end of the day, there was a cardiac emergency, resulting in subjects C07 and C10 being called away, resulting in one ten-minute recording for C07 and no recording from C10.

6.3.2 Data acquisition and analysis equipment

Blood pressure (BP; mmHg) was recorded through a finger cuff CNAP module connected to a LiDCOrapid monitor [105]. The BP signals were sampled on a beat by

Table 6.2: Datasheet information for subject group. A sample datasheet can be found in Appendix A. A green highlighted row denotes the patients where recordings were successful. Date of implantation represents the date the VAD was inserted. For the diagnosis column, 1= Ischaemic cardiomyopathy and 2= Non-ischaemic cardiomyopathy. PI is the pulsatility index obtained from the LVAD's external display. The subject group had a mix of HeartMate 2 and 3's inserted, the HeartMate column reflects which model the patient has.

Study Identifier	Age	Gender	Date of Implantation	Diagnosis	Beta Blocker	VAD output (rpm)	PI	HeartMate model
V01	69	M	05-11-2013	1	N	9,400	5.6	2
V02	61	F	24-10-2022	-	-	5,500	3.5	3
V03	44	M	22-12-2022	1	Y	5,200	4.9	3
V04	25	M	01-04-2022	2	Y	5,200	4.5	3
V05	62	M	11-12-2017	-	-	9,000	7.1	2
V06	60	M	10-02-2020	-	-	6,000	3.0	3
V07	62	M	02-03-2020	2	N	5,300	3.2	3
V08	52	M	22-03-2021	-	-	5,700	4.4	2
V09	63	M	17-07-2017	-	-	10,400	4.4	2
V10	65	M	10-05-2021	-	-	5,800	2.4	3

Table 6.3: Datasheet information for control group.

Study Identifier	Age	Gender	Beta Blocker
C01	55	M	N
C02	37	M	N
C03	40	M	N
C04	56	M	N
C05	28	M	N
C06	27	M	N
C07	32	M	N
C08	33	M	N
C09	30	F	N
C10	-	M	N

beat basis, meaning a systolic, mean, and diastolic BP reading was taken at the peak of each heart beat. The acquisition equipment export data signals in a .lvu file format, which contain measurement signals in a binary form and any additional event markers noted during recording, to a USB memory stick. From the USB memory stick, the files were uploaded onto a PC. The .lvu files were then opened on a computer using LiDCOViewPro software, where they can be exported as .xlsx files (excel files), which were then imported into MATLAB for analysis. All data analysis was carried out in MATLAB.

6.3.3 Acquisition challenges

The unique shape and amplitude of BP waveforms observed in VAD patients makes it particularly challenging to obtain complete, accurate measurements of BP in clinics. The difficulty arises due to the low amplitude and infrequency of BP beats, both of which vary person to person, making it difficult to design algorithms that identify valid peaks. In VAD patients, invasive arterial catheters measurements are considered the gold standard for monitoring BP in VAD patients, but its use is limited to in-patients and cannot be performed quickly and easily during out-patient appointments. Currently, the Doppler ultrasound is the gold standard used to obtain BP measurements in out-patient appointments, but it is highly inaccurate, requires additional training and it's unclear if the number obtained corresponds to a mean or systolic pressure reading [20].

As detailed in Section 6.3.2, the non-invasive BP acquisition hardware works off the detection of beats. While there is residual pulsatility from the native ventricle, the strength of the "beat" can vary from day to day in the same patient. If the beats are weaker on the day of recording, like those shown in (c) in Figure 6.3, the BP measurement device might fail to record any BP signal. In our subject group of ten, BP recordings were successfully obtained from four patients, giving a 40% success rate. This is significantly lower than that observed in other clinical trials using similar finger cuff based technology to measure BP in VAD patients. [113] used the Nexfin BP measurement device, noting a 93% success rate (29 out of 31 patients). [63] a pulse oximeter with a plethysmogram, noting a success rate of 87.5% (7 out of 8 patients) in phase I and 98.4% in phase II (62 out of 63 recordings) . [191] used digital pulse oximetry combined with manual sphygmomanometry to estimate BP, and found it has a success rate of 93% (28 out of 30 patients) initially, but could determine accurate BP in the 2 unsuccessful patients on subsequent visits once the technique was adapted to account for their unique physiological conditions.

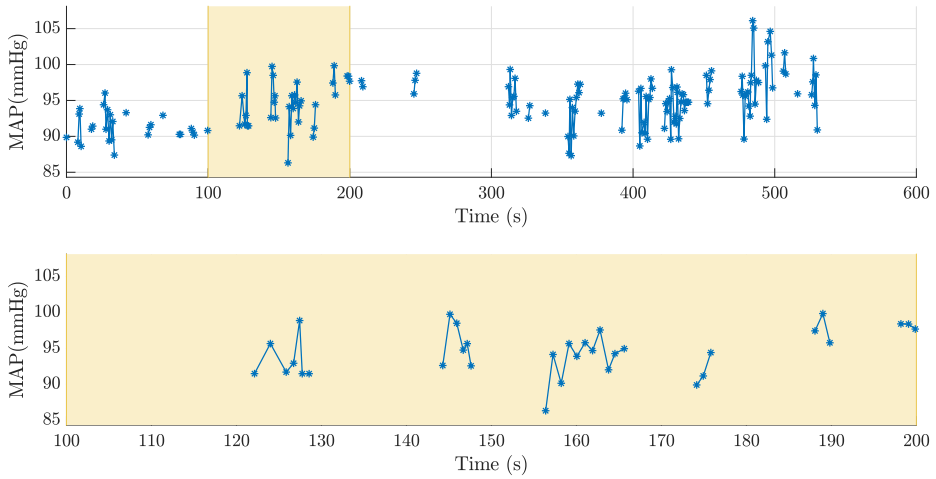

Figure 6.5: Example of an irregularly sampled, sparse, MAP signal from a VAD patient

6.4 Assessing Mayer wave identifiability in irregularly sampled, sparse data

Another challenge introduced by the measurement modality, as a result of the unique BP waveform of VAD patients, observed in the recordings, is the prevalence of sparse data. Sparse data occurs during the recording when the BP measurement device fails to identify a peak, leading to one, or more, missing data points. The degree to which sparsity occurs varies from patient to patient. An example of an extremely sparse MAP signal recorded is shown in Figure 6.5. At times the CNAP module is capable of identifying a single beat, while at others it can identify several consecutive beats.

6.4.1 The impact of sparse date on the MAP frequency spectrum through a test case

Unfortunately, the BP measurement device failed to capture the complete MAP signal in some subjects. Nonetheless, the aim of the study is to ascertain the presence, or absence, of a 0.1Hz wave in the MAP signal. In an attempt to utilise all datasets recorded, the effect of various interpolation methods on the frequency spectrum is investigated. Considering that the "true" spectrum of the VAD patient's MAP signal is unknown, the EuroBaVar dataset (see Section 4.4.1) has been employed to test a variety of interpolation methods[99]. Unlike the MAP signals recorded in the trial, the EuroBaVar dataset has two complete ten-minute, beat-by-beat, MAP signals for 21 subjects [99].

For an interpolation method to be useful in the current application, it must not add frequency components around the region of interest, i.e. $0.1Hz$. To validate the interpolation methods, the frequency spectrum for the complete signal is obtained, random data points were removed, then the frequency spectrum of the sparse dataset was obtained. The complete and sparse frequency spectra were compared to determine two things: (a) the level of sparsity that can occur before it is no longer possible to identify a 0.1Hz wave, and (b) the effect of interpolation on the frequency range of interest.

For this investigation, 4 of the EuroBaVar datasets were used [99], files with identifiers: A004, A005, B003, B004, were selected.
The MAP signals were interpolated onto a regular time interval of 1s using spline, and then the frequency spectrum for the complete data sets were obtained using the FFT. Figure 6.6 shows both the time domain MAP signal and the frequency spectrum for all four cases. Subjects A005, B003 and B004 have $0.1Hz$ waves present, with varying prevalences.

To test the effect of sparse data on the frequency spectrum, roughly 50%, 70% and 90% of data, in each case, were removed. Two interpolation methods were explored:

- Spline interpolation: Is a piecewise function that fits low-degree polynomials to small subsets of data throughout the complete dataset.
- Zero order hold interpolation: Pads the missing data points with the last known value. A crude interpolation method, but normally introduces extremely low frequency parasitic dynamics, which would ideally not cloud our region of interest.

Unlike the traditional use of interpolation, the objective of data interpolation here is not centred around reproducing an accurate time-domain MAP signal. Instead, the focus is on minimising the introduction of parasitic frequency components around 0.1Hz. To examine the introduced frequency components by various interpolation techniques, the wavelet transform for each method was obtained. Wavelet transforms are a useful tool to investigate the changes of signal frequency over time. The Wavelet transform shows both the frequencies present and the time corresponding to those frequencies. Appendix C shows the time domain signals, along with the resulting Wavelet transform and frequency spectrum plots for all four datasets, with vary degrees of sparsity.

When analysing cases where approximately 30% and 50% of the data is authentic, such as Figures 6.8 and 6.7, the frequency spectrum obtained using both spline

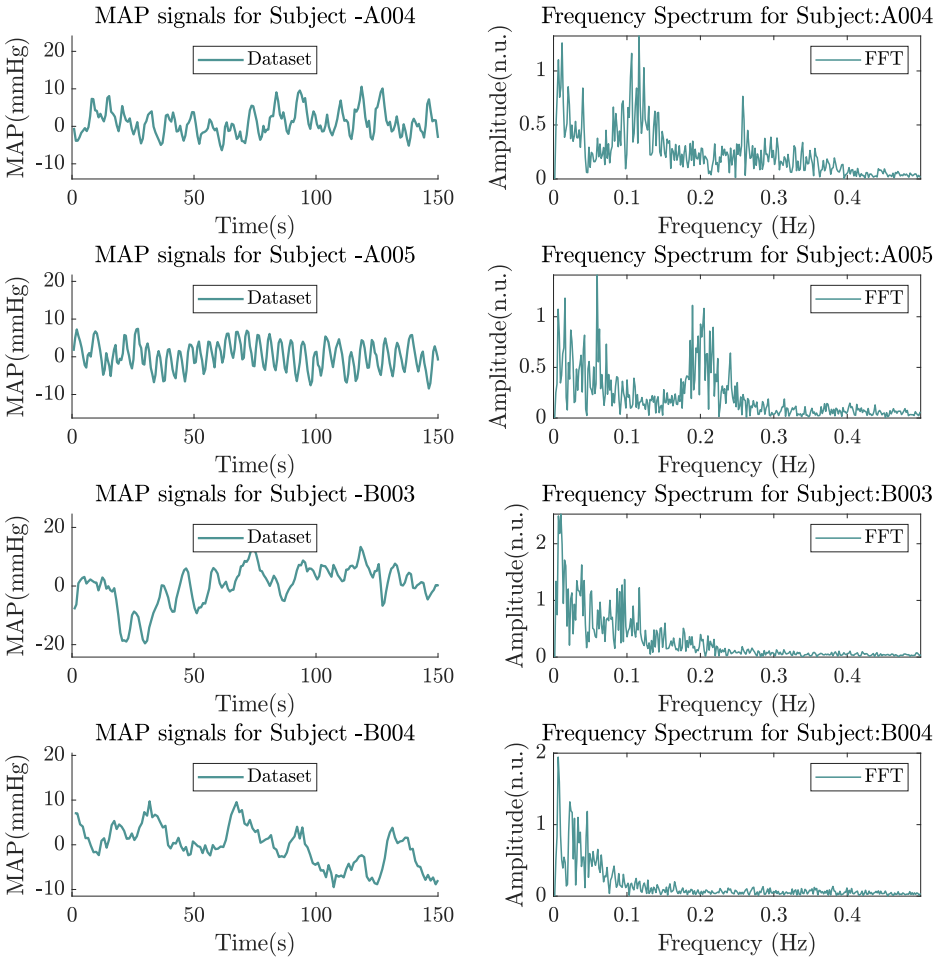

Figure 6.6: Frequency spectrum for the complete MAP dataset

interpolation and ZOH interpolation are very similar. For the cases where 30% and 50% of the data is authentic, there are no significant frequency components added to the region of interest. Consequently, any peaks observed in the region of interest can be considered a direct result of the underlying MAP signal, with the regions of interest unaffected by the interpolated data points. However, considering the scenarios where approximately 10% of the data is authentic, like Figure 6.9, this is not the case. While the spline interpolation method does not add additional data in the frequency range of interest, the peak around $0.1Hz$ has a lower amplitude compared to the frequency spectrum of the complete dataset. Additionally, the occurrence of large gaps between data points results in the interpolation of large, low order polynomials in these gaps. This results in pronounced peaks in the region of $0Hz$ to $0.05Hz$, making it more difficult to identify peaks centred around $0.1Hz$. This effect is further visualised in

the Wavelet transforms in Figure 6.9 and Appendix C in the cases where there is 10% authentic data, where the $0Hz$ to $0.05Hz$ regions are visible as having strong frequency components and all other frequency components appear to be weak, or non-existent.

It is important to note that, in the case of 10% authentic data, the reduced amplitude of a $0.1Hz$ component is observed when using both spline and ZOH, such as observed in Figure 6.9. Therefore, in some cases, it may be concluded that there is no $0.1Hz$ wave present when the frequency spectrum of the complete dataset suggests the contrary.

6.5 Results

In this section, an overview of the findings from both the animal and human studies is presented. Both the frequency spectrum of the sheep and human data will be presented and analysed. The primary focus of the analysis will be to determine if there is a $0.1Hz$ centred peak observed in each case. Subsequent statistical analysis will be employed to determine both the magnitude of the differences found between the subject and control groups, and the statistical significance of the results. Appropriate tests will be selected based on the sample size and number of groups in the studies.

6.5.1 Animal study

The acquisition software of the pre-clinical trial recorded regularly sampled BP signals, with no interpolation methods required. The FFT was employed to obtain the frequency spectrum of the 12 BP signals recorded in the sheep. The resulting plots are shown in Figures 6.10 through 6.13. Each plot was analysed to ascertain whether, or not, a peak centred at $0.1Hz$ was observed, Table 6.4 shows the resulting classification of the 12 datasets.

The results of Table 6.4 are summarised in a 2x2 contingency table, to allow for analysis of the interrelationship between the two groups. The contingency table is a table showing the distribution of one variable in rows and another in columns, used to study the correlation between the two variables, shown in Table 6.5.

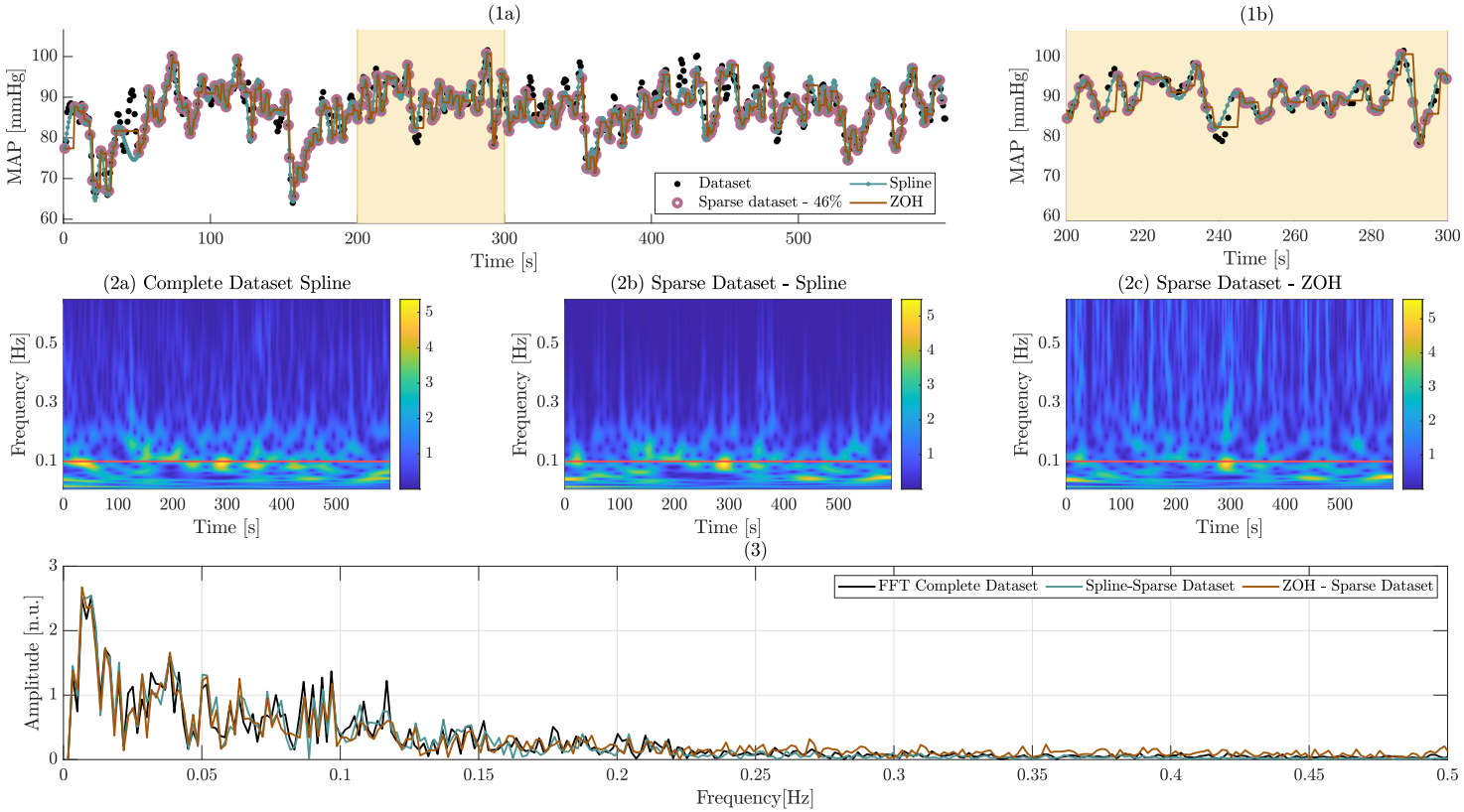

Figure 6.7: Eurobavar Subject B003 - investigating the effect of interpolation on the FFT in the case of sparse data with 50% of the original complete dataset

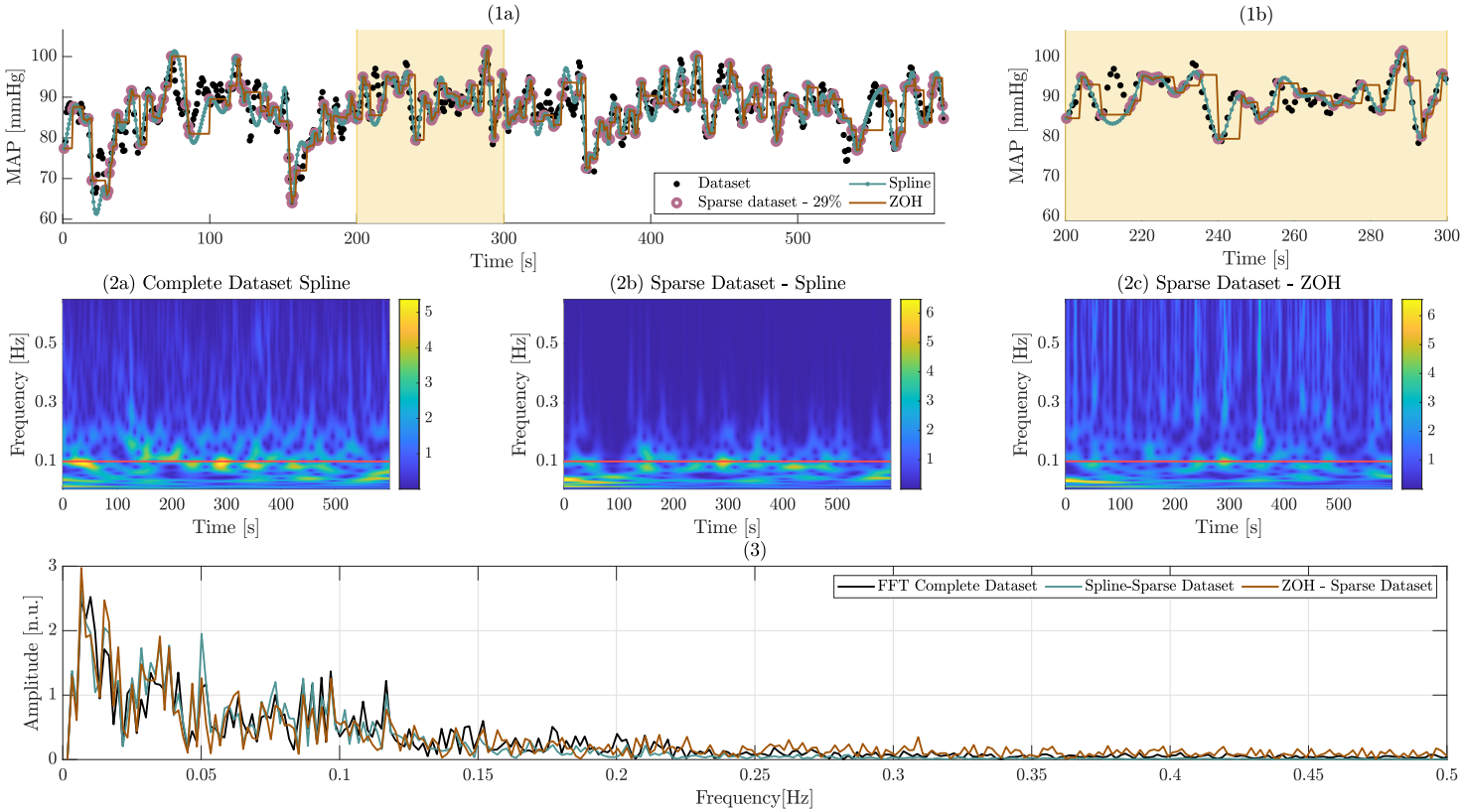

Figure 6.8: Eurobavar Subject B003 - investigating the effect of interpolation on the FFT in the case of sparse data with 30% of the original complete dataset

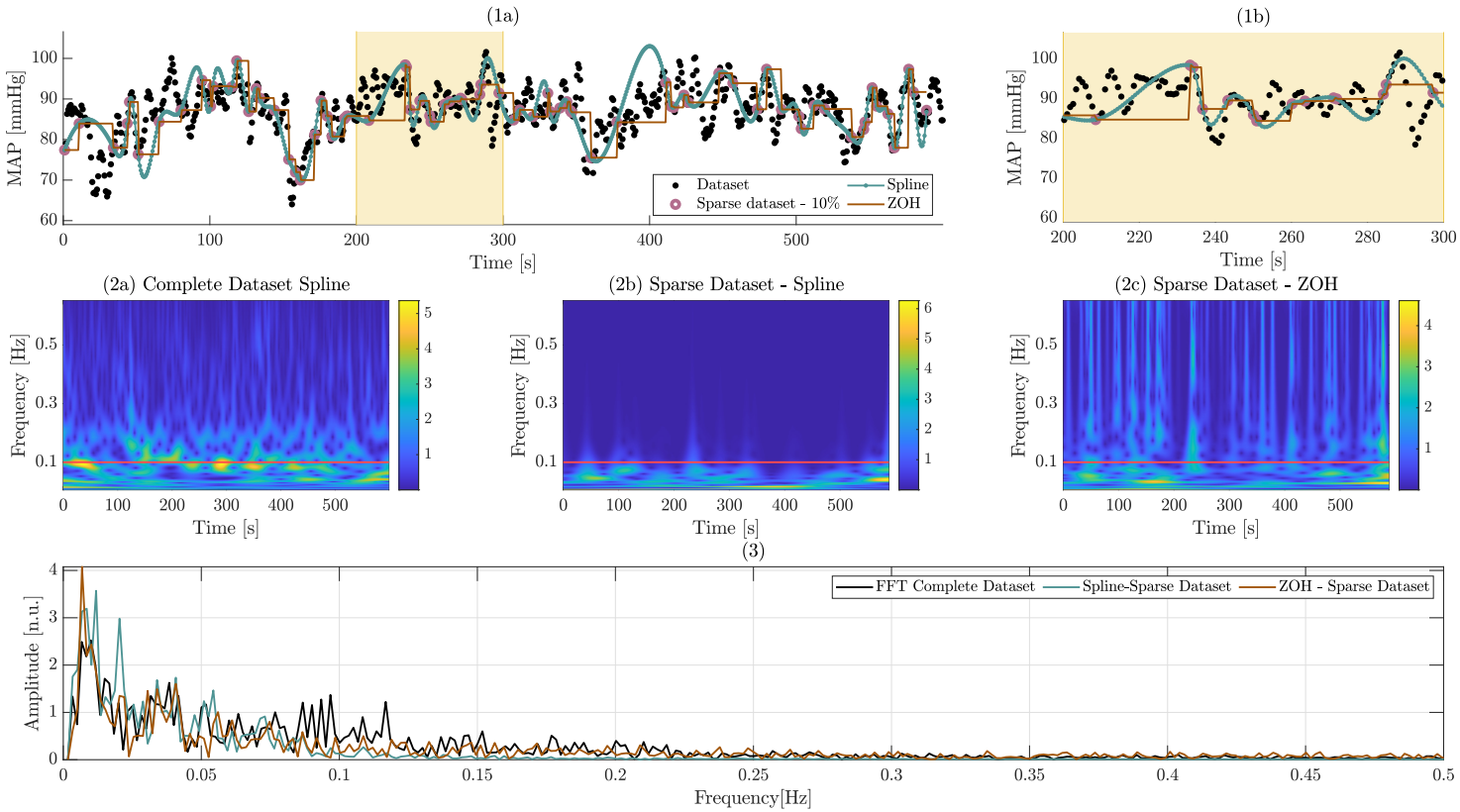

Figure 6.9: Eurobavar Subject B003 - investigating the effect of interpolation on the FFT in the case of sparse data with 10% of the original complete dataset

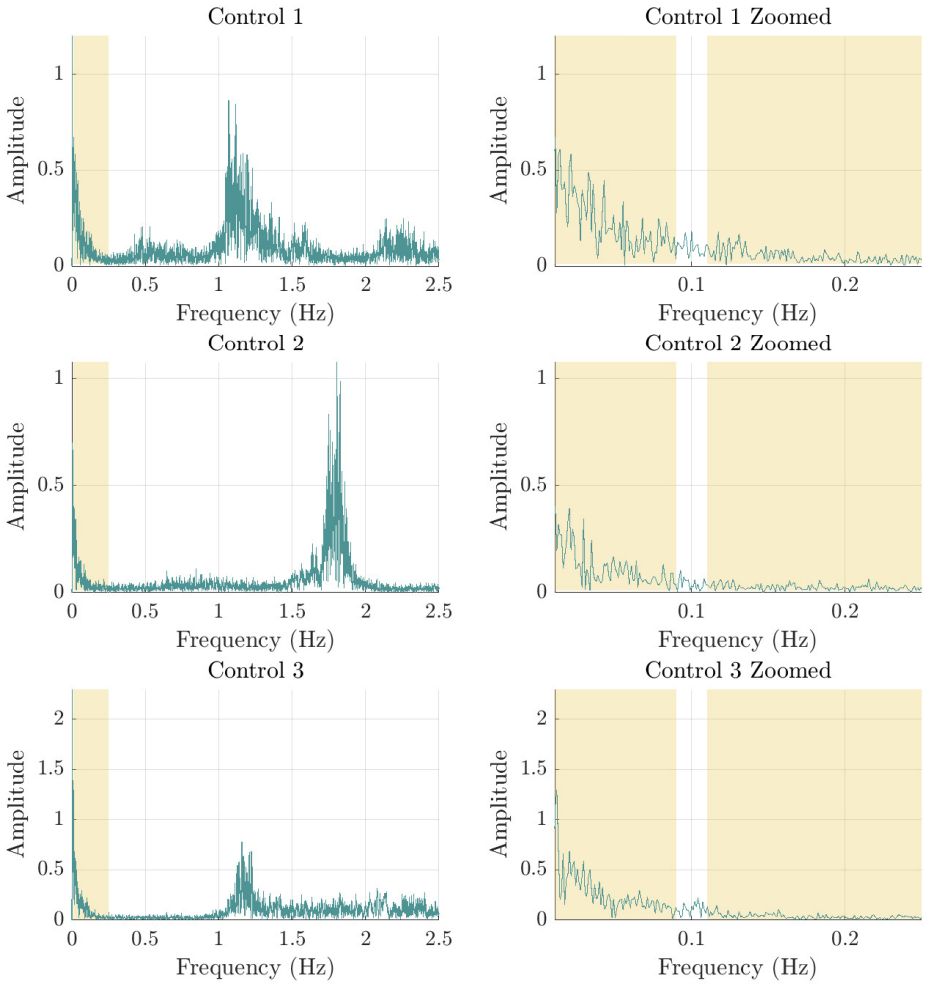

Figure 6.10: Control subjects 1 through 3

Table 6.4: Which sheep have Mayer waves?

Control Group		**CHF Group**	
Subject	Mayer wave Present?	Subject	Mayer wave present?
1	Yes	1	Yes
2	No	2	Yes
3	No	3	No
4	No	4	No
5	No	5	No
6	No	6	Yes
Total	1	**Total**	3

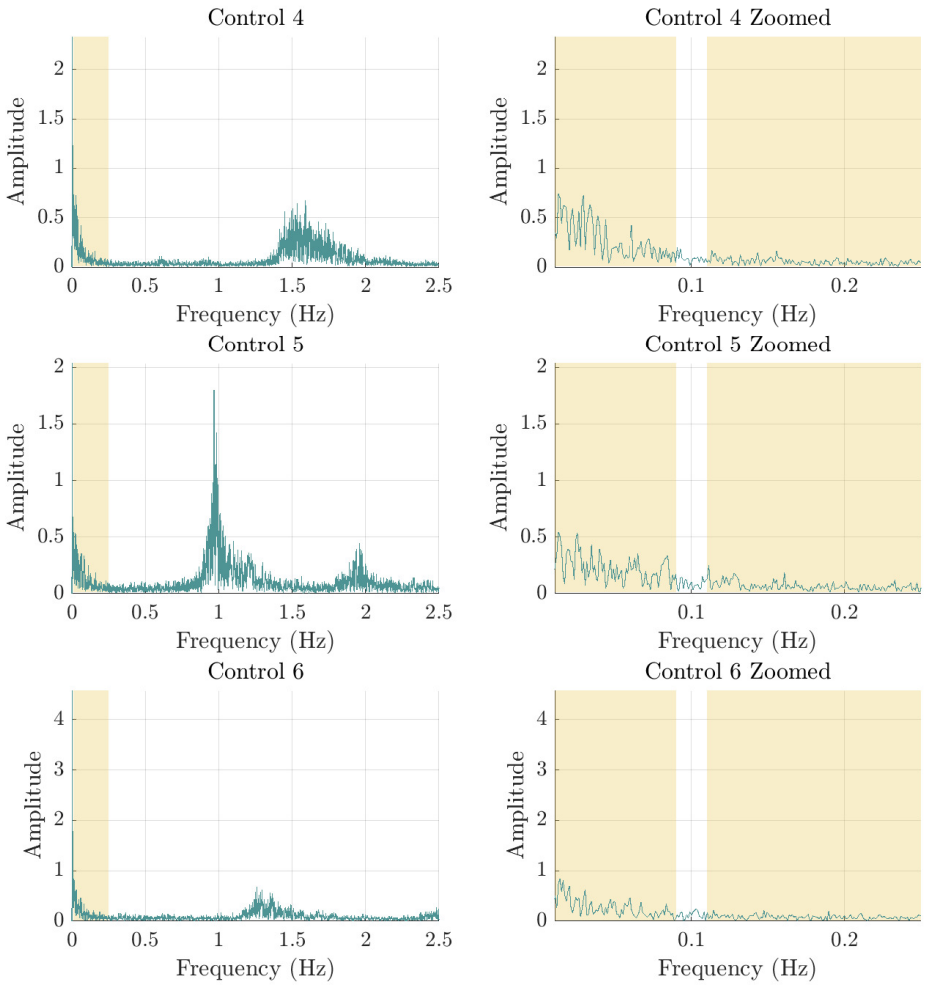

Figure 6.11: Control subjects 4 through 6

Table 6.5: Contingency table corresponding to the results shown in Table 6.4

	CHF	**Control**	**Total**
Mayer Waves	3	1	4
No Waves	3	5	8
Total	6	6	12

An effect size test, called the odds ratio (OR), was applied to the contingency table[180]. Effect size tests help to determine the magnitude of differences found, irrespective of sample size. The odds ratio test was chosen due to it's ability to accurately account for 2x2 contingency tables and as they are frequently used in epidemiological studies.

First, the odds in the CHF group is calculated:

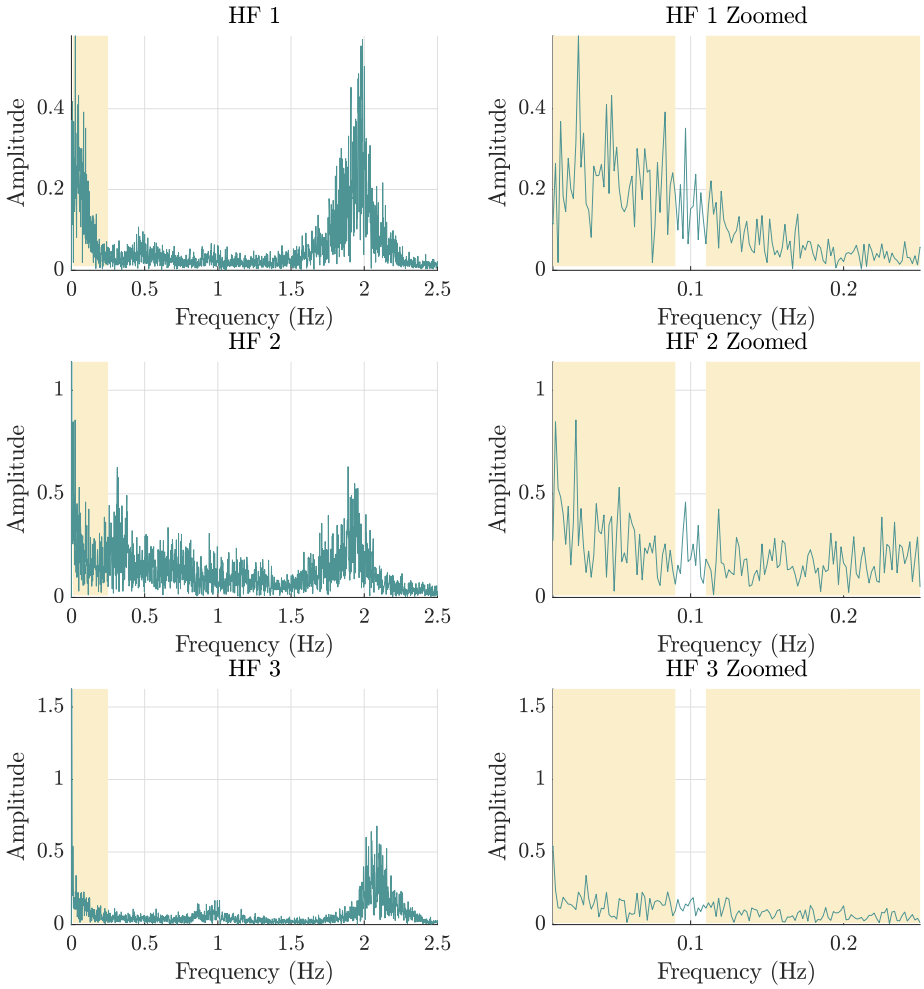

Figure 6.12: Control subjects 1 through 3

$$\text{Odds in CHF group} = \frac{\text{HF with Mayer waves}}{\text{HF without Mayer waves}} = \frac{3}{3} = 1 \tag{6.1}$$

Then, the odds in the Control group is calculated:

$$\text{Odds in Control group} = \frac{\text{Control with Mayer waves}}{\text{Control without Mayer waves}} = \frac{1}{5} = 0.2 \tag{6.2}$$

Finally, the odds ratio and the confidence interval is calculated:

$$\text{Odds ratio (OR)} = \frac{\text{Odds in CHF group}}{\text{Odds in Control group}} = \frac{1}{0.2} = 5 \tag{6.3}$$

$$\text{Upper 95\% CI} = e^{ln(OR)+1.96\sqrt{1/3+1/1+1/3+1/5}} = 72.7667 \tag{6.4}$$

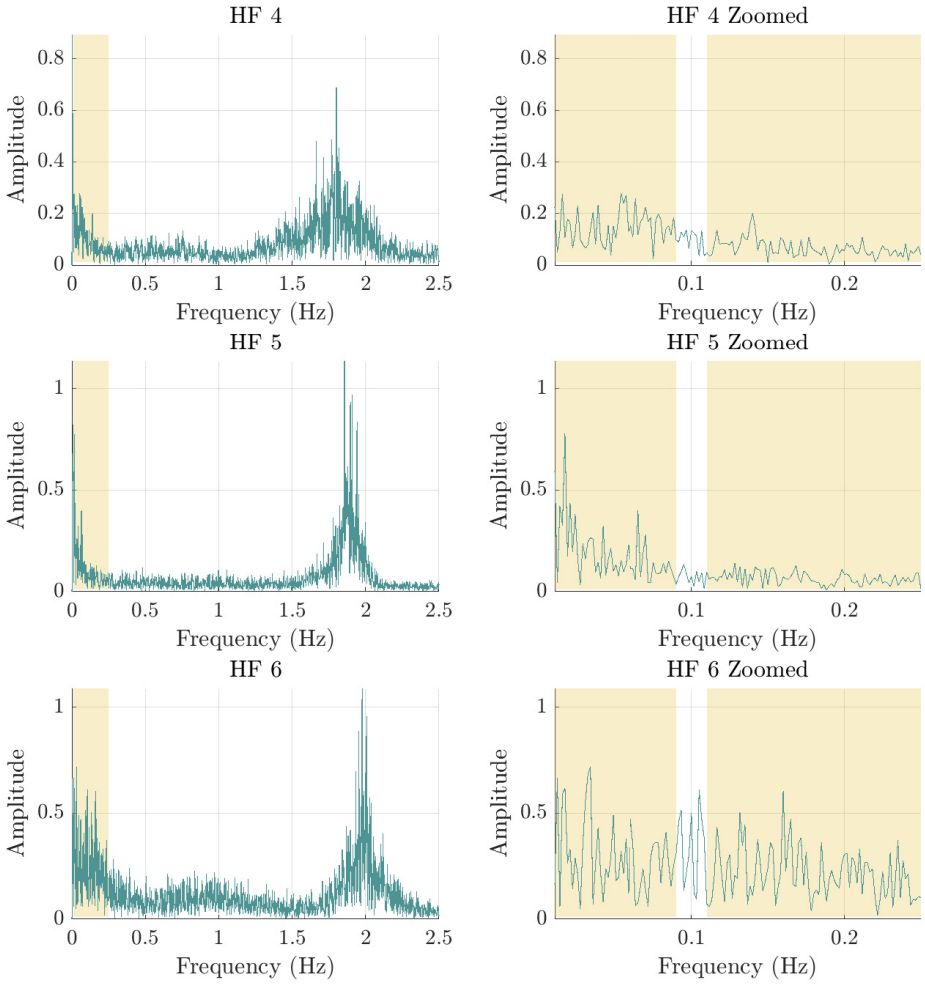

Figure 6.13: Control subjects 4 through 6

$$\text{Lower 95\% CI} = e^{ln(OR)-1.96\sqrt{1/3+1/1+1/3+1/5}} = 0.3436 \tag{6.5}$$

The odds ratio for the animal study was calculated to be OR $= 5$, with a 95% confidence interval of $[0.3436\ 72.7667]$. An odds ratio greater than 1 implies greater odds of observing Mayer waves in CHF group than the control group [180]. The confidence interval provides an expected range for the true odds ratio of the population. The confidence interval is particularly informative for studies with smaller sample sizes. It is important to note that a confidence interval containing 1, as calculated in this case, indicates that the calculated odds ratio is not statistically significant.

Another approach to assess statistical significance is Fisher's Exact test [43]. Fisher's Exact test is specifically designed for a 2x2 contingency table in studies with less

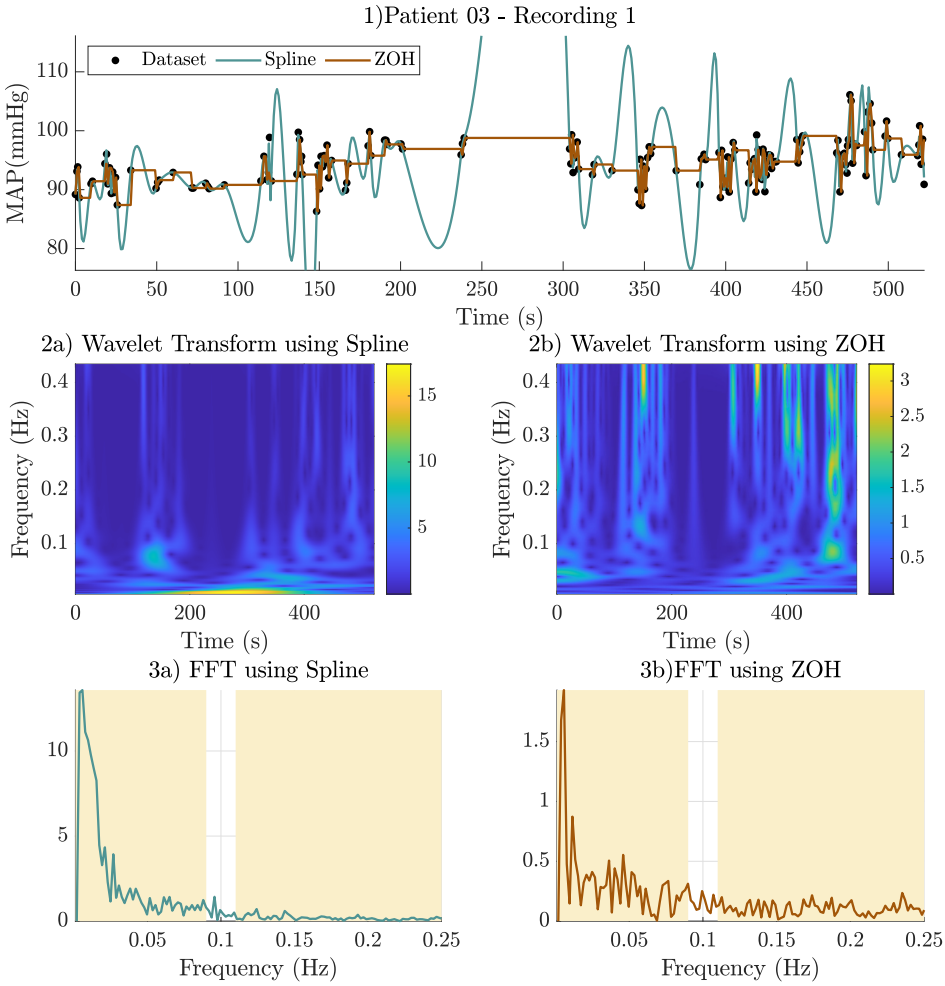

Figure 6.14: Patient 2 - Recording 1

than 20 participants [43]. The Fisher's exact test yields a p value $= 0.5455$ at a 95% confidence level. A p value greater than 0.05, as shown above, indicates that the results are not statistically significant.

6.5.2 Human study

The human study resulted in 4 successful BP recordings from 10 VAD patients. Among the 4 successful recordings there are varying degrees of sparsity, with the sparsest having approximately 30% of the data recorded over the recording period. The recorded data for this case can be seen in Figure 6.14 plot 1.

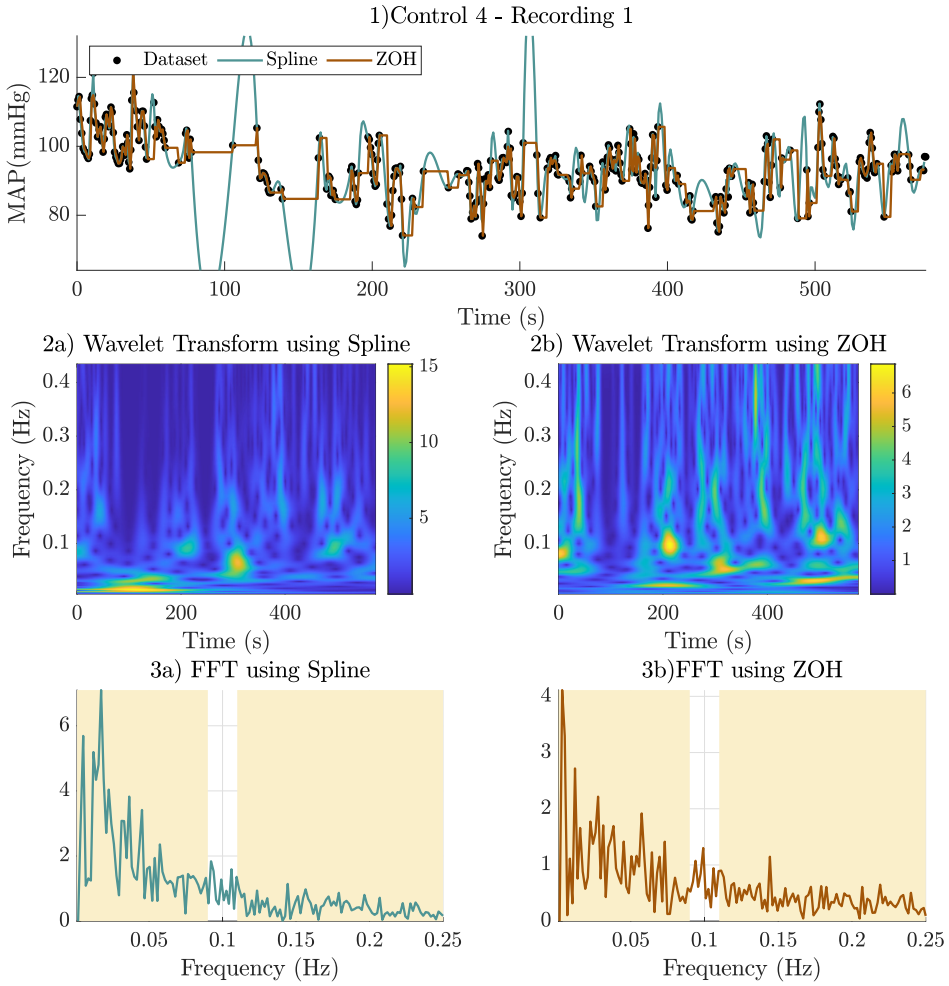

Figure 6.15: Control 4 - Recording 1

Missing data also occurs in the control group, but to a lesser extent. Missed data can be caused by a number of sporadic movements caused by the subject, such as finger tapping, shuffling of their position in the chair, etc. The shifting in position of the subject's hand causes the finger cuff to move, which can result in a loss of contact between the cuff's sensor and the subject's finger. An example of missing data in the control group is in Figure 6.15.

Using the interpolation methods detailed in Section 6.4.1, the BP signals for all study subjects were interpolated onto regular time intervals. Subsequently, both the Wavelet transform and the FFT were obtained for each case. The plots for all 14 study subjects (4 VAD, 10 controls) can be found in Appendix B.

Table 6.6: Which subjects have Mayer waves?

Control Group			VAD Group				
Subject	Mayer wave Present?		Subject	Mayer wave Present?			
	R1	R2		R1	R2	R3	R4
C01	No	No	V01	Yes	Yes	No	No
C02	Yes	Yes	V02	-	-	-	-
C03	No	No	V03	No	No	-	-
C04	Yes	Yes	V04	Yes	Yes	-	-
C05	Yes	No	V05	-	-	-	-
C06	Yes	Yes	V06	-	-	-	-
C07	Yes	-	V07	No	No	-	-
C08	No	No	V08	-	-	-	-
C09	Yes	No	V09	-	-	-	-
C10	-	-	V10	-	-	-	-
Total	6	3	**Total**	2	2	0	0

Table 6.7: Contingency table corresponding to the results shown in Table 6.6

	VAD	**Control**	**Total**
Mayer Waves	6	2	8
No Waves	4	2	6
Total	10	4	14

Similar to Section 6.5.1, the frequency spectra were analysed to determine the presence, or absence, of a 0.1Hz wave. The results of this analysis is shown in Table 6.6.

The results of Table 6.6 were summarised in a 2x2 contingency table, shown in Table 6.7. The odds ratio for the human study is OR $= 0.667$ with a confidence interval $[0.065\ 6.906]$. An odds ratio less than 1 suggests that there is not a higher incidence of Mayer waves in the subject group in comparison to the control group. However, the CI contains 1, meaning that the results are not statistically significant. The Fisher's exact test yielded a p value $= 1$ at a 95% confidence interval, reiterating that the result is not considered statistically significant.

6.6 Observations and limitations

It should be noted, that this study is an exploratory study in a number of ways, the first being the method of measurement. While the gold standard for BP in VAD patients is a catheter recording, they are only used for in-patients, leading to the use of a non-invasive BP monitor. There was a large amount of uncertainty around

whether or not it is possible to get non-invasive BP recordings over a period of time in VAD patients. Upon reviewing the state of the art on non-invasive BP recordings in VAD patients, the BP measurement device operates on an algorithm based on similar principles to those discussed in Section 6.3.3 [113], suggesting that the BP measurement device selected would achieve a similar success rate.

While it was anticipated that the recordings may fail in a few cases, the low success rate of 40% was unexpected. Consequently, the BP measurement device introduced a subject selection bias that must be considered when analysing the recorded data. This does have a knock-on effect on all statistical analysis carried out. Considering that the BP measurement device was not able to detect the beats in certain VAD patients, would suggest that the patients' residual contractions were too small for the BP measurement device to register. These unmeasured subjects were subjects with less residual pulsatility, i.e, that the subjects whose BP signals would potentially show Mayer waves, according to the original hypothesis.

In addition, it is important to consider the use of beta blockers in several subjects. Beta blockers have been known to attenuate low frequency components, such as Mayer waves [158]. As shown in Table 6.2, of the four successful recordings, two were on beta blockers (V03 and V04). While V04's BP recordings showed Mayer waves, the amplitude of the $0.1Hz$ peak was quiet low. In the case of V03, there is a small peak centred at 0.1Hz, however its amplitude isn't higher than those surrounding it, hence it was concluded that Mayer waves were not present. While this may be a case where no Mayer waves are present, it is also worth noting that the wave itself may have been attenuated by the beta blockers.

6.7 Conclusions

This chapter outlines two studies designed to investigate the presence of Mayer waves as pulsatility decreases. As a result of the sparsity in some BP recordings, a brief analysis was conducted to assess the identifiability of Mayer waves in irregularly sampled, sparse data.

The analysis revealed that neither spline nor ZOH interpolation introduce additional frequency components to the region of interest for all three cases (10%, 30% and 50% of authentic data). However, when long periods of missing data occur, the spline method may introduce frequency components with significant peaks in the region

of 0 to $0.05Hz$, making it difficult to identify a peak centred at 0.1Hz. It is also noteworthy that, in the case of 10% residual data, the FFT using both spline and ZOH suggests an absence of Mayer wave in cases where the FFT for the complete dataset indicates their presence.

The results from the animal study align with work carried out in previous publications [143, 194], indicating that a higher incidence of Mayer waves occur with a decrease in pulsatility. While the data obtained in the animal study provided valuable insights, recording BP signals before and after CHF was induced would allow further investigation into whether, or not, the decrease in pulsatility could be a factor in the manifestation of Mayer waves.

Drawing any conclusions from the human study is challenging due to the low success rate in obtaining BP recordings from VAD patients, and the selection bias introduced by the BP measurement device. A more comprehensive study, potentially involving invasive BP recordings, is required before confirming or refuting the hypothesis.

7

Conclusion and future work

Contents

7.1 Summary and conclusions 133
7.2 Future work 135

This thesis presents a collection of work attempting to broaden the knowledge of the neural baroreflex and its functionality. Section 7.1 will present the conclusions reached through the analysis carried out in each study. Section 7.2 provides an overview of possible approaches for future work, based on the results shown in this thesis.

7.1 Summary and conclusions

The continual prevalence of hypertension among the global population, and associated risk for adverse events, calls for continued research into the body's regulation of blood pressure. As mentioned in Chapter 2, the majority of antihypertensive medications prescribed target the peripheral resistance branch of the baroreflex. The high percentage of unmanaged and resistant hypertension, among the adult population, suggests that alternative approaches need to be developed. In order to tackle blood pressure related problems, additional understanding of the neural baroreflex is required.

Chapter 3 proposes a protocol for the identification of the open loop dynamics for the neural baroreflex, using closed loop BP data. The protocol allows for the identification

of both time- and frequency- domain models, where the domain approach should be selected based on the specific application of the model. Additional understanding of the frequency characteristics of the neural baroreflex can aid the development of an alternative anti-hypertension treatment known as baroreflex activation therapy.

Another avenue of investigation, is the ability to detect changes in the functionality of the baroreflex. One well regarded measurement of functionality being the BRS estimation, where the current gold standard is invasive and unsafe to perform on patients with an array of medical conditions. While non-invasive alternatives are pivotal in the widespread monitoring of BRS, determining the accuracy of their results is equally so. Chapter 4 provides a theoretical-based evaluation of the reliability of a popular non-invasive BRS method. The analysis concludes that the continual overestimation observed in BRS methods obtained using the sequence method is due to the selection of the sequences themselves, and not the application of linear regression. It was also demonstrated that the degree to which the method overestimates the gain is linked to the level of noise present in the measurements. The noise could be measured in the synthetically generated case, but quantifying noise present during BP recordings is challenging. A secondary analysis concluded that recent refinements to the sequence selection process offer some improvement to BRS estimates, but still fails in the cases where large quantities of noise is present. The third limitation of the sequence method is its inability to obtain a BRS estimate in the impaired subject cases.

Understanding the baroreflex also aids in the identification and investigation of anomaly occurrences. Chapter 2 provides a comprehensive description of a baroreflex model, which is then extended to include both pulsatility and a compliance model in Chapter 5. Using the augmented model, the conditions for which LFOs occur were established. The analysis highlights the significant role played by increasing CNS gain in mediating the occurrence of LFOs, which can be initiated by an array of physiological stressors, such as Haemorrhage and hypoxia. The inclusion of pulsatility in the model through the use of an equivalent non linearity, representing a combination of the pulsatile BP signal and the baroreflex curve, reveals an overall decrease in baroreflex gain. When pulsatility is absent, or reduced, for example due to the insertion of a left ventricular assist device or turbine-based artificial heart, the analysis shows that a significant increase in BRS may occur. The physical manifestation of an increased BRS may lead to the development of CHF. When analysed, LFOs are observed when pulsatility is absent, due to the increase in BRS as a result of the reduction in pulsatility. This suggests that as pulsatility decreases, the likelihood of LFOs increases.

Chapter 6 builds on the analysis conducted in Chapter 5 by exploring experimentally, the hypothesis that a decrease in pulsatility leads to an increase in the occurrence of LFOs. The initial analysis carried out in the animal study, suggests an increased incidence of Mayer waves in sheep with CHF, compared to a control group. However, due to the inability to measure BP non-invasively in the majority of the human subject group, in this instance it is not possible to explore this hypothesis in VAD patients.

One overall conclusion of this work is that the insertion of LVADs, or turbine-based artificial hearts, while dealing with the reduction of blood flow in patients with CHF and other conditions, also reduces pulsatility. While the full benefits (or otherwise) of pulsatility are not completely understood, the analysis in this thesis suggests that it may help to modulate BRS in a favourable way i.e. a reduction in baroreflex gain. To this end, the detection, or absence, of Mayer waves may prove to be a useful diagnostic tool.

However, further work needs to be done to categorically verify the value of of Mayer waves as a diagnostic tool experimentally.

The studies presented in this thesis attempt to provide additional information regarding the neural baroreflex. Chapter 2 introduces the baroreflex and to what extent it has been modelled to date, while also providing explanations for a number of physiological terms and phenomenons. It also provides information on the state of the art of some of the topics discussed and investigated in the rest of this thesis. Chapter 3 aims to propose a protocol to identify characteristics of the neural baroreflex, with the method based firmly using the control sciences. While Chapter 4 provides a theoretical analysis of a popular non invasive method to assess the functionality of the baroreflex. Chapter 5 uses and extends existing baroreflex models in an attempt to provide additional understanding on the occurrence of Mayer waves. The hypothesis that is a result of this analysis is then examined experimentally and clinically in Chapter 6. While each study doesn't directly follow on from the previous one, they all contribute building blocks to the understanding of the neural baroreflex. They either shed light on its mechanisms or endeavour to ensure accurate assessment of its function.

7.2 Future work

The work carried out in this thesis leaves room for future work in the form of several projects:

- The protocol developed in Chapter 3 serves as a step towards understanding how to obtain open loop dynamical information from closed loop data on the neural baroreflex. A larger study can be carried out using the proposed protocol to provide conclusions on the frequency characteristics of the neural baroreflex.

- The work carried out in Chapter 4 provides analysis on the sequence method and its current refinements, concluding that in certain cases large amounts of noise in the output signal can lead to large overestimations of the gain. To determine if the inclusion of baroreflex stimulating movements would help to improve the accuracy of the sequence method, an additional study must be carried out. The study would record BP measurements non-invasively, while the subjects complete a number of planned, baroreflex stimulating movements, such as Valsalva maneuver, timed sit-to-stand manoeuvre, or the neck chamber technique is applied.

- In addition, a study comparing BRS estimates obtained using non-invasive methods with BRS estimates obtained using the Oxford method, could be carried out. Not only would it allow for comparison of BRS estimated obtained invasively and non-invasively, it would potentially allow for the definition of a BRS threshold used to identify an impaired baroreflex.

- The inability to obtain non-invasive BP recordings in VAD patients prevented any definitive conclusions from being drawn in Chapter 6. To investigate the hypothesis, a study where the experimental protocol in Chapter 6 is replicated with invasive, arterial line BP measurements could be carried out. However, considering invasive BP recordings are only carried out on in-patients, careful consideration should be given to the patient criteria and exclusion criteria. Such criteria should account for adequate time post VAD implantation, to allow for anaesthesia, and other medications that can attenuate Mayer waves, to leave the patient's system.

Appendices

A

Clinical trial documentation

Contents

A.1 Consent forms and information leaflets 141
A.1.1 Patient 141
A.1.2 Participant 145
A.2 Datasheet 148

A.1 Consent forms and information leaflets

A.1.1 Patient

Mater Misericordiae University Hospital
Sisters of Mercy

Ospidéal Ollscoile Mater Misericordiae
Siúracha na Trócaire

Eccles Street, Dublin 7, Ireland.
Tel: +353 1 8032000 Fax: +353 1 8032404 Email: mmh@mater.ie Web: www.mater.ie

Not for prescription purposes

PATIENT INFORMATION LEAFLET

1. **Research Study Title**
   Blood Pressure Variability in the Presence of Continuous Flow Left Ventricular Assist Devices

2. **What is the purpose of the research study?**
   The aim of the study is to determine whether natural signals that control blood pressure variability are amplified in the presence of continuous flow left ventricular assist devices.

3. **Why have I been chosen?**
   You have had a Heartmate II left ventricular assist device implanted.

4. **Who is organising the research study?**
   This study is organized by Prof. Niall Mahon (Mater Hospital) and Prof. John Ringwood (NUI Maynooth).

5. **What will happen to me if I take part?**
   Your participation is entirely voluntary. If you initially decide to take part you can subsequently change your mind without difficulty. This will not affect your future treatment in any way. If you agree to participate, we will record your blood pressure and heart rate over two 10 minute periods in a single clinic session. There are no other requirments or subsequent visits or sample collection.

6. **Are there other ways of treating my condition?**
   Participation in this study will not affect your current treatment.

7. **Are there any disadvantages in taking part in this research study?**
   There are no disadvantages in taking part in this study.

8. **What are the possible risks of taking part?**
   There are no risks associated with the recordings.

9. **What are the possible benefits of taking part?**
   You will not benefit directly from taking part in this study but the information we will obtain may provide further knowledge with regard to human physiology in the presence of continuous flow ventricular assist devices.

10. **Is my doctor being paid for including me in the research study?**
    No.

11. **Will patient expenses be met?**
    No expenses will be incurred

12. **What happens when the study stops?**
    This is a one off sample and you will not be asked for any follow up samples.

Eccles Street, Dublin 7, Ireland.
Tel: +353 1 8032000 Fax: +353 1 8032404 Email: mmh@mater.ie Web: www.mater.ie

13. **Are there any restrictions on what I might eat or do?**
No

14. **What if something goes wrong?**
It is extremely unlikely that anything will go wrong recording blood pressure over 10 minute periods. If you are harmed due to someone's negligence, then you may have grounds for a legal action. Regardless of this, if you have any cause to complain about any aspect of the way you have been approached or treated during the course of this research study, the normal Health Service complaints mechanisms are available to you

15. **Confidentiality – who will know I am taking part in the research study?**
All information, which is collected about you during the course of the research will be kept strictly confidential. All information about you, which leaves the hospital, will contain no information as to your identity so that you cannot be recognised from it. Your identity will remain confidential. A study number will identify you. Your name will not be published or disclosed to anyone. An encrypted password-protected file linking your code to your hospital number will be kept on site at the Mater Hospital, will not leave this site, and will be destroyed at the end of the study. The anonymized files will made be available to future researchers and further work, based on the project, can incorporate data with reference to ethical approval and intellectual property rights for up to 10 years.

16. **GP Notification**
Your GP will normally be informed that you are taking part in this study.
If this is a problem for you, you should discuss it with your study researcher

17. **Hospital Research Ethics Committee Approval**
The Mater Hospital Research Ethics Committee have reviewed and approved this study

18. **What will happen to the results of the research study?**
Any signficant findings with regard to blood pressure variability in the presence of continuos flow ventricular assist devices will be published in peer-reviewed scientific/medical journal

19. **Procedure to be used if assistance or advice is required**
In the event of a research related question please contact Elaine Gilroy, Cardiovascular Research Office, Mater Misericordiae University Hospital, tel 01 8034741.

20. **Voluntary Participation**
It is up to you to decide whether to take part or not. If you do decide to take part you will be given an information leaflet and consent form. Even if you do decide to take part, you are free to withdraw at any time and without giving a reason. In the event that you wish to withdraw data will be deleted. This will not affect the standard of care you will receive. Your doctor will not be upset if you decide not to take part.

21. **If you have already been involved in a drug trial study within the past twelve weeks (three months) you are not eligible to take part in this research study**
On behalf of the Investigators we wish thank you for considering taking part in this research study.

Directors: Mr. John Morgan (Chairman), Fr. Kevin Doran, Mr. Eamon Clarke, Mr. Don Mahony, Sr. Margherita Rock, Mr. Martin Cowley, Mr. Kevin O'Malley, Mrs. Anne Carrigy, Mr. Brian Conlon, Sr. Eugene Nolan, Dr. Anthony Clarke, Mr. Kevin Murphy, Dr. Nuala Healy.

Registered in Ireland No. 351402 **Charity No.** CHY203 **Registered Office:** Eccles Street, Dublin 7.

Mater Misericordiae University Hospital
Sisters of Mercy

Ospidéal Ollscoile Mater Misericordiae
Siúracha na Trócaire

Eccles Street, Dublin 7, Ireland.
Tel: +353 1 8032000 Fax: +353 1 8032404 Email: mmh@mater.ie Web: www.mater.ie

Not for prescription purposes

CONSENT FORM

Title of Research Study: Blood Pressure Variability in the Presence of Continuous Flow Left Ventricular Assist Devices
Name of Sponsor: University College Dublin

Patient Name:
Name of Doctor and Telephone Number: Dr. Niall Mahon, tel: (01) 8032000

1. I confirm that I have read and understood the information leaflet dated…….. ...for the above research study and received an explanation of the nature, purpose, duration, and foreseeable effects and risks of the research study and what my involvement will be ☐

2. I have had time to consider whether to take part in this research study. My questions have been answered satisfactorily and I have received a copy of the Patient Information Leaflet ☐

3. I understand that my participation is voluntary (my choice) and that I am free to withdraw at any time without my medical care or legal rights being affected ☐

4. I have to the best of my knowledge informed the investigator of my previous or present illnesses and medication and of any consultation that I have had with a doctor for the last four months. I have not participated in any other clinical trial in the past three months ☐

5. I understand that my General Practitioner Dr…… will be informed by Prof. Niall Mahon that I am taking part in this research study ☐

6. I will contact the research investigator immediately if I suffer any unexpected or unusual symptoms during the research study. I will notify the research investigator if I have any other medical treatments or procedures during the course of the research study ☐

7. I am willing to allow access to my medical records by the principal and co-investigators at the Mater Misericordiae University Hospital with the understanding that confidentiality will be maintained. ☐

8. I agree to take part in the above research study ☐

……	……	……
Name of Patient (in block letters)	Date	Signature
……	……	……
Name of Doctor/Researcher	Date	Signature
……	……	……
Doctor/Researcher	Date	Signature

1 copy for patient, 1 copy for researcher, 1 copy to be inserted in hospital notes

A.1.2 Participant

Mater Misericordiae University Hospital
Sisters of Mercy

Ospidéal Ollscoile Mater Misericordiae
Siúracha na Trócaire

Eccles Street, Dublin 7, Ireland.
Tel: +353 1 8032000 Fax: +353 1 8032404 Email: mmh@mater.ie Web: www.mater.ie

Not for prescription purposes

PARTICIPANT INFORMATION LEAFLET

1. **Research Study Title**
   Blood Pressure Variability in the Presence of Continuous Flow Left Ventricular Assist Devices

2. **What is the purpose of the research study?**
   The aim of the study is to determine whether natural signals that control blood pressure variability are amplified in the presence of continuous flow left ventricular assist devices.

3. **Why have I been chosen?**
   You are considered healthy and well matched to a patient in the study.

4. **Who is organising the research study?**
   This study is organized by Prof. Niall Mahon (Mater Hospital) and Prof. John Ringwood (NUI Maynooth).

5. **What will happen to me if I take part?**
   Your participation is entirely voluntary. If you initially decide to take part you can subsequently change your mind without difficulty. This will not affect your future treatment in any way. If you agree to participate, we will record your blood pressure and heart rate over two 10 minute periods in a single clinic session. There are no other requirments or subsequent visits or sample collection.

6. **Are there any disadvantages in taking part in this research study?**
   There are no disadvantages in taking part in this study.

7. **Are there any disadvantages in taking part in this research study?**
   There are no disadvantages in taking part in this study.

8. **What are the possible risks of taking part?**
   There are no risks associated with the recordings.

9. **What are the possible benefits of taking part?**
   You will not benefit directly from taking part in this study but the information we will obtain may provide further knowledge with regard to human physiology in the presence of continuous flow ventricular assist devices.

10. **Is my doctor being paid for including me in the research study?**
    No.

11. **Will patient expenses be met?**
    No expenses will be incurred

12. **What happens when the study stops?**
    This is a one off sample and you will not be asked for any follow up samples.

B.1.4 Control 4

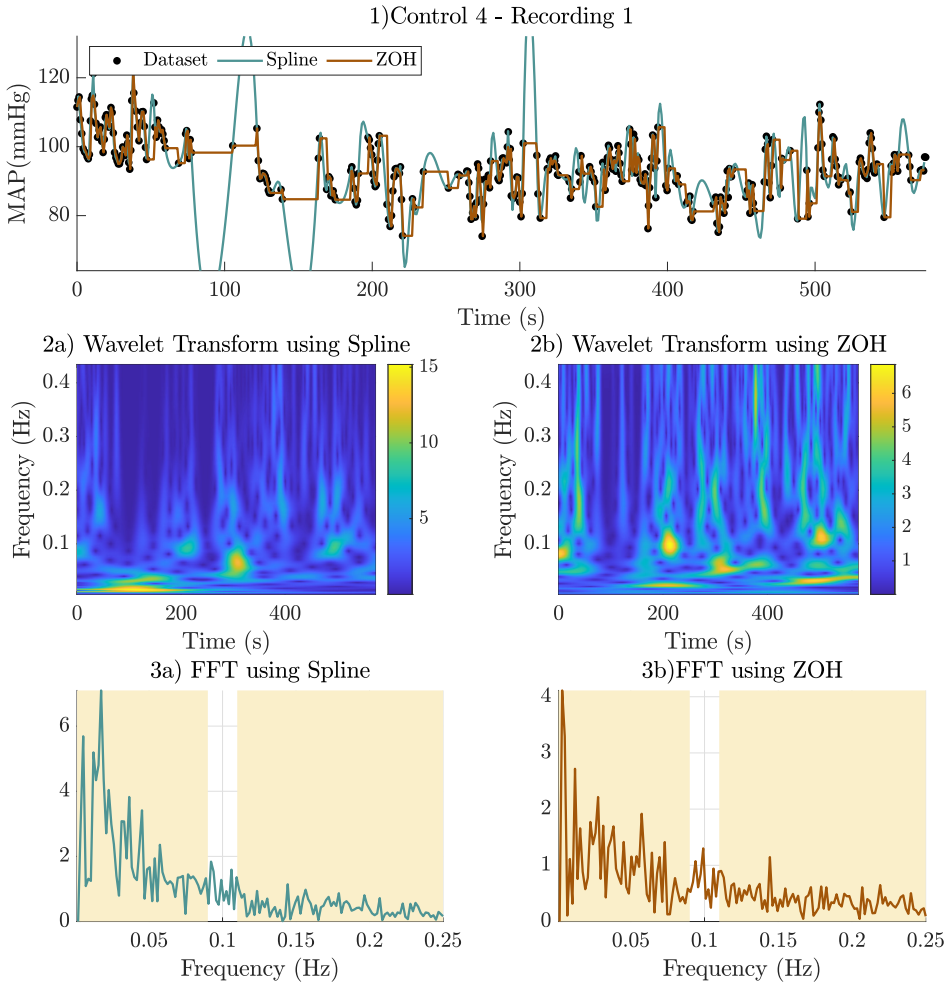

Figure B.7: Control 4 - Recording 1

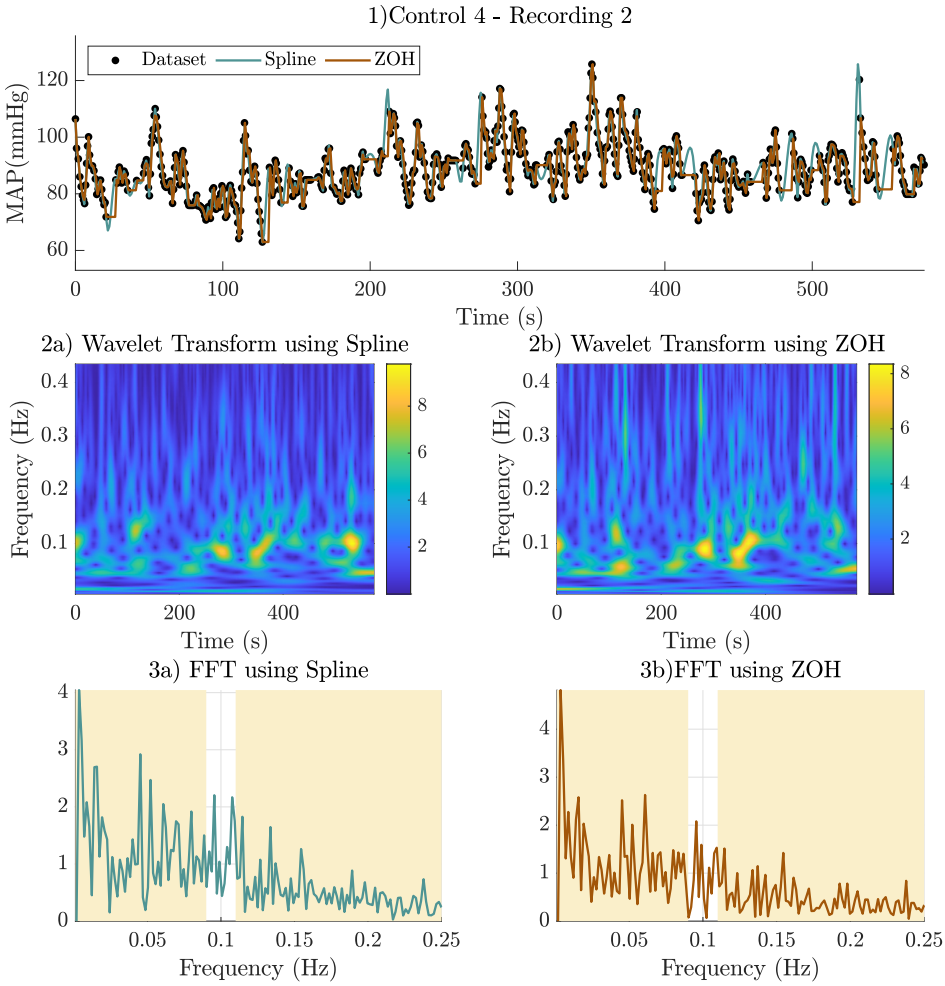

Figure B.8: Control 4 - Recording 2

B.1.5 Control 5

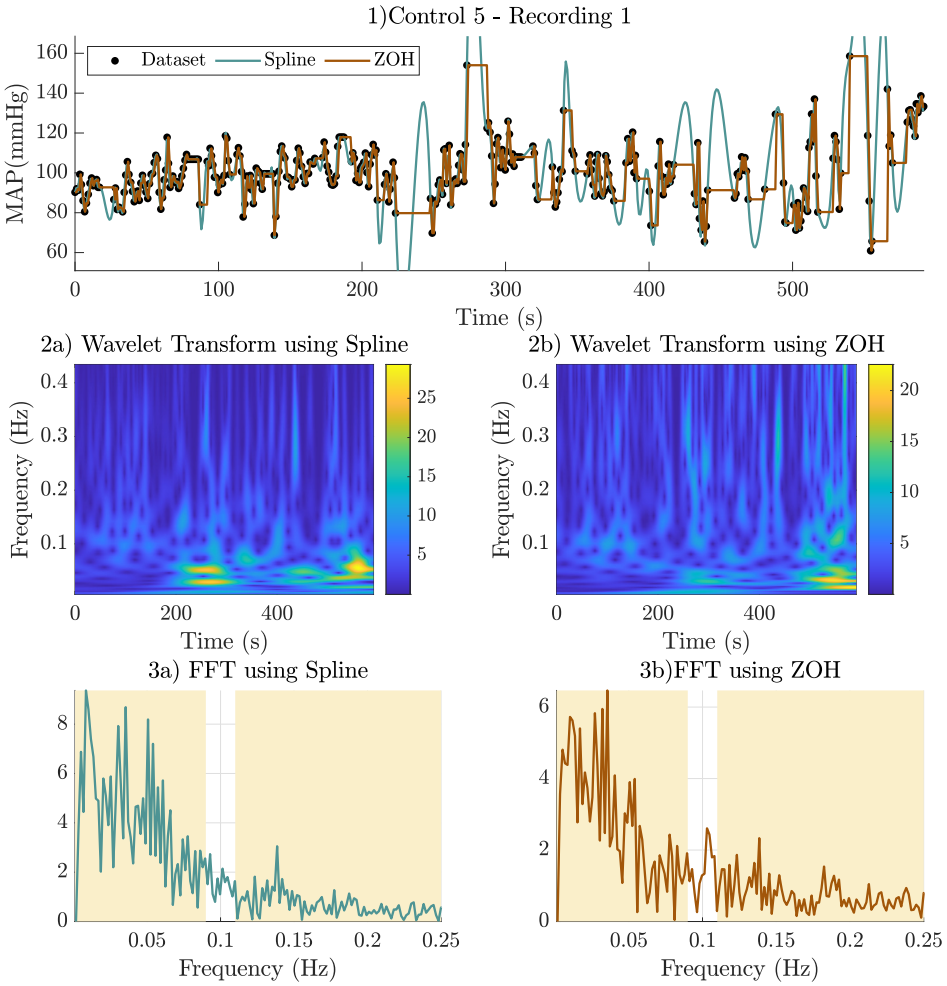

Figure B.9: Control 5 - Recording 1

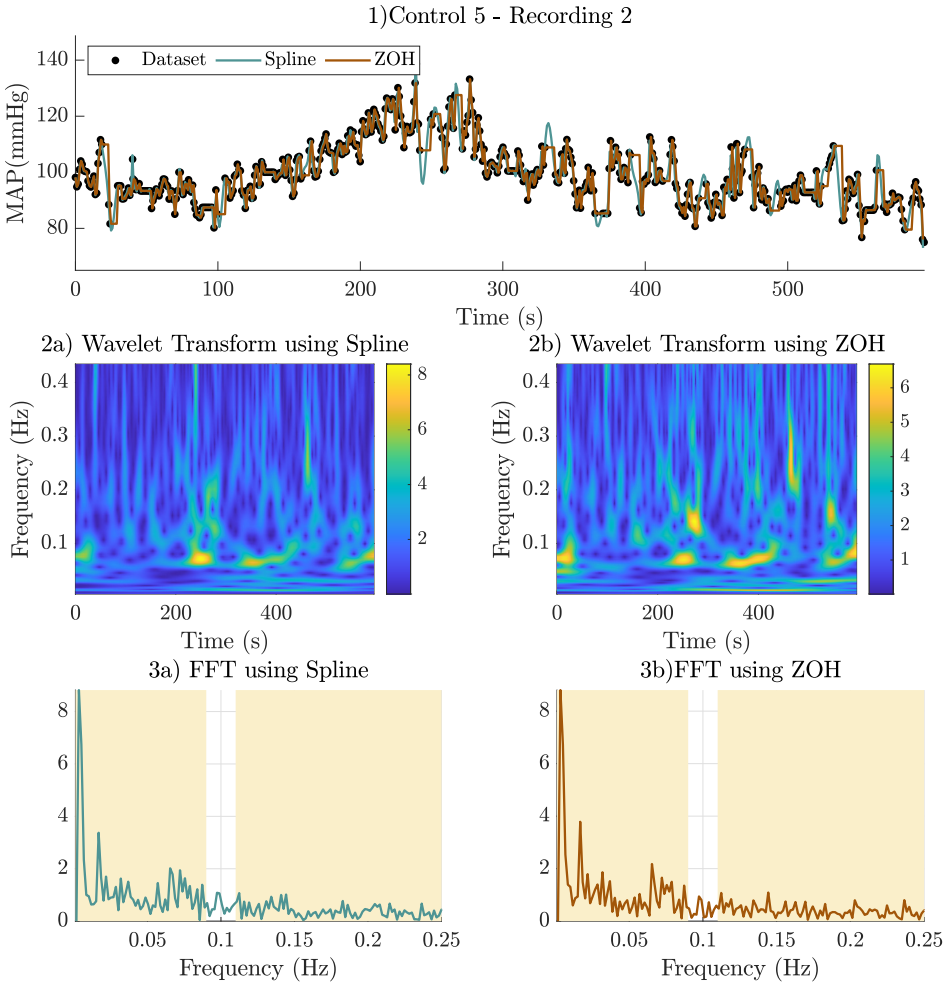

Figure B.10: Control 5 - Recording 2

B.1.6 Control 6

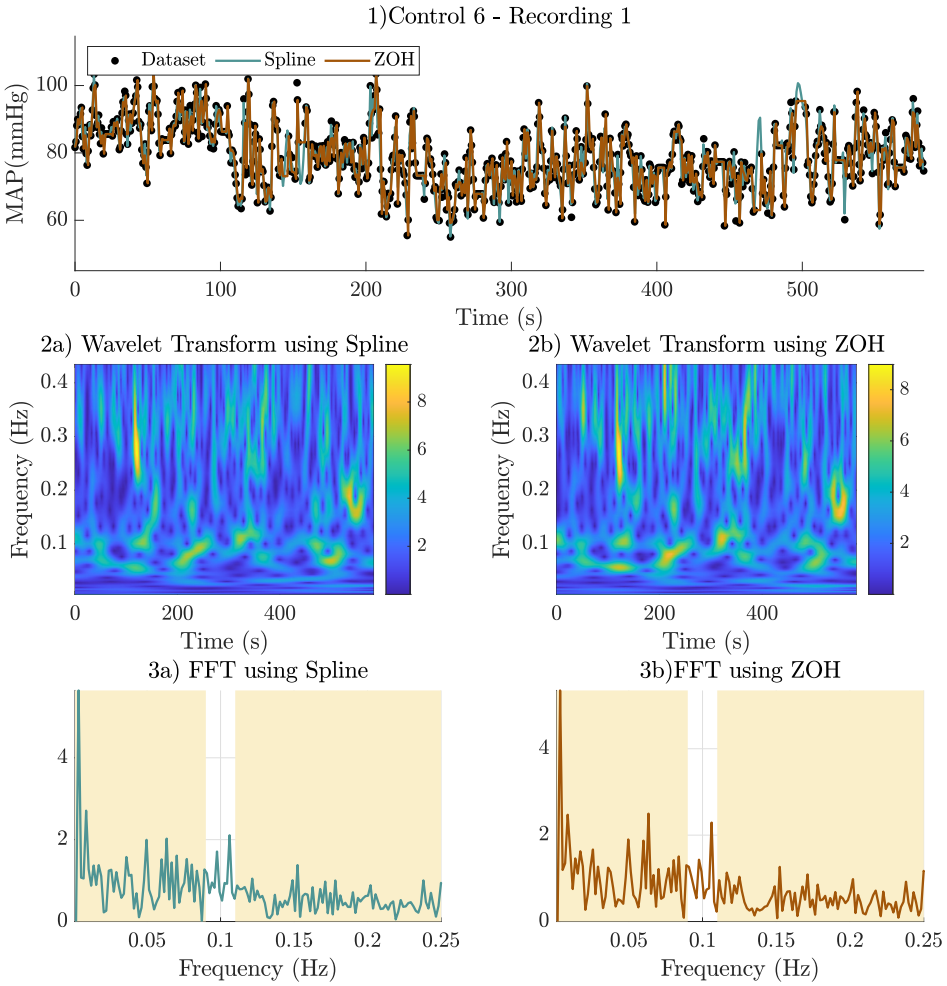

Figure B.11: Control 6 - Recording 1

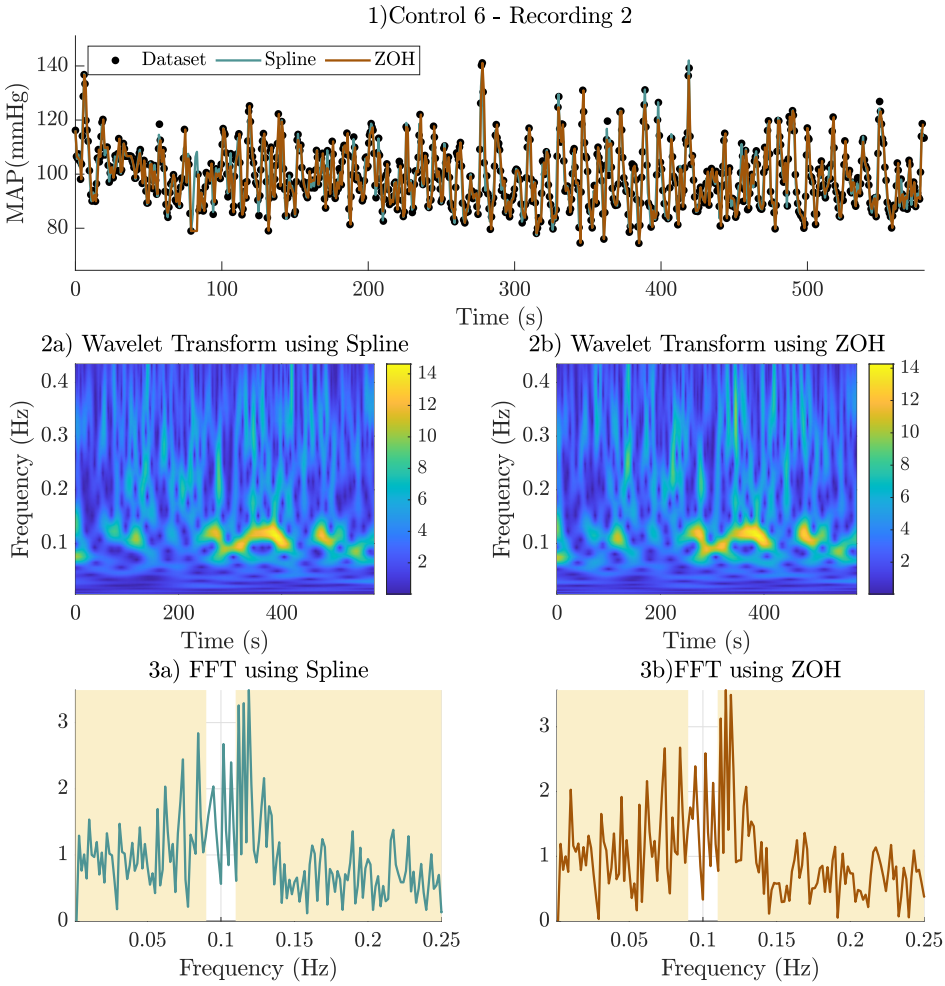

Figure B.12: Control 6 - Recording 2

B.1.7 Control 7

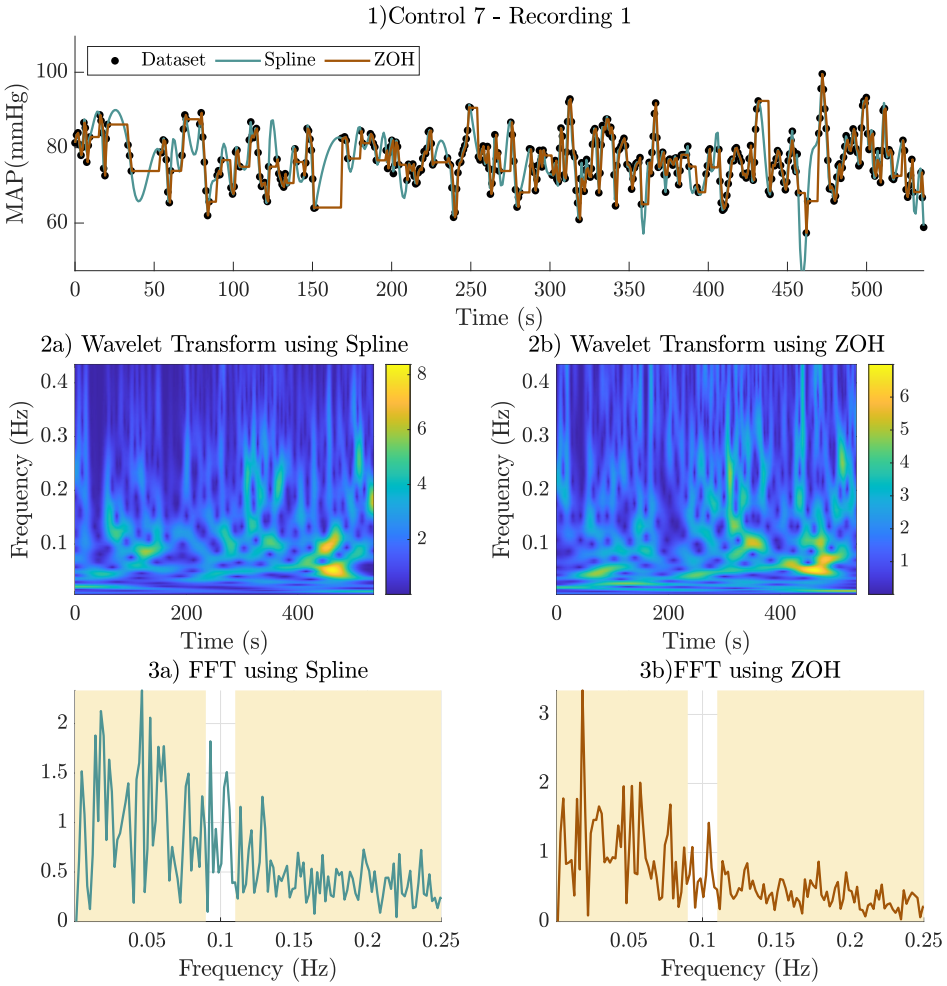

Figure B.13: Control 7 - Recording 1

B.1.8 Control 8

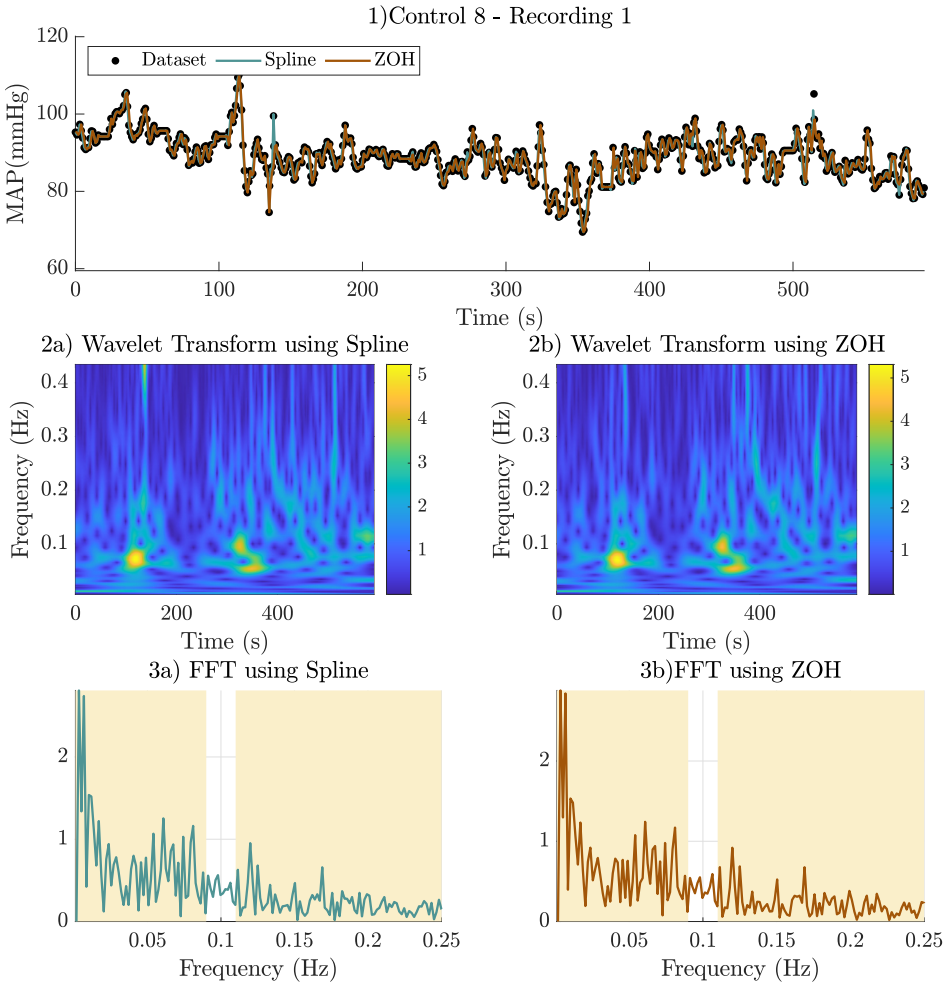

Figure B.14: Control 8 - Recording 1

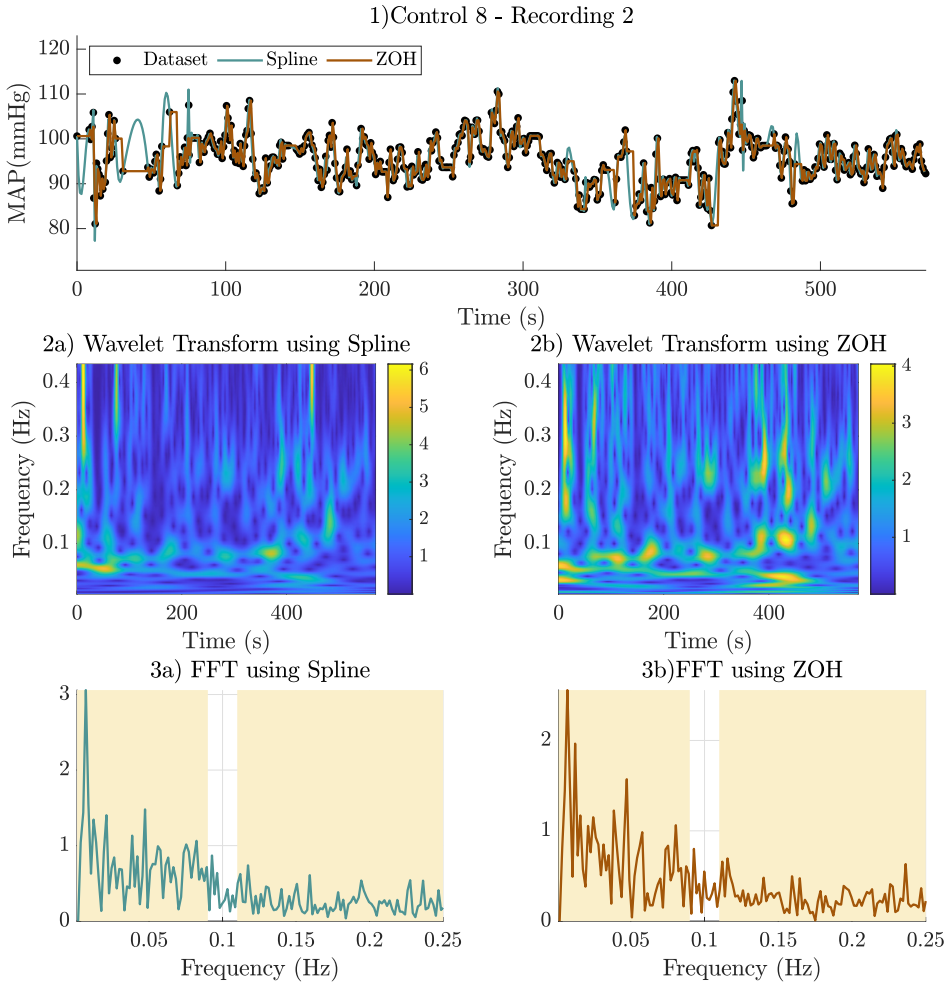

Figure B.15: Control 8 - Recording 2

B.1.9 Control 9

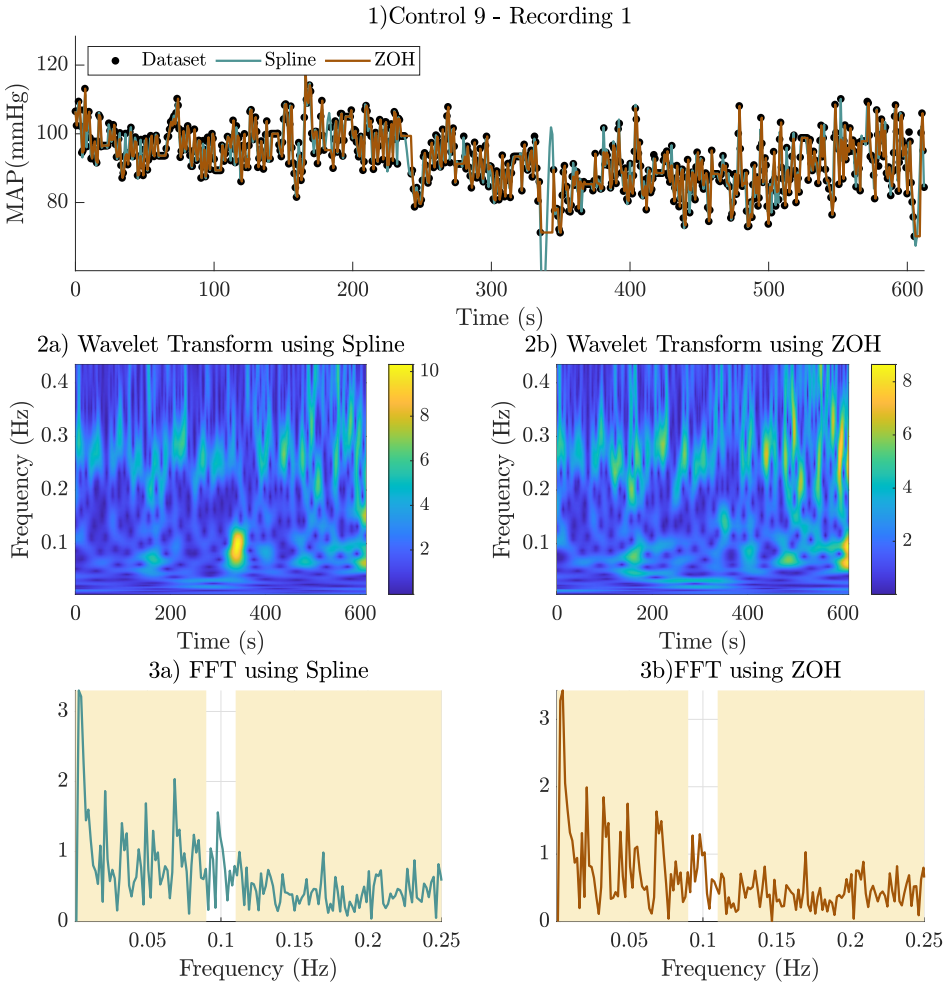

Figure B.16: Control 9 - Recording 1

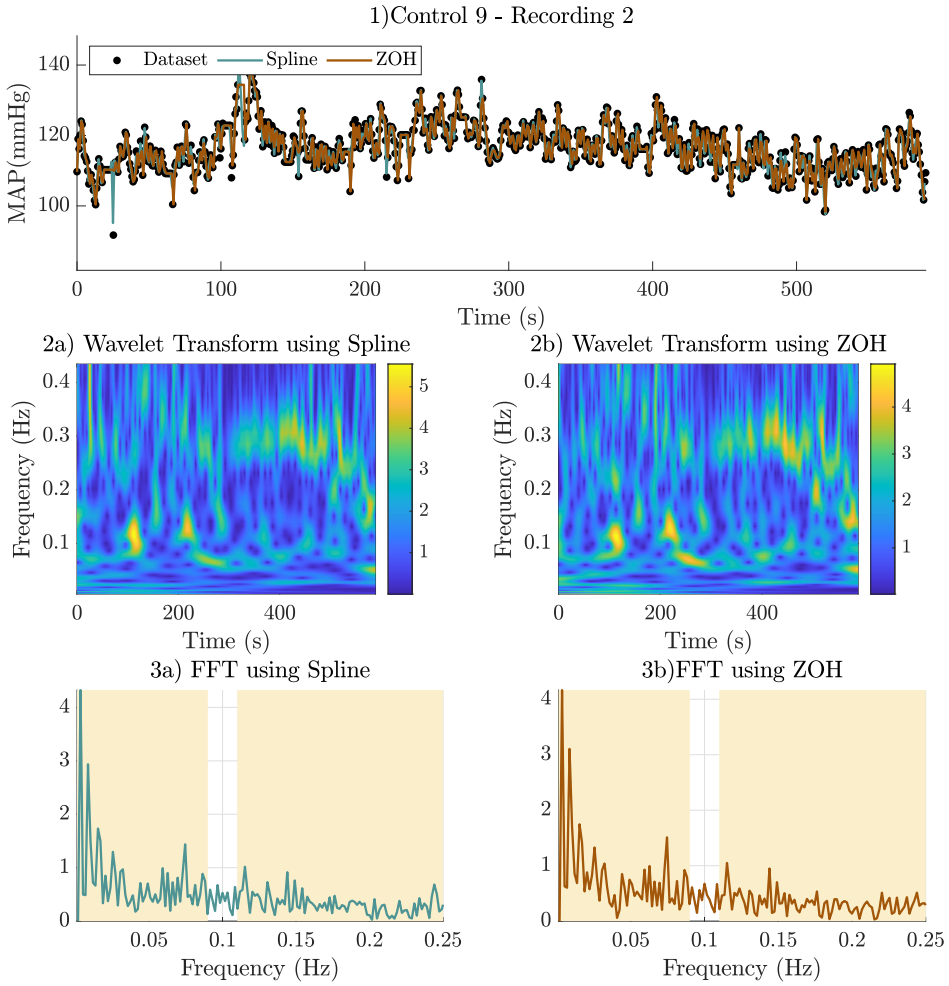

Figure B.17: Control 9 - Recording 2

B.1.10 Patient 01

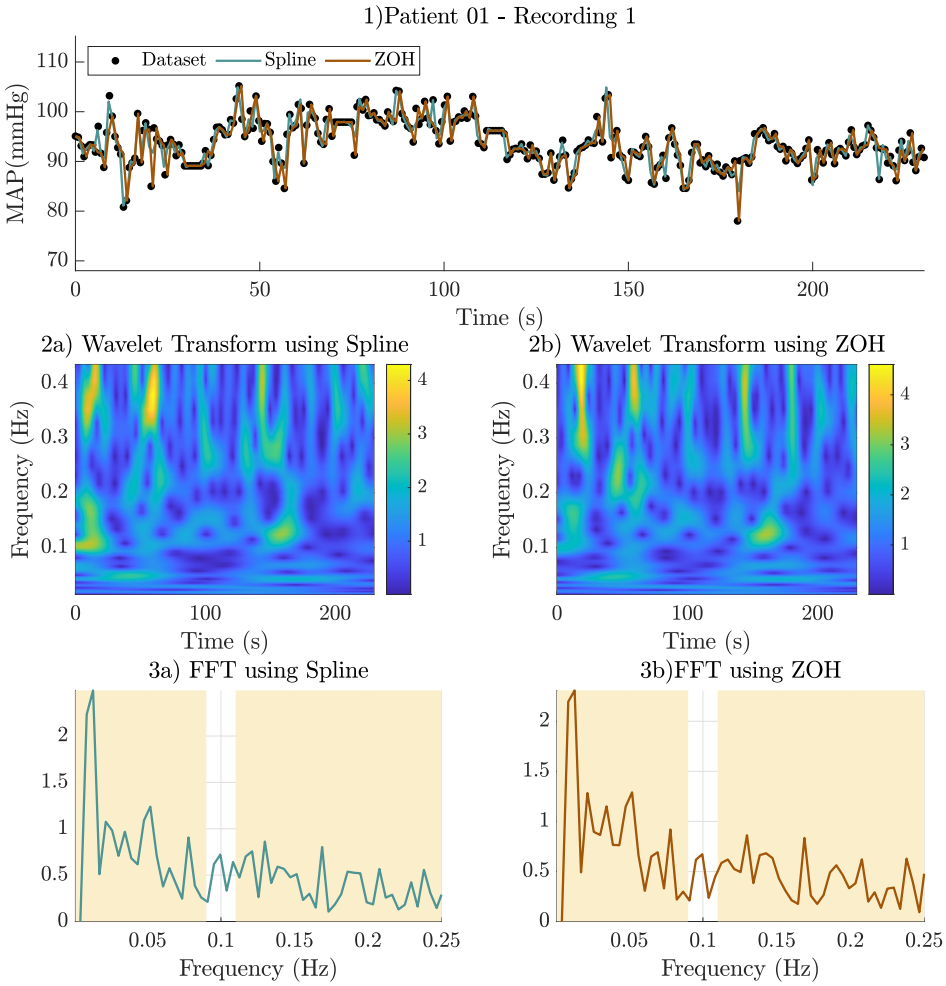

Figure B.18: Patient 01 - Recording 1

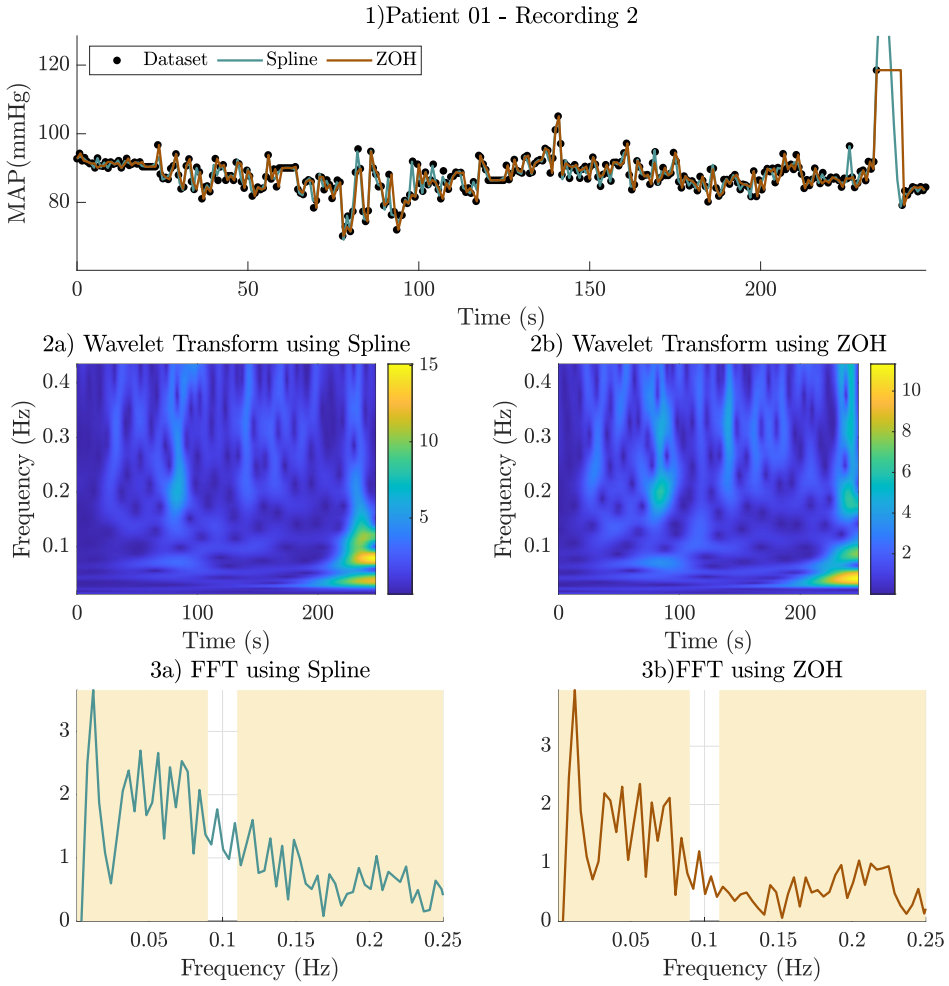

Figure B.19: Patient 01 - Recording 2

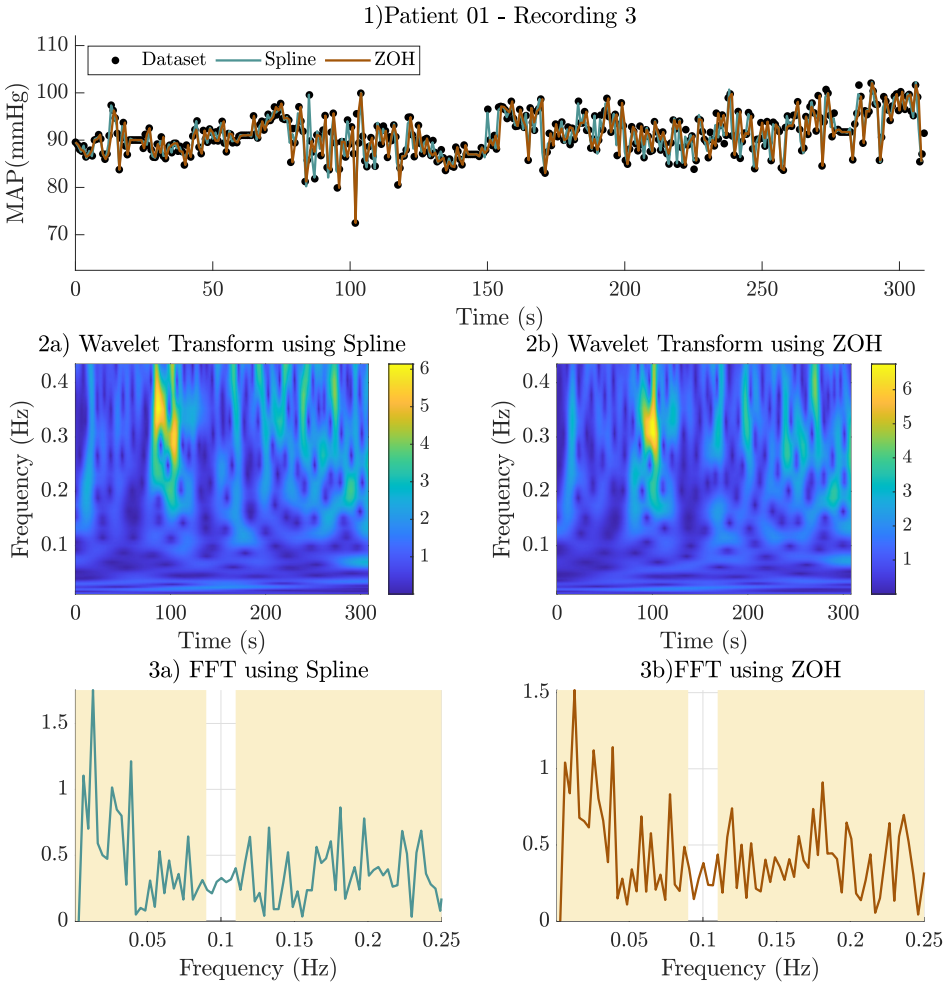

Figure B.20: Patient 01 - Recording 3

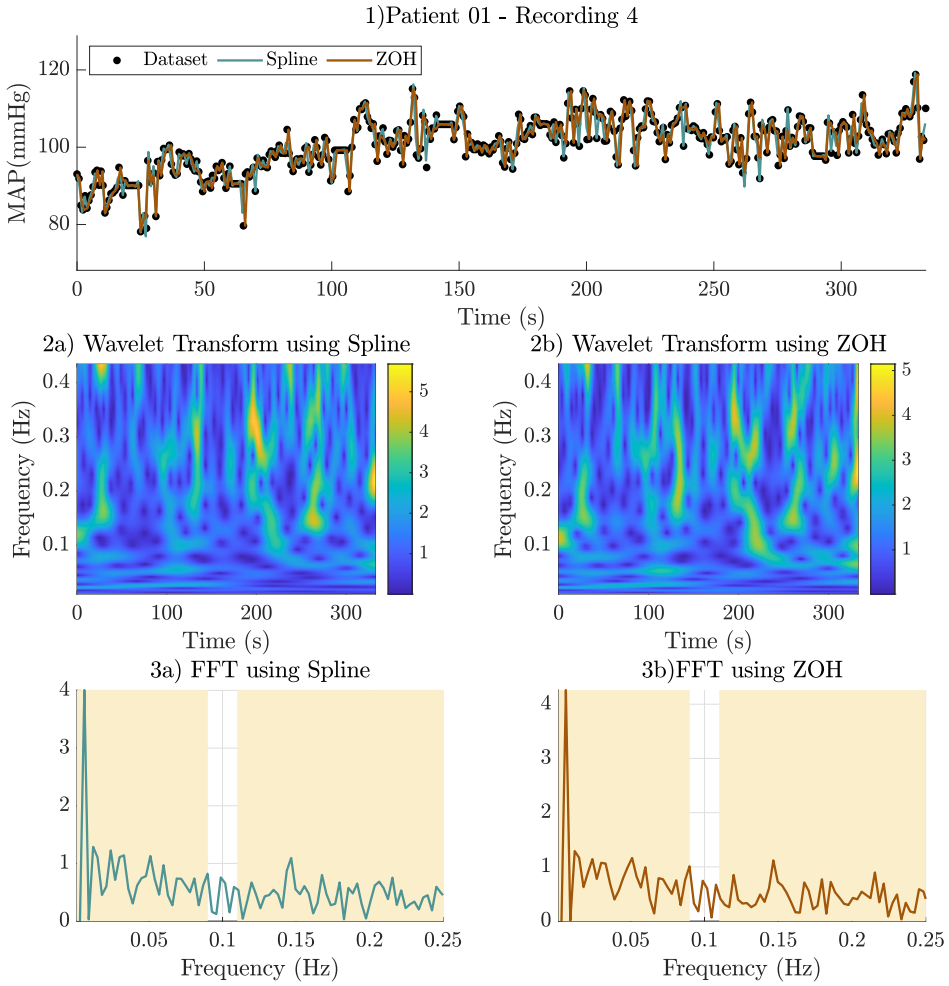

Figure B.21: Patient 01 - Recording 4

B.1.11 Patient 03

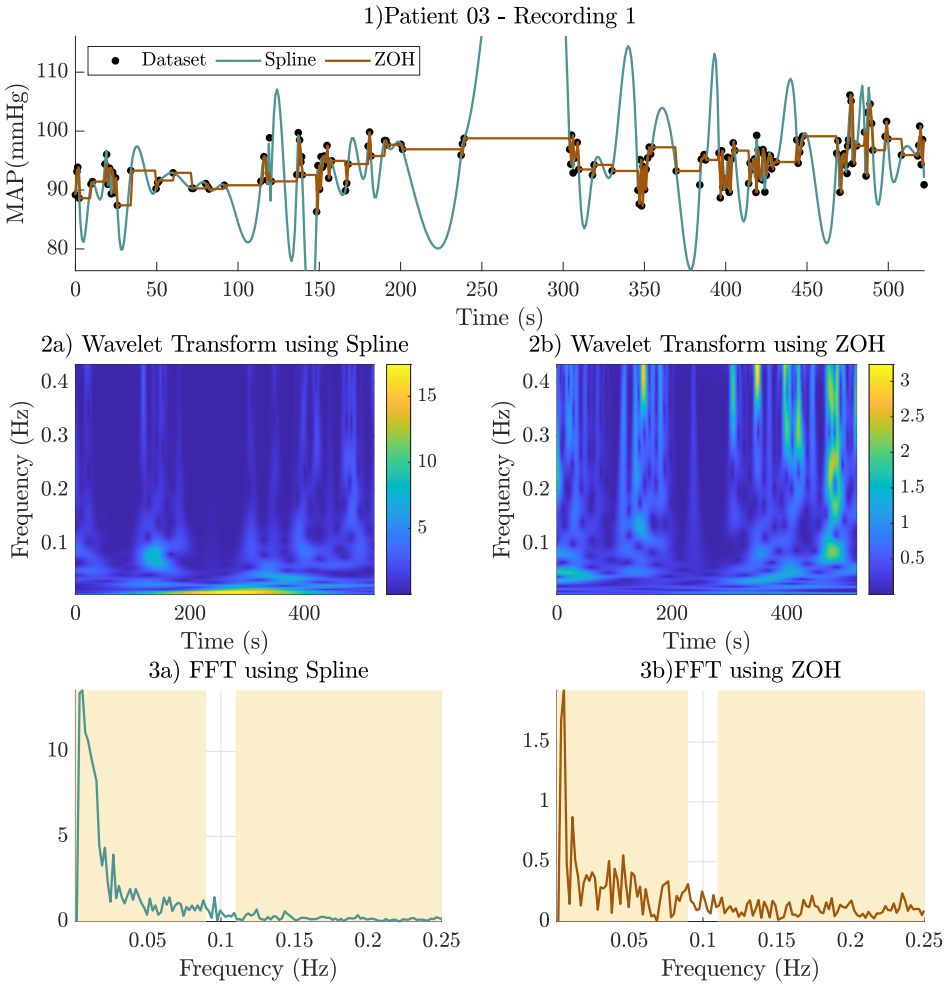

Figure B.22: Patient 03 - Recording 1

B.1.12 Patient 04

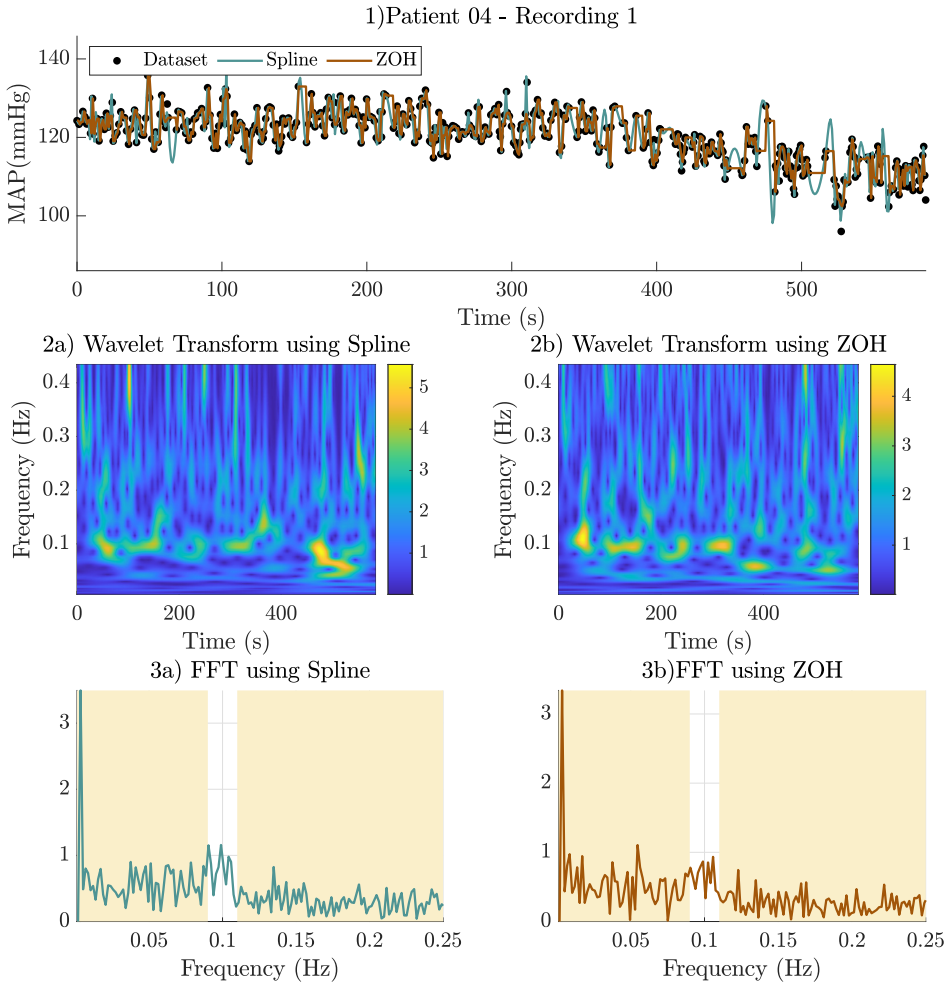

Figure B.23: Patient 04 - Recording 1

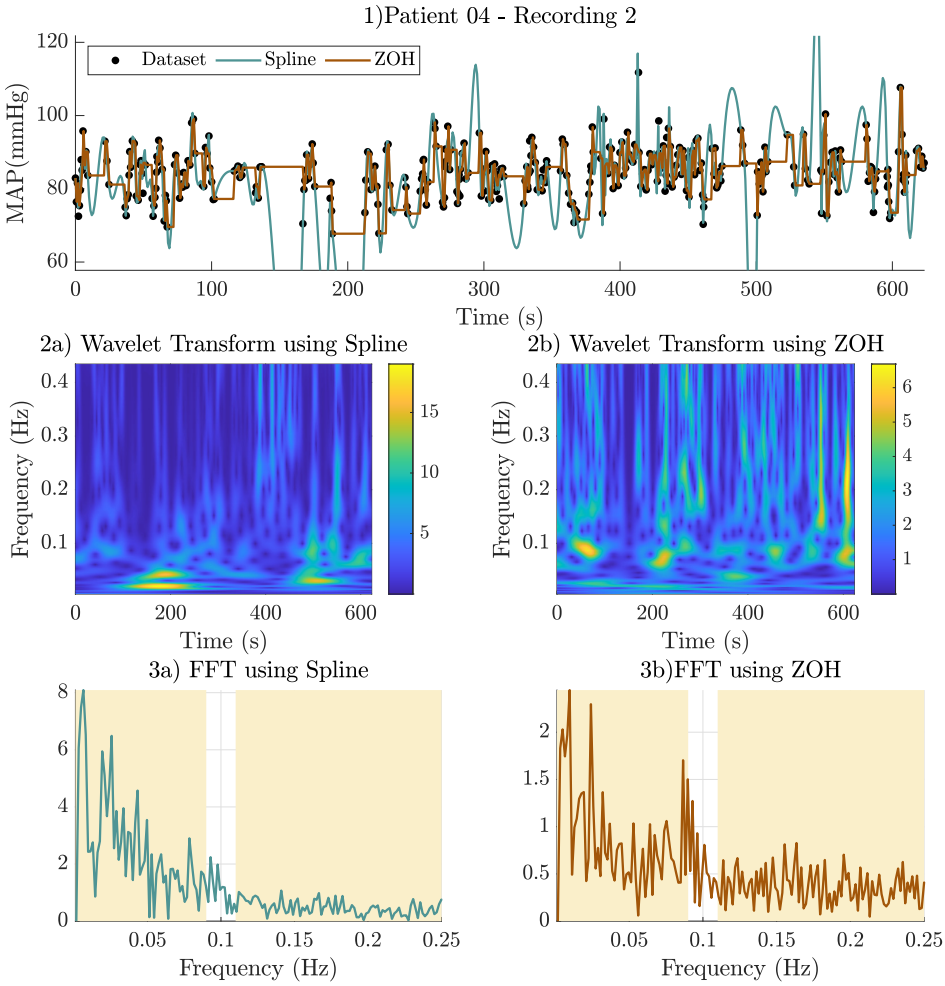

Figure B.24: Patient 04 - Recording 2

B.1.13 Patient 07

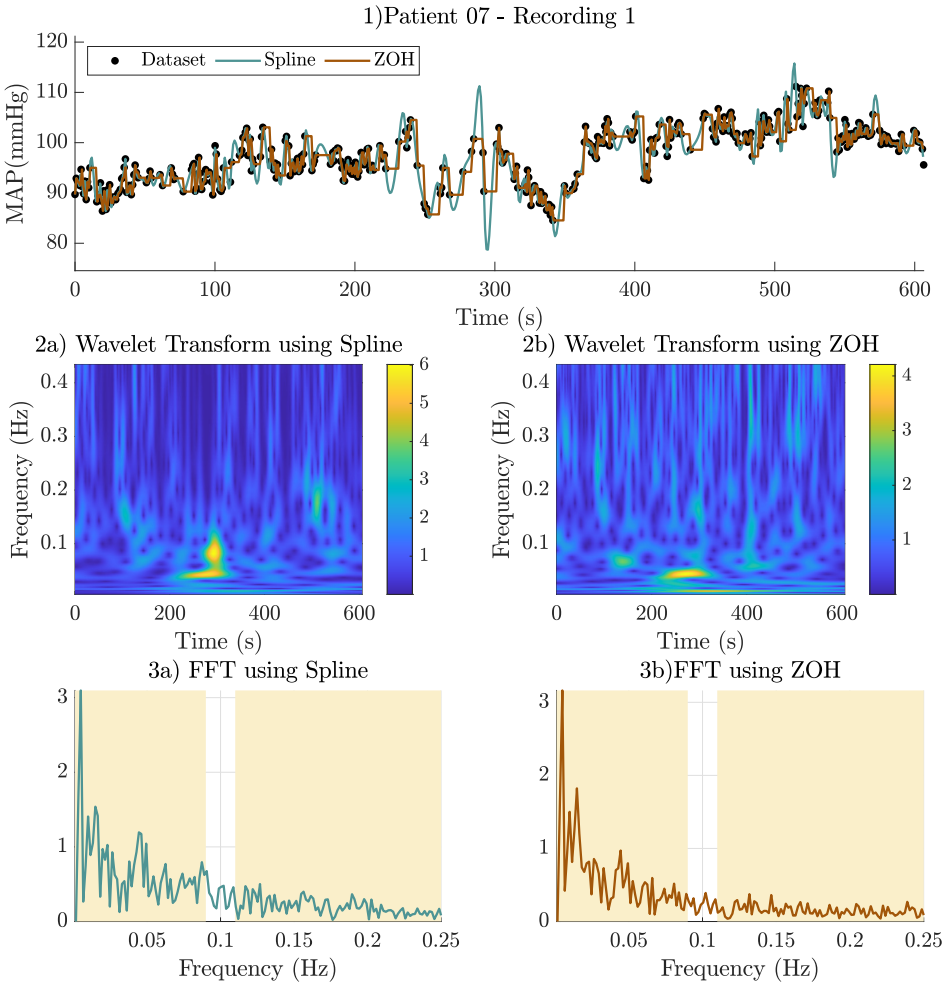

Figure B.25: Patient 07 - Recording 1

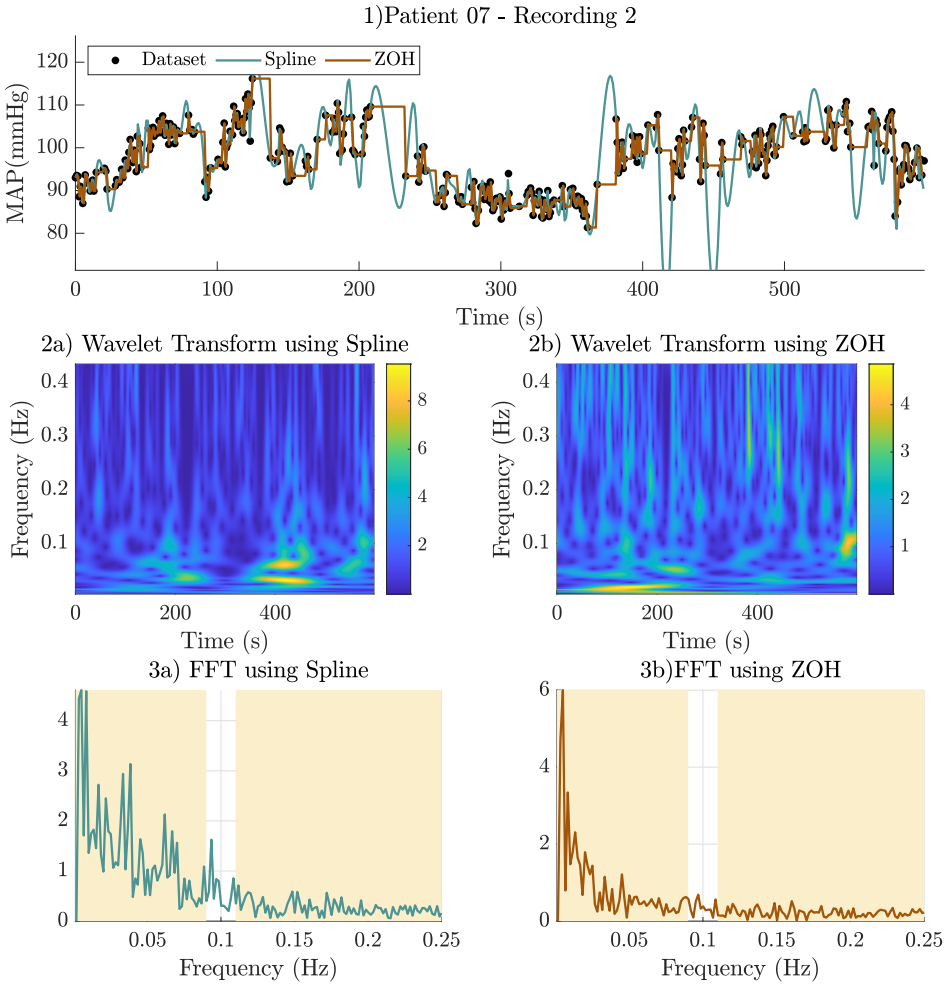

Figure B.26: Patient 07 - Recording 2

C

EuroBaVar sparse data test case

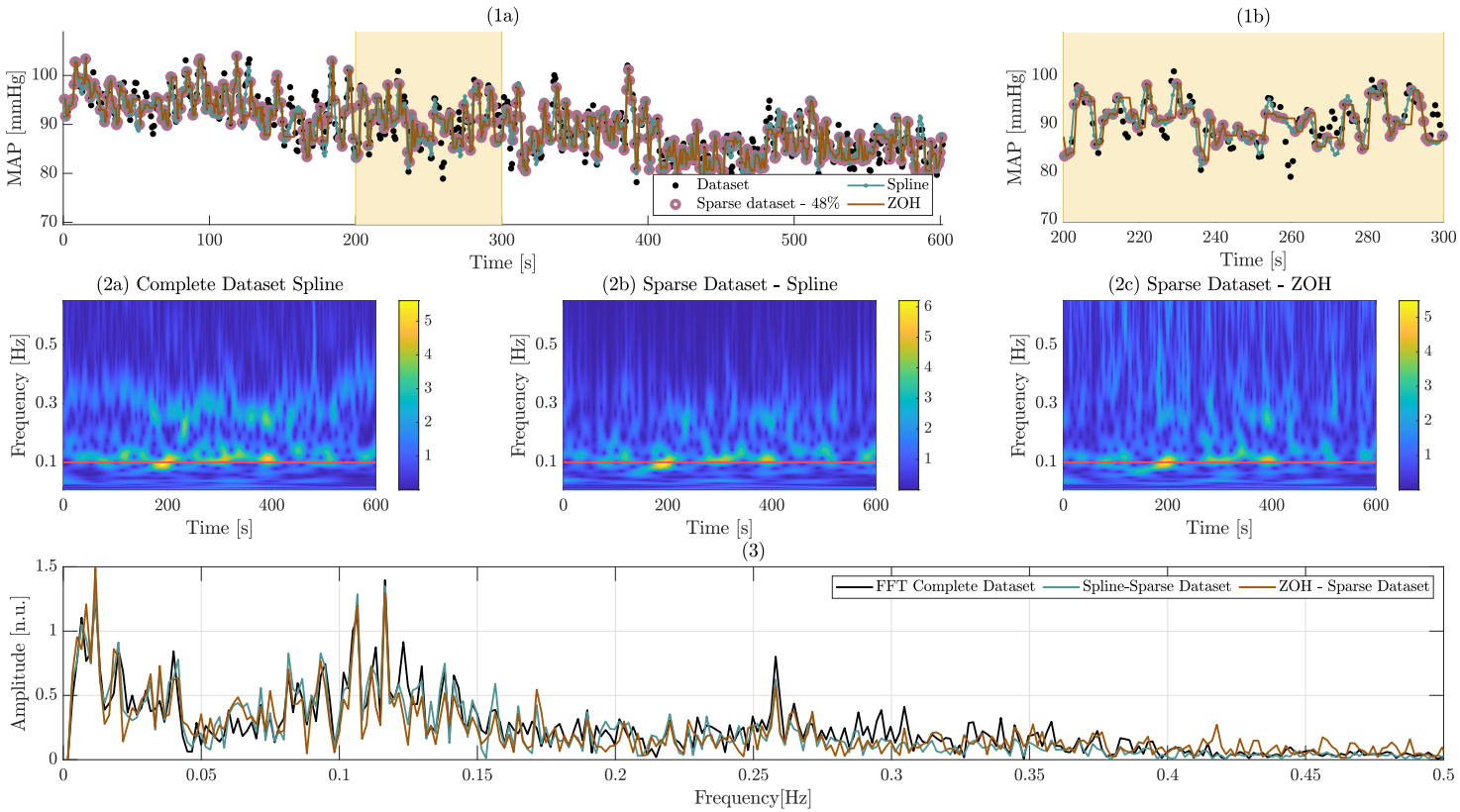

Figure C.1: Eurobavar Subject A004 - investigating the effect of interpolation on the FFT in the case of sparse data with 50% of the original complete dataset

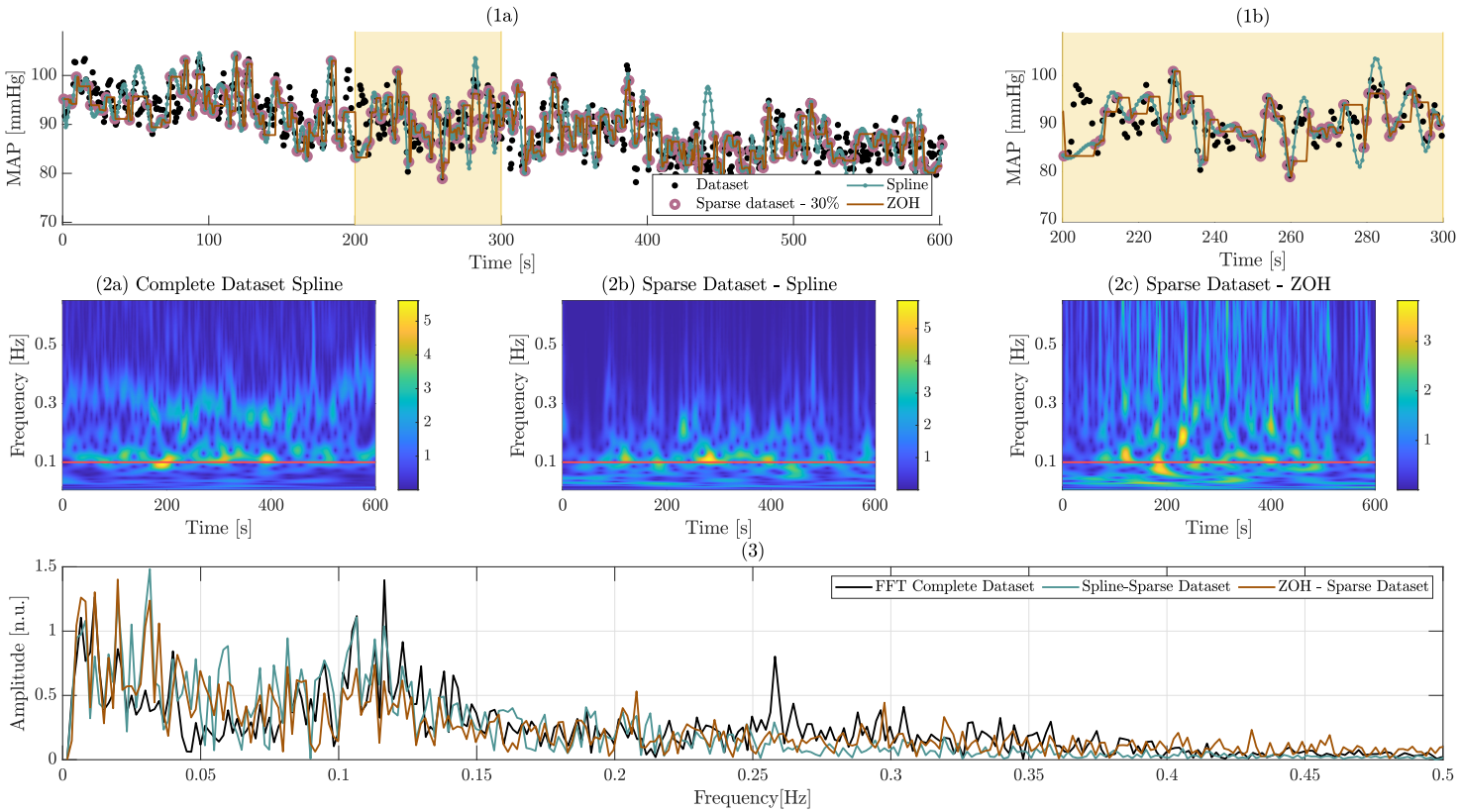

Figure C.2: Eurobavar Subject A004 - investigating the effect of interpolation on the FFT in the case of sparse data with 30% of the original complete dataset

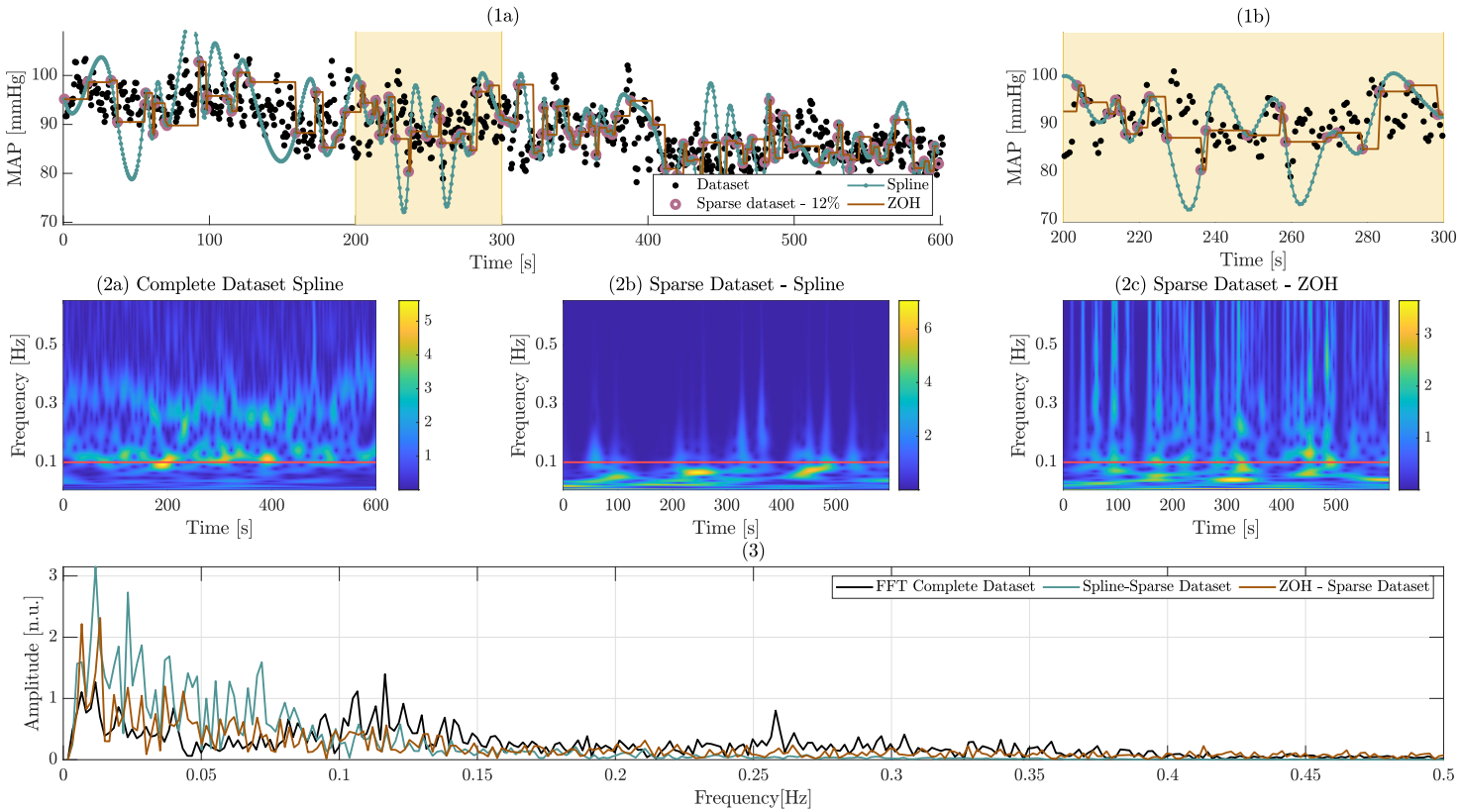

Figure C.3: Eurobavar Subject A004 - investigating the effect of interpolation on the FFT in the case of sparse data with 10% of the original complete dataset

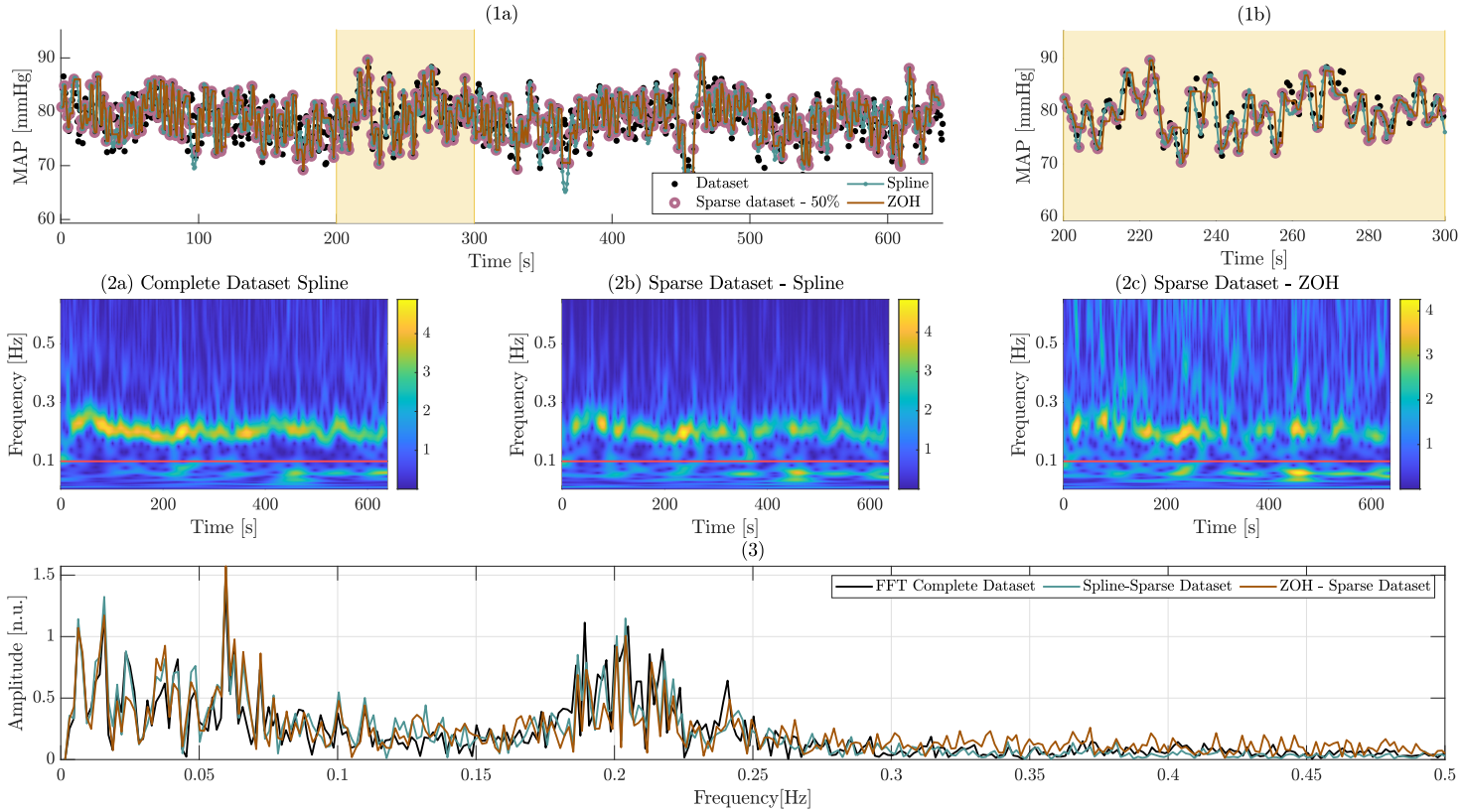

Figure C.4: Eurobavar Subject A005 - investigating the effect of interpolation on the FFT in the case of sparse data with 50% of the original complete dataset

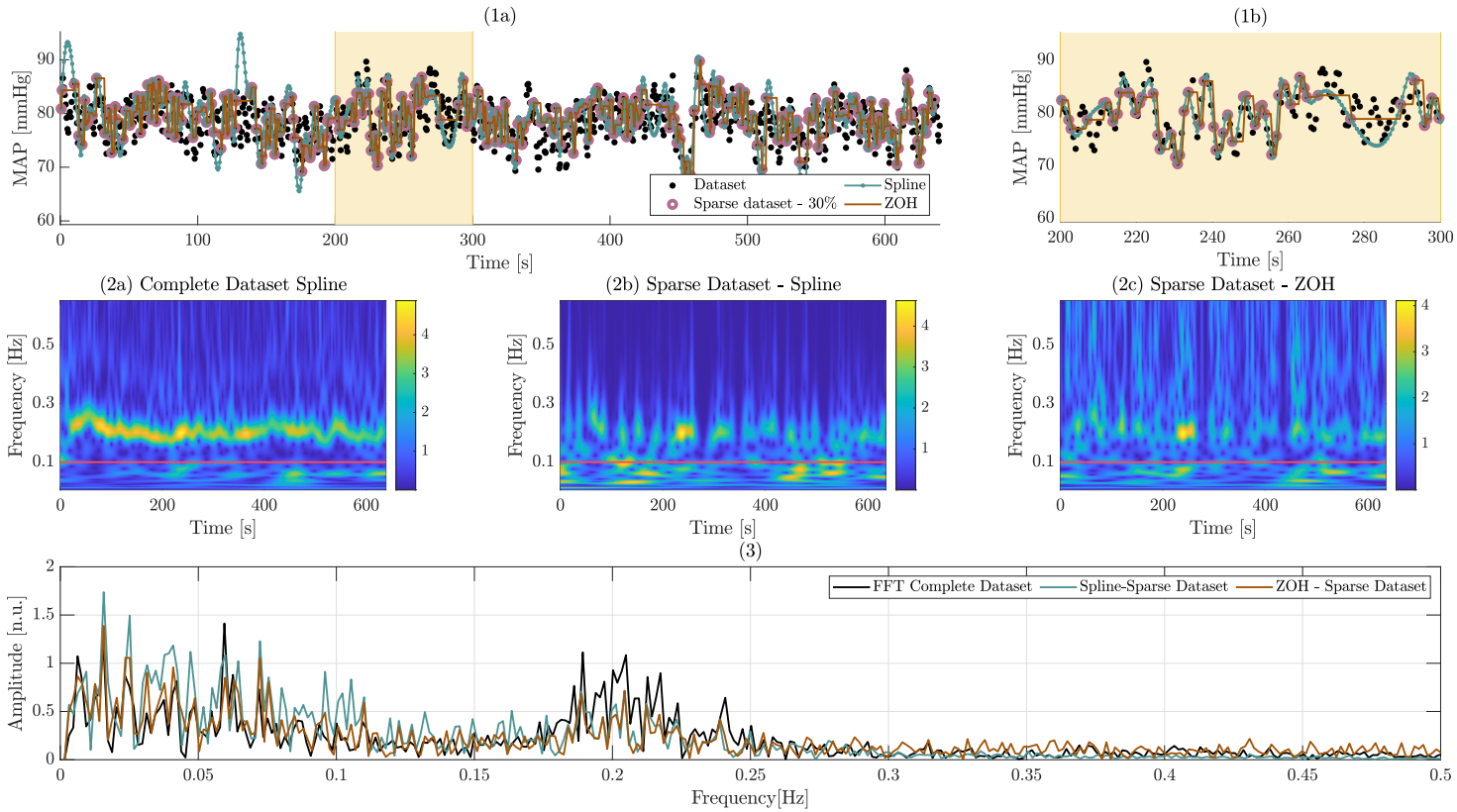

Figure C.5: Eurobavar Subject A005 - investigating the effect of interpolation on the FFT in the case of sparse data with 30% of the original complete dataset

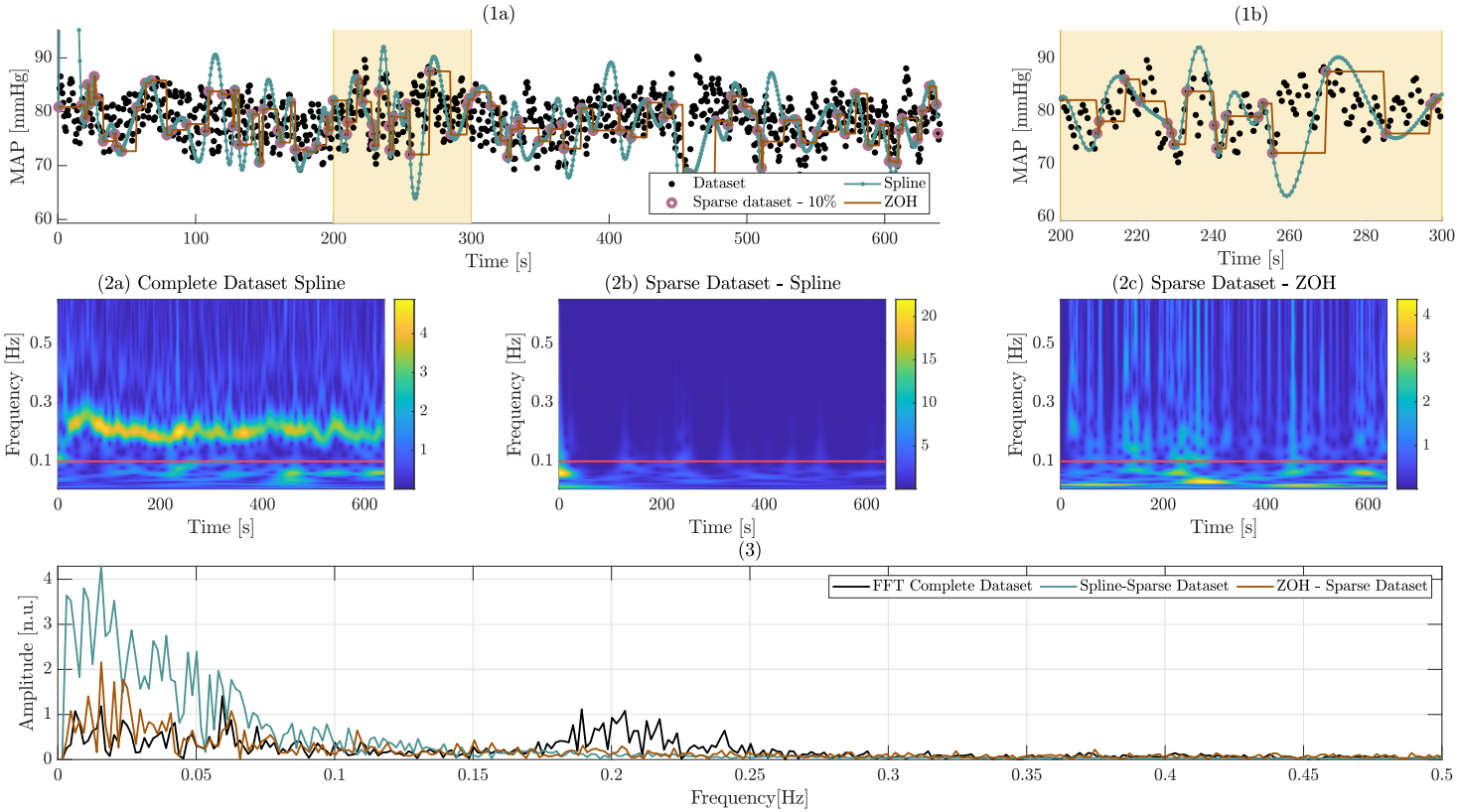

Figure C.6: Eurobavar Subject A005 - investigating the effect of interpolation on the FFT in the case of sparse data with 10% of the original complete dataset

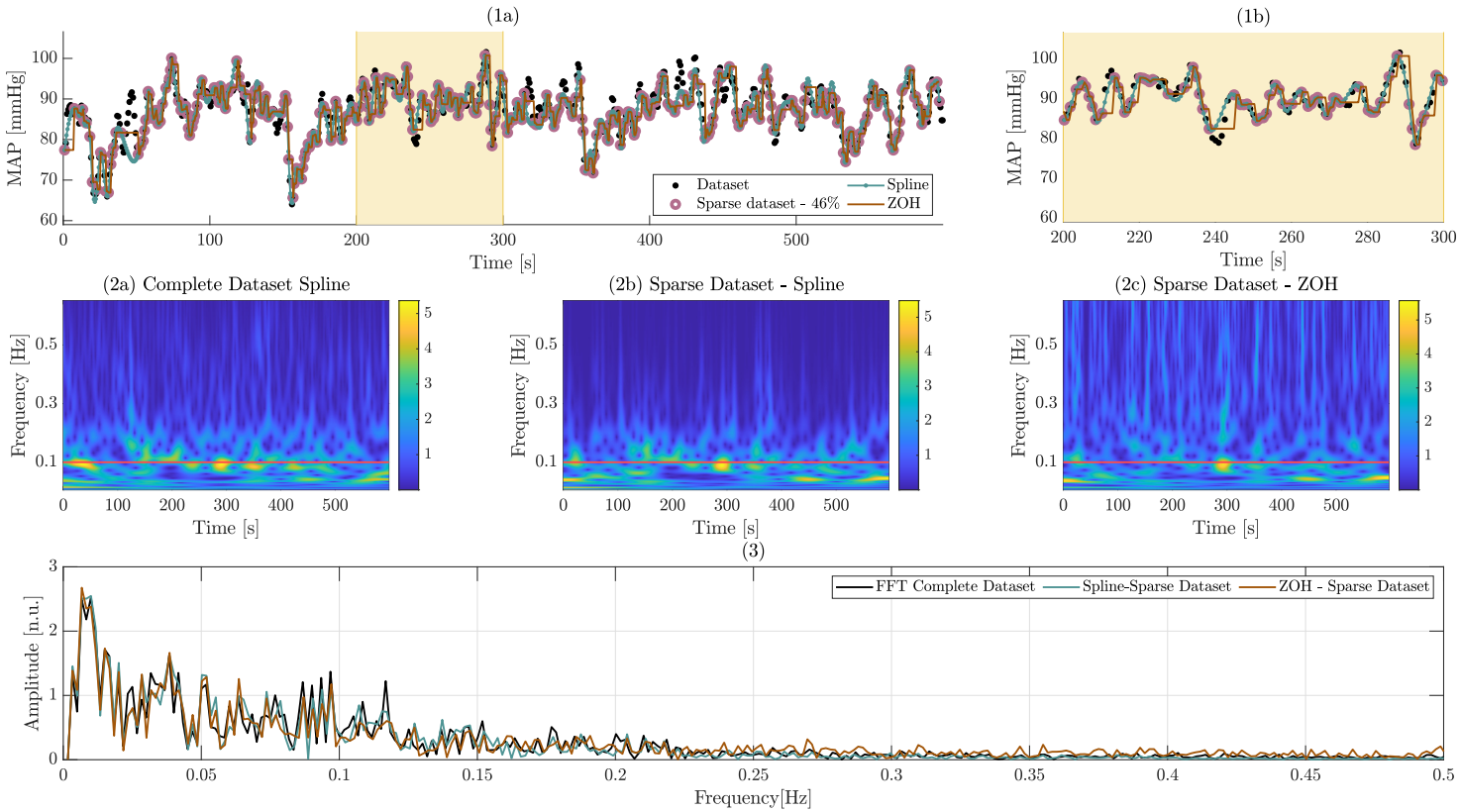

Figure C.7: Eurobavar Subject B003 - investigating the effect of interpolation on the FFT in the case of sparse data with 50% of the original complete dataset

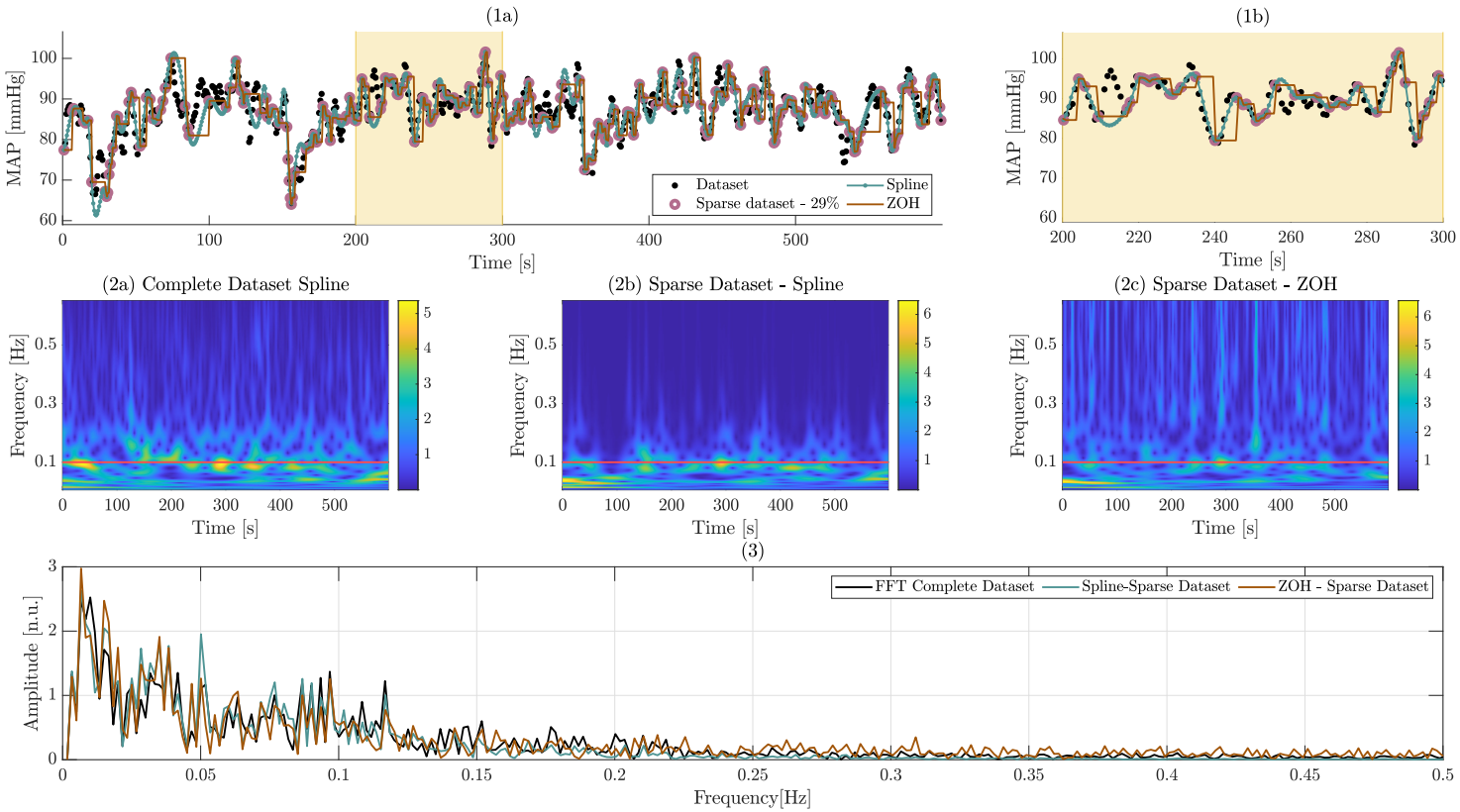

Figure C.8: Eurobavar Subject B003 - investigating the effect of interpolation on the FFT in the case of sparse data with 30% of the original complete dataset

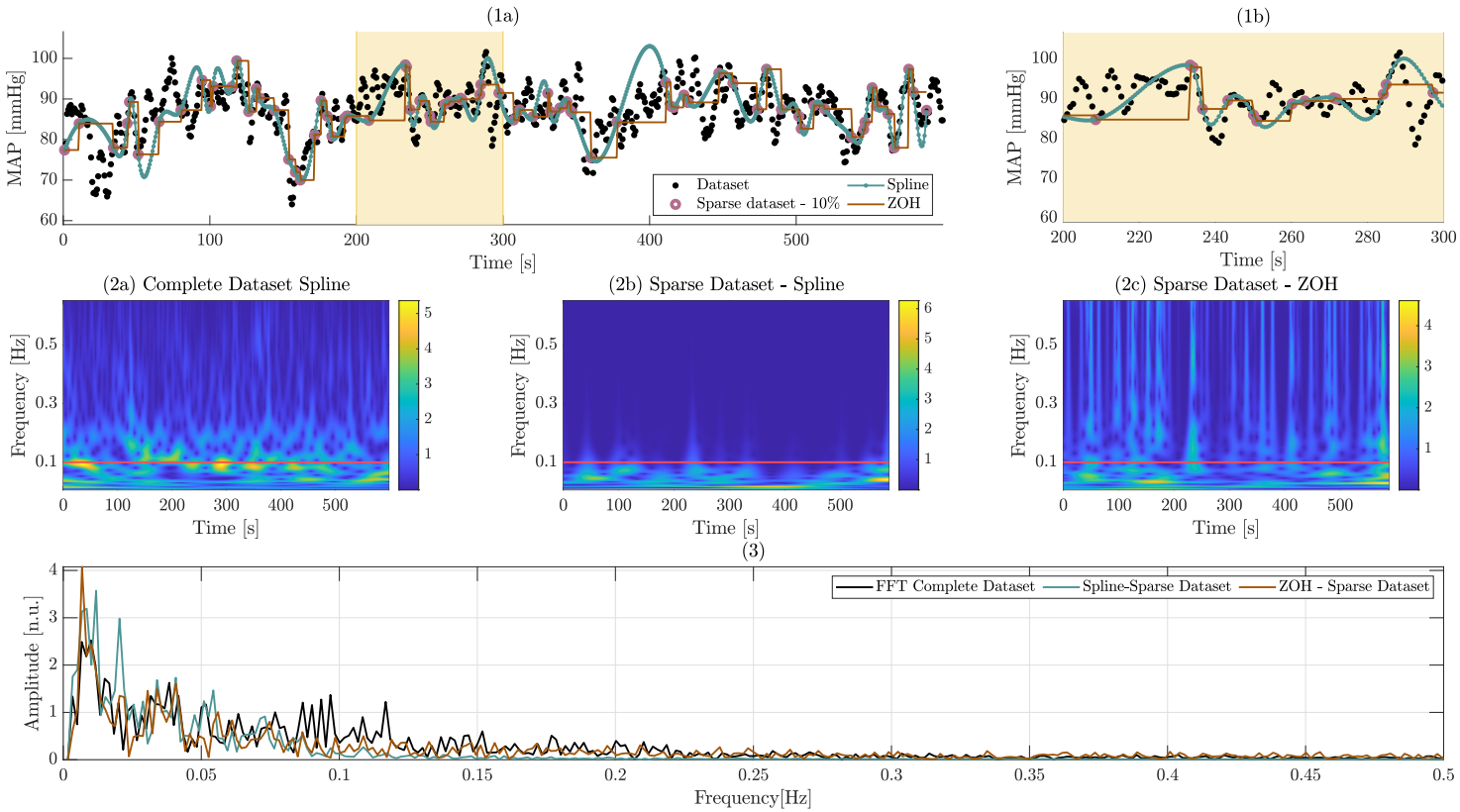

Figure C.9: Eurobavar Subject B003 - investigating the effect of interpolation on the FFT in the case of sparse data with 10% of the original complete dataset

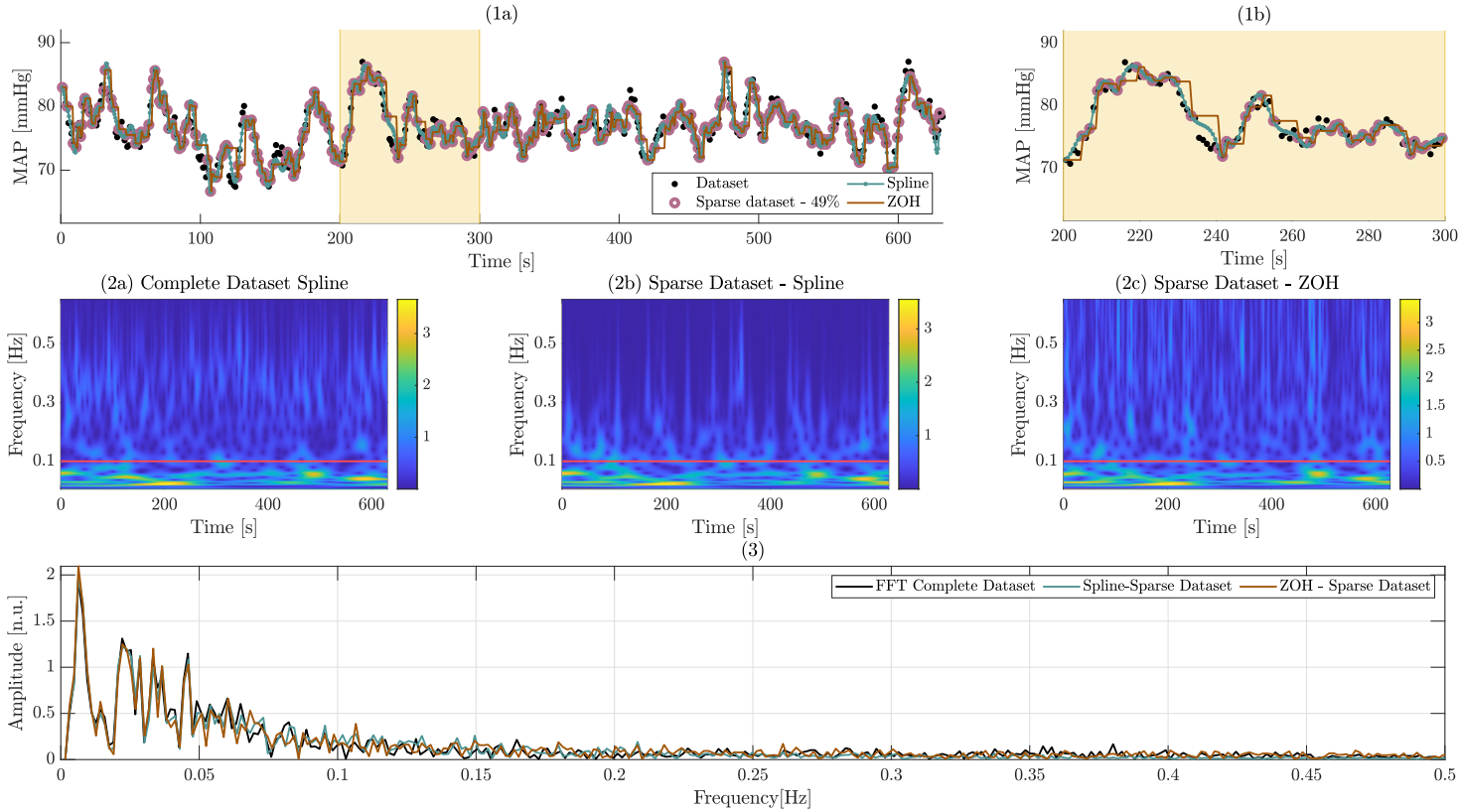

Figure C.10: Eurobavar Subject B004 - investigating the effect of interpolation on the FFT in the case of sparse data with 50% of the original complete dataset

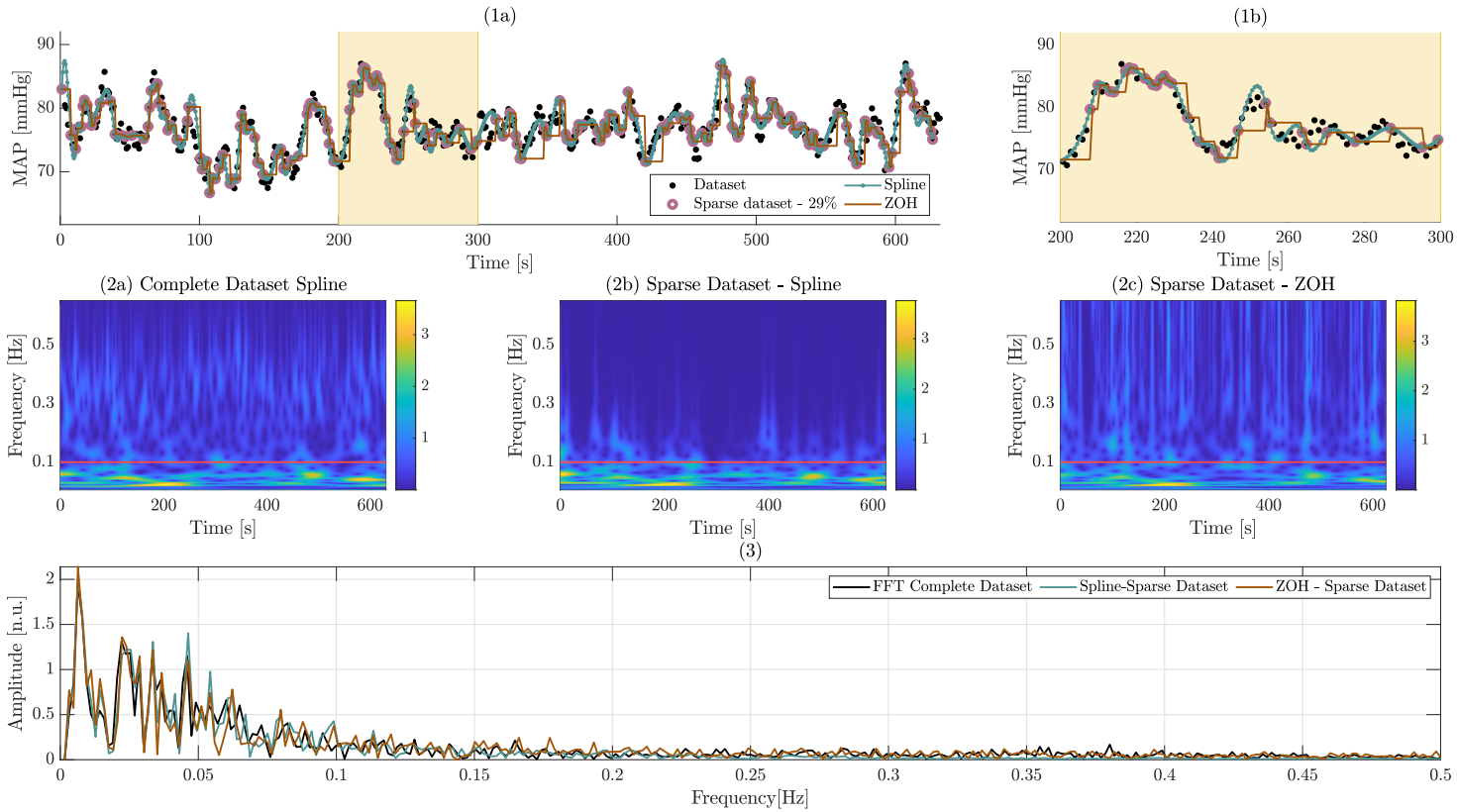

Figure C.11: Eurobavar Subject B004 - investigating the effect of interpolation on the FFT in the case of sparse data with 30% of the original complete dataset

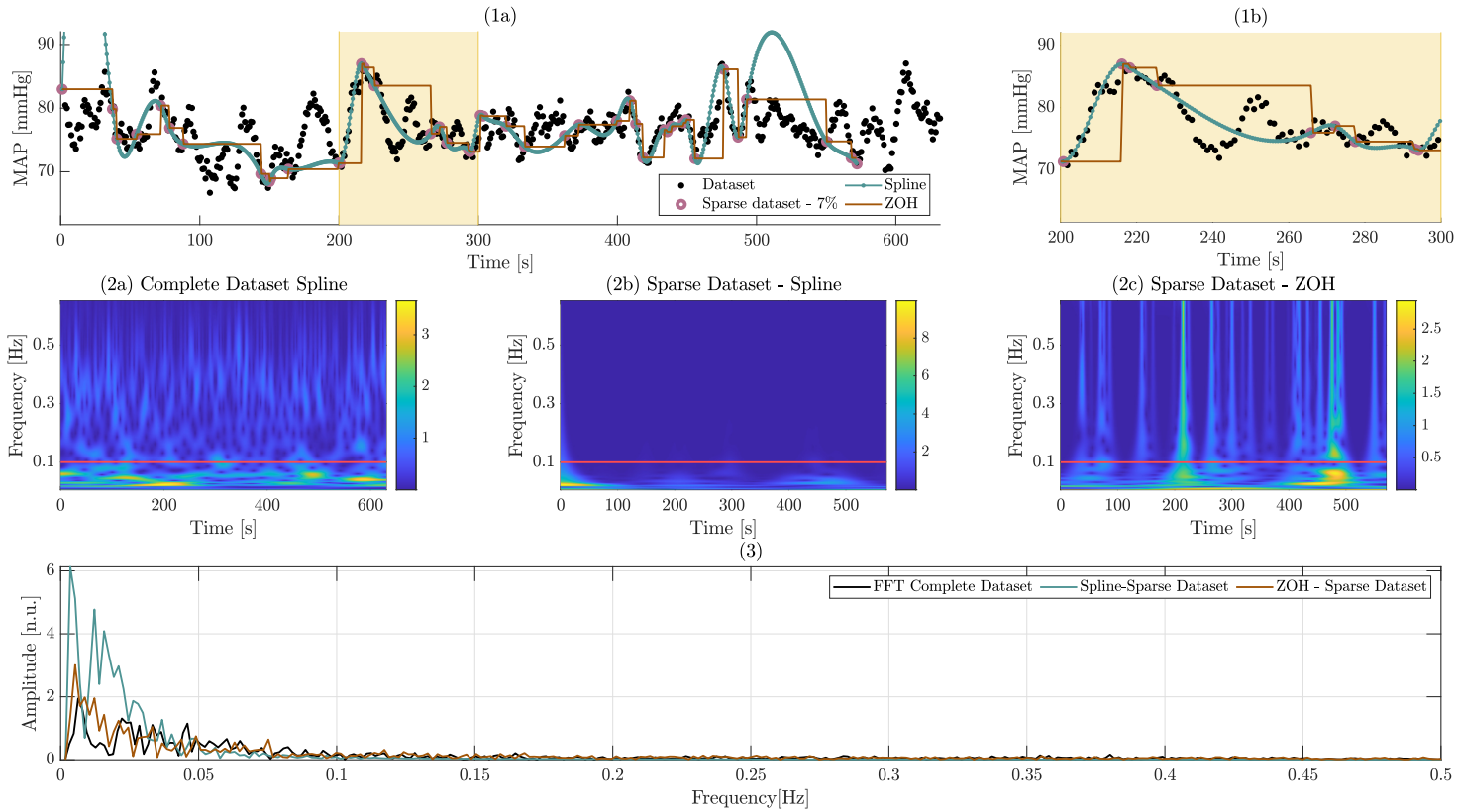

Figure C.12: Eurobavar Subject B004 - investigating the effect of interpolation on the FFT in the case of sparse data with 10% of the original complete dataset

Bibliography

[1] 1926 Association for the Publication of the Journal of Internal Medicine. Part II: The heart's minute-volume and stroke-volume in rabbits in normal condition and during experimental pneumonia. *Journal of Internal Medicine*, 64(s17):60–182, 1926.

[2] Abbott. Heartmate 3™ left ventricular assist device pump parameter overview. Technical report, Abbott, 2020.

[3] N. Aljuri and R.J. Cohen. Theoretical considerations in the dynamic closed-loop baroreflex and autoregulatory control of total peripheral resistance. *American Journal of Physiology-Heart and Circulatory Physiology*, 287(5):H2252–H2273, 2004.

[4] N. Aljuri, R. Marini, and R.J. Cohen. Test of dynamic closed-loop baroreflex and autoregulatory control of total peripheral resistance in intact and conscious sheep. *American Journal of Physiology-Heart and Circulatory Physiology*, 287(5):H2274–H2286, 2004.

[5] M. Armstrong, C.C. Kerndt, and R.A. Moore. Physiology, baroreceptors. In *StatPearls [Internet]*. StatPearls Publishing, 2021.

[6] American Heart Association. EKG strip showing a normal heartbeat.

[7] D. P. Atherton. *Nonlinear Control Engineering*. Van Nostrand Reinhold Company, 1975.

[8] H. Bagnall Hare and J.V. Ringwood. The modulation of neural blood pressure control by blood pressure pulsatility. In *2019 30th Irish Signals and Systems Conference (ISSC)*, pages 1–6. IEEE, 2019.

[9] C. J. Barrett, S. J. Guild, R. Ramchandra, and S. C. Malpas. Baroreceptor denervation prevents sympathoinhibition during angiotensin II-induced hypertension. *Hypertension*, 46(1):168–72, 2005.

[10] C.J. Barrett, R. Ramchandra, S.-J. Guild, A. Lala, D.M. Budgett, and S.C. Malpas. What sets the long-term level of renal sympathetic nerve activity: A role for Angiotensin II and baroreflexes? *Circulation Research*, 92(12):1330–1336, 2003.

[11] G. Baselli, S. Cerutti, F. Baidilni, L. Biancardi, A. Porta, M. Pagani, F. Lombardi, O. Rimoldi, R. Furlan, and A. Malliani. Model for the assessment of heart period and arterial pressure variability interactions and respiration influences. *Medical and Biological Engineering and Computing*, 32:143–152, 1994.

[12] G. Baselli, S. Cerutti, S. Civardi, A. Malliani, and M. Pagani. Cardiovascular variability signals: Towards the identification of a closed-loop model of the neural control mechanisms. *IEEE Trans on Biomed Eng*, 35 (12):1033–1046, 1988.

[13] G. Bertinieri, M. Di Rienzo, A. Cavallazzi, A.U. Ferrari, A. Pedotti, and G. Mancia. Evaluation of baroreceptor reflex by blood pressure monitoring in unanesthetized cats. *American Journal of Physiology-Heart and Circulatory Physiology*, 254(2):H377–H383, 1988.

[14] R. Bighamian, B. Parvinian, C.G. Scully, G. Kramer, and J.-O. Hahn. Control-oriented physiological modeling of hemodynamic responses to blood volume perturbation. *Control Engineering Practice*, 73:149–160, 2018.

[15] G.E.P. Box, G.M. Jenkins, G.C. Reinsel, and L. Ljung. *Time Series Analysis: Forecasting and Control*. John Wiley & Sons, 2015.

[16] P. Brodal. *The central nervous system: structure and function*. Oxford University Press, 2004.

[17] R. Burattini and S. Natalucci. Complex and frequency-dependent compliance of viscoelastic Windkessel resolves contradictions in elastic Windkessels. *Medical Engineering and Physics*, 20(7):502–514, 1998.

[18] D.A. Calhoun, D. Jones, S. Textor, D.C. Goff, T.P. Murphy, R.D. Toto, A. White, W.C. Cushman, W. White, D. Sica, et al. Resistant hypertension: diagnosis, evaluation, and treatment: a scientific statement from theAmerican Heart Association Professional Education Committee of the Council for High Blood Pressure Research. *Hypertension*, 51(6):1403–1419, 2008.

[19] O. A. Carretero and S. Oparil. Essential hypertension: part I: definition and etiology. *Circulation*, 101(3):329–335, 2000.

[20] Francesco Castagna, Eric J Stöhr, Alberto Pinsino, John R Cockcroft, Joshua Willey, A Reshad Garan, Veli K Topkara, Paolo C Colombo, Melana Yuzefpolskaya, and Barry J McDonnell. The unique blood pressures and pulsatility of LVAD patients: current challenges and future opportunities. *Current Hypertension Reports*, 19:1–7, 2017.

[21] M. Castellano, D. Rizzoni, M. Beschi, M. L. Muiesan, E. Porteri, G. Bettoni, M. Salvetti, A. Cinelli, R. Zulli, and E. Agabiti-Rosei. Relationship between sympathetic nervous system activity, baroreflex and cardiovascular effects after acute nitric oxide synthesis inhibition in humans. *Journal of Hypertension*, 13(10):1153–1161, 1995.

[22] S. Cerutti, M. Ducher, M.-P. Gustin, J.-P. Fauvel, G. Cuisinaud, and C. Paultre. Statistical dependence approach for the estimation of the spontaneous baroreflex sensitivity in rats and humans. *Methodology and Clinical Applications of Blood Pressure and Heart Rate Analysis*, pages 1–12, 1999.

[23] P.-W. Chen, C.-K. Lin, W.-M. Liu, Y.-C. Chen, S.-T. Tsai, and A.-B. Liu. A novel assessment of baroreflex activity through the similarity of ternary codes of oscillations between arterial blood pressure and R-R intervals. *Journal of Medical and Biological Engineering*, 40(5):727–734, 2020.

[24] Y. Choi, S.-B. Ko, and Y. Sun. Effect of postural changes on baroreflex sensitivity: A study on the EuroBaVar data set. In *Proc. 2006 IEEE Canadian Conference on Electrical and Computer Engineering - CCEC/CCGEI'06*, pages 110–114, Ottawa, May 2006.

[25] T. F. Coleman and Y. Li. An interior trust region approach for nonlinear minimization subject to bounds. *SIAM Journal on Optimization*, 6(2):418–445, 1996.

[26] R.L. Cooley, N. Montano, C. Cogliati, P. Van de Borne, W. Richenbacher, R. Oren, and V.K. Somers. Evidence for a central origin of the low-frequency oscillation in RR-interval variability. *Circulation*, 98(6):556–561, 1998.

[27] G. Coppolino, A. Pisano, L. Rivoli, and D. Bolignano. Renal denervation for resistant hypertension. *Cochrane Database of Systematic Reviews*, 2, 2017.

[28] V. Creigen, L. Ferracina, A. Hlod, S. van Mourik, K. Sjauw, V. Rottschäfer, M. Vellekoop, and P. Zegeling. Modeling a heart pump. *European Study Group Mathematics with Industry*, 7, 2007.

[29] L. Davies, D. Francis, P. Jurak, T. Kara, M. Piepoli, and A. Coats. Reproducibility of methods for assessing baroreflex sensitivity in normal controls and in patients with chronic heart failure. *Clinical Science*, 97:515–522, 1999.

[30] M. De Cecco and A. Angrilli. Measurement of human baroreceptor reflex sensitivity by means of parametric identification. *Measurement*, 24:187–196, 1998.

[31] A. de Paor and J.V. Ringwood. A simple soft limiter describing function for biomedical applications. *IEEE Transactions on Biomedical Engineering*, 53(7):1233–1240, 2006.

[32] Michael E DeBakey. Left ventricular bypass pump for cardiac assistance: clinical experience. *The American Journal of Cardiology*, 27(1):3–11, 1971.

[33] M. Di Rienzo, G. Bertinieri, G. Mancia, and A. Pedotti. A new method for evaluating the baroreflex role by a joint pattern analysis of pulse interval and systolic blood pressure series. *Medical and Biological Engineering and Computing*, 23 (Supp I):313 – 314, 1985.

[34] M. Di Rienzo, P. Castiglioni, G. Mancia, A. Pedootti, and G. Parati. Advancements in estimating baroreflex function. *IEEE Engineering in Medicine and Biology*, 20 (2):25–32, 2001.

[35] J.F. Dixon and C.D. Farris. The abiomed bvs 5000 system. *AACN Advanced Critical Care*, 2(3):552–561, 1991.

[36] M. Ducher, J. Fauvel, M. Gustin, C. Cerutti, R. Najem, G. Cuisinaud, M. Laville, N. Pozet, and C. Paultre. A new non-invasive statistical method to assess the spontaneous cardiac baroreflex in humans. *Clinical Science (Colch)*, 88:651–655, 1995.

[37] S. Duschek, E. Matthia, and R. Schandry. Essential hypotension is accompanied by deficits in attention and working memory. *Behavioral Medicine*, 30(4):149–160, 2005.

[38] J. Ernsting and D.J. Parry. Some observations on the effects of stimulating the stretch receptors in the carotid artery of man. In *Journal of Physiology-London*, volume 137, pages P45–P46. Cambridge Univ Press, New York, 1957.

[39] M. Esler. The sympathetic nervous system in hypertension: back to the future? *Current Hypertension Reports*, 17(2):11, 2015.

[40] L. Faes, G. Nollo, A. Porta, and F. Ravelli. Noninvasive assessment of baroreflex sensitivity in post-MI patients by an open-loop parametric model of RR-systolic pressure interactions. *Computers in Cardiology*, 26:217–220, 1999.

[41] D. J. Farrar, J. D. Hill, D.G. Pennington, L.R. McBride, W.L. Holman, R.L. Kormos, D. Esmore, L.A. Gray Jr, P.E. Seifert, G.P. Schoettle, et al. Preoperative and postoperative comparison of patients with univentricular and biventricular support with the thoratec ventricular assist device as a bridge to cardiac transplantation. *The Journal of Thoracic and Cardiovascular Surgery*, 113(1):202–209, 1997.

[42] R. Filogonio, K.F. Orsolini, S.A. Castro, G.M. Oda, G.C. Rocha, D. Tavares, A.S. Abe, and C.A.C. Leite. Evaluation of the sequence method as a tool to assess spontaneous baroreflex in reptiles. *Journal of Experimental Zoology Part A: Ecological and Integrative Physiology*, 331(7):374–381, 2019.

[43] Ronald Aylmer Fisher. Statistical methods for research workers. In *Breakthroughs in statistics: Methodology and distribution*, pages 66–70. Springer, 1970.

[44] J.S. Floras. Blood pressure variability: a novel and important risk factor. *Canadian Journal of Cardiology*, 29(5):557–563, 2013.

[45] U. Forssell and L. Ljung. Closed-loop identification revisited. *Automatica*, 35:1215–1241, 1999.

[46] C. D. Gammon. Carotid sinus reflexes in patients with hypertension. *The Journal of Clinical Investigation*, 15:153, 1936.

[47] C.M. Gerveshi. *The dynamic response of the baroreceptor reflex loop in the rabbit: estimated using a statistical signal approach*. PhD thesis, Imperial College London, 1982.

[48] M. Glos, D. Romberg, S. Endres, and I. Fietze. Estimation of spontaneous baroreflex sensitivity using transfer function analysis: effects of positive pressure ventilation. *Biomedizinische Technik*, 52:66–72, 2007.

[49] D.S. Goldstein and W.P. Cheshire. Beat-to-beat blood pressure and heart rate responses to the Valsalva maneuver. *Clinical Autonomic Research*, 27(6):361–367, 2017.

[50] S. Gouveia, A. Rocha, P. Laguna, and P. Lago. Time domain baroreflex sensitivity assessment by joint analysis of spontaneous SBP and RR series. *Biomedical Signal Processing and Control*, 4 (3):254–261, 2009.

[51] S. Gouveia, A. Rocha, P. Laguna, P. Van de Borne, and P. Lago. Improved BRS assessment using the global approach in the sequences technique. *Computers in Cardiology*, 33:641–644, 2006.

[52] S. Gouveia, A. Rocha, P. Van de Borne, and P. Lago. Assessing baroreflex sensitivity in the sequence technique: local versus global approach. *Computers in Cardiology*, 32:279–282, 2005.

[53] B.P. Griffith, R.L. Kormos, H.S. Borovetz, K. Litwak, J.F. Antaki, V.L. Poirier, and K.C. Butler. Heartmate ii left ventricular assist system: from concept to first clinical use. *The Annals of Thoracic Surgery*, 71(3):S116–S120, 2001.

[54] E.H. Groenland and W. Spiering. Baroreflex amplification and carotid body modulation for the treatment of resistant hypertension. *Current Hypertension Reports*, 22(4):1–8, 2020.

[55] S.-J. Guild. Private Communication, 2018.

[56] S.-J. Guild, P.C. Austin, M. Navakatikyan, J.V. Ringwood, and S.C. Malpas. Dynamic relationship between sympathetic nerve activity and renal blood flow: a frequency domain approach. *American Journal of Physiology-Regulatory, Integrative and Comparative Physiology*, 281(1):R206–R212, 2001.

[57] I. Gustavsson, L. Ljung, and T. Söderström. Identification of processes in closed loop—identifiability and accuracy aspects. *Automatica*, 13(1):59–75, 1977.

[58] A.C. Guyton, T.G. Coleman, and H.J. Granger. Circulation: overall regulation. *Annual Review of Physiology*, 34(1):13–44, 1972.

[59] T. Guyton and J. Hall. *Textbook of Medical Physiology*. Saunders, 2006.

[60] M. E. Hall, J. M. do Carmo, A. A. da Silva, L. A. Juncos, Z. Wang, and J. E. Hall. Obesity, hypertension, and chronic kidney disease. *International Journal of Nephrology and Renovascular Disease*, 7:75, 2014.

[61] J. Hauser, J. Parak, M. Lozek, and J. Havlik. System analyze of the Windkessel models. *Space*, 100:5, 2012.

[62] S. Hegde, I. Ahmed, and N. Aeddula. Secondary hypertension. *StatPearls*, 2023.

[63] Yaron Hellman, Adnan S Malik, Kathleen A Lane, Changyu Shen, I-Wen Wang, Thomas C Wozniak, Zubair A Hashmi, Sarah D Munson, Jeanette Pickrell, Marco A Caccamo, et al. Pulse oximeter derived blood pressure measurement in patients with a continuous flow left ventricular assist device. *Artificial Organs*, 41(5):424–430, 2017.

[64] K. Heusser, J. Tank, S. Engeli, A. Diedrich, J. Menne, S. Eckert, T. Peters, F.C.G.J. Sweep, H. Haller, A.M. Pichlmaier, et al. Carotid baroreceptor stimulation, sympathetic activity, baroreflex function, and blood pressure in hypertensive patients. *Hypertension*, 55(3):619–626, 2010.

[65] S. Hiller-Sturmhöfel and A. Bartke. The endocrine system: an overview. *Alcohol Health and Research World*, 22(3):153, 1998.

[66] H.M. Horsman, Y.C. Tzeng, D.C. Galletly, and K.C. Peebles. The repeated sit-to-stand maneuver is a superior method for cardiac baroreflex assessment: a comparison with the modified Oxford method and Valsalva maneuver. *American Journal of Physiology-Regulatory, Integrative and Comparative Physiology*, 307(11):R1345–R1352, 2014.

[67] H. Hytti, R. Takalo, and H. Ihalainen. Tutorial on multivariate autoregressive modelling. *Journal of Clinical Monitoring and Computing*, 20:101–108, 2006.

[68] Y. Ikeda, T. Kawada, M. Sugimachi, O. Kawaguchi, T. Shishido, T Sato, H. Miyano, W. Matsuura, J. Alexander Jr, and K. Sunagawa. Neural arc of baroreflex optimizes dynamic pressure regulation in achieving both stability and quickness. *American Journal of Physiology-Heart and Circulatory Physiology*, 271(3):H882–H890, 1996.

[69] Y.M. Ishbulatov, A.R. Kiselev, E.N. Mureeva, Y.V. Popova, A.V. Kurbako, V.I. Gridnev, B.P. Bezruchko, M.A. Simonyan, E.I. Borovkova, O.M. Posnenkova, et al. Diagnostics of coupling between low-frequency loops in cardiovascular autonomic control in adults, newborns and mathematical model using cross-recurrence analysis. *Russian Open Medical Journal*, 8(4):1–5, 2019.

[70] Jessica R Ivy and Matthew A Bailey. Pressure natriuresis and the renal control of arterial blood pressure. *The Journal of Physiology*, 592(18):3955–3967, 2014.

[71] V Jahmunah, Shu Lih Oh, Joel Koh En Wei, Edward J Ciaccio, Kuang Chua, Tan Ru San, and U Rajendra Acharya. Computer-aided diagnosis of congestive heart failure using ECG signals–a review. *Physica Medica*, 62:95–104, 2019.

[72] B.J. Janssen, S. C. Malpas, S. L. Burke, and G. A. Head. Frequency-dependent modulation of renal blood flow by renal nerve activity in conscious rabbits. *American Journal of Physiology - Regulatory, Integrative and Comparative Physiology*, 273(2):R597–R608, 1997.

[73] C. Julien. The enigma of Mayer waves: facts and models. *Cardiovascular Research*, 70(1):12–21, 2006.

[74] C. Julien. An update on the enigma of Mayer waves. *Cardiovascular Research*, 116(14):e210–e211, 2020.

[75] Loay S Kabbani, Semeret Munie, Judith Lin, Mauricio Velez, Iyad Isseh, Sara Brooks, Stephanie Leix, and Alexander D Shepard. Flow patterns in the carotid arteries of patients with left ventricular assist devices. *Annals of Vascular Surgery*, 39:182–188, 2017.

[76] W.B. Kannel, P. Sorlie, W.P. Castelli, and D. McGee. Blood pressure and survival after myocardial infarction: the Framingham study. *The American Journal of Cardiology*, 45(2):326–330, 1980.

[77] AS Karavaev, Yu M Ishbulatov, VI Ponomarenko, BP Bezruchko, AR Kiselev, and MD Prokhorov. Autonomic control is a source of dynamical chaos in the cardiovascular system. *Chaos*, 29(12):121101, 2019.

[78] A. Kardos, G. Watterich, R. de Mendeez, M. Csanady, B. Casadei, and L. Rudas. Determinants of spontaneous baroreflex sensitivity in a healthy working population. *Hypertension*, 37:911–916, 2001.

[79] T. Kawada, T. Miyamoto, R. Mukkamala, and K. Saku. Linear and nonlinear identification of the carotid sinus baroreflex in the very low-frequency range. *Physiological Reports*, 10(14):e15392, 2022.

[80] T. Kawada, T. Sato, T. Shishido, M. Inagaki, T. Tatewaki, Y. Yanagiya, M. Sugimachi, and K. Sunagawa. Summation of dynamic transfer characteristics of left and right carotid sinus baroreflexes in rabbits. *American Journal of Physiology-Heart and Circulatory Physiology*, 277(3):H857–H865, 1999.

[81] T. Kawada, T. Shishido, M. Inagaki, T. Tatewaki, C. Zheng, Y. Yanagiya, M. Sugimachi, and K. Sunagawa. Differential dynamic baroreflex regulation of cardiac and renal sympathetic nerve activities. *American Journal of Physiology-Heart and Circulatory Physiology*, 280(4):H1581–H1590, 2001.

[82] T. Kawada, C. Zheng, Y. Yanagiya, K. Uemura, T. Miyamoto, M. Inagaki, T. Shishido, M. Sugimachi, and K. Sunagawa. High-cut characteristics of the baroreflex neural arc preserve baroreflex gain against pulsatile pressure. *American Journal of Physiology-Heart and Circulatory Physiology*, 282(3):H1149–H1156, 2002.

[83] A. Kazimierska, M. M Placek, A. Uryga, P. Wachel, M. Burzyńska, and M. Kasprowicz. Assessment of baroreflex sensitivity using time-frequency analysis during postural change and hypercapnia. *Computational and Mathematical Methods in Medicine*, 2019, 2019.

[84] H. Khalil and R. Zeltser. Antihypertensive medications. In *StatPearls*. StatPearls Publishing, 2022.

[85] B. A. Kingwell, G. A. McPherson, and P. I. Korner. Assessment of gain of tachycardia and bradycardia responses of cardiac baroreflex. *American Journal of Physiology*, 260(4 Pt 2):H1254–63, 1995.

[86] James K Kirklin, David C Naftel, Francis D Pagani, Robert L Kormos, Lynne W Stevenson, Elizabeth D Blume, Marissa A Miller, J Timothy Baldwin, and James B Young. Sixth intermacs annual report: a 10,000-patient database. *The Journal of Heart and Lung Transplantation*, 33(6):555–564, 2014.

[87] MA Kirkman and M Smith. Intracranial pressure monitoring, cerebral perfusion pressure estimation, and ICP/CPP-guided therapy: a standard of care or optional extra after brain injury? *British journal of anaesthesia*, 112(1):35–46, 2014. Publisher: Oxford University Press.

[88] R.I. Kitney. A nonlinear model for studying oscillations in the blood pressure control system. *Journal of Biomedical Engineering*, 1(2):89–99, 1979.

[89] K. Kotani, Z.R. Struzik, K. Takamasu, H.E. Stanley, and Y. Yamamoto. Model for complex heart rate dynamics in health and diseases. *Physical Review E*, 72(4):041904, 2005.

[90] M. T. La Rovere, G. D. Pinna, and G. Raczak. Baroreflex sensitivity: measurement and clinical implications. *Annals of Noninvasive Electrocardiology*, 13(2):191–207, 2008.

[91] M. T. La Rovere, G.D. Pinna, R. Maestri, E. Robbi, A. Caporotondi, G. Guazzotti, P. Sleight, and O. Febo. Prognostic implications of baroreflex sensitivity in heart failure patients in the beta-blocking era. *Journal of the American College of Cardiology*, 53(2):193–199, 2009.

[92] M. T. La Rovere, G. Specchia, A. Mortara, and P. Schwartz. Baroreflex sensitivity, clinical correlates, and cardiovascular mortality among patients with a first myocardial infarction. A prospective study. *Circulation*, 78:816–824, 1988.

[93] M.T. La Rovere, J.T. Bigger Jr, F.I. Marcus, A. Mortara, P.J. Schwartz, ATRAMI (Autonomic Tone and Reflexes After Myocardial Infarction) Investigators, et al. Baroreflex sensitivity and heart-rate variability in prediction of total cardiac mortality after myocardial infarction. *The Lancet*, 351(9101):478–484, 1998.

[94] M.T. La Rovere, R. Maestri, and G.D. Pinna. Baroreflex sensitivity assessment-latest advances and strategies. *Eur Cardiology*, 7(2):89–92, 2011.

[95] M.T. La Rovere, G.D. Pinna, R. Maestri, and P. Sleight. Clinical value of baroreflex sensitivity. *Netherlands Heart Journal*, 21:61–63, 2013.

[96] J. C. Lagarias, J. A. Reeds, M. H. Wright, and P. E. Wright. Convergence properties of the Nelder–Mead simplex method in low dimensions. *SIAM Journal on Optimization*, 9(1):112–147, 1998.

[97] P. Lanfranchi and V. Somers. Arterial baroreflex function and cardiovascular variability: interactions and implications. *Americal Journal of Physiology-Regulatory, Integrative and Comparative Physiology*, 283:815–826, 2002.

[98] D. Laude, V. Baudrie, and J.-L. Elghozi. Tuning of the sequence technique. *IEEE engineering in medicine and biology magazine*, 28(6):30, 2009.

[99] D. Laude, J.-L. Elghozi, A. Girard, E. Bellard, M. Bouhaddi, P. Castiglioni, C. Cerutti, A. Cividjian, M. Di Rienzo, J.-O. Fortrat, et al. Comparison of various techniques used to estimate spontaneous baroreflex sensitivity (the EuroBaVar study). *American Journal of Physiology-Regulatory, Integrative and Comparative Physiology*, 286(1):R226–R231, 2004.

[100] K. Li, H. Rüdiger, R. Haase, and T. Ziemssen. An innovative technique to assess spontaneous baroreflex sensitivity with short data segments: multiple trigonometric regressive spectral analysis. *Frontiers in physiology*, 9:10, 2018.

[101] Y.-D. Lin and S. I. Zida. Estimation of baroreflex sensitivity by Gaussian average filtering decomposition. *Biomedical Signal Processing and Control*, 68:102576, 2021.

[102] H.-K. Liu, S.-J. Guild, J. V. Ringwood, C. J. Barrett, Bridget L. L., S.-K. Nguang, and S. C. Navakatikyan, M. Aand Malpas. Dynamic baroreflex control of blood pressure: influence of the heart vs. peripheral resistance. *American Journal of Physiology - Regulatory, Integrative and Comparative Physiology*, 283(2):R533–R542, 2002.

[103] L. Ljung. *System identification: Theory for the user (2nd Ed.)*. Prentice-Hall, 1999.

[104] T.E. Lohmeier and J.E. Hall. Device-based neuromodulation for resistant hypertension therapy: too early for prime time? *Circulation Research*, 124(7):1071–1093, 2019.

[105] M. Lorenzo, J. Rico-Feijoo, J. Martín, C. Adecoa, and C. Garcia-Bernardo. Evaluation of leff ventricle stroke volumen with the new lidco rapidv2 monitor with cnap module versus transthoracic echocardiography in post-operative critical care patients: 3ap4-8. *European Journal of Anaesthesiology| EJA*, 31:41, 2014.

[106] J. Ludbrook, G. Mancia, A. Ferrari, and A. Zanchetti. Factors influencing the carotid baroreceptor response to pressure changes in a neck chamber. *Clinical Science and Molecular Medicine*, 51(s3):347s–349s, 1976.

[107] S. MacMahon, R. Peto, R. Collins, J. Godwin, J. Cutler, P. Sorlie, R. Abbott, J. Neaton, A. Dyer, and J. Stamler. Blood pressure, stroke, and coronary heart disease: part 1, prolonged differences in blood pressure: prospective observational studies corrected for the regression dilution bias. *The Lancet*, 335(8692):765–774, 1990.

[108] R. Maestri, G. Pinna, A. Mortara, M. La Rovere, and L. Tavazzi. Assessing baroreflex sensitivity in post-myocardial infarction patients: comparison of spectral and phenylephrine techniques. *Journal of the Americal College of Cardiology*, 31 (2):344–351, 1998.

[109] A. Malliani, F. Lombardi, and M. Pagani. Power spectrum analysis of heart rate variability: a tool to explore neural regulatory mechanisms. *British Heart Journal*, 71:1–2, 1994.

[110] S.C. Malpas, R.D. Bendle, G.A. Head, and J.H. Ricketts. Frequency and amplitude of sympathetic discharges by baroreflexes during hypoxia in conscious rabbits. *American Journal of Physiology - Heart and Circulatory Physiology*, 271(6):H2563–H2574, 1996.

[111] S.C. Malpas, R.G. Evans, G.A. Head, and E.V. Lukoshkova. Contribution of renal nerves to renal blood flow variability during hemorrhage. *American Journal of Physiology - Regulatory, Integrative and Comparative Physiology*, 274(5):R1283–R1294, 1998.

[112] K. B. Margulies and J. E. Rame. Adaptations to pulsatile versus nonpulsatile ventricular assist device support, 2011.

[113] J. R. Martina, B. E. Westerhof, N. de Jonge, J. van Goudoever, P. Westers, S. Chamuleau, D. van Dijk, B. F.M. Rodermans, B. A.J.M. de Mol, and J.R. Lahpor. Noninvasive arterial blood pressure waveforms in patients with continuous-flow left ventricular assist devices. *ASAIO Journal*, 60(2):154–161, 2014.

[114] Masimo. Masimo lidco™ noninvasive hemodynamic monitoring. Technical report, Masimo, 2021.

[115] V. McLoone. *Modelling of Long and Short Term Blood Pressure Control Systems*. PhD thesis, Maynooth University, 2014.

[116] Legacy Medsearch. Physiological mechanism of action in heart failure, 2019. Online; Accessed April 19,2023.

[117] F.H. Messerli, B. Williams, and E. Ritz. Essential hypertension. *The Lancet*, 370(9587):591–603, 2007.

[118] D.C. Montgomery, E.A. Peck, and G.G. Vining. *Introduction to linear regression analysis*. John Wiley & Sons, 2021.

[119] J.J. Moré. The Levenberg-Marquardt algorithm: implementation and theory. In *Numerical Analysis*, pages 105–116. Springer, 1978.

[120] H. Morimatsu, K. Ishikawa, C.N. May, M. Bailey, and R. Bellomo. The systemic and regional hemodynamic effects of phenylephrine in sheep under normal conditions and during early hyperdynamic sepsis. *Anesthesia & Analgesia*, 115(2):330–342, 2012.

[121] M. Nalini, E. Oranuba, H. Poustchi, S.G. Sepanlou, A. Pourshams, M. Khoshnia, A. Gharavi, S.M. Dawsey, C.C. Abnet, P. Boffetta, et al. Causes of premature death and their associated risk factors in the Golestan Cohort Study, Iran. *BMJ open*, 8(7):e021479, 2018.

[122] E. Nava and S. Llorens. The paracrine control of vascular motion. A historical perspective. *Pharmacological research*, 113:125–145, 2016.

[123] G.L. Navar. Integrating multiple paracrine regulators of renal microvascular dynamics. *American Journal of Physiology-Renal Physiology*, 274(3):F433–F444, 1998.

[124] G. Nollo, A. Porta, L. Faes, M. Del Greco, M. Disertori, and F. Ravelli. Causal linear parametric model for baroreflex gain assessment in patients with recent myocardial infarction. *American Journal of Physiology Heart Circulatory Physiology*, 280:1830–1839, 2001.

[125] S. Ogoh, P.J. Fadel, P. Nissen, Ø. Jans, C. Selmer, N.H. Secher, and P.B. Raven. Baroreflex-mediated changes in cardiac output and vascular conductance in response to alterations in carotid sinus pressure during exercise in humans. *The Journal of Physiology*, 550(1):317–324, 2003.

[126] H. Oka, S. Mochio, M. Yoshioka, M. Morita, and K. Inoue. Evaluation of baroreflex sensitivity by the sequence method using blood pressure oscillations and R-R interval changes during deep respiration. *European Neurology*, 50:230–243, 2003.

[127] World Health Organization et al. *Tracking universal health coverage: 2021 global monitoring report*. World Health Organization, 2021.

[128] O. Ormezzano, J.-L. Cracowski, J.-L.. Quesada, H. Pierre, J.-M.. Mallion, and J.-P. Baguet. EVAluation of the prognostic value of BARoreflex sensitivity in hypertensive patients: the EVABAR study. *Journal of Hypertension*, 26:1373–1378, 2008.

[129] J. W. Osborn. Hypothesis: set-points and long-term control of arterial pressure. a theoretical argument for a long-term arterial pressure control system in the brain rather than the kidney. *Clinical and Experimental Pharmacology and Physiology*, 32(5-6):384–393, 2005.

[130] K. J. Osterziel, D. Hänlein, R. Willenbrock, C. Eichhorn, F. Luft, and R. Dietz. Baroreflex sensitivity and cardiovascular mortality in patients with mild to moderate heart failure. *Heart*, 73(6):517–522, 1995.

[131] M. Pagani, V. Somers, R. Furlan, S. Dell'Orto, J. Conway, G. Baselli, S. Cerutti, P. Sleight, and A. Malliani. Changes in autonomic regulaion induced by physical training in mild hypertension. *Hypertension*, 12:600–610, 1988.

[132] T.G. Papaioannou, R. Fasoulis, P. Toumpaniaris, C. Tsioufis, P. Dilaveris, D. Soulis, D. Koutsouris, and D. Tousoulis. Assessment of arterial baroreflex sensitivity by different computational analyses of pressure wave signals alone. *Computer Methods and Programs in Biomedicine*, 172:25–34, 2019.

[133] R. Parmer, J. Cervenka, and R. Stone. Baroreflex sensitivity and heredity in essential hypertension. *Circulation*, 85:497–503, 1992.

[134] C.B. Patel, J.A. Cowger, and A. Zuckermann. A contemporary review of mechanical circulatory support. *The Journal of Heart and Lung Transplantation*, 33(7):667–674, 2014.

[135] D. Patton, J. Triedman, M. Perrott, A. Vidian, and J. Saul. Baroreflex gain: characterization using autoregressive moving average analysis. *American Journal of Physiology: Heart Circculatory Physiology*, 39:1240–1249, 1996.

[136] L. Paulis, U.M. Steckelings, and T. Unger. Key advances in antihypertensive treatment. *Nature Reviews Cardiology*, 9(5):276–285, 2012.

[137] G. W. Pcikering, M. Kissin, and P. Rothschild. Relationship of the carotid sinus mechanism to persistent high blood pressure in man. *Clinical Science*, 2:193, 1936.

[138] T.G. Pickering, G.A. Harshfield, H.D. Kleinert, S. Blank, and J.H. Laragh. Blood pressure during normal daily activities, sleep, and exercise: comparison of values in normal and hypertensive subjects. *Jama*, 247(7):992–996, 1982.

[139] M. Pitzalis, F. Mastropasqua, F. Massari, A. Passantino, R. Colombo, A. Mannarini, C. Forleo, and P. Rizzon. Effect of respiratory rate on the relationships between RR interval and systolic blood pressure fluctuations: a frequency-dependent phenomenon. *Cardiovascular Research*, 38:332–339, 1998.

[140] J. Ponte and M.J. Purves. Measurement of the frequency response of carotid sinus baroreceptors in the cat. *Medical and Biological Engineering*, 12(6):800–802, 1974.

[141] J. Ponte and M.J. Purves. Receptor dynamics using correlation techniques. *Medical and Biological Engineering*, 12(6):792–799, 1974.

[142] A. Porta, G. Baselli, O. Rimoldi, A. Malliani, and M. Pagani. Assessing baroreflex gain from spontaneous variability in conscious dogs: role of causality and respiration. *American Journal of Physiology: Heart Circulatory Physiology*, 279:2558–2567, 2000.

[143] G. Preiss and C. Polosa. Patterns of sympathetic neuron activity associated with Mayer waves. *American Journal of Physiology-Legacy Content*, 226(3):724–730, 1974.

[144] R. Ramchandra. Private Communication, 2023.

[145] P. B. Raven and M. W. Chapleau. Blood pressure regulation XI: overview and future research directions. *European Journal of Applied Physiology*, 114:579–586, 2014.

[146] I.A. Reid. Interactions between ang II, sympathetic nervous system, and baroreceptor reflexes in regulation of blood pressure. *American Journal of Physiology-Endocrinology And Metabolism*, 262(6):E763–E778, 1992.

[147] Centers for Disease Control and Prevention (CDC). Hypertension cascade: Hypertension prevalence, treatment and control estimates among us adults aged 18 years and older applying the criteria from the American College of Cardiology and American Heart Association's 2017 hypertension guideline—NHANES 2015–2018, 2017.

[148] J. Ringwood, S. Malpas, and Kinnane O. Prediction of low frequency blood pressure oscillations via a combined heart/resistance model. *IFAC Proceedings Volumes*, 38(1):60–65, 2005.

[149] J. V. Ringwood. On Windkessel models, December 2007.

[150] J. V. Ringwood, V. Mangourova, S. J. Guild, and S. Malpas. A Nonlinear Model for Vasoconstriction, September 2006. Type: Conference Paper.

[151] J.V. Ringwood and S.C. Malpas. Slow oscillations in blood pressure via a nonlinear feedback model. *American Journal of Physiology-Regulatory, Integrative and Comparative Physiology*, 280(4):R1105–R1115, 2001.

[152] J.V. Ringwood, F. Taussi, and A.M. de Paor. The effect of pulsatile blood flow on blood pressure regulatory mechanisms. In *2012 IEEE International Conference on Control Applications*, pages 609–614. IEEE, 2012.

[153] H. Robbe, L. Mulder, H. Ruddel, W. Langewitz, J. Veldman, and G. Mulder. Assessment of baroreflex reflex sensitivity by means of spectral analysis. *Hypertension*, 10:538–543, 1987.

[154] R.C. Robbins and P.E. Oyer. Bridge to transplant with the novacor left ventricular assist system. *The Annals of Thoracic Surgery*, 68(2):695–697, 1999.

[155] H. Rüdiger, L. Klinghammer, and K. Scheuch. The trigonometric regressive spectral analysisï¿½a method for mapping of beat-to-beat recorded cardiovascular parameters on to frequency domain in comparison with fourier transformation. *Comput Meth and Prog in Biomed*, 58:1–15, 1999.

[156] K. Sagawa. Baroreflex control of systemic arterial pressure and vascular bed. In *Handbook of Physiology The Cardiovascular System: Peripheral Circulation and Organ Blood Flow*, volume III, chapter 14, pages 453–496. Am. Physiol. Soc., 1983.

[157] I.M. Salman, O.Z. Ameer, S. McMurray, S.F. Hassan, A. Sridhar, S.J. Lewis, and Y.-H. Hsieh. Low intensity stimulation of aortic baroreceptor afferent fibers as a potential therapeutic alternative for hypertension treatment. *Scientific Reports*, 12(1):1–12, 2022.

[158] Giulia Sandrone, Andrea Mortara, Daniela Torzillo, Maria Teresa La Rovere, Alberto Malliani, and Federico Lombardi. Effects of beta blockers (atenolol or metoprolol) on heart rate variability after acute myocardial infarction. *The American Journal of Cardiology*, 74(4):340–345, 1994.

[159] F. Sansone, E. Zingarelli, R. Flocco, G. M. A. Dato, F. Parisi, G. Punta, P. G. Forsennati, G. L. Bardi, S. Del Ponte, F. Patanè, et al. Pulsed or continuous flow in long-term assist devices: a debated topic. *Transplantation Reviews*, 26(4):241–245, 2012.

[160] C. Schmid, T.DT. Tjan, C. Etz, C. Schmidt, F. Wenzelburger, M. Wilhelm, M. Rothenburger, G. Drees, and H.H. Scheld. First clinical experience with the incor left ventricular assist device. *The Journal of Heart and Lung Transplantation*, 24(9):1188–1194, 2005.

[161] R.M. Schmidt, M. Kumada, and K. Sagawa. Cardiovascular responses to various pulsatile pressures in the carotid sinus. *American Journal of Physiology-Legacy Content*, 223(1):1–7, 1972.

[162] H. Seidel and H. Herzel. Bifurcations in a nonlinear model of the baroreceptor-cardiac reflex. *Physica D: Nonlinear Phenomena*, 115(1-2):145–160, 1998.

[163] J Shanks, Yonis Abukar, NA Lever, M Pachen, IJ LeGrice, DJ Crossman, Alain Nogaret, JFR Paton, and Rohit Ramchandra. Reverse re-modelling chronic heart failure by reinstating heart rate variability. *Basic Research in Cardiology*, 117(1):4, 2022.

[164] Kiran Shekar, Shaun D Gregory, and John F Fraser. Mechanical circulatory support in the new era: an overview. *Critical Care*, 20:1–12, 2016.

[165] L.E.V. Silva, D.P.M. Dias, C.A.A. Da Silva, H.C. Salgado, and R. Fazan Jr. Revisiting the sequence method for baroreflex analysis. *Frontiers in Neuroscience*, 13:17, 2019.

[166] R. J. Simpson and H. M. Power. Applications of high frequency signal injection in non-linear systems. *International Journal of Control*, 26(6):917–943, 1977.

[167] A. Singh, B. Singh Saini, and D. Singh. A new baroreflex sensitivity index based on improved Hilbert–Huang transform for assessment of baroreflex in supine and standing postures. *Biocybernetics and Biomedical Engineering*, 36(2):355–365, 2016.

[168] M. S. Slaughter, J. G. Rogers, C. A. Milano, S. D. Russell, J. V. Conte, D. Feldman, B. Sun, A. J. Tatooles, R. M. 3rd Delgado, J. W. Long, T. C. Wozniak, W. Ghumman, D. J. Farrar, and O. H. Frazier. Advanced heart failure treated with continuous-flow left ventricular assist device. *The New England Journal of Medicine*, 361:2241–51, Dec 2009.

[169] H.S. Smyth, P. Sleight, and G.W. Pickering. Reflex regulation of arterial pressure during sleep in man: a quantitative method of assessing baroreflex sensitivity. *Circulation Research*, 24(1):109–121, 1969.

[170] C.M. Sorensen, P.P. Leyssac, O. Skott, and N.-H. Holstein-Rathlou. Role of the renin-angiotensin system in regulation and autoregulation of renal blood flow. *American Journal of Physiology-Regulatory, Integrative and Comparative Physiology*, 279(3):R1017–R1024, 2000.

[171] K. G. Soucy, S. C. Koenig, G. A. Giridharan, M. A. Sobieski, and M. S. Slaughter. Rotary pumps and diminished pulsatility: do we need a pulse? *ASAIO Journal*, 59(4):355–366, 2013.

[172] M. P. Spencer and A. B. Denison. Pulsatile blood flow in the vascular system. *Handbook of Physiology*, 2:839–864, 1963.

[173] J.A. Staessen, J. Wang, G. Bianchi, and W.H. Birkenhäger. Essential hypertension. *The Lancet*, 361(9369):1629–1641, 2003.

[174] C. A. Swenne. Baroreflex sensitivity: mechanisms and measurement. *Netherlands Heart Journal*, 21(2):58–60, 2013.

[175] Zihui Tan, Martin Besser, Simon Anderson, Caroline Newey, Ray Iles, John Dunning, and Florian Falter. Pulsatile versus nonpulsatile flow during cardiopulmonary bypass: Extent of hemolysis and clinical significance. *Asaio Journal*, 66(9):1025–1030, 2020.

[176] E. Tanai and S. Frantz. Pathophysiology of heart failure. *Comprehensive Physiology*, 6(1):187–214, 2011.

[177] A.K. Tangirala. *Principles of System Identification: Theory and Practice*. CRC Press, 2018.

[178] Task Force of the European Society of Cardiology and the North American Society of Pacing and Electrophysiology. Heart rate variability, standards of measurement, physiological interpretation, and clinical use. *Eur Heart J*, 17:354–381, 1996.

[179] C.E. Taylor, T. Witter, K. El Sayed, S.L. Hissen, A.W. Johnson, and V.G. Macefield. Relationship between spontaneous sympathetic baroreflex sensitivity and cardiac baroreflex sensitivity in healthy young individuals. *Physiological Reports*, 3(11):e12536, 2015.

[180] Steven Tenny and Mary R Hoffman. Odds ratio. 2017.

[181] T.N. Thrasher. Baroreceptors, baroreceptor unloading, and the long-term control of blood pressure. *American Journal of Physiology-Regulatory, Integrative and Comparative Physiology*, 288(4):R819–R827, 2005.

[182] D. Timms. A review of clinical ventricular assist devices. *Medical Engineering & Physics*, 33(9):1041 – 1047, 2011.

[183] T. Tohyama, K. Hosokawa, Y. Saku, K.and Oga, H. Tsutsui, and K. Sunagawa. Smart baroreceptor activation therapy strikingly attenuates blood pressure variability in hypertensive rats with impaired baroreceptor. *Hypertension*, 75(3):885–892, 2020.

[184] H. Van de Vooren, M. Gademan, C. Swenne, B. Ten Voorde, M. Schalij, and E. Van der Wall. Baroreflex sensitivity, blood pressure buffering, and resonance: what are the links? Computer simulation of healthy subjects and heart failure patients. *Journal of Applied Physiology*, 102:1348–1356, 2007.

[185] E. Vanoli and P. B. Adamson. Baroreflex sensitivity: methods, mechanisms, and prognostic value. *Pacing and Clinical Electrophysiology*, 17(3):434–445, 1994.

[186] S. Vari, S.-J. Guild, B. George, and R. Ramchandra. Intracranial baroreflex is attenuated in an ovine model of renovascular hypertension. *Scientific Reports*, 11(1):5816, 2021.

[187] J. Vašků, J. Wotke, P. Dobšák, A. Baba, A. Rejthar, Š. Kuchtíčková, K. Imachi, Y. Abe, I. Saito, T. Isoyama, et al. Acute and chronic consequences of non-pulsatile blood flow pattern in long-term total artificial heart experiment. *Pathophysiology*, 14(2):87–95, 2007.

[188] N. Wessel, A. Gapelyuk, J.F. Kraemer, K. Berg, and J. Kurths. Spontaneous baroreflex sensitivity: sequence method at rest does not quantify causal interactions but rather determines the heart rate to blood pressure variability ratio. *Physiological Measurement*, 41(3):03LT01, 2020.

[189] N. Wessel, A. Gapelyuk, J. Weiß, M. Schmidt, J.F. Kraemer, K. Berg, H. Malberg, H. Stepan, and J. Kurths. Instantaneous cardiac baroreflex sensitivity: xBRS method quantifies heart rate blood pressure variability ratio at rest and during slow breathing. *Frontiers in Neuroscience*, 14, 2020.

[190] S. Westaby, A.P. Banning, R. Jarvik, O.H. Frazier, D.W. Pigott, X.Y. Jin, P.A. Catarino, S. Saito, D. Robson, A. Freeland, et al. First permanent implant of the jarvik 2000 heart. *The Lancet*, 356(9233):900–903, 2000.

[191] K. Woldendorp, S. Gupta, J. Lai, K. Dhital, and C.S. Hayward. A novel method of blood pressure measurement in patients with continuous-flow left ventricular assist devices. *The Journal of Heart and Lung Transplantation*, 33(11):1183–1186, 2014.

[192] T. Wu, C. Chen, and T. Kao. Baroreflex sensitivity evaluation by Volterra Wiener model and the Laguerre expansion technique. *Computers in Cardiology*, 35:741–744, 2008.

[193] T. Yambe, S. Kobayashi, S. Nanka, S. Naganuma, S. Nitta, H. Matsuki, K.-I. Abe, M. Yoshizawa, T. Fukuju, K.-I. Tabayashi, et al. Fluctuations of the hemodynamic derivatives during left ventricular assistance using oscillated blood flow. *Artificial Organs*, 20(5):637–640, 1996.

[194] T. Yambe, S. Nitta, Y. Katahira, T. Sonobe, S. Naganuma, Y. Kakinuma, S. Kobayashi, M. Tanaka, M. Miura, N. Sato, et al. Mayer waves in dogs with total artificial heart. *The International Journal of Artificial Organs*, 15(10):601–605, 1992.

[195] T. Yambe, S. Nitta, S. Nanka, S. Kobayashi, S. Naganuma, Y. Katahira, M. Yoshizawa, T. Fukuju, N. Uchida, and K. Tabayashi. Spectral analysis of hemodynamics during left ventricular assistance. *The International Journal of Artificial Organs*, 19(6):367–371, 1996.

[196] T. Yambe, S.-I. Nitta, T. Sonobe, S. Naganuma, Y. Kakinuma, S.-I. Kobayashi, S. Nanka, N. Ohsawa, H. Akiho, M. Tanaka, et al. Origin of the rhythmical fluctuations in the animal without a natural heartbeat. *Artificial Organs*, 17(12):1017–1021, 1993.